

AD-A082 535 STANFORD UNIV CALIF GUIDANCE AND CONTROL LAB F/6 17/7
MODELING AND ERROR ANALYSIS OF A SUPERCONDUCTING GRAVITY GRADIO--ETC(U)
AUG 79 K Y WANG AFOSR-76-2913

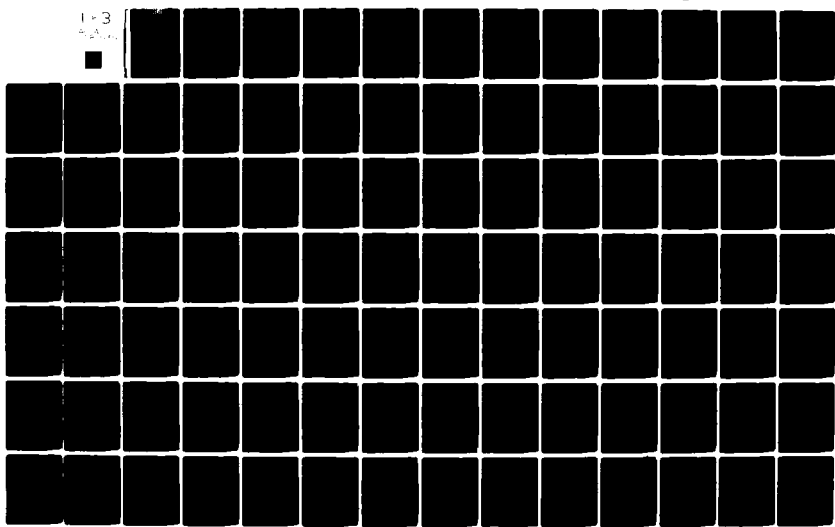
UNCLASSIFIED

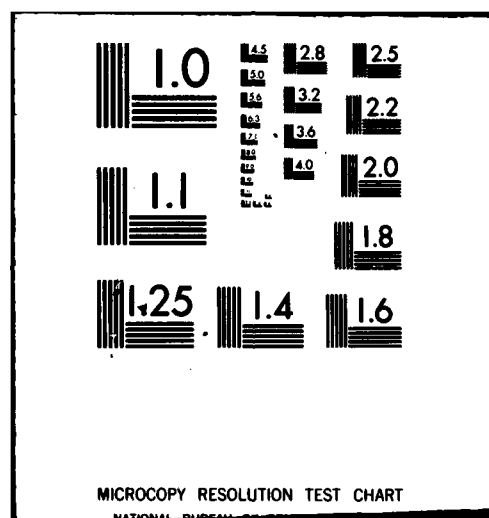
AFOSR-TR-80-0219

NL

1-3

2-3





ACA 082535

DDC FILE COPY

18 AFOSR/TR-80-0219 19 LEVEL II

6 MODELING AND ERROR ANALYSIS
OF A SUPERCONDUCTING GRAVITY GRADIOMETER.

by

10 Kai Yuen Wang

9 Final rept. 4

SC

Department of Aeronautics and Astronautics
Guidance and Control Laboratory

and the

Department of Physics

STANFORD UNIVERSITY
STANFORD, CALIFORNIA 94305

DTIC
ELECTED
S MAR 27 1980
D

This research was supported by

U.S. Air Force Office of Scientific Research
Bolling Air Force Base
Washington, D.C. 20332

15 Grant AFOSR-76-2913

16 2307 17 1A1

E

1 AUG 1979

Approved for public release;
distribution unlimited.



407256

80 3 20 027

UNCLASSIFIED

SECURITY CLASSIFICATION OF THIS PAGE (When Data Entered)

REPORT DOCUMENTATION PAGE		READ INSTRUCTIONS BEFORE COMPLETING FORM
1. REPORT NUMBER AFOSR-TR- 80-0219	2. GOVT ACCESSION NO.	3. RECIPIENT'S CATALOG NUMBER
4. TITLE (and Subtitle) MODELING AND ERROR ANALYSIS OF A SUPERCONDUCTING GRAVITY GRADIOMETER		5. TYPE OF REPORT & PERIOD COVERED Final
7. AUTHOR(s) Kai Yuen Wang		6. CONTRACT OR GRANT NUMBER(s) AFOSR 76-2913
9. PERFORMING ORGANIZATION NAME AND ADDRESS Department of Physics Stanford University Stanford, CA 94305		10. PROGRAM ELEMENT, PROJECT, TASK AREA & WORK UNIT NUMBERS 2309/A1 61102F
11. CONTROLLING OFFICE NAME AND ADDRESS AFOSR/NP Bolling AFB, Bldg. #410 Wash DC 20332		12. REPORT DATE August 1979
14. MONITORING AGENCY NAME & ADDRESS (if different from Controlling Office)		13. NUMBER OF PAGES 265
		15. SECURITY CLASS. (of this report) unclassified
		15a. DECLASSIFICATION/DOWNGRADING SCHEDULE
16. DISTRIBUTION STATEMENT (of this Report) Approved for public release; distribution unlimited.		
17. DISTRIBUTION STATEMENT (of the abstract entered in Block 20, if different from Report)		
18. SUPPLEMENTARY NOTES		
19. KEY WORDS (Continue on reverse side if necessary and identify by block number)		
20. ABSTRACT (Continue on reverse side if necessary and identify by block number) The demand for higher accuracy in inertial navigation systems has pushed the development of more accurate accelerometers and gyroscopes. Inertial navigation systems (INS) can now be built with error stemming mainly from the uncertainty of the vertical along the flight path (Savet, 1970). The deflection of the vertical is produced by mass anomalies on the surface of the earth. The error can be corrected by measuring the gravity gradient and using it in the navigation equations. This possibility has generated intensive interest and research in the field of gravity gradiometry. The lower bound of		

UNCLASSIFIED

SECURITY CLASSIFICATION OF THIS PAGE(When Data Entered)

the resolution of room temperature gravity gradiometers is thermal (Brownian) noise. By lowering the temperature to 4 K, the noise level is smaller by an order of magnitude. A comparatively simple gravity gradiometer can be built using some newly developed superconducting technology.

Unclassified

MODELING AND ERROR ANALYSIS
OF A SUPERCONDUCTING GRAVITY GRADIOMETER

by

Kai Yuen Wang

Department of Aeronautics and Astronautics
Guidance and Control Laboratory

and the

Department of Physics

STANFORD UNIVERSITY
STANFORD, CALIFORNIA 94305

This research was supported by
U.S. Air Force Office of Scientific Research
Bolling Air Force Base
Washington, D.C. 20332
Grant AFOSR-76-2913

Accession For	
NTIS	GRA&I
DDC TAB	<input checked="" type="checkbox"/>
Unannounced	<input type="checkbox"/>
Justification _____	
By _____	
Distribution/ _____	
Availability Codes _____	
Dist	Avail and/or
	special
A	

AUGUST 1979

A. D. Iacob
D. Iacob
A. D. Iacob
Technical Information Officer

I is

12 (7b).

ABSTRACT

The demand for higher accuracy in inertial navigation systems has pushed the development of more accurate accelerometers and gyroscopes. Inertial navigation systems (INS) can now be built with error stemming mainly from the uncertainty of the vertical along the flight path [Savet, 1970]. The deflection of the vertical is produced by mass anomalies on the surface of the earth. The error can be corrected by measuring the gravity gradient and using it in the navigation equations. This possibility has generated intensive interest and research in the field of gravity gradiometry.

The lower bound of the resolution of room temperature gravity gradiometers is thermal (Brownian) noise. By lowering the temperature to 4 K, the noise level is smaller by an order of magnitude. A comparatively simple gravity gradiometer can be built using some newly developed superconducting technology.

In this research, the feasibility of a cryogenic gravity gradiometer is demonstrated. For a baseline of 0.1 m, the instrument has a theoretical resolution of 10^{-2} E (Eötvos). A pair of superconducting accelerometers were constructed and tested in a push-pull arrangement. The resolution of the experimental unit is estimated to be about 50 E.

A theoretical study to model the responses of the gravity gradiometer to the various external inputs is conducted. The mathematical equations derived are used in the design of the loaded diaphragm proof mass. The error sources of the gravity gradiometer are identified. Their error contributions are reduced where possible; otherwise limits on the errors are set. Test facilities, especially the gravity gradient generator, are designed and built.

The theoretical investigations and experimental results show that the noise-induced vibrations of the proof masses of the gradiometer at their natural frequencies must be damped. To minimize additional thermal noise produced by resistive damping, feedback damping is used. The

theory of electronic damping for the cryogenic device is developed. An experimental circuit for the "noiseless" damping of a single accelerometer was built. The theoretical predictions were validated by the test results.

In the course of the research, the art of fabrication of the various gradiometer components are refined and improved to a high degree. For significant improvement of the sensitivity of the accelerometer, new technology has to be explored and developed. Building the sensing coil of the diaphragm by thick film deposition is but one of the techniques.

For some missions, such as geophysical surveys using a satellite-based gravity gradiometer, the resolution of the instrument required is an order of magnitude better than those of current room temperature gravity gradiometers. The cryogenic gravity gradiometer is found to be a viable alternative.

ACKNOWLEDGMENTS

I wish to extend my gratitude to my advisor, Professor Daniel B. DeBra for his advice, guidance, and encouragement throughout the course of this research. I also wish to thank Professors William Fairbank, Robin Giffard, and Dave Powell for their thorough reviews and helpful criticism of this dissertation. Special thanks go to Dr. Ho Jung Paik for his fruitful collaboration in the design and testing of the goniometer.

I would also like to express my thanks to my colleagues, Terry Orlando, Evan Mapoles, and Jim Hollenhorst who have assisted me in various stages of the project. The efforts of Bill Richman in the machining and fabrication of this research is greatly appreciated.

My appreciation is extended to Ms. Ida M. Lee for her super editing and typing of this dissertation.

Particular gratitude is expressed to the United States Air Force, Office of Scientific Research, who provided the financial support for this research under AFOSR Grant 76-2913.

A special note of thanks go to Nelly Ramos, who gave me much support and encouragement during the period of this research.

TABLE OF CONTENTS

<u>Chapter</u>		<u>Page</u>
	ABSTRACT	iii
	ACKNOWLEDGMENTS	v
	TABLE OF CONTENTS	vii
	List of Figures	xi
	List of Tables	xiv
	List of Symbols	xv
	English Letters	xv
	Greek Letters	xx
	Mathematical Symbols: Prefix, Suffixes, subscripts, etc.	xxii
	Abbreviations Used in Text	xxiii
I.	<u>INTRODUCTION</u>	1
	A. BACKGROUND	1
	B. THESIS OUTLINE	3
	C. CONTRIBUTION	4
	C-1 Accelerometer Optimization	4
	C-2 Gravity Gradiometer	4
	C-3 Electronic Cooling	4
II.	<u>GRAVITY GRADIOMETER FUNDAMENTALS</u>	5
	A. GRAVITY GRADIENT FIELD	5
	B. GRAVITY GRADIOMETERS	7
	B-1 Hughes Rotating Mass Gravity Gradiometer	8
	B-2 Bell Aerospace's Rotating Gravity Gradiometer	8
	B-3 Draper Lab's Flotation Gravity Gradiometer	11
	B-4 Micro-Balance Gravity Gradiometer	13
	B-5 Horizontal Gravity Gradiometer	13
	B-6 Vibrating String Gradiometer	16
	B-7 Sensitivity Dependence on Size	16
	B-8 Gradiometer Design Considerations	19
	C. SOME PRINCIPLES OF SUPERCONDUCTIVITY	19
	D. SUPERCONDUCTING ACCELEROMETER	26
	D-1 Principle of Accelerometer	26
	D-2 Optimum Performance	34
	D-3 Thermal Noise	36

TABLE OF CONTENTS (Cont)

<u>Chapter</u>		<u>Page</u>
	E. SUMMARY	38
III.	<u>THE DESIGN OF A SUPERCONDUCTING GRAVITY GRADIOMETER</u>	41
	A. OPTIMIZATION OF THE CRYOGENIC ACCELEROMETER	41
	A-1 Centrally Loaded Diaphragm	41
	A-2 The Ideal Accelerometer Model	47
	A-3 Static Deflection of the Loaded Diaphragm	47
	A-4 Large Deflection of Diaphragm	51
	A-5 Optimization of Dimensions of Proof Mass	56
	B. THE CURRENT DIFFERENCING GRAVITY GRADIOMETER	65
	C. THE DISPLACEMENT DIFFERENCING GRAVITY GRADIOMETER	75
	D. SUMMARY	81
	D-1 Gradiometer Design	81
	D-2 Superconducting Gravity Gradiometers	81
IV.	<u>NOISE AND ERROR SOURCES</u>	83
	A. THERMAL NOISE	83
	A-1 Thermal Noise of the Diaphragm	83
	A-2 Dynamic Range of Accelerometer	86
	A-3 Q and Dynamic Range of Accelerometer	89
	B. Q REDUCTION BY FEEDBACK	91
	B-1 Thermal Noise and Feedback Damping	91
	B-2 Feedback Circuit Design	94
	B-3 The Minimum Q Achievable	97
	C. ERROR SOURCES	102
	C-1 Drift	102
	C-2 Bias	103
	C-3 Effects of Rotation on Noise	104
	C-4 Axes Misalignment	109
	C-5 Scale Factor Matching	114
	D. SUMMARY	116

TABLE OF CONTENTS (Cont)

<u>Chapter</u>		<u>Page</u>
V.	<u>SUPERCONDUCTING HARDWARES</u>	121
	A. CONSTRUCTION OF THE CRYOGENIC GRADIOMETER	121
	B. SUPERCONDUCTING JOINTS	126
	B-1 Ultra Low Resistance	127
	C. THE SQUID DETECTION SYSTEM	132
	D. DAMPING BY FEEDBACK	139
	D-1 Test Circuit for Feedback Damping	139
	D-2 Noise of Feedback	146
	E. GRAVITY GRADIENT GENERATORS	148
	E-1 Planar Swing	148
	E-2 Symmetric Swing	151
	E-3 Mass Quadrapole	154
	F. SUMMARY	157
VI.	<u>TESTING OF CRYOGENIC GRAVITY GRADIOMETER</u>	159
	A. EXPERIMENTAL SETUP	159
	A-1 Cryogenic Space	159
	A-2 Shaker and Vibration Isolation	161
	A-3 Persistent Current Storage and Adjustment	164
	B. GRADIOMETER EXPERIMENTAL RESULTS	169
	B-1 Frequency-Current Relation	169
	B-2 Gradiometer Balancing	172
	B-3 Gradiometer Calibration	175
	C. DISCUSSION	183
VII.	<u>CONCLUSIONS AND RECOMMENDATIONS</u>	185
	A. CONCLUSIONS	185
	B. RECOMMENDATIONS	187

TABLE OF CONTENTS (Cont)

	<u>Page</u>
APPENDIX A: SCALE FACTOR OF A CRYOGENIC ACCELEROMETER	189
APPENDIX B: MOTIONS OF DIAPHRAGM WITH CENTRAL LOAD	191
APPENDIX C: LARGE DEFLECTIONS OF THIN PLATES	195
APPENDIX D: VIBRATIONAL MODELS OF THE GRADIOMETER	221
APPENDIX E: SPECTRAL DENSITY OF RANDOM VIBRATION OF A SINGLE DEGREE-OF-FREEDOM SYSTEM	235
REFERENCES	241

LIST OF FIGURES

<u>Fig. No.</u>		<u>Page</u>
II-1	HUGHES ROTATING MASS GRAVITY GRADIOMETER	9
II-2	BELL AEROSPACE'S ROTATING GRAVITY GRADIOMETER	10
II-3	DRAPER LAB'S FLOTATION GRAVITY GRADIOMETER	12
II-4	MICRO-BALANCE GRAVITY GRADIOMETER	14
II-5	HORIZONTAL GRAVITY GRADIOMETER	15
II-6	VIBRATING STRING GRAVITY GRADIOMETER	17
II-7	SCHEMATIC OF VARIABLE INDUCTANCES	22
II-8	BLOCK DIAGRAM OF SQUID	24
II-9	SPECTRAL DENSITY OF SQUID NOISE	25
II-10	DETAIL DRAWING OF A NIOBIUM DIAPHRAGM	28
II-11	CROSS-SECTIONAL VIEW OF THE SUPERCONDUCTING ACCELEROMETER	29
II-12	EFFECT OF MAGNETIC PRESSURE ON THE RESONANT FREQUENCY OF NIOBIUM DIAPHRAGM	32
II-13	STEPDOWN MATCHING TRANSFORMER	37
III-1	CROSS-SECTIONAL VIEW OF THE CENTRALLY LOADED DIAPHRAGM	43
III-2	VARIATION OF FREQUENCY RATIO VS RADIUS RATIO	45
III-3	CROSS-SECTIONAL VIEW OF THE OPTIMALLY SHAPED PROOF MASS	46
III-4	DEFLECTION OF THE DIAPHRAGM	50
III-5	RECTIFICATION ERROR	55
III-6	ERROR IN DISPLACEMENT ESTIMATE AS A RESULT OF UNCERTAINTY IN γ_3	57
III-7	THICKNESS EFFECTS ON THE THERMAL NOISE	64
III-8	CURRENT DIFFERENCING SCHEMES	66
III-9	SCHEMATIC DIAGRAM OF CURRENT DIFFERENCING GRAVITY GRADIOMETER	67
III-10	SCHEMATIC DIAGRAM OF THE DISPLACEMENT DIFFERENCING GRAVITY GRADIOMETER	75

LIST OF FIGURES (Cont)

<u>Fig. No.</u>		<u>Page</u>
IV-1	POWER SPECTRUM OF THE THERMAL NOISE AT THE OUTPUT OF THE ACCELEROMETER	84
IV-2	ELECTRICAL EQUIVALENT CIRCUIT OF THE RESONANT MODE OF THE DIAPHRAGM ACCELEROMETER	92
IV-3	EQUIVALENT CIRCUIT OF FEEDBACK DAMPING OF THE ACCELEROMETER	93
IV-4	BLOCK DIAGRAM OF FEEDBACK CIRCUIT	95
IV-5	BLOCK DIAGRAM OF FEEDBACK FOR GRADIOMETER	96
IV-6	BLOCK DIAGRAM OF CLOSED-LOOP FEEDBACK	97
IV-7	THE INDUCTANCES OF THE FEEDBACK DAMPING CIRCUIT	98
IV-8	ACCELEROMETER AXES ALIGNMENT FOR A ROTATING GRAVITY GRADIOMETER	105
IV-9	PLANAR PROJECTION OF THE GRAVITY FORCES ACTING ON THE PROOF MASSES OF A ROTATING GRAVITY GRADIOMETER	106
IV-10	COORDINATE FRAME OF THE GRADIOMETER	110
IV-11	FREQUENCY PLOTS OF SCALE FACTORS OF THE TWO GRAVITY GRADIOMETER ACCELEROMETERS	117
IV-12	GRADIOMETER ERROR COMPENSATION MODEL	118
V-1	SUPERCONDUCTING ACCELEROMETER COMPONENTS	122
V-2	CROSS-SECTIONAL VIEW OF THE CURRENT DIFFERENCING GRAVITY GRADIOMETER	123
V-3	CROSS-SECTIONAL VIEW OF THE CENTRALLY LOADED DIAPHRAGM	125
V-4	CROSS-SECTIONAL VIEW OF THE SUPERCONDUCTING "BUS-BAR" CONNECTIONS	127
V-5	PICTORAL SKETCH OF THE ULTRA-LOW RESISTANCE RESISTOR	128
V-6	SCHEMATIC OF TUNING CIRCUIT	129
V-7	ENERGY DECAY OF PERSISTENT CURRENT	131
V-8	MATCHING TRANSFORMER COIL FORM	134
V-9	CIRCUIT FOR THE TESTING OF TRANSFORMER	136

LIST OF FIGURES (Cont)

<u>Fig. No.</u>		<u>Page</u>
V-10	CIRCUIT FOR INDUCTANCE MEASUREMENTS OF THE MATCHING TRANSFORMER	137
V-11	GRADIOMETER FEEDBACK DAMPING CIRCUIT	141
V-12	TRANSFER FUNCTIONS OF THE BANDPASS FILTER AND THE OVERALL FEEDBACK	142
V-13	THE VARIATION OF RESONANCE DECAY TIME VS FEEDBACK GAIN	144
V-14	VECTOR DIAGRAM OF "IN-OUT" PENDULUM SWING	149
V-15	VECTOR DIAGRAM OF CROSS PENDULUM SWING	152
V-16	VECTOR DIAGRAM OF ROTATING ARM	154
V-17	MASS QUADRAPOLE GRAVITY GRADIENT GENERATOR	158
VI-1	CROSS-SECTONAL VIEW OF THE EXPERIMENTAL SETUP	160
VI-2	BLOCK DIAGRAM OF THE BALANCING GRADIOMETER	162
VI-3	GRADIOMETER CALIBRATION SETUP	163
VI-4	CAPACITANCE BRIDGE TO DETECT RESONANCES OF BIMORPH	165
VI-5	SHIFTS IN THE RESONANT FREQUENCY OF THE NIOBIUM DIAPHRAGM	166
VI-6	PERSISTENT CURRENT CHARGING CIRCUIT	168
VI-7	FREQUENCY RESPONSE OF THE TWO ACCELEROMETERS IN CDGG	171
VI-8	BALANCING OF THE CURRENT DIFFERENCING GRAVITY GRADIOMETER	174
VI-9	FREQUENCY RESPONSES OF THE CDGG	176
VI-10a,b	NOISE OUTPUT OF THE GRADIOMETER AT REST WITHOUT CALIBRATION SIGNAL	177 178
VI-11	GRADIENT SIGNAL OF THE SWINGING PENDULUM	180
VI-12	RESPONSE OF CDGG TO A SWINGING PENDULUM IN A CALIBRATION EXPERIMENT	182

LIST OF TABLES

<u>Table No.</u>		<u>Page</u>
II-1	TABLE OF OPTIMUM PERFORMANCE FOR THREE DIAPHRAGMS OF DIFFERENT FREQUENCIES.	35
IV-1	EFFECT OF Q ON NOISE	88
IV-2	THE TOLERABLE GRAVITY FOR 1% ERROR	114
V-1	ENERGY DECAY OF INDUCTANCE COIL	130
V-2	CHARACTERISTICS OF (S.H.E.) SYSTEM 330	132
V-3	DATA OF TRANSFORMER TESTING	138
V-4	COEFFICIENTS OF THE HARMONIC COMPONENTS OF THE GRADIENT GENERATORS	156
VI-1	CHARACTERISTICS OF THE ACCELEROMETERS	170

LIST OF SYMBOLS

a	Ch. III	outer radius of diaphragm
\bar{a}	Ch. III	common acceleration along the gradiometer
a_x		acceleration component along the x axis
A_c		area of pick-up coil
A	Ch. IV	spectral power density of acceleration noise
A_M		maximum A
A_a		spectral power density of accelerometer
A_g		spectral power density of gradiometer
b	Ch. III	inner radius of diaphragm
c		locally defined constant
C		capacitance
C_{rf}		capacitance in rf circuit
d		spacing between coil and diaphragm
d	Ch. V	length of vector \bar{d}
d_{min}		spacing that will produce the maximum sensitivity of accelerometer
D	Ch. III	flexural rigidity of material
E	Ch. III	Young's modulus
E		energy in joules
E_{max}		maximum energy transferred
E_N		noise energy in J/Hz
E_S		SQUID noise energy
f		frequency in Hz
f_r		resonant frequency
F	Ch. III	electromagnetic force acting on diaphragm
\bar{F}	Ch. II	gravitational field

LIST OF SYMBOLS (Cont)

g		earth's gravity (9.8 m/sec ²)
\bar{g}		gravity vector
g_x		x component of \bar{g}
G		universal gravitational constant
G_{fb}	Ch. IV	gain of feedback circuit
G_M	Ch. IV	current gain factor of feedback transformer
G_S	Ch. IV	gain of SQUID
G_V	Ch. IV	gain of voltage-to-current converter
G_V		earth vertical gradient component
G_H		earth horizontal gradient component
h		diaphragm thickness
h'		thickness of central load
H		magnetic intensity
H_i		heater switch i
H_a		applied magnetic field intensity
H_c		critical magnetic field intensity
H_I		transfer function of integrator
H_t	Ch. II	tangential magnetic field
H_z		vertical magnetic field
i		instantaneous current
i_s		instantaneous SQUID input current
i_3		instantaneous current in L_3
i_{fb}		feedback current
I		steady state current
I_j		steady-state current in element j

LIST OF SYMBOLS (Cont)

I_e		error current
I_s		SQUID current
I_{fb}		feedback current
I_{ij}		current stored in coil ij
I_{opt}		current that will yield maximum sensitivity
k	Ch. II	Boltzmann's constant
k		coupling coefficient of transformer
k_i		locally defined constant
K_{ij}	Ch. III	coupling coefficient between systems i and j
l		distance between proof masses of gradiometer
L		coil inductance
\bar{L}		vector
L_0		inductance of pick-up coil
L_a		inductance of primary coil of stepdown transformer
L_b		inductance of secondary coil of stepdown transformer
L_c		inductance of primary coil of matching transformer
L_d		inductance of primary coil of matching transformer
L_{eq}		equivalent inductance
L_i		inductance of coil i
L'_i		inductance of coil i after diaphragm displacement
L_{int}		internal inductance of system
L_p		parallel inductance of gradiometer
L_{rf}		inductance of rf circuit
L_s		inductance of SQUID input coil
LH_1		low resistance heat switch i

LIST OF SYMBOLS (Cont)

m	mass of proof mass
M	Ch. II mass of body
M	mutual inductance of transformer
\hat{n}	unit vector normal to a surface
N	turn ratio of solenoidal transformer
N_0	thermal noise of diaphragm
N_f	turn ratio of feedback transformer
N_p	turn ratio of pick-up transformer
p	Ch. III load factor (dimensionless)
P	central load of diaphragm
q	uniform load intensity of diaphragm
Q	quality factor
Q_E	quality factor of electrical system
Q_{fb}	quality factor of system with feedback damping
Q_M	quality factor of mechanical system
Q_T	quality factor of total system
r	radial distance
r_{int}	internal resistance of system
r_{opt}	optimum radial arm length of gradient generator
R	resistance in ohms
R	outer radius of plate
R	Ch. V length of vector \bar{R}
R_{eq}	equivalent resistance
R_{fb}	equivalent resistance with feedback damping
R_i	resistance of element i
R_L	load resistance

LIST OF SYMBOLS (Cont)

S	sensitivity of gradiometer in A/g
S	Ch. III vertical shear (dimensionless)
S_0	power density of white noise
S_{out}	power density of output signal
T	torque
T	absolute temperature in Kelvin
T_0	mean time between failures
T_c	critical temperature of superconductivity
U	scalar gravitational potential
v	voltage in volts
V	shear force at radial distance r
V_{fb}	feedback voltage
V_I	voltage of element I
V_N	equivalent noise voltage
V_S	SQUID output voltage
w	vertical displacement of an element of diaphragm
w_i	spectral density for item i
w_a	acceleration spectral density
x	displacement of diaphragm under acceleration
x	x axis of rectangular coordinates
x	Ch. III radial distance (dimension)
y	y axis of rectangular coordinates
y_m	maximum deflection of diaphragm (dimensionless)
z	z axis of rectangular coordinates
z_{fb}	equivalent impedance of feedback

LIST OF SYMBOLS (Cont)

Greek Symbols

α	Ch. III	radius ratio of diaphragm
α	Ch. II	slope of straight curve
α_a	Ch. IV	acceleration noise
α_i		misalignment angle i
β	Ch. III	square of radius ratio α
β		locally defined constants
β_T		coupling coefficient
γ		inductance ratio
γ	Ch. III	thickness ratio of diaphragm
γ_i		coefficient of Y_m to the power of i
$\tilde{\Gamma}$		gravity gradient tensor
Γ_{xy}		x, y components of the gravity gradient tensor
δ		ratio of inductance change to displacement
Δa		differential acceleration over the gradiometer
Δa_{\min}		the smallest Δa resolvable
ϵ	App. D	spring rate
ϵ_i		component of unit vector along axis i
ζ		damping ratio (excepting App. D)
η		geometric factor of curvature
θ		twist angle
λ	Ch. III	locally defined constant
λ	Ch. IV	maximum level of displacement
μ		Poisson's ratio
μ_0		permeability of free space

LIST OF SYMBOLS (Cont)

ν		Poisson's ratio
ξ	Ch. II	locally defined constant
ξ	Ch. III	displacement to radius ratio of diaphragm
ξ	Ch. IV	error
ξ	App. D	damping factor
ρ		density of diaphragm
ρ	Ch. IV	angle of swing
σ_i		sensitivity of accelerometer i
σ_{\max}	Ch. II	maximum tensile stress
σ_x	Ch. IV	standard deviation of distribution x
τ		time constant
τ	Ch. III	locally defined constant
ϕ	Ch. IV	tilt angle
ϕ		magnetic flux
ϕ_0		a flux quantum
ϕ_{ij}		magnetic flux linking elements i and u
ϕ_N		noise flux of SQUID
ω		natural angular frequency
ω_f		angular frequency of forcing function
ω_i		natural angular frequency of diaphragm i
ω_r		angular frequency of resonance
Ω		angular velocity of rotation

Prefix

Δx	small change in X
------------	---------------------

LIST OF SYMBOLS (Cont)

Suffixes

X(t)	time function of X
X(f)	frequency function of X
X(ω)	angular frequency function of X
X(s)	Laplace transform of X(t)

Subscripts

() ₀	steady state or original state
() _d	model designation
() _{max}	maximum value

Superscripts

\bar{A}	vector
\hat{A}	unit vector (in the direction of \bar{A})
$\bar{\bar{A}}$	tensor A

Miscellaneous

$\langle \rangle$	expected value
$ $	absolute value
*	convolution
$\hat{1}$	idem vector
//	parallel component, i.e., $L_1//L_2 \equiv (L_1^{-1} + L_2^{-1})^{-1}$

Abbreviations Used

A	amperes
BPF	bandpass filter
CDGG	current differencing gravity gradiometer
c.g.	center of gravity
dB/db	decibel
DDGG	displacement differencing gravity gradiometer
DOF	degree of freedom
E	Eötvos unit
INS	inertial navigation system
mA	milliamperes
MFP	multiple function probe
m/s^2	meters per second squared
p-p	peak-to-peak
PSD	power spectral density
psi	pounds per square inch
PZT	lead zirconate titanate
rf/RF	radio frequency
rms	root mean square
SAH	sensitive axis horizontal
SAV	sensitive axis vertical
SCU	SQUID control unit
SNR	signal-to-noise ratio
SPU	signal processing unit
SQUID	superconducting quantum interference device
TBAN	tolerable background acceleration noise
VIC	voltage to current converter

Chapter 1

INTRODUCTION

A. BACKGROUND

The demand for higher accuracy in inertial navigation systems has pushed the development of more accurate accelerometers and gyroscopes. Inertial navigation systems (INS) can now be built with error stemming mainly from the uncertainty of the vertical along the flight path [Savet, 1970]. The deflection of the vertical is produced by mass anomalies on the surface of the earth. The error can be corrected by measuring the gravity gradient and using it in the navigation equations. This possibility has generated intensive interest and research in the field of gravity gradiometry.

The first gravity gradiometer was built by Baron von Eötvos in 1888. It was a simple torsion-balance type of device with sensitivity comparable to the modern gravity gradiometers. Despite its long integration time, it was once employed for geophysical survey until it was supplanted by the more versatile gravimeter. Other than navigation, the gravity gradiometer may be used in satellite geodetic survey and geophysical survey from an aircraft. For these purposes, the moving-base gravity gradiometer must have a sensitivity of 0.1 to 1 E (Eötvos) ($\approx 10^{-10} \text{ g/m}$) with 10 sec averaging.

The measurement of gravity gradient involves detection of differential force of very minute magnitudes typically of the order of 10^{-12} Newtons. It is imperative to isolate the instrument from environmental noise. In addition, the instrument design must facilitate separating the signal from the residual noise. The approach to minimize noise through isolation is exemplified by the flotation gradiometer built by Trageser [1970] of the Draper Laboratory. The other approach of spectrum separation through rotation is adopted by Bell Aerospace [1977] and Hughes [1973]. Regardless of the approach, the fundamental limit to instrument

sensitivity is the thermal noise of the sensor. For the gradiometer design outlined above, the best sensitivity achievable for the physical size allowed is 1 E. Thus it seems appropriate that a totally different approach is needed to overcome this problem.

To this end a novel idea has been provided by a recent development in the field of Superconductive Physics. Paik [1974] developed a super-sensitive transducer to detect the minute vibrations induced in a 1 ton, cryogenically cooled and magnetically levitated gravitational wave antenna. The antenna concept was conceived by Fairbank and Hamilton of Stanford in 1965, to minimize thermal noise of the antenna owing to molecular Brownian noise. The works of Joseph Weber [1969, 1979] on gravitational wave detection in 1969 intensified the research in this field. In 1974, Paik reported his resonance transducer.

The transducer is mounted on the end face of the antenna. It has a thin diaphragm as the proof mass. Vibrations of the antenna induced by gravitational wave are coupled to the diaphragm which is tuned to the frequency of the antenna. The vibrations of the diaphragm are detected using a superconducting quantum interference device (SQUID) [Lounasmaa, 1974]. At Stanford, diaphragm displacement down to 10^{-16} m has been resolved.

As Paik's transducer is essentially a specific force device, it is straightforward to use it as an accelerometer. In this research, a gravity gradiometer has been constructed of a pair of these superconducting accelerometers and some specific superconducting technology has been developed. At 4 K, the thermal noise of the cryogenic gradiometer is ten times smaller than room temperature equivalents. In addition, there is very little creep since materials are very stable at the low temperature. The cryogenic space also eliminates error due to thermal gradient. Moreover, superconducting materials are perfect electromagnetic shields. This property and some special circuit technology allow detection of extremely small signals in a virtually clean environment. A theoretical sensitivity of 0.1 E for the cryogenic instrument is readily achieved.

B. THESIS OUTLINE

In Chapter II, a survey of modern gravity gradiometers is given. It is followed by a review of the properties of superconductivity used in the superconducting accelerometer. The accelerometer is then described and its thermal noise calculated. Using the output relation of the accelerometer, the condition for optimal performance is determined. Although this chapter is primarily a review, the work on optimal performance is original.

The analysis to optimize the sensitivity of the accelerometer is covered in Chapter III. This leads to the design of a "loaded" diaphragm. The equations governing the deflection and the frequency of the diaphragm are determined. The signal-to-thermal-noise ratio is used as the criterion for the optimization.

The system descriptions of the two models of superconducting gradiometers are given. The first model utilized the concept of differencing the output currents of two accelerometers. This is the Current Differencing Gravity Gradiometer (CDGG) which is the principal research subject of this dissertation; the second, measuring the displacement difference of two proof masses directly. It is the Displacement Differencing Gravity Gradiometer (DDGG) which is currently being built by E. Mapoles at Stanford.

Chapter IV determines the relation between dynamic range, the sensor Q , and the thermal noise of the cryogenic accelerometer. An 'electronic' cooling technique to reduce the mechanical Q is investigated, and the design of an electronic feedback is given. In addition, various error sources of the gradiometer are given, some design criteria are derived, and isolation requirements are determined.

In Chapter V the various hardware and techniques relevant to the cryogenic gradiometer are described. Topics covered include superconducting joints, ultra-low resistance and transformers.

The electronic circuit implementing the feedback damping of the previous chapter is designed. Some experimental results validating the theoretical predictions are included.

Three methods of generating test gradient signals are also given in this chapter.

In Chapter VI, the experimental results of the testing of the Current Differencing Gravity Gradiometer are documented. The experimental set-up and procedures of these tests are described.

Conclusions and Recommendations are given in Chapter VII.

C. CONTRIBUTIONS

The principal contributions of this dissertation are as follows.

C.1 Accelerometer Optimization

- (1) Development and optimization of the loaded diaphragm sensor.
- (2) Determination of the optimal values of the variable parameters of a superconducting accelerometer.

C.2 Gravity Gradiometer

- (1) Derivation of the current differencing circuit and the mathematical output equation of the gravity gradiometer.
- (2) Investigation of the error sources of the gradiometer.
- (3) Construction and testing a prototype of the current differencing gravity gradiometer. Design and construction of affiliated hardware.

C.3 Electronic Cooling

- (1) Conceptualization of feedback to produce damping without increasing noise proportionally.
- (2) Experimental verification of the application of electronic cooling to the superconducting accelerometer.

Chapter II

GRAVITY GRADIOMETER FUNDAMENTALS

The use of a superconducting device to measure the gradients of a gravity field becomes feasible following the work of Paik [1974]. Paik developed a very sensitive superconducting specific-force meter. In this chapter, the nature of the gravity field will be analysed and some of the instruments currently under development will be discussed. The superconducting accelerometer will be described briefly after the relevant principles of superconductivity have been reviewed.

A. GRAVITY GRADIENT FIELD

The gravitational field of a mass can be described by classical potential theory [Savet, 1970]. The gravitational field, \bar{F} , outside a body is solenoidal and unrotational in nature. Denoting its scalar potential by $U(x, y, z)$, these basic properties can be written as

$$\bar{\nabla}U = -\bar{F} \quad (2.1a)$$

$$\nabla^2U = 0 \quad (2.1b)$$

$$\bar{\nabla} \times \bar{F} = 0 \quad (2.1c)$$

using standard vector notations. For a point mass, M , its gravitational potential at distance r is given by

$$U(x, y, z) = G \frac{M}{r} \quad (2.2)$$

where G is the universal gravitational constant with a value of $6.67 \times 10^{-11} \text{ N}\cdot\text{m}^2/\text{kg}^2$.

From (2.1), we deduced that $U(x, y, z)$ and its gradient $\bar{\nabla}U$ are harmonic functions. Hence the first and second derivatives have non-zero values in space, unless the potential is everywhere constant.

That is to say, any conceivable field, except the constant field, is nonuniform in space. Being a vector field, changes arise from both changes in magnitude and direction. Furthermore, while the field itself varies as square of the distances, its gradient varies as the cube. These considerations offer great possibilities for exploration if the field itself can be eliminated in the measurement of a relatively weak gradient.

The term "gravity gradient" denotes the 3 second partial space derivatives of the potential, usually arranged as a tensor

$$\begin{bmatrix} \Gamma_{xx} & \Gamma_{xy} & \Gamma_{xz} \\ \Gamma_{yx} & \Gamma_{yy} & \Gamma_{yz} \\ \Gamma_{zx} & \Gamma_{zy} & \Gamma_{zz} \end{bmatrix} . \quad (2.3)$$

The unrotational structure of the field yields three equations as a result of (2.1c). They are

$$\Gamma_{xy} = \Gamma_{yx} \quad (2.4a)$$

$$\Gamma_{xz} = \Gamma_{zx} \quad (2.4b)$$

$$\Gamma_{zy} = \Gamma_{yz} . \quad (2.4c)$$

The solenoidal feature viewed in a stationary system yields another, viz.,

$$\Gamma_{xx} + \Gamma_{yy} + \Gamma_{zz} = 0 \quad (2.5)$$

which is the Laplace equation. This can be derived from (2.1b). Thus only five gradient components are independent and they form the components of a second-rank covariant tensor. One gradiometer of the type discussed in this thesis can measure two of these components. Thus a

combination of three gradiometers arranged in the proper spatial orientation would allow for the determination of the tensor. Since six quantities are measured when only five are independent, the extra measurement can be used as a redundancy check. Such orientations have been worked out by Pelka [1977] and Trageser [1970].

B. GRAVITY GRADIOMETERS

Gravity gradiometers can be used instead of gravimeters for detailed geophysical surveys. Unlike gravimeters, measurements using a gravity gradiometer could be done in a moving vehicle. Such a system is capable of producing free air gravity anomaly data of essentially the same quality as those obtained by fixed site gravimeter observation and leveling [Savet, 1970].

Another application of the gravity gradiometer is the correction of the deflection of the vertical in inertial navigation systems (INS) [Crowley, 1959]. The major error source of a state-of-the-art INS is the uncertainty in the vertical. Roberson [1961] and Diesel [1964] demonstrated the determination of the vertical using gravity gradient. A triad of three gradiometers, mounted on the same platform, will supply the required inputs to reduce this error [Pelka, 1977].

In addition, gradiometers can be orbited in satellites for geodesy surveys [Forward, 1973]. These and other applications [Beyer, 1973] require an instrument sensitivity of 1 Eötvos (E) or better [Heller, 1975].

The Eötvos is defined as

$$1 \text{ Eötvos} \triangleq 10^{-9} \text{ sec}^{-2}. \quad (2.6)$$

The baseline (distance between c.g.'s of proof masses) of a typical instrument is 0.1 meter. Thus a gradiometer of 1 E sensitivity must be able to measure a force differential of $10^{-11} g$ (earth's gravity) over its baseline. This is especially demanding in the presence of earth's gravity field.

Some of the gradiometers being developed are basically a matched pair of accelerometers separated by a given distance. The others sense the torque produced by the gradient field on the sensor. Since the best commercially available accelerometers have a quoted sensitivity of 10^{-7} g, building an accelerometer-derived instrument would not be easy. Five gradiometers presently in existence or under development are described in the following sections.

B-1 Hughes Rotating Mass Gravity Gradiometer

The rotating mass gradiometer is a resonant spring-mass system with a torsional vibration mode. Figure II-1 gives a schematic of the instrument [Forward, 1973]. The sensor rotates about its torsionally resonant axis at an angular rate which is exactly half the torsional resonant frequency. The differential force resulting from the gradient of a gravity field excites the vibrational modes of the structure of the sensor. The differential torque amplified by the resonance of the structure is coupled into the sensor output at twice rotation frequency.

This instrument has the following features:

- linear acceleration is cancelled mechanically;
- gradient signal appears at twice frequency while system noise appear at the rotation frequency;
- signal is preamplified by structural resonance, and
- doubly differential design distinguishes gradient torques from case torques.

This instrument has achieved a sensitivity of 1 E with its sensitive axis horizontal. However, it has a significant bias with questionable stability.

B-2 Bell Aerospace's Rotating Gravity Gradiometer

Bell's instrument consists of four Bell accelerometers mounted equidistance from the center of a rotating disc platform as shown in Fig. II-2. Their sensitive axes are tangential to the circle and are therefore insensitive to centrifugal acceleration.

The matched accelerometer pairs, a_1, a_2 and a_3, a_4 sense the differential acceleration of the gravity field. Similar to the Hughes'

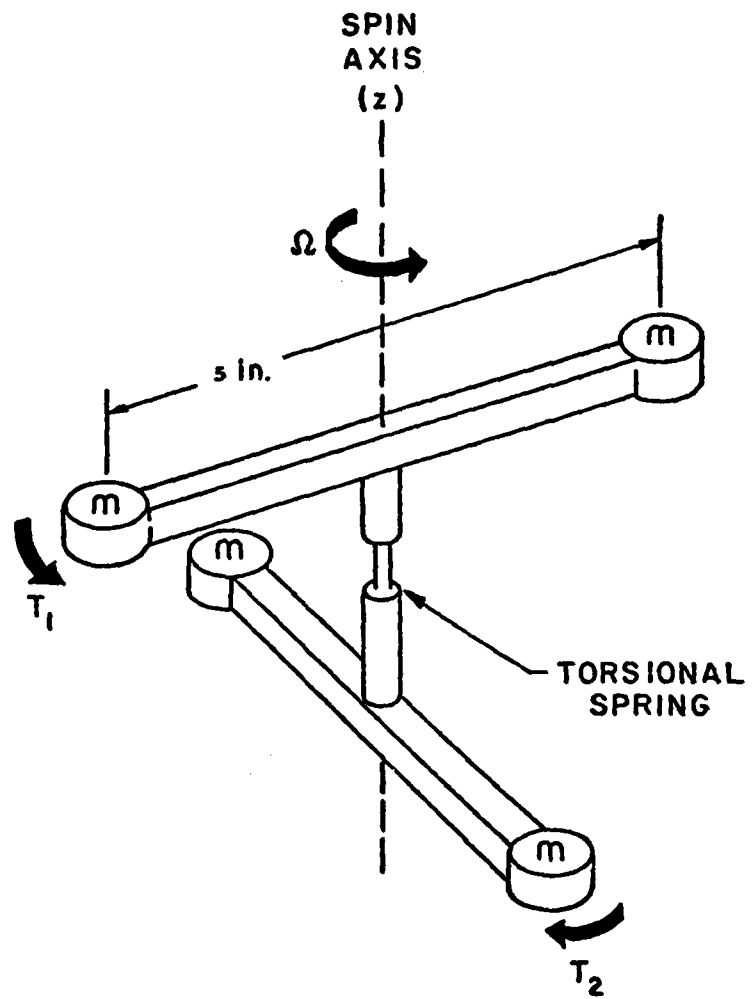


FIG. II-1 HUGHES COMPANY ROTATING GRAVITY GRADIOMETER [from Forward, 1973]. The spin frequency of the rotating structure, Ω , is exactly half the torsional frequency. As a result of the rotation, the gradient signal has a frequency of twice the spin rate. This signal is mechanically amplified by the structure and detected by a transducer at the torsional spring.

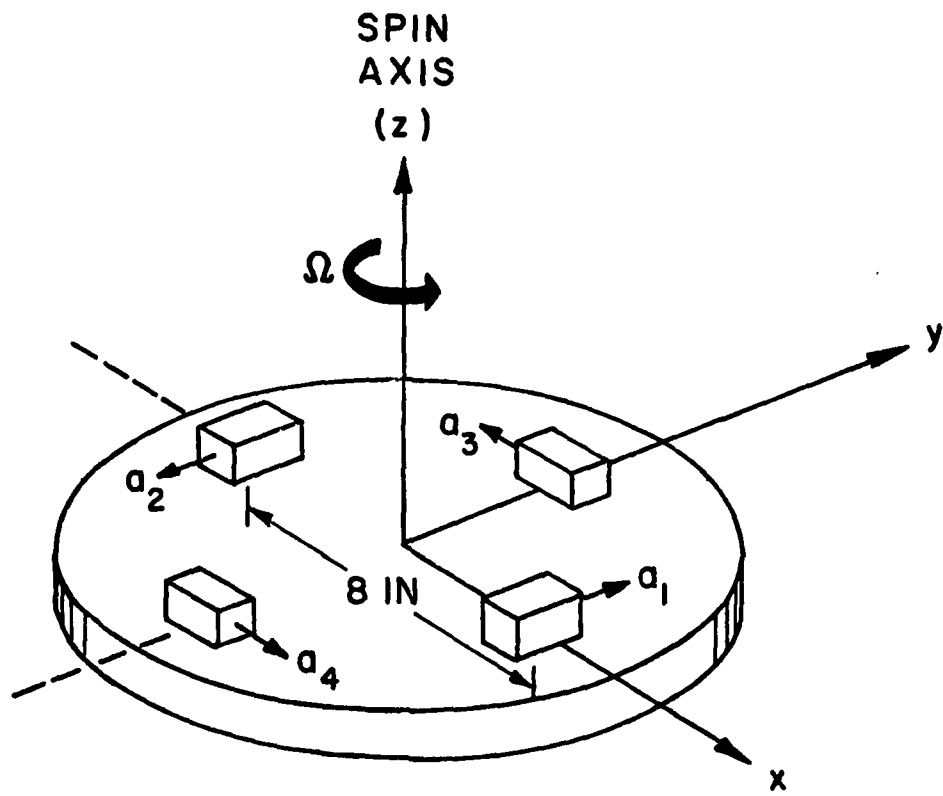


FIG. II-2 BELL AEROSPACE CORP.'s ROTATING GRAVITY GRADIOMETER [Bell, 1977]. The accelerometers are placed at equal radial distance from the center of the rotation platform and aligned with their axes tangential. The output difference of a matched pair of radial accelerometers is a function of the gravity gradient modulated at twin-spin rate. The gradient signal is isolated from low frequency noise and other rotation related environmental noise.

device, rotating the disc modulates the gradient information which appears at twice frequency.

The force rebalance accelerometers must be built to achieve an acceleration sensitivity of $10^{-11} g$ in the narrow bandwidth of the output from a synchronous phase sensitive demodulator at twice the rotation frequency. Brownian noise becomes the limiting factor at acceleration below $10^{-8} g$ in the standard instrument. To overcome this limit, modification of the proof mass and internal damping were necessary. Sensitivity of close to 1 E has been demonstrated and reduction of many systematic errors is in progress.

B-3 Draper Lab's Flotation Gravity Gradiometer

The flotation technology used in this instrument by Draper Lab. is derived from their successful flotation gyroscope. Figure II-3 shows a sketch of the spherical float of the gravity gradiometer [Trageser, 1970; Trageser, 1975]. An earlier model has a cylindrical float with the dense material forming two diametrically opposite strips down the inside of the cylinder.

The sensor body is floated in a fluid which fills the gap between the float and the gradiometer housing. The freon fluid density provides nearly perfect support for the float by neutral buoyancy. Small centering forces up to one dyne are applied by means of electric fields. Temperature control is used to adjust the buoyancy to minimize these forces. To achieve the buoyancy required, the temperature of the fluid must be maintained to a few tens of 10^{-6}°F .

The mass of the float is concentrated in two weights as shown. The gravity gradient of the earth produces a small torque of close to 1 $\mu\text{dyne-cm}/\text{E}$. This torque acts on the float to produce a rotation relative to the stabilized housing. The angle of rotation is sensed and is applied as a feedback restoring torque electromagnetically. This torque is a measurement of the gradient.

The flotation gradiometer has a sensitivity fundamentally limited by Brownian noise. This limits the sensitivity to 0.104 and 1.07 E at integration times of 10 and 1.80 sec respectively. Hardware

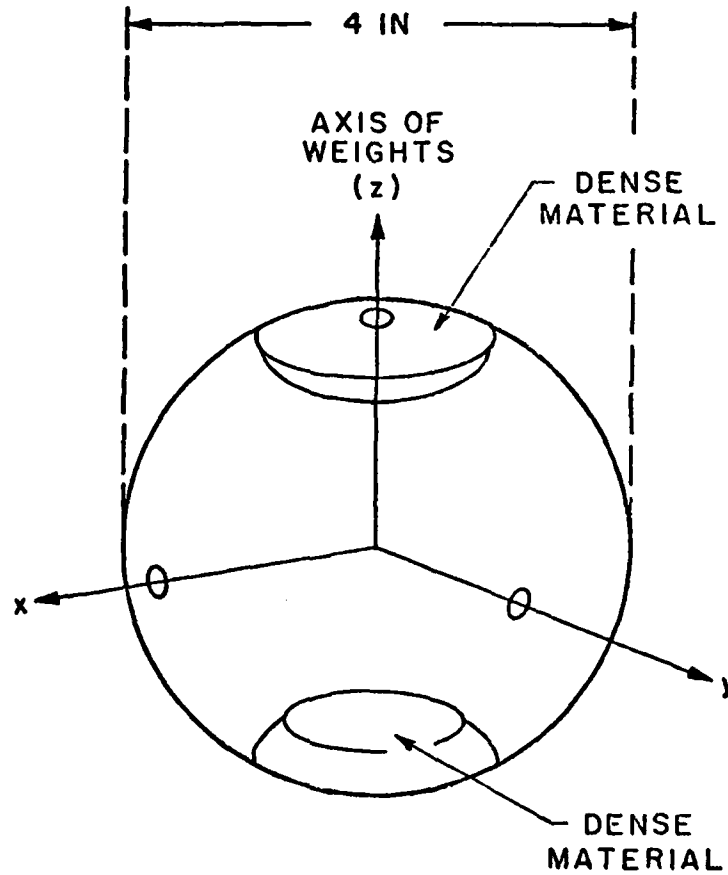


FIG. II-3 DRAPER LAB'S FLOTATION GRAVITY GRADIOMETER
[Trageser, 1975]. The flotation sphere is immersed in a fluid and held in neutral buoyancy. The feedback torque is generated through field windings to maintain the orientation of the sphere. The feedback current producing the torque is a measurement of the gravity gradient.

development problems have slowed the experimental evaluation of other systematic error sources.

B-4 Micro-Balance Gravity Gradiometer

Figure II-4 shows a sketch of the gravity gradiometer [Thompson, 1970]. The sensor is essentially a sensitive fused quartz balance. The two proof masses are 10 gm each and a gradient will cause the balance arm to tilt through a certain angle of deflection. This angle is proportional to the gradient and can be calibrated. It can be measured optically or by capacitive transducer. The sensitivity is adjusted by varying a small weight on the central hook.

This instrument is not much different from the torsion balance used by Baron von Eötvos in 1888 and has the same limitation. Thompson [1970] claimed that this gradiometer can be operated in a moving vehicle, particularly in the quiet environment of a submarine or a high flying aircraft. The assertion is not generally accepted and has not been demonstrated.

B-5 Horizontal Gravity Gradiometer

The design by Hansen [1971] of the horizontal gravity gradiometer made use of the ultra-sensitive tiltmeter technology of Hughes Research Lab. Four servo-controlled tiltmeters are mounted under a single quartz flat as shown in Fig. II-5. The horizontal gravity gradient of the earth produces an apparent tilt of the vertical at each bubble. The gradiometer contains eight servomotors, two for each bubble. These are controlled by currents which are driven by the motion of the bubbles, producing forces to level, bend, and twist the quartz flat until the bubbles stop moving. The three components of the gradient in the plane of the quartz flat can be read from the currents in the servomotors. Sensitivity of the device was recorded at 10 E.

As a result of its design, the gradiometer is limited to measure only the horizontal component of the gravity field.

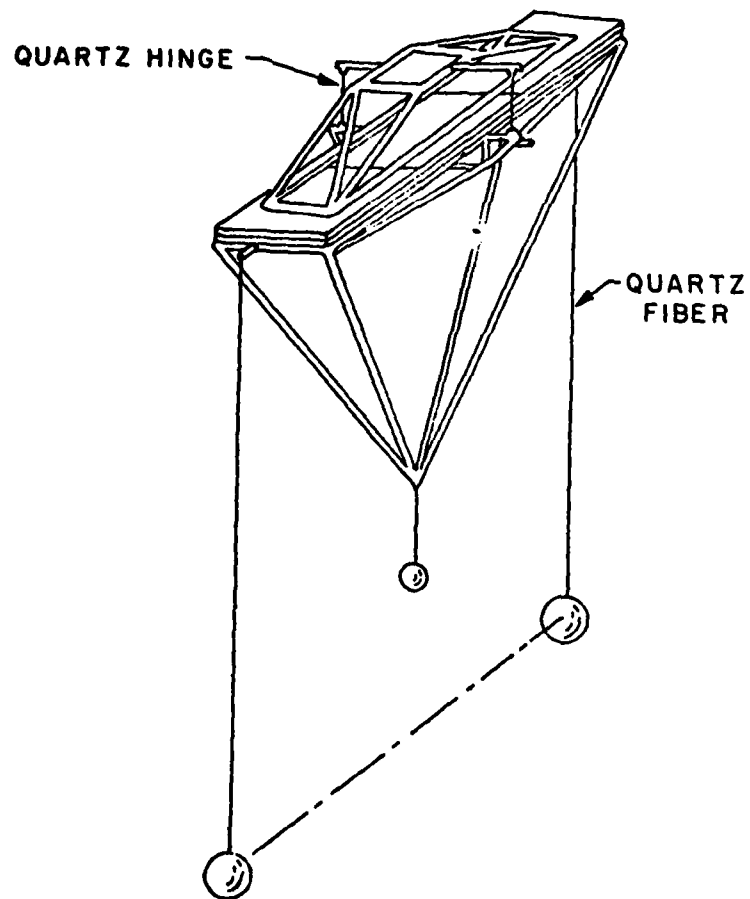


FIG. II-4 MICROBALANCE GRAVITY GRADIOMETER [Thompson, 1970].
The angle by which the balance beam deviated from the horizontal is a function of the gradient of the gravity field. The sensitivity of the balance is adjusted by raising or lowering the small mass attached to the center of the beam.

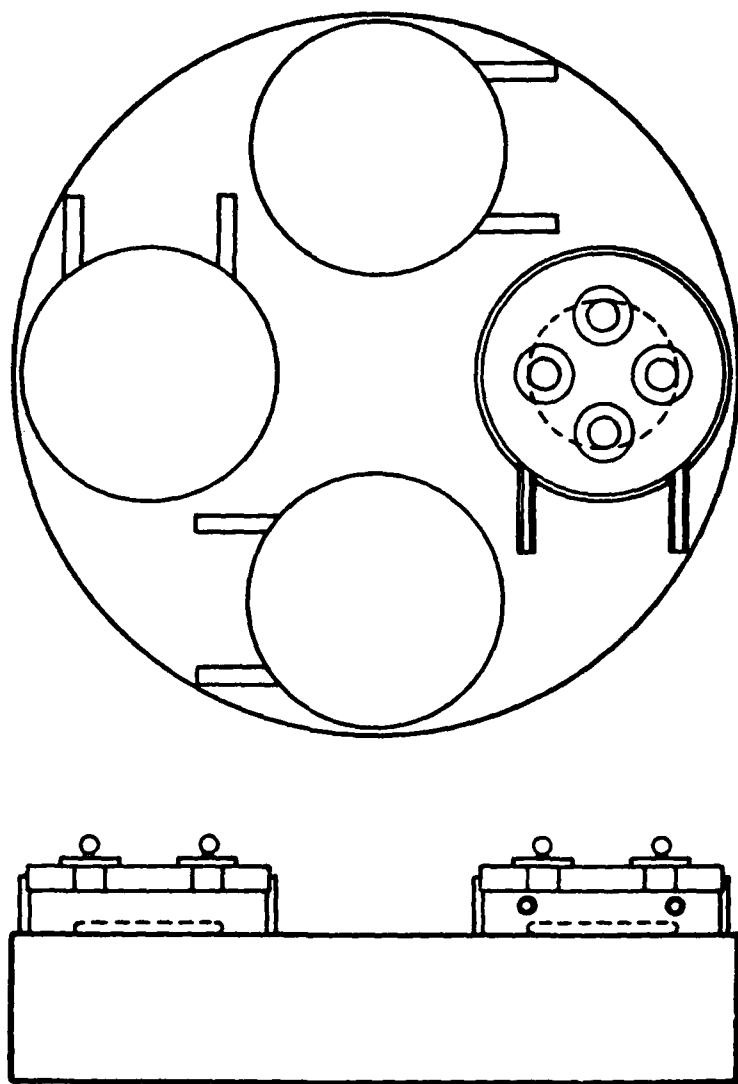


FIG. II-5 HORIZONTAL GRAVITY GRADIOMETER. The gradiometer consists of four bubble tilt meters placed on an optically flat quartz disc. To maintain each individual bubble fixed in its reference frame, each individual bubble fixed in its reference frame, the disc is contoured using the electromechanical thrustors associated with each bubble. The gradiometer model will output the gradient using the currents in all thrustors as input.

B-6 Vibrating String Gradiometer

Of all the accelerometer principles, the vibrating string accelerometer is the only one that naturally lends itself to the design of a gradiometer [Thompson, 1965; Thompson, 1966] [Forward, 1973].

The schematic of the vibrating string gradiometer is given in Fig. II-6. In this instrument, two proof masses are identically suspended by their supports and restraining springs. The relative motion of the masses under different acceleration is sensed by the change of the vibration frequency of the spring as its tension changes. The requirement for matching masses, maintaining proper bias tension, and the radial strain sensitivity which is less suited to rotation than the shear configuration employed by Bell, have made it a less desirable candidate for development for moving base applications.

This concept is revived in the displacement differencing gravity gradiometer proposed independently by Paik of Stanford. A brief outline of the device is given in a later section.

B-7 Sensitivity Dependence on Size

Two observations are made from the survey of the gradiometer. The resolution of all five instruments under development are limited by Brownian noise at their present size.

The second relates the sensitivity of a given instrument to its size. In all cases, the sensitivity of the instrument, σ , is proportional to $1/\omega_0^2$ where ω_0 is the natural frequency of the proof mass. The time constant, τ , is proportional to $1/\omega_0 \zeta$ where ζ is the damping ratio. The relations are

$$\sigma \propto \frac{1}{\omega_0^2} \quad (2.7a)$$

$$\tau \propto \frac{1}{\omega_0 \zeta} \quad (2.7b)$$

Combining the two equations give

$$\sigma/\tau^2 = \text{constant} \quad (2.8)$$

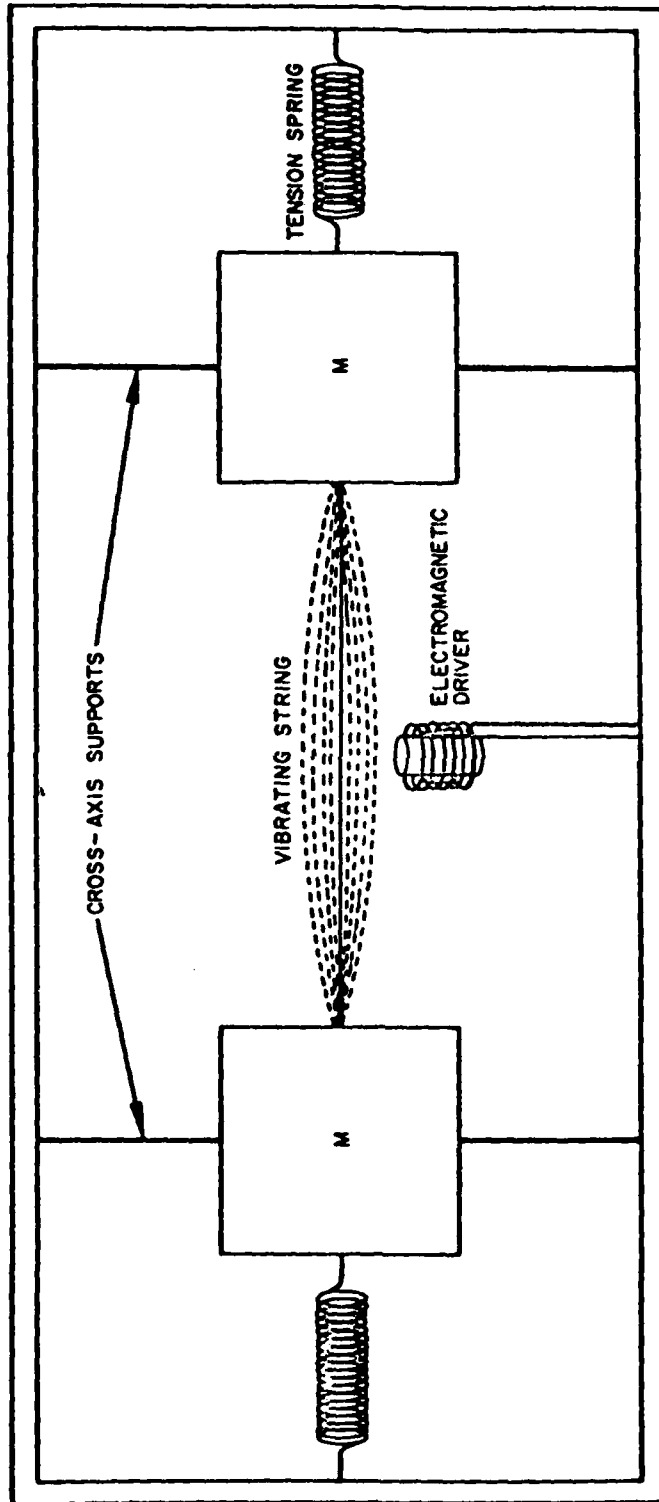


FIG. II-6 VIBRATING STRING GRAVITY GRADIOMETER. The relative displacements of the two proof masses will change the resonant frequency of the vibrating string. The frequency change is a function of the gravity gradient.

This universal relation shows that to improve the sensitivity of a given instrument, one has to accept a longer time of response.

Equation (2.7a) shows that the sensitivity of the instrument can be improved by reducing the natural frequency. The equation relating the natural frequency of a transducer with its size and weight is typically nonlinear and unique to the given configuration. Thus detailed analysis of the dependence of the sensitivity of a sensor upon its size can only be done on a case-by-case basis. Such an analysis for the diaphragm proof mass used in the cryogenic accelerometer is given in Ch. III.

On the other hand, small vibrations of the fundamental natural frequency of most proof masses can be approximated by the simple harmonic motion of an equivalent simple pendulum. If l_{eq} is the length of the equivalent simple pendulum, the natural frequency can be expressed as

$$\omega_0 = \sqrt{\frac{g}{l_{eq}}} . \quad (2.9)$$

Substituting (2.9) into (2.7), we have

$$\sigma \propto l_{eq} \quad (2.10a)$$

and

$$\tau \propto \frac{1}{\sqrt{l_{eq}}} \quad (2.10b)$$

with g being a constant. Thus in the equivalent model, sensitivity is directly proportional to the size of the instrument.

The Brownian noise of a proof mass in the low frequency range of the spectrum is given by Eq. (E-5). The acceleration noise expressed in mean square is given in Eq. (4.1). The equation (4.1) shows that when the mass is increased or when the natural frequency is decreased, the Brownian noise power is reduced. Thus, from the consideration of sensitivity and noise, it is advantageous to have as large and as heavy an instrument as possible. The designs of some seismographs reflect these concepts where the long response time is acceptable.

For the moving base applications envisioned for the gravity gradiometer, a design baseline of 10 cm is the size constraint. Given this constraint on the physical size, reduction in the natural frequency becomes an exercise for ingenuity. For the diaphragm proof mass studied in this research, the design is given in Ch. III-A-4.

B-8 Gradiometer Design Considerations

The gradiometer studied in this research is built using a pair of accelerometers. The requirements are

- a) achieving accelerometer sensitivity of 10^{-8} g or better,
- b) matching the two scale factors to at least 1 part in 10^8 ,
- c) calibration and having a built-in stability such that the scale factors remain matched with the passage of time,
- d) tolerances to large common mode accelerations (1 g or more) for moving base operation.

Since the force to be measured is extremely small, gradiometer designs must be immune to the following: magnetic field, electrostatic field, thermal gradient, and acoustically coupled noise.

These are very stringent requirements. In view of these, the properties of cryogenics look very promising. The feasibility of using the cryogenic technology to overcome some of the fundamental limitations is investigated in the next section.

C. SOME PRINCIPLES OF SUPERCONDUCTIVITY

In the previous section, the sensitivity of an instrument is related to its natural frequency in (2.7a). The sensitivity of an accelerometer is the smallest acceleration it can detect in a totally noise-free environment. Even when all the external noise is eliminated by careful isolation, the noise produced by the Brownian motion of the molecules in the proof mass itself remains. It is noted in the survey that the gradiometers are currently measuring gradient down to the thermal noise level. Further improvement in sensitivity will be meaningful only if the thermal noise can be reduced.

From the Nyquist Theorem, the voltage noise of an equivalent resistor, R , of a proof mass is

$$\langle v_n^2 \rangle = 4 kRT \Delta f . \quad (2.11)$$

The noise is expressed in mean square volt for a given 1 Hz bandwidth. The Boltzman constant is k , R is in ohms, and T is in Kelvins.

For room temperature devices, the only way to reduce thermal noise is to reduce R . This is the equivalent resistance that accounts for the internal dissipative losses in the molecular structure of the material. There is no easy way to reduce these losses significantly.

On the other hand, lowering the temperature would reduce the thermal noise and can be done readily. Most materials undergo a radical change in their physical properties at low temperatures. The internal losses of the materials are reduced significantly. A notable example is lead, which will ring when struck at cryogenic temperatures. From experimental measurements of the Q 's of the resonant vibrations of niobium diaphragms studied in this research, losses are reduced by a factor of at least 100. Coupled this with the reduction of temperature, the root mean square value of noise is at least 80 times smaller at cryogenic temperatures. Thus the potential for improvement by going to cryogenics is quite high. Owing to other noise sources, this potential improvement has not been achieved. Chapter II-D-3 discusses the actual sensitivity of the cryogenic accelerometer.

Superconductivity also offers some new technology and properties that are useful in the design of a gravity gradiometer. Niobium, the material used in the gradiometer is a perfect electromagnetic shield and has great structural stability when it is superconducting. The superconducting quantum interference device (SQUID) is an extremely sensitive flux detector and can be employed to make an extremely sensitive position detector.

H.J. Paik [1974] has developed a very sensitive cryogenic seismic sensor. The resolution of the readout of this specific force meter is

10^{-14} cm which, at its design resonant frequency of 860 Hz, is equivalent to an acceleration sensitivity of 3×10^{-10} g. This accelerometer is described in the next section. For those who are unfamiliar with the properties of superconductivity, a brief introduction will be given here. The details of these properties can be found in the literature [Rose-Innes, 1969].

When the temperature of a superconducting material is lowered gradually, there is a temperature below which its resistance to the flow of an electric current is absolutely zero. Since there is no resistance to dissipate the energy, a current flowing in a superconducting ring will flow forever. The temperature at which the transition from normal to superconducting occurs is known as the critical temperature (T_c). For niobium, the material used in the construction of the accelerometer, T_c , is 9.3 K. This is the highest transition temperature among the metallic elements.

As the material becomes superconducting, it also expels all magnetic flux from its interior provided the magnetic intensity is below a certain level. This property of perfect diamagnetism is known as the Meissner effect. As the applied magnetic intensity, H_a , is increased, it will reach a critical value, H_c . At this point, the magnetic field will penetrate into the material and cause the material to revert to normal. This will occur even though the temperature is kept below T_c . When the transition is abrupt, the material is known as Type I superconductor. When the transition is gradual, the material is known as Type II. Niobium lead is Type I and niobium-titanium (T-48) is Type II.

Thus superconducting materials form almost perfect electromagnetic shield [Cabrera, 1973]. Moreover, the total magnetic flux threading a superconducting loop cannot change so long as the circuit remains resistless. This can be expressed as

$$\phi = LI = \text{constant} . \quad (2.12)$$

Thus if the inductance L_1 is increased, the persistent current, I , will decrease to keep magnetic flux ϕ constant. This relation is the fundamental principle upon which the accelerometer is designed. We have

$$L_1 I_1 = L'_1 I'_1$$

(2.13)

giving the decrease in current as

$$\Delta I = I_1 - I' = I_1 \left(\frac{L'_1 - L_1}{L'_1} \right). \quad (2.14)$$

This change in current can be detected by the SQUID. Figure II-7a is the schematic of such a circuit.

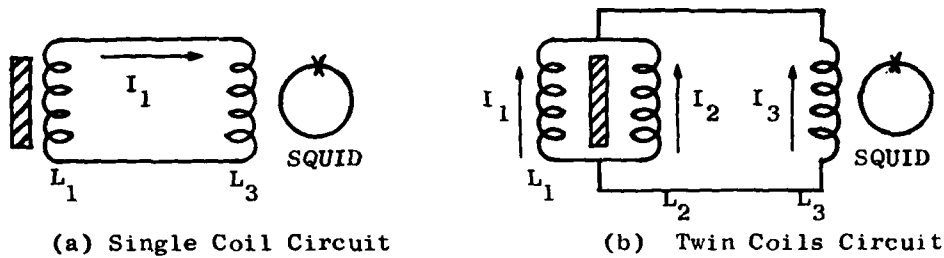


FIG. II-7 SCHEMATIC OF VARIABLE INDUCTANCES.

The inductance L_1 is modulated by the displacement of a superconducting surface in its vicinity. The stored persistent current I_1 will change per Eq. (2.14). This current flows through the input coil of the SQUID (superconducting quantum interference device). It is an unsound arrangement since any inductance changes not associated with the displacement will produce a current change in L_3 .

To rectify this, a matched pair of inductance coils are placed on either side of the surface. It is assumed that the surface is thin and flat. At equilibrium, the stored persistent current flows through L_1 and L_2 and none flows through L_3 , Fig. II-7b. Thus $I_1 = -I_2$, $I_3 = 0$. If the surface is displaced towards L_2 , L_2 will decrease and L_1 will increase. The differential current due to this "push-pull" effect will be sensed by the SQUID. This is the basic transducer principle used in the superconducting accelerometer [Paik, 1974]. The equations relating the differential current and the displacement will be given in the next section.

The SQUID referred to above is the most sensitive flux detector known today. The reader is referred to the literature [Lounasmaa, 1974] for a thorough discussion of its physics. The block diagram of a radio frequency biased SQUID is shown in Fig. II-8.

Referring to Fig. II-8, the single weak link junction which completes the loop of the superconducting ring is the sensor. A small rf coil, L_{rf} , is inserted into the hole of the superconducting ring. This coil forms a resonant circuit with a superconducting capacitance which is connected in parallel. An rf oscillator driving the $L_{rf} - C_{rf}$ circuit at the resonant frequency is loosely coupled to the tuned circuit by the small variable capacitor. The low frequency sweep is used to tune the circuit and provides input signal for calibration. The change in the resonant circuit due to an internal flux is detected by the phase sensitive detector and nulled by the feedback path of the integrator. The voltage of the integrator output is then a measure of input flux.

The sensor is effectively a parametric up-converter in which a d-c or low frequency input signal is mixed with an rf bias signal. The input signal appears as sidebands of the bias signal and is detected as an amplitude modulation of the total signal level.

The flux change $\Delta\phi$ in the SQUID produced by an input current ΔI is

$$\Delta\phi = M\Delta I \quad (2.15)$$

where M is the mutual inductance of the input coil to the SQUID. Negative flux feedback is provided by the phase sensitive detector and integrator to cancel the flux change. The voltage in the feedback loop provides a highly linear readout of the input.

The commercial SQUID package used in our experiments is provided by SMC Corporation in San Diego. The output voltage-to-input current gain is 20 V/ μ A. The noise in the system is contributed mainly by the SQUID and has the characteristics shown in Fig. II-9. In the frequency

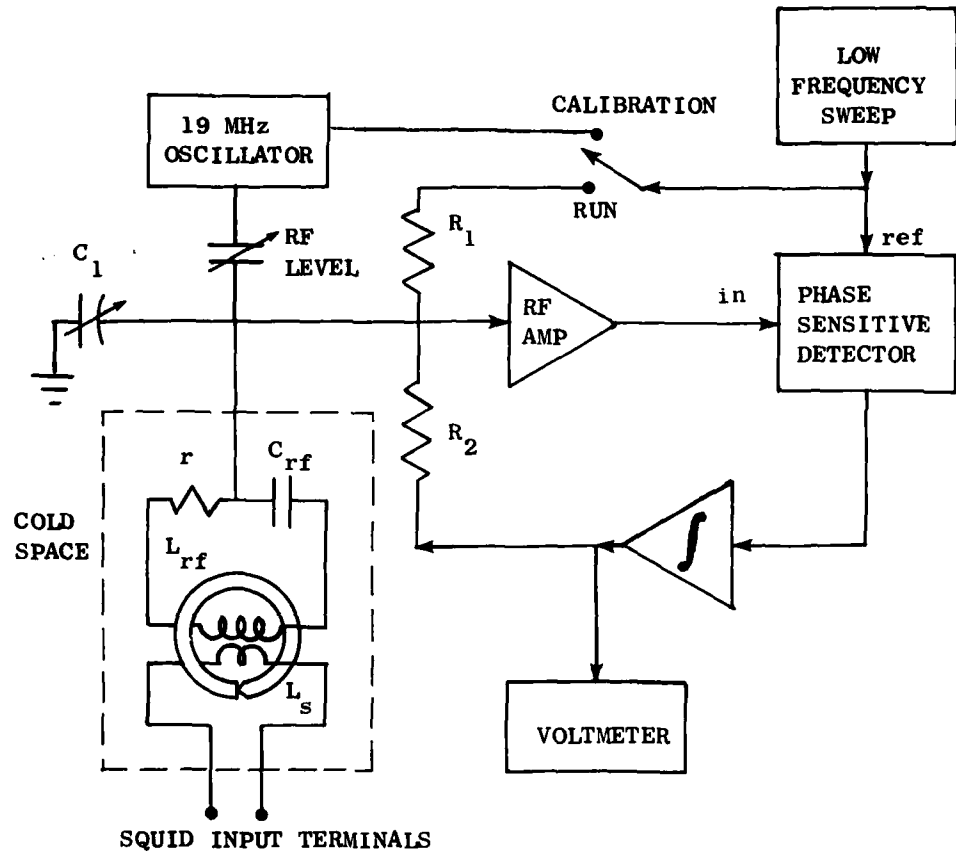
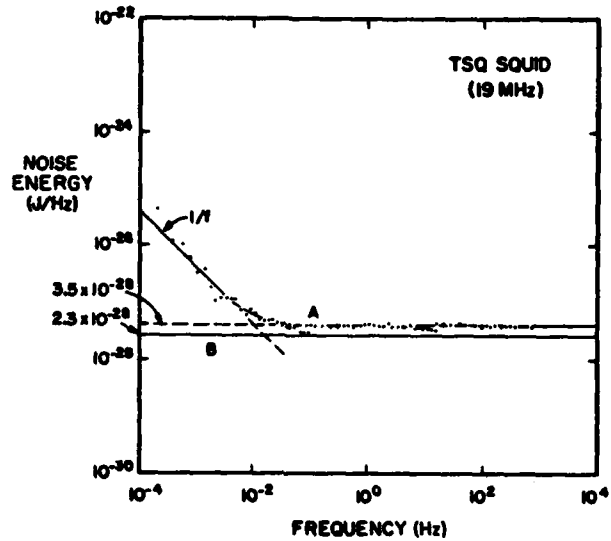


FIG. II-8 BLOCK DIAGRAM OF AN RF BIASED SQUID [modified from Lounasmaa, 1974]. In simplest terms, the feedback circuit comprising the rf amplifier, phase sensitive detector, and the integrator will keep the flux inside the superconducting loop constant. A low frequency current flowing in L_s will be detected by the SQUID and the integrator will drive a current through L_{rf} that will cancel the effect of the input current. The voltage output of the integrator is a measure of the input current.



range of 0.1 Hz to 5 kHz, the detector noise is about $1.1 \times 10^{-5} \mu\text{A}$ rms/ $\sqrt{\text{Hz}}$. Note the 1/f noise starting at 0.01 Hz.

In a typical setup, the SQUID may be able to resolve flux change down to one part per thousand of a flux quantum (2×10^{-15} Wb). Evidently, meticulous care must be used to shield the SQUID from electromagnetic interference. Fortunately, superconductors are themselves almost perfect shields. A hollow lead cylindrical shield surrounding the vacuum space is a standard feature of our experiments. Cabrera [1974] has shown that the magnetic field inside a cylinder with an open end may be given, on the center line of the cylinder for the axial component, by

$$H_z = H_0 e^{-3.4z/r} \quad (2.16 \text{ a})$$

and for the transverse component, by

$$H_t = H_0 e^{-1.8z/r} \quad (2.16 \text{ b})$$

where H_0 is the uniform external field, z is the depth from the open end, and r is the radius of the hollow cylinder. For $r = 10$ cm $z = 20$ cm, H_z and H_t are much smaller than the external field.

We conclude the great mechanical stability and superior thermal isolation at the cryogenic environment minimized the difficulties of building a sensitive gradiometer. The provision of the cryogenic space is an inconvenient complication which is a serious limitation for moving base operation.

D. SUPERCONDUCTING ACCELEROMETER

D.1 Principle of Accelerometer

The accelerometer used in this research was developed by Ho Jung Paik of Stanford University [Paik, 1974; 1976]. It was developed as a resonant detector of gravitational radiation generated by cosmic events such as supernovae. It is a passive specific-force meter with a thin

(0.017 in.) circular niobium diaphragm as a proof mass. The diaphragm and its rim support are machined out of a piece of solid stock of niobium. The flatness of the diaphragm is maintained to optical quality. The diaphragm is heat treated to relieve stress and electro-polished to improve the quality (Q) of its resonance. A typical diaphragm is shown in Fig. II-10. Modified diaphragms with higher acceleration sensitivity are discussed in the next chapter. The relevant information of the diaphragm are:

Material: Stanford grade niobium;

Weight (diaphragm alone): 30 gm;

Diameter (diaphragm alone): 3.5 in.;

(rim inclusive): 5 in.;

Diaphragm thickness: 0.017 in

Rim thickness: 0.6175 in.

Two pancake-shaped coils are placed very close to either side of the diaphragm. These coils are wound spirally of 300 turns of niobium-titanium wire 0.0025 in. in diameter in a single layer on a G-10 former. The G-10 formers are mounted on niobium backup plates. Niobium-zirconium is used when the supply of niobium becomes depleted. A cross-section view of the accelerometer is shown in Fig. II-11. The G-10 is used for its magnetic properties and its thermal expansion coefficient which closely matches that of niobium. McAshan, a research physicist at Stanford, came up with the idea of winding the coil in the narrow gap produced by a lucite disk and the G-10 former [Paik, 1974]. Epoxy is used as the binding agent which also served as the lubricant during coil winding. The cover plates and the rim of the diaphragm formed a complete protective enclosure for the diaphragm producing a rugged instrument. The niobium enclosure also serves as superior electromagnetic shield against interference.

The pickup coils have the same inductance, say, L_0 , when placed at the same distance d_0 from the diaphragm. When the diaphragm deflects under acceleration, the inductances vary with distance, increasing as the

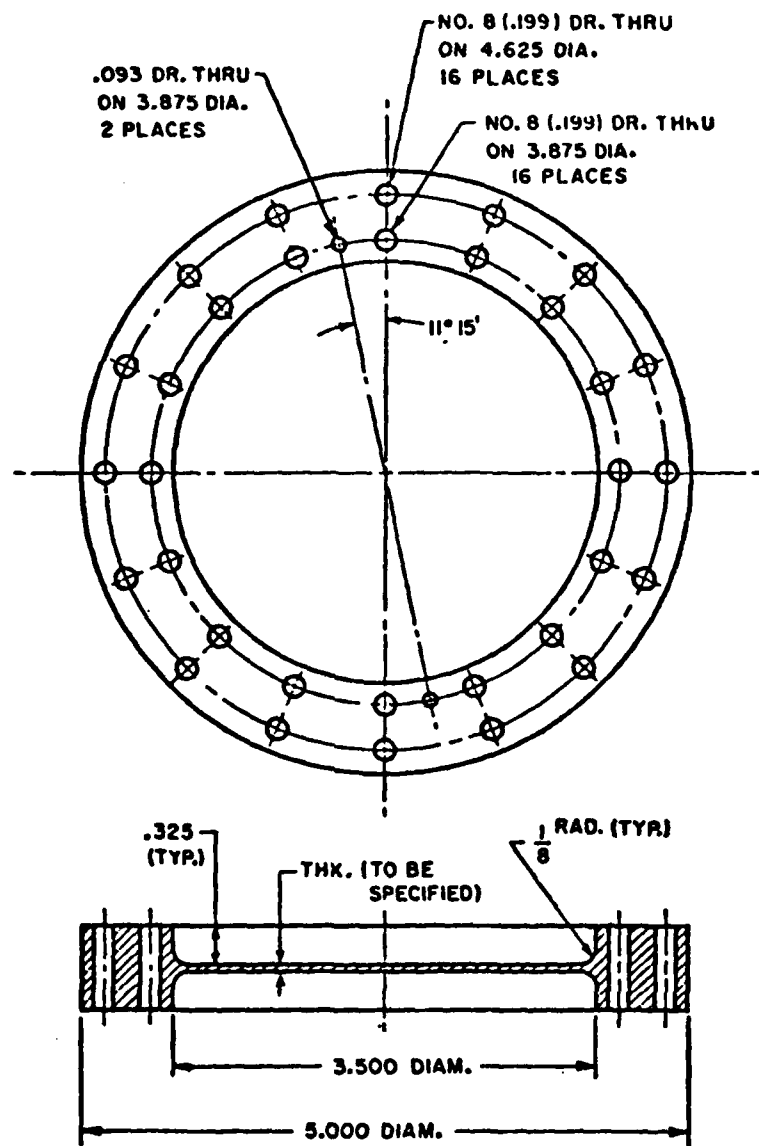


FIG. II-10 DETAILED DRAWING OF A NIOBIUM DIAPHRAGM
[from Paik, 1974].

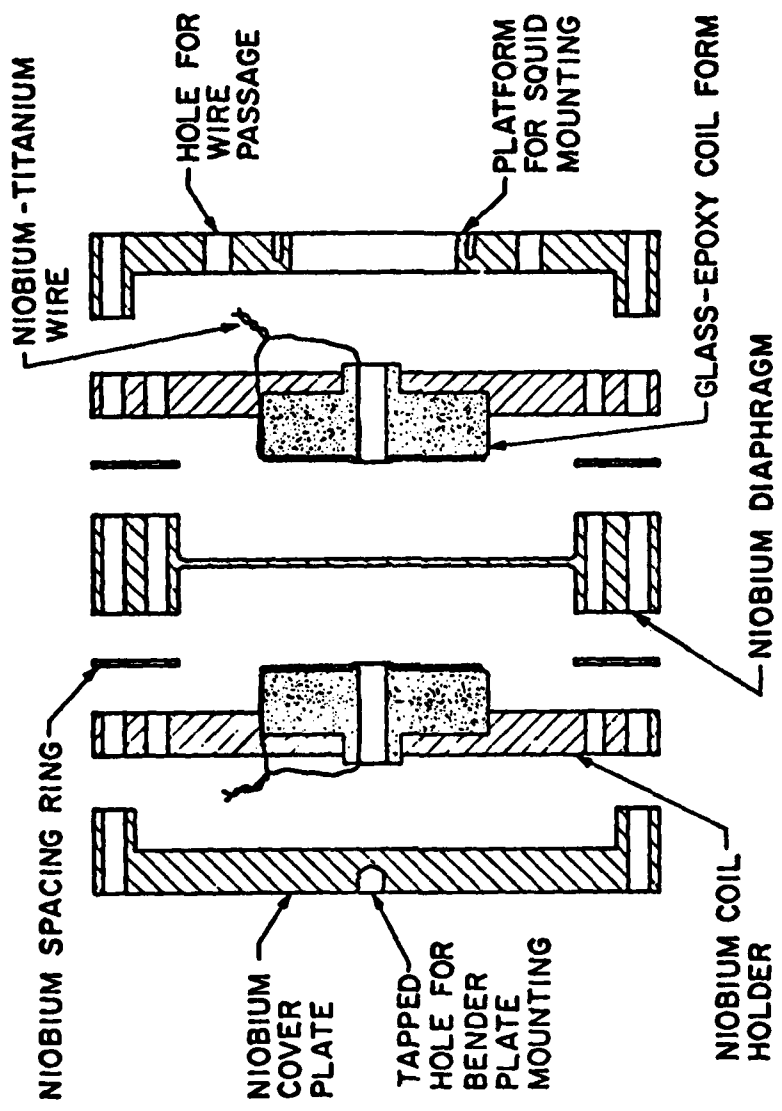


FIG. II-11 EXPLODED CROSS-SECTIONAL VIEW OF THE SUPERCONDUCTING ACCELEROMETER
[from Paik, 1974].

spacing increases and vice versa. In the region of interest, the change of inductance ΔL , may be considered to be directly proportional to the equivalent displacement, x , viz.,

$$\Delta L = \frac{L_0}{\eta d_0} x \quad (2.17)$$

where η is a geometric factor accounting for the curvature of the diaphragm. Paik [1974] has shown that η is very close to unity.

With reference to Fig. II-7, if the diaphragm moves to the right, the inductances becomes

$$L_1(x) = L_0 \left(1 + \frac{x}{\eta d_0}\right) \quad (2.18a)$$

$$L_2(x) = L_0 \left(1 - \frac{x}{\eta d_0}\right) \quad (2.18b)$$

If the currents flowing in the coils at any instant are denoted as I_1 , I_2 , and I_3 as shown in Fig. II.7b, we have

$$L_1 I_1 + L_3 I_3 = \phi_{13} \quad (2.19a)$$

$$L_1 I_1 + L_2 I_2 = \phi_{12} \quad (2.19b)$$

$$I_1 + I_2 + I_3 = 0 \quad (2.19c)$$

where L_3 is the inductance of the input coil of the SQUID, ϕ_{13} and ϕ_{12} are the constant magnetic flux linking L_1 , L_3 and L_1 , L_2 respectively. The first two equations of (2.19) are the direct result of the flux conservation principle of (2.12). The last equation of (2.19) is Kirchoff's current law. The solution for I_3 is

$$I_3 = \frac{L_1 \phi_{12} - (L_1 + L_2) \phi_{13}}{L_1 L_2 + (L_1 + L_2) L_3} \quad (2.20)$$

Since I_3 is typically zero at the null position, (2.20) gives the instantaneous output current i_3 due to displacement. Substituting (2.18) into (2.20) and simplifying, we have

$$i_3 = \frac{2}{1+\gamma} \frac{I_0}{\eta d_0} x + e \quad (2.21)$$

where γ is the ratio of $L_3/(L_1//L_2)$ where $L_1//L_2$ is the parallel inductance of L_1 and L_2 . For $L_1 = L_2 = L_0$ at null, γ is equal to $2L_3/L_0$. I_0 is the steady current stored in the loop, L_1 and L_2 at $x = 0$; e is the error term due to the higher-order terms ignored. It is shown to be very small for small displacements [Paik, 1974]. Equation (2.21) gives the output current of the accelerometer as a function of the displacement of the proof mass.

The current flowing into the SQUID for a given displacement is directly proportional to the magnitude of the stored current, I_0 , per (2.21). Paik predicted and experimentally verified that the frequency of the fundamental mode will increase as stored current is increased. The frequency shift is depicted in Fig. II-12. This figure is reproduced from Paik [1973].

The shift may be qualitatively described as the increase in spring rate of the diaphragm owing to an increase in magnetic pressure as the stored current is increased.

The straight line portion of the curve may be described by

$$f_r^2 = f_0^2 + \alpha I_0^2, \quad (2.22)$$

where f_0 is the frequency with $I_0 = 0$ and f_r is the frequency with $I_0 \neq 0$. Paik had verified this equation experimentally. For a diaphragm of 850 Hz, the value of α is typically 7.5×10^5 (Hz/A)².

In Fig. II-12, as the stored current is increased beyond 5 amp, the magnetic intensity in the gap exceeds the critical field strength of niobium which is about 1 KGauss. After flux penetration has occurred, the physics of the device would be totally different from that described

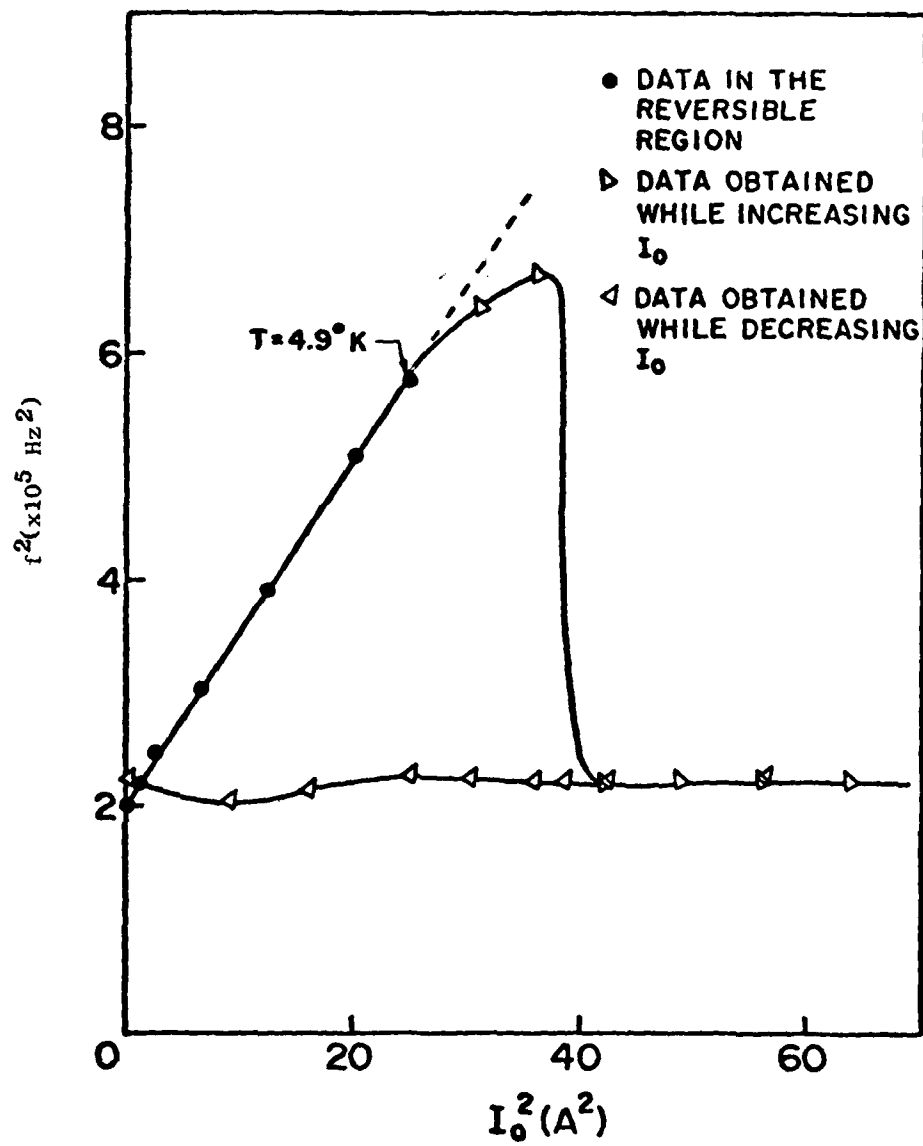


FIG. II-12 EFFECT OF MAGNETIC PRESSURE ON THE RESONANT FREQUENCY OF THE NIOBIUM DIAPHRAGM TRANSDUCER. The deviation from straight line occurs when the flux begins to penetrate the superconducting diaphragm. Note that penetration once occurred is irreversible. To recover, the diaphragm must be warmed to a temperature above the critical temperature of niobium (approximately 10 K).

in this section. The original state can only be restored by raising the temperature of the diaphragm above its critical value. Thus it is necessary to keep the persistent current in loop below 5 A, the critical value for the present accelerometer design.

The output relation of the accelerometer, (2.21), can be expressed in terms of the acceleration it experienced. From the implicit first-order equivalent spring-mass system, the displacement is

$$x = \frac{a}{\sqrt{(\omega_f^2 - \omega_r^2)^2 + \omega_f^2 \omega_r^2 / Q^2}} \quad (2.23)$$

where

a = acceleration of the proof mass

ω_r = resonant frequency of the proof mass

ω_f = frequency of the acceleration

Q = quality factor of the proof mass.

If ζ is the damping factor of the system, we have

$$\zeta = \frac{1}{2Q} \quad (2.24)$$

Details of this analysis is given in App. D.

When the signal frequency is much lower than the resonant frequency, i.e., $\omega_f \ll 0.22 \omega_r$, (2.23) may be simplified as

$$x = \frac{a}{2\omega_r} \quad (2.25)$$

This approximation is especially good if Q is large. Substituting this equation into (2.21), we have

$$i_3 = \frac{2}{1+\gamma} \frac{I_0}{\eta d_0} \frac{a}{\omega_r^2} \quad (2.26)$$

This is the equation Paik has derived for the output of the accelerometer.

The energy transferred to L_3 is

$$E = \frac{1}{2} L_3 i_3^2 . \quad (2.27)$$

The maximum energy transfer occurs when $\gamma = 1$ and is

$$E_{\max} = \frac{1}{2} L_3 \left(\frac{I_0}{\eta d_0} \frac{a}{\omega_r^2} \right)^2 \quad (2.28a)$$

$$= \frac{1}{2} L_3 I_0^2 \left(\frac{a}{\eta d_0 \omega_r^2} \right)^2 . \quad (2.28b)$$

D-2 Optimum Performance

If ω_r in (2.26) were a constant, the output current for a given acceleration would be proportional to the stored current I_0 . It would be advantageous to make I_0 as large as possible. Indeed, in the early part of this research, great time and effort were spent trying to achieve a 5 A persistent current stored.

Equation (2.22) shows that ω_r is a function of the stored current I_0 . After substituting for ω_r ($2\pi f_r$) in (2.26), we have

$$i_3 = \frac{1}{2\eta d_0 (1+\gamma)\pi^2} \frac{I_0}{f_0^2 + \alpha I_0^2} a \quad (2.29)$$

where α is

$$\alpha = \frac{1}{2\pi^2} \frac{1}{1+\gamma} \frac{L_0}{m(\eta d_0)^2} . \quad (2.30)$$

The equivalent mass of the diaphragm is m . Equation (2.30) was derived by Paik [1974] and has been verified independently by a different approach. Using (2.30), the output current becomes

$$i_3 = \frac{m\eta d_0}{L_0} \frac{I_0}{I_0^2 + (f_0^2/\alpha)} a \quad (2.31a)$$

$$= \xi \frac{I_0}{I_0^2 + (f_0^2/\alpha)} a \quad (2.31b)$$

where $\xi = m\eta d_0/L_0$ which is a constant of the accelerometer. The accelerometer is most sensitive to acceleration when the stored current satisfied the following equation, i.e.,

$$I_{\text{opt}} = \frac{f_0}{\sqrt{\alpha}} . \quad (2.32)$$

With this value of stored current, (2.31) becomes

$$i_{3_{\text{max}}} = \xi \frac{a}{2I_{\text{opt}}} . \quad (2.33)$$

The slope of the curve in Fig. II-12 is α . From experimental results using three different accelerometers, the optimum current of each is determined and tabulated in Table II-1.

Table II-1
TABLE OF OPTIMUM PERFORMANCE FOR THREE DIAPHRAGMS OF
DIFFERENT FREQUENCIES

Diaphragm Characteristics	Mid Freq.	High Freq.	Low Freq.
$m(\text{gm})$	13	30	300
$f_0 (\text{Hz})$	447.2	850	63.8
$\alpha(\text{Hz}^2/\text{A}^2)$	1.37×10^4	8000	56.43
$i_{\text{opt}} (\text{A})$	3.82	9.5	8.5
$S (\text{A/g})$	2.22	2.6	17.6

In Table II-1, the sensitivity figure S is defined as

$$S = \frac{i_{\max}}{a} \frac{d_0}{L_0} = \frac{m}{2I_{\text{opt}}} \frac{1}{\eta} . \quad (2.34)$$

Sensitivity, S , may be interpreted as the response gain in A/g. Identical for all three accelerometers are d_0 and L_0 . For the first two diaphragms, $\eta = 0.766$, and for the last diaphragm which has a solid central mass, $\eta = 1$. The values of m and η used in the calculations for Table II-1 are given by Paik [1974].

The results show that good sensitivity can be attained by several designs. One of these is to increase the mass of the diaphragm sensor. This is discussed in the next chapter.

D-3 Thermal Noise

In the cryogenic environment in which the accelerometer operates, the thermal noise produced by Brownian motion of the diaphragm is insignificant in the output. A detailed discussion of this noise is given in Ch. IV.

The resolution of the accelerometer is governed by the noise of the SQUID. This noise is typically characterized by ϕ_N , the equivalent noise flux referred to the input coil. The energy of this noise is

$$E_N = \frac{1}{2} \frac{\phi_N^2}{L_s} \quad (2.35)$$

where L_s is the inductance of the input coil of the SQUID. Thus if the energy of a signal is less than this value, the signal could not be discerned from the noise. Using (2.28b) and equating it to (2.35), the resolvable acceleration is

$$\delta a = \left[\frac{\phi_N^2}{L_s L_3 I_0^2} \right]^{\frac{1}{2}} d_0 \omega_r^2 . \quad (2.36)$$

The value of η in (2.28b) has been set to unity in (2.36).

Typically, L_3 is the equivalent SQUID input inductance reflected to the primary of a step-down transformer. The schematic is shown in Fig. II-13. A transformer is used since input inductance of the SQUID

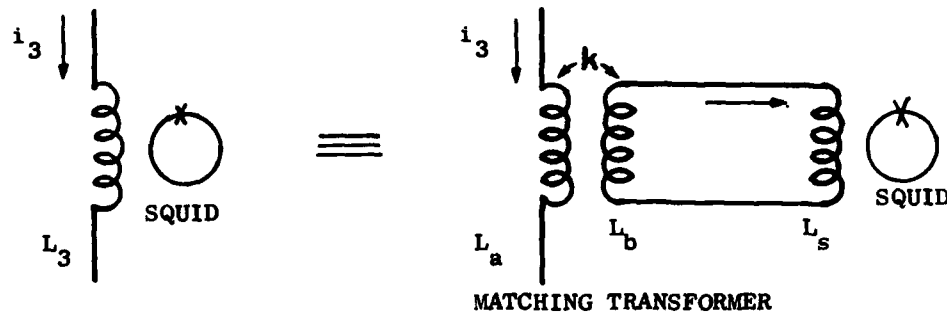


FIG. II-13 STEPDOWN MATCHING TRANSFORMER. The inductance presented by the SQUID is the equivalent inductance of the circuit given on the right of the diagram. The matching transformer is a stepdown transformer since L_s is $2\mu\text{H}$ and L_p , the parallel inductance of the gradiometer is of the order of $25\mu\text{H}$.

is not of the correct value for maximum energy transfer. The inductance and current relations for Fig. II-13 are

$$L_3 = L_a \left(1 - \frac{k^2 L_b}{L_b + L_s} \right) \quad (2.37)$$

$$I_s = \frac{M}{L_b + L_s} i_3 \quad (2.38a)$$

$$= \frac{k\sqrt{L_a L_b}}{L_b + L_s} i_3 \quad (2.38b)$$

The energy of a signal is

$$E_s = \frac{1}{2} L_s i_s^2 \quad (2.39a)$$

$$= \frac{1}{2} L_s k^2 \left(\frac{I_0}{d_0} \frac{a}{\omega_r} \right)^2 \quad (2.39b)$$

where

$$k_t^2 = \frac{k^2 L_a L_b}{(L_b + L_s)^2} . \quad (2.40)$$

Equation (2.38b) is used for i_s .

Similarly the resolvable acceleration is obtained by equating (2.39) and (2.35). We have

$$\delta a = \frac{d_0}{I_0} \frac{\phi_N}{d_t L_s} \omega_r^2 . \quad (2.41)$$

For a typical design, $d_0 = 10^{-4}$ m, $I_0 = 5A$, $\phi_N = 2 \times 10^{-28}$ J/Hz, $k_t \approx 1$, $L_s = 2\mu H$, $\omega_r = 2\pi(50) s^{-1}$, the smallest acceleration discernable for frequencies above 0.01 Hz is

$$\delta a = 2.8 \times 10^{-11} \text{ m/s}^2/\sqrt{\text{Hz}} . \quad (2.42)$$

This resolution is indeed superior to current accelerometers.

E. SUMMARY

The nature of the gravity gradient and the instruments being built for the measurement of the gradient are discussed in this chapter. We noted that the theoretical sensitivities of the instruments are limited to the order of 1 E by Brownian noise.

We suggest that the properties of cryogenics may be used to overcome the problem. The advantages of a superconducting gradiometer includes the following:

1. The kT noise is much lower at 4.2K;
2. Materials are less lossy mechanically at low temperature producing higher Q for a given mechanical structure;
3. SQUID is a very sensitive flux detector;
4. Superconducting materials make superior electromagnetic shields;

5. The careful thermal isolation necessary for the cold space also reduces thermal gradient in the instrument, eliminating a troublesome error source, and
6. Mechanical creep is negligible at 4.2K.

However, it is necessary to provide a cold space. A heavy dewar with some kind of refrigeration, either a liquid helium reservoir or a closed cycle liquid helium system, must be used. The bulk of the dewar render it difficult to isolate from environmental vibration. A mechanical test bed to shake the gradiometer sinusoidally would be very expensive indeed, whether done internally at low temperature or as a system to shake the dewar.

Moreover, the sensitivity of the superconducting accelerometer depends on the persistent current stored. Unless the device is kept at superconducting temperature, it becomes necessary to calibrate the accelerometer after each cool-down. The process is very time consuming and tedious.

Given the superior performance of the superconducting accelerometer, we concluded that it is a viable component for the gravity gradiometer.

Similar advantages can be obtained for inertial instruments. Digital computers can be built using superconducting technology. Thus the possibility exists for an inertial navigation system of great accuracy incorporating all components in a low temperature environment.

Chapter III

THE DESIGN OF A SUPERCONDUCTING GRAVITY GRADIOMETER

A. OPTIMIZATION OF THE CRYOGENIC ACCELEROMETER

The accelerometer type used in the gradiometer experiments discussed in Ch. VI was designed by Paik [1974]. Paik designed the accelerometer to achieve maximum coupling with the Stanford cryogenic gravity wave bar antenna which is a highly specialized application. The instrument can therefore be improved for a gravity gradient application which has different requirements. In this section, the dimensions of the accelerometer will be optimized with respect to thermal noise and acceleration sensitivity.

A-1 Centrally Loaded Diaphragm

The cryogenic accelerometer is a specific-force meter which determines the force on the proof mass by measuring the displacement of the proof mass deflecting the diaphragm spring. It is clear from Eq. (2.26) that the sensitivity of the accelerometer will improve as the natural frequency of a given proof mass is made smaller.

One means of achieving this is to reduce the thickness of the diaphragm, thus making it more pliable. The mass reduces linearly but the stiffness decreases approximately as the thickness cubed. However, it becomes increasingly difficult to maintain the same degree of flatness and uniformity for the diaphragm as the thickness is decreased during the process of machining. So far the lowest frequency we have achieved by this process is about 400 Hz with a niobium diaphragm of thickness of 0.017 in. (0.4 mm), and a diameter of 3.5 in. It is judged that a 0.010 in. thick diaphragm may be the thinnest machinable, without incurring exorbitant costs.

Alternatively, the frequency of the diaphragm can be reduced by attaching centrally located masses to the diaphragm (initially suggested by Dr. Paik).

Figure III-1 shows the sketches of such a modified diaphragm. In this way the same improvement in sensitivity can be achieved without having to work with an inordinately thin diaphragm.

In the analysis of the natural frequency of the loaded diaphragm, h and a denote the thickness and the radius of the diaphragm; the same quantities for the central load are denoted as h' and b . The natural frequency f_0 of this diaphragm is determined by analysing the axial motions of the circular plate. The equation governing the motion of an axisymmetric body is best derived in polar coordinates. It is derived as [Handelmann, 1957]

$$\left(\frac{1}{r} \frac{d}{dr} r \frac{d}{dr}\right) \left(\frac{1}{r} \frac{d}{dr} r \frac{dw}{dr}\right) = \frac{\omega^2}{c^2} w(r) \quad (3.1)$$

where w = the displacement of the diaphragm

ω = the frequency of vibration,

$c^2 = D/\rho h$, D is the flexual rigidity, ρ is the density of the plate

$D = Eh^3/12(1-\nu^2)$, E is the Young's modulus

ν = Poisson's ratio.

The boundary conditions are the clamping of the outer edge, i.e.,

$$w(a) = \frac{dw}{dr}(a) = 0 \quad (3.2)$$

and the built-in edge of the central mass,

$$\frac{dw}{dr}(b) = 0 \quad (3.3)$$

and the equation of motion of the central mass,

$$\frac{d}{dr} \left(\frac{1}{r} \frac{d}{dr} r \frac{dw}{dr} \right) \Big|_b = \frac{\rho' h' b}{2D} \omega^2 w(b) \quad (3.4)$$

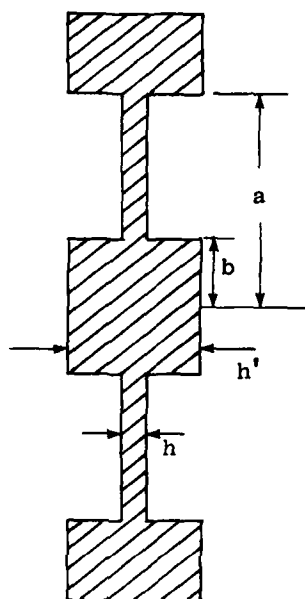


FIG. III-1 CROSS-SECTIONAL VIEW OF THE CENTRALLY LOADED DIAPHRAGM. The diaphragm of Fig. II-10 is modified by attaching a centrally located disc to the diaphragm as it is shown here.

where ρ' is the density of the central disk. Equation (3.4) is obtained by the application of Newton's Second Law of motion to the central mass and assuming harmonic natural behavior.

This problem has been analysed by Handelmann and Cohen [1957]. The solution using Rayleigh-Ritz's approximation is given in App. B. In the following discussion, the nondimensional variables, α , γ , and k are used. The ratio α is the radius of the central mass to the radius of the diaphragm; γ is the ratio of the thickness of the central mass to that of the diaphragm, and k is the frequency parameter relating the natural frequency to the physical dimensions as given in (3.5),

$$\omega_0^2 = \frac{Dk^4}{\rho a^4} = \frac{Eh^2 k^4}{\rho 12(1 - \nu^2)a^4} . \quad (3.5)$$

Equation (3.5) is derived in App. B. For niobium at room temperature, $E = 15 \times 10^6$ psi, and $\nu = 0.397$ [Wigley, 1971]. Equation (3.5) may be simplified to

$$\omega_0 = c_1 h \left(\frac{k}{a} \right)^2 \quad (3.6)$$

where c_1 has a value of 2.189×10^3 in./sec. The value of k for a given geometry may be determined using Eqs. (B.4) and (B.5). The variations of the frequency parameter k as α , the radius ratio, and γ , the thickness ratio are varied, are plotted in Fig. III-2. Note that at $\alpha = 0$, all curves originate from the same point. This is the value of k for an unloaded diaphragm. It is clear that as γ , the thickness ratio, is increased, the frequency factor k decreases as would be expected but at a rapidly decreasing rate. We also note that k is rather insensitive to α for large values of γ .

The locus of minimum frequency gives the location of the value of α that will produce the lowest k value given γ . These points are obtained by the evaluation of the exact solution (B.6) with a computer program using an iterative search algorithm.

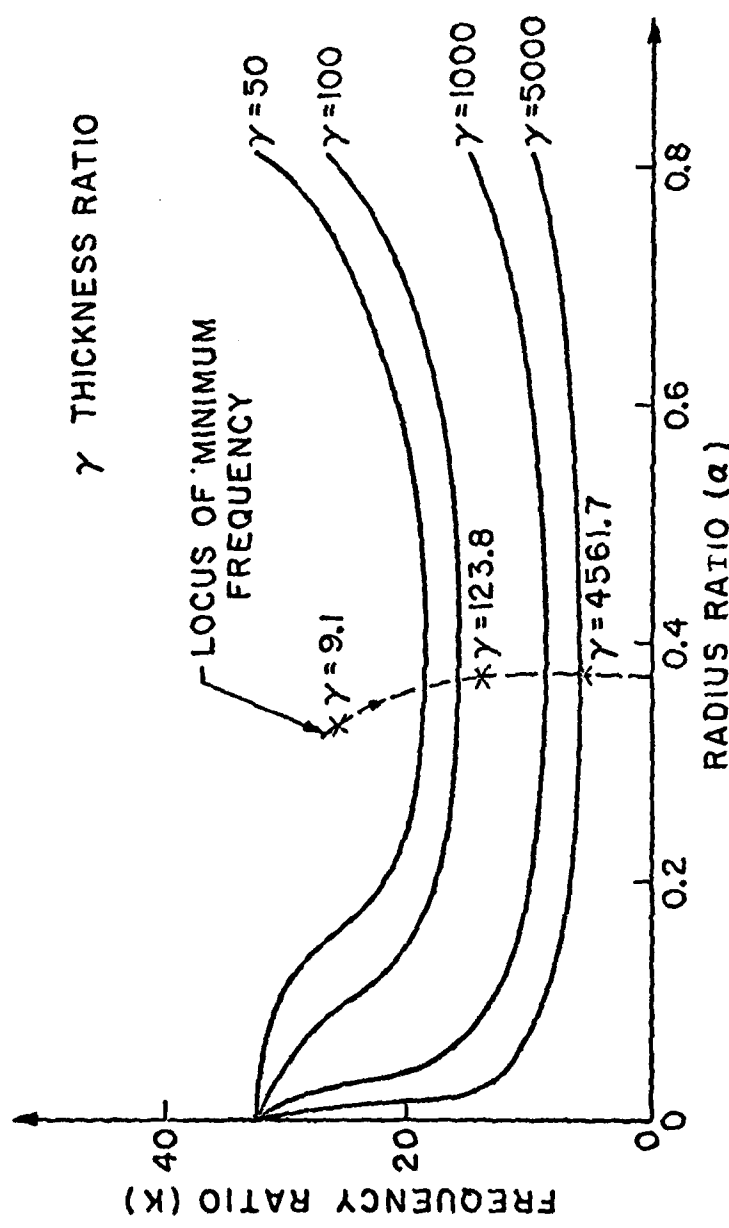


FIG. III-2 VARIATION OF THE FREQUENCY PARAMETER VS THE RADIUS RATIO PARAMETER OF THE CENTRALLY LOADED DIAPHRAGM. For a given thickness ratio, γ , the frequency ratio k has a minimum value at $\alpha = 0.37$. The sensitivity of frequency to radius ratio change at $\alpha = 0.37$ is rather small. Note also that the incremental change in k for a given change in α is a decreasing function of γ .

For sufficiently large γ , the frequency of the diaphragm will be a minimum at $\alpha = 0.37$. This is the value for α we will use in our design for the optimal accelerometer. As a quick estimation of this frequency, (B.9) can be simplified to

$$k^4 = \frac{c_2}{\gamma + c_3} \quad (3.7)$$

where $c_2 = 611.9$ and $c_3 = 0.8489$.

Given the dimensions of the diaphragm in Fig. II-10, γ is of the order of 100 for a resultant linear frequency of 50 Hz. For a diaphragm 0.020 in. thick, the overall height of the central mass would be 2 in., while the rim is typically 0.670 in. high. To preserve the compactness of the proof mass, the central mass is "folded" down into a dumbbell shape. The overall height of the central mass is equal to that of the rim, while the equivalent value of γ , the thickness ratio is kept the same. The resultant configuration is shown in Fig. III-3.

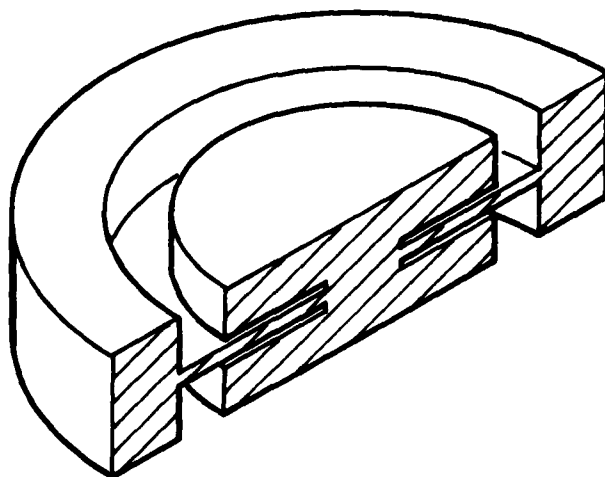


FIG. III-3 CROSS-SECTIONAL VIEW OF THE OPTIMALLY SHAPED PROOF MASS. To calculate the frequency of the diaphragm using the model, an equivalent h' which accounts for the volume of the ring is used.

A-2 The Ideal Accelerometer Model

In most of the theoretical projections in this dissertation, an ideal accelerometer is used. This accelerometer is designed as a centrally loaded diaphragm as described in the previous section. Two of these accelerometers are fabricated and will be described in Ch. VI.

The design values of the ideal accelerometer with a target frequency of 50 Hz are:

α = 0.37, the radius ratio

d = 3.5 in., the diaphragm diameter

h = 0.011 in., the diaphragm thickness.

Using (3.6) and (3.7), the mass of the central load is determined. The parameters of interest are

γ = 149.1, the thickness ratio

m = 0.304 kg, the mass of central load.

As the load is rigid, η , the geometric factor accounting for the flexure of the diaphragm in (2.17) has the value of unity.

With $d = 10^{-4}$ m, and $I_0 = 5A$, the output current of the ideal accelerometer given by (2.21) is

$$i_3(t) = c x(t) \quad (3.8)$$

where c has the value of 5×10^4 A/m. The same equation will give the current flowing into the SQUID, $i_s(t)$ with $c = 1.23 \times 10^4$ A/m incorporating the transformation ratio of the matching transformer (Ch. V-A-4).

A-3 Static Deflection of the Loaded Diaphragm

As the frequency of the diaphragm proof mass is lowered, it becomes essential for us to understand the deflections of the diaphragm under gravity. The stress and strain in the diaphragm would allow us to specify the operational environments of the specific-force meter.

The loaded diaphragm may be treated as an annular plate with a central rigid disk. The differential equation in polar coordinates describing small, axisymmetric deflection of the diaphragm is given by Love [1944] as

$$\left(\frac{\partial^2}{\partial r^2} + \frac{1}{r} \frac{\partial}{\partial r} \right) w = \frac{P}{2\pi D} \ln \frac{a}{r} + c_1 \quad (3.9)$$

where P = central load

a = outer radius of the diaphragm

D = flexural rigidity

c_1 = constant of integration.

Solving (3.9) for deflection, we obtain

$$w(r) = \frac{P}{8\pi D} \left(r^2 \ln \frac{a}{r} + r^2 \right) + \frac{1}{4} c_1 r^2 + c_2 + c_3 \ln r \quad (3.10)$$

where c_1 , c_2 , and c_3 are determined from boundary conditions which in this case are

$$w(a) = 0, \quad \left. \frac{\partial w}{\partial r} \right|_a = \left. \frac{\partial w}{\partial r} \right|_b = 0. \quad (3.11)$$

The same solution is obtained using the method of superposition as outlined in Timoshenko [1959]. After simplification, the expression for the surface of curvature under static load P is

$$w(x) = w_{\max} [\gamma_1 (x \ln x - x + 1) - A (\ln x - x + 1)] \quad (3.12a)$$

$$z = \frac{w(x)}{w_{\max}} = [\gamma_1 (x \ln x - x + 1) - A (\ln x - x + 1)] \quad (3.12b)$$

where

$$r_1 = \frac{1-\beta}{\Delta}, \quad A = \frac{\beta \ln \beta}{\Delta} \quad (3.13a)$$

$$\Delta = (1-\beta)^2 - \beta(\ln \beta)^2 \quad (3.13b)$$

$$x = \left(\frac{r}{a}\right)^2, \quad \beta = \left(\frac{b}{a}\right)^2 \quad (3.13c)$$

and

$$w_{\max} = \frac{3(1-\nu^2)}{4\pi r_1} \frac{P a^2}{E h^3} = k_1 \frac{P a^2}{E h^3} \quad (3.14)$$

and

$$\sigma_{\max} = -\frac{3}{2\pi} \left[1 + \frac{\ln \beta}{1-\beta} \right] \frac{P}{h^2} = k_2 \frac{P}{h^2}. \quad (3.15)$$

The maximum deflection of the central load is w_{\max} , and σ_{\max} is the maximum stress induced in the diaphragm. Wahl and Lobo [1930] have analysed this problem and given some numerical solutions.

For niobium, we have $\nu = 0.397$, $E = 15 \times 10^6$ psi. For the design diaphragm discussed in the previous section, we have:

$$k_1 = 0.04744 \quad (3.16a)$$

$$k_2 = 0.62257 \quad (3.16b)$$

Substituting k_1 and k_2 into (3.14) and (3.15), we have for the diaphragm under its own weight, $\xi = w_{\max}/h = 0.4430$, and $\sigma_{\max} = 3.45 \times 10^3$ psi. Since the tensile stress of niobium is 3×10^4 psi at room temperature, the safety factor is close to 10.

Section A-1 has shown that for a given diaphragm with a central mass, the frequency will be the lowest at $b/a = 0.37$. Thus (3.12b) is plotted in Fig. III-4 for x ranging from 0.37 to 1. It is denoted as the curve for flat plate theory. On the same graph, the curvature of the deflected diaphragm using the Hendelmann approximation (Eq. B.8) is compared. The closeness of fit indicates that the Hendelmann equation is accurate and the frequency estimate derived thereof in Sect. A-1 is expected to be good. This is confirmed in actual practice. Figure III-4 also shows

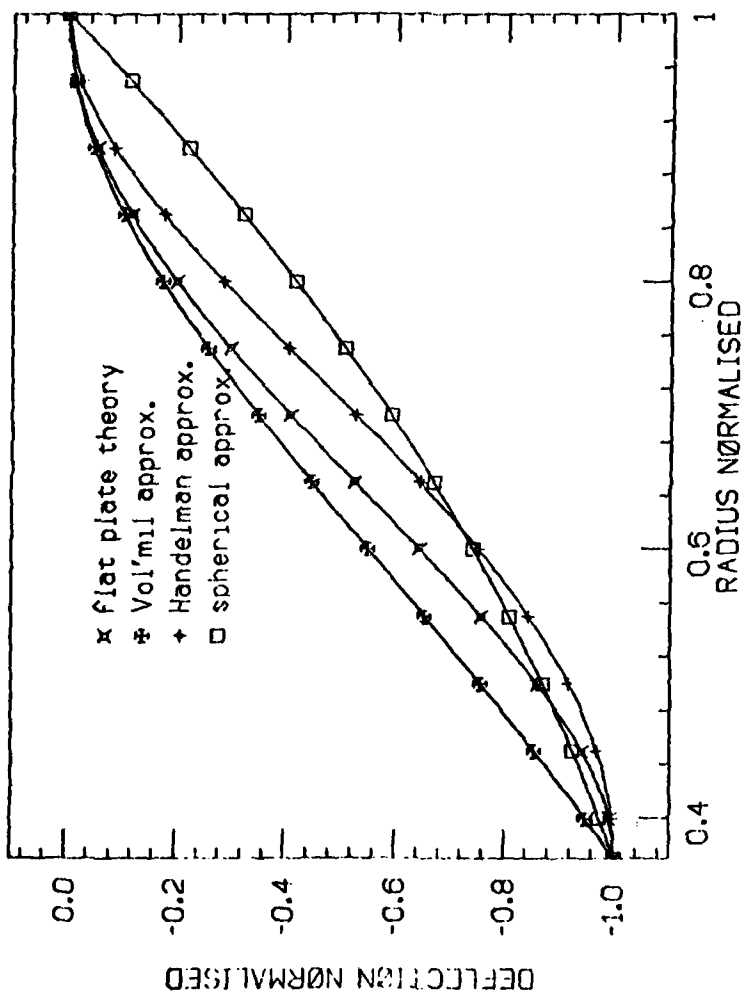


FIG. III-4 CURVATURE OF THE DEFLECTION OF THE DIAPHRAGM. The curvatures of the deflected diaphragm using different theory are plotted. The deflection is normalized with respect to the radius of the diaphragm.

some of the approximation equations used in the literature for the curvature of the deflected surfaces. Volmir [1967] approximation is good at $x = 1$ but does not reflect the actual curvature of the built-in edge at $x = 0.37$. Approximating the curvature of the deflected diaphragm as part of the surface of a sphere is totally inadequate.

The analysis in this section is valid only for small deflections of thin plates and becomes inadequate when we try to use it in the optimization of the proof mass in Sect. A-4. Small deflections give us a linear model for the force and displacement for the sensor. We would like to know the effects of rectification on displacement due to small sinusoidal acceleration, especially in the presence of 1 g. These considerations lead us to the thick plate analysis of the next section.

A-4 Large Deflection of Diaphragm

The differential equations for large deflection of thin circular plates are given by Karman as

$$D \left[\frac{1}{r} \frac{d}{dr} r \frac{d}{dr} \right] \left[\frac{1}{r} \frac{d}{dr} r \frac{dw}{dr} \right] = \frac{1}{r} \frac{d}{dr} \left(rNr \frac{dw}{dr} \right) + q \quad (3.17)$$

$$r \frac{d}{dr} \frac{1}{r} \frac{d}{dr} (r^2 Nr) + \frac{Eh}{2} \left(\frac{dw}{dr} \right)^2 = 0 \quad (3.18)$$

where E is the modulus of elasticity, D is the flexural rigidity, w is the lateral deflection, N_r is the radial membrane stress, and q is the intensity of the uniform load.

Multiplying (3.17) with rdr and integrating it from zero to r , we have

$$D \frac{d}{dr} \frac{1}{r} \frac{d}{dr} r \frac{dw}{dr} = Nr \frac{dw}{dr} + V \quad (3.19)$$

where V is the shearing force at a distance r from the center. For the loading condition of the diaphragm, $V = P/2\pi r$ where P is the central

load. The boundary conditions are

$$w = 0, \quad \frac{dw}{dr} = 0, \quad r \frac{dN_r}{dr} + (1-\mu)N_r = 0 \quad \text{at } r = a \quad (3.20)$$

$$\frac{dw}{dr} = 0, \quad r \frac{dN_r}{dr} + (1-\mu)N_r = 0 \quad \text{at } r = b. \quad (3.21)$$

Yeh [1952] has solved this particular problem using the perturbation method. First of all, the Karman equations are transformed into dimensionless forms by introducing new variables:

$$x = \left(\frac{r}{a}\right)^2, \quad y = \sqrt{3(1-\mu^2)} \frac{w}{h}, \quad S = 3(1-\mu^2) \frac{a^2 N_r}{Eh^3} \quad (3.22a)$$

$$p = \frac{1}{4} [3(1-\mu^2)]^{3/2} \frac{a^2 P}{\pi Eh^4}, \quad \beta = \frac{b^2}{a^2}, \quad \frac{1}{\lambda} = 1 - \mu. \quad (3.22b)$$

Equation (3.18) and (3.19) becomes

$$\frac{d^2}{dx^2} x \frac{dy}{dx} = S \frac{dy}{dx} + p \quad (3.23)$$

$$\frac{d^2}{dx^2} (xs) + \frac{1}{2} \left(\frac{dy}{dx}\right)^2 = 0. \quad (3.24)$$

The corresponding boundary conditions are transformed to

$$y = 0, \quad \frac{dy}{dx} = 0, \quad 2\lambda x \frac{ds}{dx} + s = 0 \quad \text{at } x = 1 \quad (3.25)$$

$$\frac{dy}{dx} = 0, \quad 2\lambda x \frac{ds}{dx} + s = 0 \quad \text{at } x = \beta. \quad (3.26)$$

In the perturbation method, all the independent variables, as well as the concentrated load p are expanded in ascending power series of Y_M . Here, Y_M is the maximum deflection of the plate, thus

$$Y_M = y|_{x=0} \quad (3.27)$$

and

$$p = \gamma_1 Y_M + \gamma_3 Y_M^3 + \dots \quad (3.28a)$$

$$y = y_1(x)Y_M + y_3(x)Y_M^3 + \dots \quad (3.28b)$$

$$s = s_2(x)Y_M^2 + \dots \quad (3.28c)$$

where γ_1 and γ_3 are constant, and y_1, y_3, \dots , as well as $s_2 \dots$ are functions of x to be determined.

The expressions (3.28) are substituted into (3.23) and (3.24), as well as the boundary conditions (3.25) and (3.26). By collecting terms of the successive order in Y_M , we obtain a sequence of linear differential equations for $\gamma_1, y_1, s_2, \gamma_3, y_3$, etc., with the corresponding boundary conditions. These equations can be integrated to provide closed form solutions. The interested reader is referred to Yeh's work for details in the intermediate steps. Owing to the lengthy integration involved, Yeh apparently simplified his results and his solutions are not accurate when b/a becomes large ($b/a > 0.36$). It is shown earlier that $b/a = 0.37$ is the optimal design value for a low-frequency diaphragm.

The author is fortunate to have access to the MACSYMA program of the MATHLAB group at the Mass. Institute of Technology through the help of Shahid Mujtaba of the Artificial Intelligence Lab. at Stanford University. This program can perform integration symbolically and is used to determine the closed form solutions as performed by Yeh. The results are shown in App. C.

For the dimensions of the niobium diaphragm described in Sect. A-2, $p = 2.9855$ in the earth's gravitational field with the sensitive axis vertical. From Table C-1 in App. C, the values of γ_1 and γ_3 for $\mu = 0.397$ are 4.2388 and 1.1393 respectively. Equation (3.28a) has only one real root. Using standard solution for a cubic equation, the displacement Y_M is given by

$$Y_M = \left(\frac{p}{2\gamma_3} \right)^{1/3} \left[(1+\tau)^{1/3} + (1-\tau)^{1/3} \right] \quad (3.29a)$$

$$\tau = \left[1 + \frac{4}{27} \frac{\gamma_1^3}{\gamma_3^p} \right]^{1/2} \quad (3.29b)$$

For the steady 1 g field, $Y_M = 0.6354$ which is obtained by substituting the values of p , γ_1 , and γ_3 given the above into (3.29). Using (3.22a), the equivalent central deflection $\xi = w/h = 0.3997$. This should be compared with $\xi = 0.4430$ given by linear small deflection analysis for the same diaphragm.

Owing to this nonlinearity in the force-displacement relation (3.28), a sinusoidal acceleration superimposed on the steady 1 g will produce a shift in the steady-state displacement. This is illustrated in Fig. III-5 where variation in p is the sinusoidal input.

If γ_1 and γ_3 are known accurately, the effect of the rectification can be calculated and compensated. Typically, γ_1 can be estimated accurately from the fundamental frequency which can be measured experimentally. Since γ_3 is difficult to determine, its uncertainty would be the major source of error in any compensation scheme.

Equation (3.29) is used to calculate the time-varying displacement $Y_M(t)$ due to the time-varying load

$$p(t) = p(1 + \frac{a}{g} \cos \omega t) \quad (3.30)$$

where ω is the frequency of the sinusoidal acceleration of magnitude a . Since an over-estimate of γ_3 would produce unnecessary errors, an

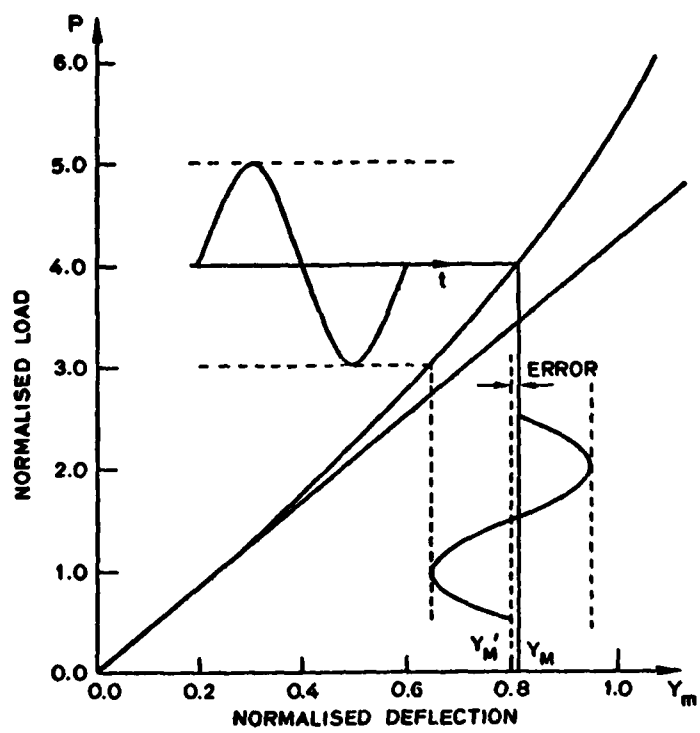


FIG. III-5 RECTIFICATION ERROR. The error produced by the third-order nonlinearity as a result of a sinusoidal variation in the load is illustrated.

under-estimation of $\gamma_{3,est}$ where

$$\gamma_{3,est} = \gamma_3(1 - \Delta) \quad (3.31)$$

is used. Fourier synthesis is then applied to the solution (3.29) to determine the "dc" value of the calculated value of Y_M , i.e., Y'_M . Using the parameters obtained for the design diaphragm, the errors in displacements, $Y_M - Y'_M$, for different values of Δ are calculated. The results are plotted in Fig. III-6. When a , the sinusoidal acceleration changes all the way from 0 to 1 g, the error for a given value of Δ does not change significantly even for large values of Δ . Clearly, in trying to compensate for the rectification error, the error contribution due to the uncertainty in γ_3 dominated those due to rectification.

A-5 Optimization of Dimensions of Proof Mass

The physical dimensions of the current accelerometers are derived from Dr. Paik's prototype. These dimensions are designed for the gravity wave antenna experiment in which a resonant frequency of 850 Hz was required. They are not necessarily optimal for an accelerometer. For a field instrument, we would like to minimize the physical dimensions, especially that of the diameter of the diaphragm without compromising its acceleration sensitivity or increasing unduly its Brownian noise.

In the optimization process, we will assume the following:

- (1) The diaphragm proof mass with a central load and radius ratio, $b/a = 0.37$, will be used;
- (2) The area of the pancake coil A_c , and the number of turns N , remain constant;
- (3) The accelerometer system Q is a constant.

The first assumption is reasonable as we would want the frequency of the proof mass as low as possible. The second assumption is made because preliminary calculations have shown that in most cases, the current design diameter of the coil, 2 in., is not a bound in the optimization. Later consideration will show that the inductance of the sensor coils are

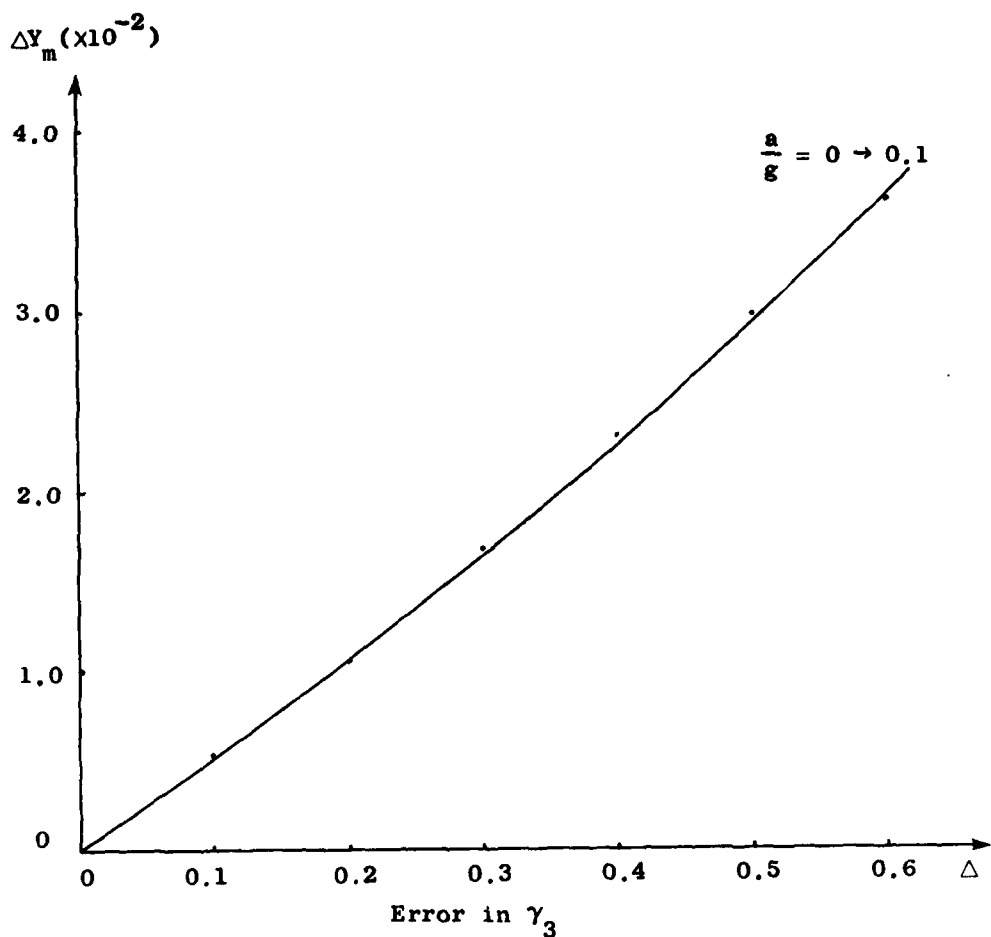


FIG. III-6 ERROR IN DISPLACEMENT ESTIMATE AS A RESULT OF UNCERTAINTY IN γ_3 . The curve is very close to being a straight line. As the magnitude of the vibrational acceleration, a , changes from 0 to 0.1 g, the change in ΔY_m is not discernable.

independent of the area. Moreover, A_c is determined by the size of the wires used. Currently, the coils are wound of 300 turns, 0.003 in. with Nb-Ti. wire. Reducing the area would imply either smaller wire be used or the number of turns be decreased. Reducing the number of turns will decrease the sensitivity of the pick-up. On the other hand, other than the mechanical difficulties associated with the thinner wires, one has to be concerned with the higher magnetic field that will be produced by a coil of thinner wire. The field produced in the current design with a 5A current is close to the critical value [Paik, 1974, p. 195].

The assumption on system Q is more controversial. Paik [1974, p. 108] has derived relation of the quality of the system Q_T , to the electrical component Q_E and the mechanical component Q_M . It is

$$\frac{1}{Q_T} = \frac{1 - \beta_T}{Q_M} + \frac{\beta_T}{Q_E} \quad (3.32)$$

where β_T is the coupling coefficient, and Q_M is determined by measuring the decay of the oscillations of the diaphragm alone in a vacuum at cryogenic temperature. Its value is determined experimentally to be much higher than 10^6 . Since Q_M is governed by internal dissipative mechanisms of the crystal structure of the material, it is independent of geometry. It has been suggested that mechanical Q_M may depend strongly on surface effects. If this is so, Q_M will only increase further as the dimensions of the diaphragm is made larger.

On the other hand, Q_T of the accelerometer is determined experimentally to be of the order of 2×10^5 for all the accelerometer systems tested (unpublished experimental results by Paik, Wang, and Napoles of Stanford University). Since Q_M is high, it is the electrical losses that determines the resultant system Q . In the optimization of the accelerometer, this value of Q_T will be used and regarded as a constant.

The inherent thermal noise in equivalent acceleration is given by (4.1) which is given below for convenience:

$$\langle a^2(t) \rangle^{\frac{1}{2}} = \left(\frac{4kT\omega}{mQ} \right)^{\frac{1}{2}}.$$

The acceleration sensitivity of the accelerometer is given in Sect. II-D-3 as

$$\Delta a_{\min} = \omega^2 d_0 \left[\frac{\phi_N^2}{k_p^2 L_p I_0^2} \right]^{\frac{1}{2}}, \quad \text{m/s}^2. \quad (3.33)$$

We will now simplify these expressions. The term L_p is the parallel combination of the inductances of the coils on either side of the diaphragm. The inductance, L_p , for an accelerometer is given by

$$L_p = \frac{1}{2} L_0 = \frac{1}{4} \mu_0 n^2 A_c d_0 \quad (3.34)$$

using basic principles, where

μ_0 = magnetic permeability of free space

n = turn density per unit length

A_c = area of the coil

d_0 = spacing between coil and diaphragm.

In the coils we have constructed, A_c the area of the coil, and n the turn density are given by

$$A_c = \pi(R_2^2 - R_1^2) \quad (3.35a)$$

and

$$n = \frac{N}{R_2 - R_1}, \quad (3.35b)$$

where N is the number of turns in the coil; and R_2 is the outer radius and R_1 , the inner radius of the coil. Substituting into (3.34) we have

$$L_p = \frac{1}{4} \left(\frac{R_2 + R_1}{R_2 - R_1} \right) \mu_0 \pi N^2 d_0. \quad (3.36)$$

For $R_2 = 1.0$ in., $R_1 = 0.125$ in., $\mu_0 = 4\pi \times 10^{-7}$, $N = 300$, and

$d_0 = 0.005$ in., $L_p = 14.5 \mu\text{H}$. The design value is $25 \mu\text{H}$.

The natural frequency of the accelerometer is given by (2.22). It is modified and reproduced here as

$$\omega^2 = \omega_0^2 + 4\pi^2 \alpha I_0^2$$

where α was given by (2.30).

The value of γ is (2.30) has been set to 1. Using (2.22), (2.30), and (3.36), and with $\gamma = 1$ for maximum energy transfer, (4.1) and (3.33) become

$$\langle a^2(t) \rangle^{\frac{1}{2}} = \left(\frac{4kT}{mQ} \right)^{\frac{1}{2}} \left(\omega_0^2 + \frac{bI_0^2}{md_0} \right)^{1/4} \quad (3.37)$$

and

$$\Delta a_{\min} = \frac{2\phi N}{k_t N I_0 \sqrt{\mu_0 \pi L_s}} \left(\omega_0^2 + \frac{bI_0^2}{md_0} \right)^{\frac{1}{2}} d_0^{\frac{1}{2}}. \quad (3.38)$$

Differentiating (3.38) with respect to d_0 and equating to zero, the best acceleration sensitivity is attained when the spacing between coil and the diaphragm is

$$d_{\min} = \frac{b I_0^2}{m \omega_0^2} . \quad (3.39)$$

For the ideal accelerometer used in Sect. II-A-2, $m = 0.3 \text{ kg}$, $I_0 = 5\text{A}$, $\omega_0 = 2\pi(50) \text{ sec}^{-1}$, the value of d_{\min} is $1.5 \times 10^{-4} \text{ m}$ (0.0059 in.). For the 800 Hz diaphragm used in our experiments, $d_{\min} = 1.35 \times 10^{-5} \text{ m}$ (0.00053 in.). Owing to the dimensional tolerance of the fabrication process, this separation cannot be attained. In the subsequent optimization, it will be assumed that d_{\min} can be realized. With $d_0 = d_{\min}$, (3.37) and (3.38) become

$$\langle a^2(t) \rangle^{\frac{1}{2}} = \left(\frac{4\sqrt{2} k T \omega_0}{m Q} \right)^{\frac{1}{2}} \quad (3.40)$$

and

$$\Delta a_{\min} = \frac{2\phi_N}{k_t} \omega_0 \sqrt{\frac{2}{m L_s}} \quad (3.41)$$

where ω_0 is determined for a dumbbell-shaped proof mass by using (3.6) and (3.7); m has two components: the mass of the diaphragm and the mass of the load. The relation is

$$m = \rho \pi a^2 h [1 + \alpha^2(\gamma-1)]$$

where α , γ , ρ , a , and h are defined in Sect. A-2. For the ideal proof mass discussed in Sect. A-2, (3.41) becomes

$$\Delta a_{\min} = \frac{c_5}{c_4} \left[\frac{h}{(\gamma+c_3)(\gamma+c_4)} \right]^{\frac{1}{2}} \quad (3.42)$$

where

$$c_3 = 0.8489$$

$$c_4 = 1 - \alpha^2 / \alpha^2 \text{ and has a value of 6.305}$$

$$c_5 = \frac{2\phi_N}{k_t} \sqrt{\frac{2}{L_s}} \frac{(611.9\rho/\rho\pi)}{h}, \text{ a constant of proportionality for a given diaphragm}$$

α = geometric ratio of the diaphragm and is different from that defined in (2.30).

Note that the resolution of the accelerometer improves as h , the thickness, is decreased and as the radius, and γ the thickness ratio of the load are increased. The bounds on these variables are set by the fabrication techniques, the time constant of the instrument, its physical size, and its thermal noise.

Starting with a given dimension of the diaphragm proof mass, we

would like to determine how small the radius R can be while retaining the same acceleration sensitivity as h is made smaller. In this optimal accelerometer, the radius of the central mass is always $0.37 R$. As there are infinite combinations of R and γ , the thickness ratio that will satisfy this requirement, we would consider two cases within which bounds all possible combinations must fall. The thickness of the central load, h'_0 may be kept constant, i.e., γ will increase as h is decreased; $\gamma = (h_0/h)\gamma_0$. The subscript 0 indicates the original values of the parameters of the basic design. On the other hand, we can keep γ_0 constant allowing the thickness of the central load to decrease as h , the thickness of the diaphragm is decreased. Denoting the radius of the basic design as a , the relation of R to a for constant γ is

$$\frac{R}{a} = \sigma \sqrt{\frac{h}{h_0}} \quad (3.43)$$

and for constant thickness, h'_0 ,

$$\frac{R}{a} = \left[\frac{(\gamma_0 + c_3)(\gamma_0 + c_4)}{h_0} \frac{h^3}{(\gamma_0 h_0 + c_3 h)(\gamma_0 h_0 + c_4 h)} \right]^{1/6} \quad (3.44)$$

For the basic accelerometer design, $d = 1.75$ in., $h_0 = 0.011$ in., $\gamma_0 = 149.1$, $c_3 = 0.8489$ and $c_4 = 6.305$.

When the dimensions are decreased, the thermal noise would increase from its original value of $N_0 = 1.3 \times 10^{-12} \text{ m-s}^{-2}/\sqrt{\text{Hz}}$ per (3.39). Assuming Q remains constant as discussed earlier, the noise given in terms of N_0 are

$$\langle a^2(t) \rangle^{\frac{1}{2}} = N_0 \left(\frac{a}{R} \right)^2 \quad (3.45)$$

for constant γ and

$$\langle a^2(t) \rangle^{\frac{1}{2}} = N_0 \left(\frac{a}{R} \right)^2 \left(\frac{\gamma_0 + c_4}{\gamma_0^{h_0^{h-1}} + c_4} \right)^{\frac{1}{2}} \left(\frac{\gamma_0 + c_3}{\gamma_0^{h_0^{h-1}} + c_3} \right)^{\frac{1}{4}} \quad (3.46)$$

for constant load thickness h' ; h_0 is the original thickness of the diaphragm. In evaluating (3.45) and (3.46), the (h, R) pairs determined in (3.43) and (3.44) are used. The results are plotted in Fig. III-7. As a comparison, the thermal noise of the SQUID is equivalent to $21.5 N_0$ (Eq. 2.42) and is a constant in the bandwidth of interest. Thus in the optimization of the present accelerometer system, the process is not bound by the thermal noise of the diaphragm.

Since the thermal noise of the system is dominated by those of the SQUID, the noise contribution of the diaphragm will be ignored henceforth. In the design consideration that follows, it is assumed that γ will be constant. Thus (3.43) applies when the signal-to-noise ratio is maintained constant as the size is minimized. The design criteria are

- (a) The thickness of the diaphragm, h , is reduced as much as possible,
- (b) Eq. (3.43) is used to determine the minimum value of R that will give the same signal-to-noise (SNR) ratio.

For design values of $h_0 = 0.011$ in., $a = 1.75$ in., and $h = 0.005$ in., the smallest R value is 1.53 in.

If the SNR of the accelerometer were to be maximized while keeping the radius of the diaphragm a constant, then the thickness h must be as small as possible. In other words, SNR increases monotonically as h decreases. For the case where the value of the thickness ratio, γ , remaining constant,

$$(\text{SNR}) = (\text{SNR})_0 \sqrt{\frac{h_0}{h}} . \quad (3.47)$$

Thus, system improvement through size optimization has certain fundamental limitations.

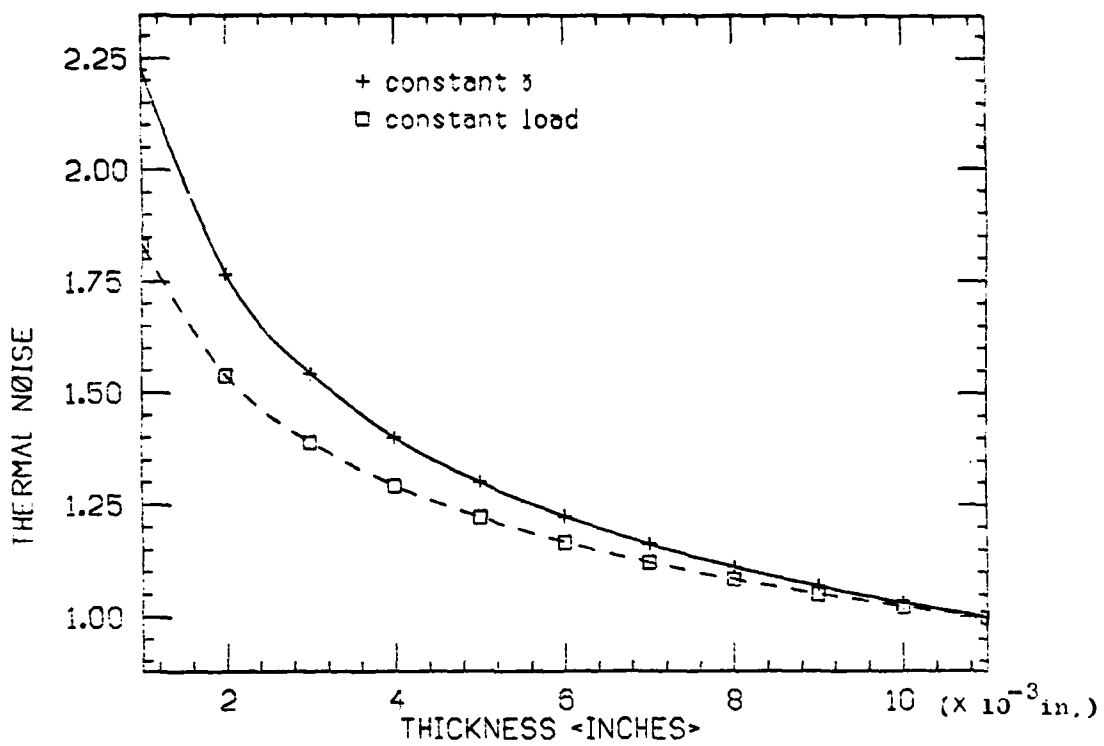


FIG. III-7 THICKNESS EFFECTS ON THE THERMAL NOISE. As the thickness of the diaphragm is reduced from its design value of 0.011 in., the thermal noise level varies as shown. The thermal noise is given in terms of the noise level of the original diaphragm.

B. THE CURRENT DIFFERENCING GRAVITY GRADIOMETER

In this gradiometer, a pair of the superconducting accelerometers are rigidly attached together. They are separated by a given distance. Their sensitive axes may be aligned along the straight line joining them or perpendicular to this line. The axes are always parallel. The outputs of the two accelerometers are differenced. The ratio of the output difference to the separation is the gradient signal.

The basic configuration adopted for the initial feasibility study of the concept is with the sensitive axes along the line joining the accelerometers. The final configuration may be that used by the Bell Aerospace Labs (Fig. II-2) in their gradiometer in which the sensitive axes are perpendicular to the line joining a pair of them. This configuration facilitates error tradeoffs through rotating the gradiometer platform. Diesel [1964] had studied such tradeoffs in a single rotating accelerometer. The comparison of the advantages of the different accelerometer configurations is given in Ch. IV-C-3.

Figure III-8 shows the three different means of differencing the outputs from the two cryogenic sensors. In all three cases, coupling between the two diaphragm proof masses exists. The mechanical coupling through the gradiometer platform can be reduced by making the platform massive. To minimize electrical coupling and yet retain circuit simplicity, the scheme using direct parallel connections shown in Fig. III-8b is used. The figure is enlarged in Fig. III-9, with the appropriate notations of the different elements.

When the test masses deflects by $x_1(t)$ and $x_2(t)$ under acceleration, the modulated inductances are given by

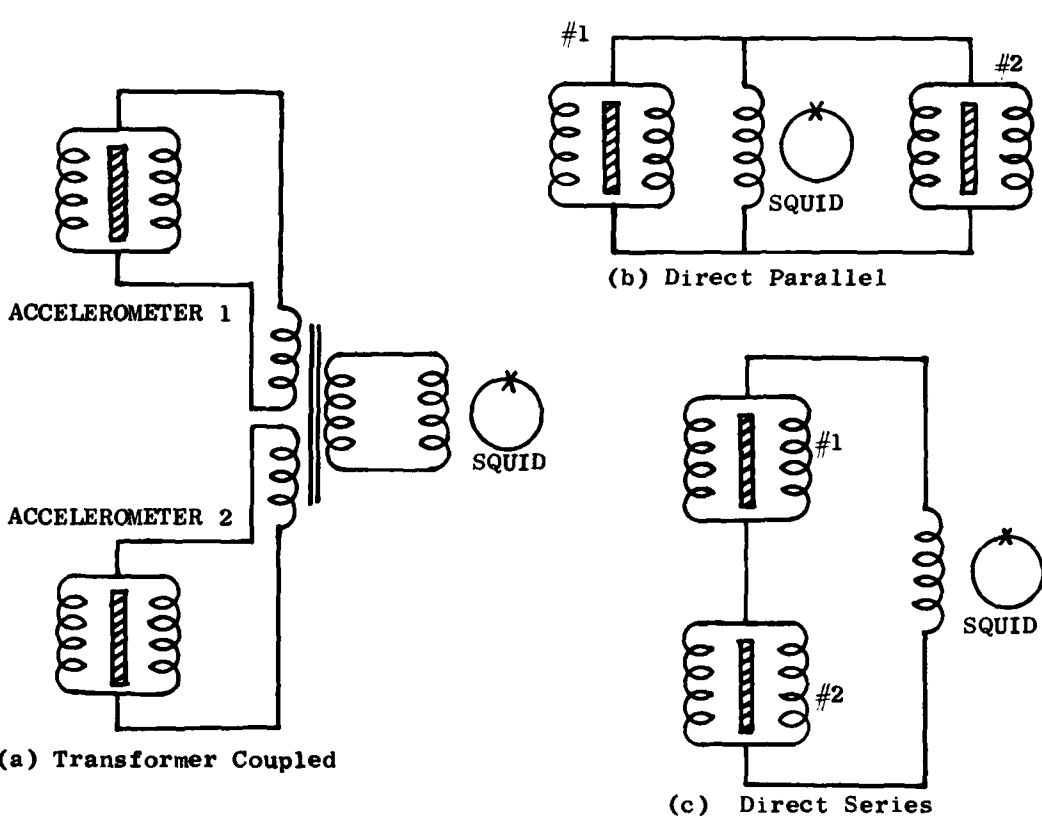
$$L_{11}(t) = L_{10}[1 + \delta_1 x_1(t)] \quad (3.48a)$$

$$L_{12}(t) = L_{10}[1 - \delta_1 x_1(t)] \quad (3.48b)$$

$$L_{21}(t) = L_{20}[1 + \delta_2 x_2(t)] \quad (3.48c)$$

$$L_{22}(t) = L_{20}[1 - \delta_2 x_2(t)] \quad (3.48d)$$

where



FIGs. III-8a,b,c SIGNAL DIFFERENCING SCHEMES. The three feasible circuits for the current differencing gravity gradiometer (CDGG) are shown. The direct parallel scheme is chosen for its simplicity and low cross-coupling.

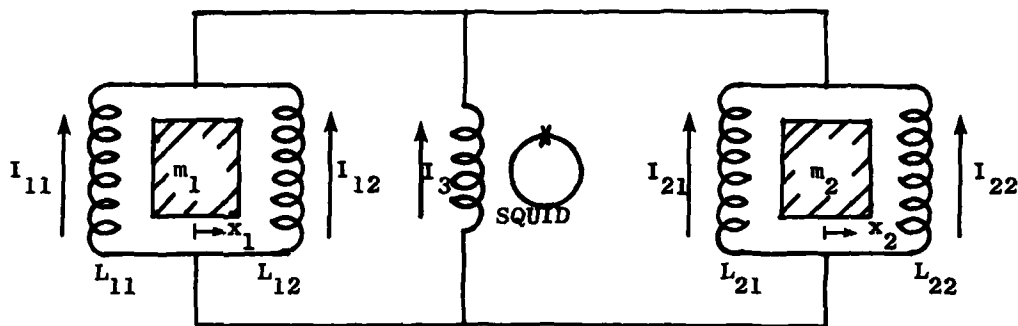


FIG. III-9 SCHEMATIC OF CURRENT DIFFERENCING GRAVITY GRADIOMETER.
The notation for current flows is used for convenience.

In the ambient mode, $I_3 = 0$, $I_{11} + I_{12} = 0$, and
 $I_{21} + I_{22} = 0$, a current will flow in L_3 when
 $x_1 \neq x_2$.

$$\delta_1 = \frac{1}{\eta_1 d_{10}} \quad (3.49a)$$

$$\delta_2 = \frac{1}{\eta_2 d_{20}} \quad (3.49b)$$

where d_{10} and d_{20} are the equilibrium spacings for the two accelerometers, η is the geometric factors accounting for the flexure in the diaphragm test masses and for all practical purposes may be assumed equal,

$$\eta_1 = \eta_2 . \quad (3.50)$$

These equations were derived by Paik [1974]. The subscripts are self-evident.

For simplicity, it is assumed that

$$L_{11}(x = 0) = L_{12}(x = 0) = L_{10} \quad (3.51a)$$

$$L_{21}(x = 0) = L_{22}(x = 0) = L_{20} . \quad (3.51b)$$

The errors introduced by these assumptions will be discussed in Ch. IV.

In operation, the persistent current I_1 and I_2 in the two accelerometers are stored independently. The currents are stored such that when the displacements $x_1(t)$ and $x_2(t)$ are in the same direction, the outputs of the accelerometers cancel one another. The cancellation will be exact if $x_1(t) = x_2(t)$ and the scale factors of the accelerometers are adjusted to be equal.

Flux is constant in each of the four loops comprising the inductances to the left of the equal sign in the following equations:

$$L_{11}I_{11} - L_{12}I_{12} = 2L_{10}I_1 = \phi_1 \quad (3.52a)$$

$$-L_{21}I_{21} + L_{22}I_{22} = 2L_{20}I_2 = \phi_2 \quad (3.52b)$$

$$L_{11}I_{11} - L_3I_3 = L_{10}I_1 = \frac{1}{2}\phi_1 \quad (3.52c)$$

$$-L_{21}I_{21} + L_3I_3 = L_{20}I_2 = \frac{1}{2}\phi_2 \quad (3.52d)$$

where I_3 is zero at the initial steady state.

Summing currents at the node connecting all the coils yield

$$I_{11} + I_{12} + I_{21} + I_{22} + I_3 = 0. \quad (3.53)$$

Solving these five equations simultaneously, we obtain

$$I_3 = \frac{\phi_2 \left(\frac{1}{L_{21}} - \frac{1}{L_{22}} \right) - \phi_1 \left(\frac{1}{L_{11}} - \frac{1}{L_{12}} \right)}{2 \left(1 + \frac{L_3}{L_p} \right)} \quad (3.54)$$

where L_p is the parallel combination of the inductances of the four coils.

$$L_p^{-1} = L_{11}^{-1} + L_{12}^{-1} + L_{21}^{-1} + L_{22}^{-1} \dots \quad (3.55)$$

It should be noted that L_{11} , L_{12} , L_{21} , and L_{22} are functions of displacements and hence time.

Substituting (3.52) into (3.54) gives

$$I_3(x_1, x_2) = \frac{2}{1+\gamma} \left(\frac{I_1 x_1}{\eta d_{10}} - \frac{I_2 x_2}{\eta d_{20}} \right) \dots \quad (3.56)$$

where $\gamma = L_3/L_p$; L_p is given by (3.55) when $x_1(t) = x_2(t) = 0$. For small displacements, errors introduced by ignoring higher order terms are negligible.

If signal frequency is much less than resonant frequencies of the diaphragms, ω_1 and ω_2 , the equivalent displacements are given by

$$x_1(t) = \frac{a_1(t)}{\omega_1^2} \quad (3.57a)$$

$$x_2(t) = \frac{a_2(t)}{\omega_2^2} \quad (3.57b)$$

where $a_i(t)$ s are the accelerations along the sensitive axis of the gradiometer at the two proof masses. Letting

$$\frac{1}{2}[a_1(t) + a_2(t)] \equiv \bar{a}(t) \text{ and } [a_2(t) - a_1(t)] \equiv \Delta a(t)$$

(3.56) simplifies to

$$I_3(t) = \frac{2}{\eta(1+\gamma)} \left[\left(\frac{I_1}{\omega_1^2 d_{10}} - \frac{I_2}{\omega_2^2 d_{20}} \right) \bar{a}(t) - \left(\frac{I_1}{\omega_1^2 d_{10}} + \frac{I_2}{\omega_2^2 d_{20}} \right) \frac{\Delta a(t)}{2} \right] . \quad (3.58)$$

If

$$\frac{I_1}{\omega_1^2 d_{10}} = \frac{I_2}{\omega_2^2 d_{20}} \quad (3.59)$$

holds, then output is given simply as

$$I_3(t) = -\frac{2}{\eta(1+\gamma)} \frac{I_1}{\omega_{10}^2 d} \Delta a(t) \dots \quad (3.60)$$

Equation (3.59) represents the condition when the scale factors of the accelerometers are balanced. When the "balanced" state is achieved, the gradiometer is insensitive to the common mode acceleration and responds only to the differential mode. Even when the two accelerometers are mechanically different, the gradiometer will balance out if the stored current ratios satisfy (3.59). The means for adjusting current will be discussed in Ch. V.

Thus superconductivity offers the dual advantages of cancellation of common mode before detection and simplicity of balancing. The high common mode rejection ratio before detection allows the gradiometer to be operated in noisier environment than it would otherwise.

The frequency ω_1^2 is given in Ch. II as (2.22)

$$\omega_1^2 = \omega_{10}^2 + 4\pi^2 \alpha I_1^2.$$

Substituting into (3.60) we have

$$I_3(t) = -\frac{2}{\eta(1+\gamma)} \frac{I_1}{\omega_{10}^2 + 4\pi^2 \alpha I_1^2} \frac{\Delta a(t)}{d_{10}}. \quad (3.61)$$

For a given gradiometer, the only adjustable parameter in (3.61) is I_1 , the stored persistent current. To maximize current output for a given gradient, the current stored should have the value given by

$$I_1 = \frac{\omega_{10}}{2\pi\sqrt{\alpha}}. \quad (3.62)$$

This is the same equation obtained for the accelerometer in (2.32). Thus the electrical spring rate should be equal to the mechanical spring rate for optimum sensitivity.

The energy transferred by $I_3(t)$ into L_3 , the output coil, is

$$E = \frac{1}{2} L_3 I_3^2(t) = \frac{2\gamma}{(1+\gamma)^2} L_p I_1^2 \left[\frac{\Delta a(t)}{\omega_1^2 \eta d_{10}} \right]^2. \quad (3.63)$$

Clearly, the energy transfer will be a maximum if $\gamma = 1$ or $L_3 = L_p$.

As shown in Fig. III-9, L_3 is the input inductance of the SQUID. In general, since the input inductance of the SQUID, denoted as L_s is rather small (for SHE SQUID, L_s is typically $2\mu H$), L_3 is the equivalent inductance of the SQUID reflected to the primary of a step-down transformer. Such a transformer will be discussed in Ch. V.

By considering the transformer action of a zero resistance transformer, we have the following relation (2.37) and (2.38b):

$$L_3 = L_a \left(1 - \frac{k^2 L_b}{L_b + L_s} \right)$$

$$I_s(t) = \frac{k \sqrt{L_a L_b}}{(L_b + L_s)} I_3(t).$$

The energy transferred into the SQUID is

$$E_s = \frac{1}{2} L_s I_s^2(t) \quad (3.64a)$$

$$= \frac{1}{2} k^2 \frac{L_s L_a L_b}{(L_b + L_s)^2} I_3^2(t) \quad (3.64b)$$

$$= \frac{1}{2} k^2 N^2 \frac{L_b^2}{(L_b + L_s)^2} L_s I_3^2(t) \quad (3.64c)$$

using the relation $L_a = N^2 L_b$ for a solenoidal transformer with turn ratios of N . From a practical consideration, L_b is chosen, as a rule of thumb, to be about three times the value of L_s , i.e., $6\mu H$. The value of N giving the maximum energy transfer may be obtained by equating

(3.64c) to $\frac{1}{2} L_p I_3^2$ where L_p is given by (3.55).

In an ideal gradiometer, its sensitivity is found by the noise energy in the SQUID. Equating (3.64c) to SQUID noise energy, E_N , and using (3.60) for I_3 , the minimum resolution in acceleration is given by

$$(\Delta a)_{\min} = \left[\frac{E_N}{\frac{1}{2} k_N^2 L_s} \right]^{\frac{1}{2}} \left(\frac{L_b + L_s}{L_b} \right) \frac{\omega_1 \eta d_{10}}{I_1} . \quad (3.65)$$

Using the design parameters for the ideal gradiometer and SHE SQUID, we have $\omega_1 = 2\pi(50)\text{sec}^{-1}$, $\eta = 1$, $d_{10} = 10^{-4}\text{m}$, $k^2 = 0.8$, $L_p = 25 \times 10^{-5}\text{H}$, $I_1 = 5\text{A}$, $L_s = 2\mu\text{H}$, $L_b = 6\mu\text{H}$, $E_N = 2 \times 10^{-28}\text{J/Hz}$ and the turn ratio of the design transformer, $N = 3.23$, the minimum resolution becomes

$$\begin{aligned} (\Delta a)_{\min} &= 1.29 \times 10^{-11} \text{ m/s}^2/\sqrt{\text{Hz}} \\ &= 1.32 \times 10^{-12} \text{ g}/\sqrt{\text{Hz}} . \end{aligned}$$

For a bandwidth of 1 Hz and a baseline separation of 10 cm, the gradient sensitivity is about 0.13 E.

For completeness, the expression for the SQUID input current as a result of differential acceleration is

$$I_s(t) = \frac{I_1}{\eta \omega_1 d_{10}} kN \left(\frac{L_b}{L_b + L_s} \right) \Delta a(t) . \quad (3.66a)$$

For the same gradiometer with parameters given above,

$$I_s(t) = 1.097 \Delta a(t) \text{ A} \quad (3.66b)$$

where $\Delta a(t)$ is given in m/s^2 .

The electrical coupling between the two accelerometers has been investigated by Paik. Any mechanical coupling through momentum transfer can be made small by making the platform relatively massive. From (3.52) and (3.53), the equations for I_{11} and I_{12} are

$$I_{11} = \frac{\phi_1}{2L_{11}} \left[1 - \frac{L_3}{1+\gamma} \left(\frac{1}{L_{11}} - \frac{1}{L_{12}} \right) \right] + \frac{\phi_2}{2L_{11}} \frac{L_3}{1+\gamma} \left(\frac{1}{L_{21}} - \frac{1}{L_{22}} \right) \quad (3.67a)$$

$$I_{12} = -\frac{\phi_1}{2L_{12}} 1 + \frac{L_3}{1+\gamma} \left(\frac{1}{L_{11}} - \frac{1}{L_{12}} \right) + \frac{\phi_2}{2L_{12}} \frac{L_3}{1+\gamma} \left(\frac{1}{L_{21}} - \frac{1}{L_{22}} \right). \quad (3.67b)$$

Note I_{22} and I_{21} are given by identical equations as (3.67) with subfixes 1 and 2 interchanged.

Considering the energy stored in the two coils of the accelerometer and differentiating with respect to displacement, the forces exerted on the test masses are

$$F_1(t) = \frac{L_{10}}{2\eta d_{10}} \left(I_{11}^2 - I_{12}^2 \right) \quad (3.68a)$$

$$F_2(t) = \frac{L_{20}}{2\eta d_{10}} \left(I_{21}^2 - I_{22}^2 \right).$$

Using (3.67) and (3.48) the forces are given to the leading order as

$$F_1(t) = -K_{11}X_1(t) - K_{12}X_2(t) \quad (3.69a)$$

$$F_2(t) = -K_{21}X_1(t) - K_{22}X_2(t), \quad (3.69b)$$

where

AD-0882 535

STANFORD UNIV CALIF GUIDANCE AND CONTROL LAB
MODELING AND ERROR ANALYSIS OF A SUPERCONDUCTING GRAVITY GRADIO--ETC(U)
AUG 79 K Y WANG

F/6 17/7

AFOSR-76-2913

AFOSR-TR-80-0219

NL

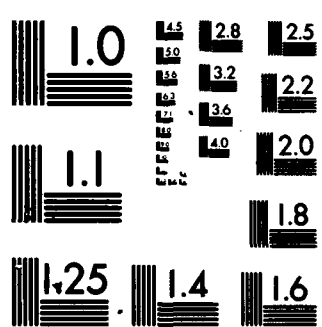
UNCLASSIFIED

2 13

2 13

13





MICROCOPY RESOLUTION TEST CHART

$$K_{11} = 2 \left(L_{10} - \frac{2}{(1+\gamma)} L_3 \right) \left(\frac{I_1}{\eta d_{10}} \right) \quad (3.70a)$$

$$K_{22} = 2 \left(L_{20} - \frac{2}{(1+\gamma)} L_3 \right) \left(\frac{I_2}{\eta d_{20}} \right)^2 \quad (3.70b)$$

$$K_{12} = K_{21} = \frac{4}{(1+\gamma)} L_3 \left(\frac{I_1}{\eta d_{10}} - \frac{I_2}{\eta d_{20}} \right) \quad (3.70c)$$

The coefficients of equations (3.70) give the coupling between the two diaphragm proof masses.

For the ideal gradiometer mentioned earlier, $\gamma = 1$, $L_3 = \frac{1}{2}L_{10} = \frac{1}{2}L_{20}$, the coefficients of (3.70) become

$$K_{11} = L_{10} \left(\frac{I_1}{\eta d_{10}} \right)^2 \quad (3.71a)$$

$$K_{22} = L_{20} \left(\frac{I_2}{\eta d_{20}} \right)^2 \quad (3.71b)$$

$$K_{12} = K_{21} = L_{10} \left(\frac{I_1}{\eta d_{10}} \right) \left(\frac{I_2}{\eta d_{20}} \right) \quad (3.71c)$$

Thus if I_1 has the same order of magnitude as I_2 , the cross-coupling coefficient has the same magnitude as that of the direct coupling. Thus, the motions of proof mass m_1 say, produces restoring forces of roughly the same magnitude on both m_1 and m_2 .

These restoring forces will be zero if $x_1(t)$ and $x_2(t)$ are zero. Thus a force rebalancing, null position accelerometer may be required to eliminate this effect.

C. THE DISPLACEMENT DIFFERENCING GRAVITY GRADIOMETER

The fundamental operating principle of this gradiometer has been derived by Paik of Stanford. Figure III-11 gives the schematic of the instrument. The two diaphragm proof masses are m_1 and m_2 ; L_1 is the pancake shaped sensor coil placed between the two proof masses. A persistent current I_0 is stored in the loop comprised of inductances L_1 and L_a . The differential deflections of m_1 and m_2 in a gradient field will modulate the inductance L_1 . As the flux enclosed in a superconducting

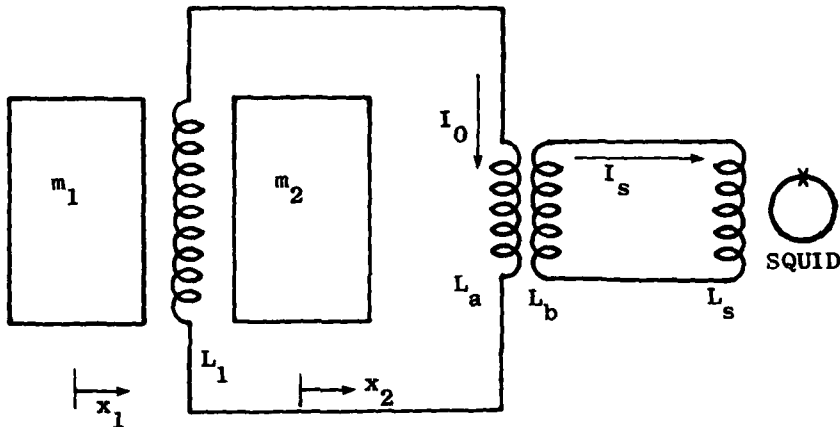


FIG. III-10 SCHEMATIC DIAGRAM OF THE DISPLACEMENT DIFFERENCING GRAVITY GRADIOMETER (DDGG)

circuit will remain a constant, I_0 will change as the inductance of coil L_1 changes. The SQUID measures the changes in current through the matching transformer which carries zero persistent current in its secondary loop.

The principle of this gravity gradiometer is very similar to that of the vibrating string gradiometer discussed in Ch. II. Instead of the vibrating string, the persistent current in the coil is used to detect the relative displacements of the proof masses. However, the distance between the mass centers of the proof masses of the displacement differencing gravity gradiometer (DDGG) is rather small (of the order of 0.25 mm or 0.010 in.). This severely limits the sensitivity of the DDGG.

In the original design, L_1 is a self-centering coil such that the single layer coil will always be exactly midway between the surfaces of the proof masses. It turned out that such a floating coil is very hard to fabricate since all materials become very rigid at the cryogenic temperature of liquid helium. The compromise of winding the coil on one of the surfaces has been adopted by E. Mapoles of Stanford. The degradation in sensitivity is considered small and acceptable.

In the following discussion, d_{10} denotes the distance between the coil and the proof mass, m_1 , on which it is wound. This distance is fixed. At the neutral position, the distance between the coil and the second proof mass, m_2 , is denoted by d_{20} . As the proof masses move relative to one another, this distance will vary and will be denoted by $d_2(t)$.

If $x_1(t)$ and $x_2(t)$ denote the displacements of the test masses m_1 and m_2 respectively, then

$$d_2(t) - d_{20} = x_2(t) - x_1(t) . \quad (3.72)$$

Using first principles, the inductance of the sensor coil at any given time is

$$L_1(t) = \mu_0 n^2 A_c \frac{d_{10} d_2(t)}{d_{10} + d_2(t)} \quad (3.73)$$

where n is the turn density per unit length, and A_c is the area of the coil. Substituting (3.72) into (3.73) and expanding, using power series, we get

$$L_1(t) = L_{10} \left[1 + \frac{d_{10}}{d_{20}} \frac{x_2(t) - x_1(t)}{d_{10} + d_{20}} \right. \\ \left. - \frac{d_{10}}{d_{20}} \left(\frac{x_2(t) - x_1(t)}{d_{10} + d_{20}} \right)^2 + O\left(\frac{x}{d_0}\right)^3 \right] \quad (3.74)$$

where L_{10} is the equilibrium value of $L_1(t)$ and is given as

$$L_{10} = u_0 n^2 A_c \left(\frac{d_{10} d_{20}}{d_{10} + d_{20}} \right) \quad (3.75)$$

To the first order, $L_1(t)$ is linearly dependent on the displacement difference. The presence of higher order terms, especially the third order, means that there will be some nonlinearity errors.

To reflect this change in inductance in the pickup coil, a persistent current I_0 is stored in the loop comprising $L_1(t)$ and L_a . The flux conservation requirement of (2.12) yields

$$I_0 [L_{10} + L_2] = I(t) [L_1(t) + L_2] \quad (3.76)$$

where (2.37) gives the value of L_2 , where L_2 is the equivalent inductance of the SQUID input coil seen by $L_1(t)$.

Solving for $I(t)$, we obtain

$$I(t) = I_0 \left[\frac{L_{10} + L_2}{L_2 + L_1(t)} \right] \quad (3.77a)$$

$$\simeq I_0 \left[1 - \frac{1}{1+\gamma} \frac{d_{10}}{d_{20}} \frac{1}{d_{10} + d_{20}} [x_2(t) - x_1(t)] + \dots \right] \quad (3.77b)$$

where $\gamma = L_2/L_{10}$ after substituting for $L_1(t)$ using (3.74).

If the gradient signal frequency is low compared to the resonant frequencies of the proof masses m_1 and m_2 , the displacements $x_1(t)$ and $x_2(t)$ are given by (3.57). Equations (3.77) can be simplified to

$$\begin{aligned} i(t) &= I_1(t) - I_0 = \frac{\lambda}{1+\gamma} I_0 [x_1(t) - x_2(t)] \\ &= \frac{\lambda I_0}{1+\gamma} \left[\frac{a_1(t)}{\omega_1^2} - \frac{a_2(t)}{\omega_2^2} \right], \end{aligned} \quad (3.78)$$

where

$$\lambda = \frac{d_{10}}{d_{20}(d_{10} + d_{20})} .$$

If $\bar{a}(t) = \frac{1}{2}[a_1(t) + a_2(t)]$ and $\Delta a(t) = a_1(t) - a_2(t)$, (3.78) becomes

$$i(t) = \frac{\lambda I_0}{1+\gamma} \left[\left(\frac{1}{2} - \frac{1}{\omega_2^2} \right) \bar{a}(t) - \left(\frac{1}{2} + \frac{1}{\omega_2^2} \right) \frac{\Delta a(t)}{2} \right]. \quad (3.79)$$

The output produced by the common mode acceleration, $\bar{a}(t)$, will vanish if ω_1 and ω_2 are such that

$$\omega_1^2 = \omega_2^2 = \omega_0^2 . \quad (3.80)$$

Equation (3.80) gives the balancing requirement of the DDGG. The balancing requirement is much simpler when compared with that of the CDGG, (3.59). In this case, only the frequencies of the proof masses are required to be equal. Fine tunings of the frequencies can be done by means of persistent currents stored in two coils placed at the outer surfaces of the proof masses.

The output current of a balanced DDGG flowing in the primary of the output transformer is

$$i(t) = \frac{\lambda I_0}{1+\gamma} \frac{\Delta a(t)}{2} . \quad (3.81)$$

The current that flows into the SQUID input coil, L_s , as a result is given by (2.38b)

$$I_s(t) = \frac{k\sqrt{L_a L_b}}{L_b + L_s} \frac{\lambda I_0}{1+\gamma} \frac{\Delta a(t)}{2} . \quad (3.82)$$

Equation (3.81) is identical to (3.60), the output equation of the CDGG save for some constants.

The energy transferred to the SQUID is

$$E_s = \frac{1}{2} L_s I_s^2(t) \quad (3.83a)$$

$$= \frac{1}{2} k^2 \frac{L_a L_b}{(L_b + L_s)^2} L_s \left[\frac{\lambda I_0}{1+\gamma} \frac{\Delta a(t)}{\omega_0^2} \right]^2 \quad (3.83b)$$

$$= \frac{1}{2} k^2 N^2 \frac{L_b^2}{(L_b + L_s)^2} L_s \left[\frac{\lambda I_0}{1+\gamma} \frac{\Delta a(t)}{\omega_0^2} \right]^2 \quad (3.83c)$$

using $L_a = N^2 L_b$ for a solenoidal transformer. Energy transferred will be a maximum when $\gamma = 1$ or $L_2 = L_{10}$ where L_2 is given by (2.37).

Assuming that the sensitivity of the DDGG is limited only by the thermal noise of the SQUID, E_N , the minimum resolvable acceleration is given by

$$(\Delta a)_{\min} = 2 \frac{\omega_0^2}{\lambda I_0} \left(\frac{L_b + L_s}{L_b} \right) \left[\frac{E_N}{\frac{1}{2} k^2 N^2 L_s} \right]^{\frac{1}{2}} \quad (3.84)$$

For an ideal gradiometer with design parameters of $k^2 = 0.8$, $\omega_0 = 2\pi(50)s^{-1}$, $I_0 = 10$ A, $L_s = 2\mu H$, $L_b = 6\mu H$, $L_{10} = 100\mu H$, $d_{10} = d_{20} = 10^4$ m and $N^2 = 41.7$, the minimum resolvable acceleration in a 1 Hz bandwidth is

$$(\Delta a)_{\min} = 1.29 \times 10^{-11}, \quad \text{m/s}^2 \quad (3.85)$$

for a standard SMC Corporation SQUID; $E_N = 2 \times 10^{-28}$ J/Hz, a design proof mass separation of 2 cm, the gradient sensitivity for a 1 Hz bandwidth above 0.01 Hz is

$$(\Delta g)_{\min} = 0.66 \quad \text{rms E.} \quad (3.86)$$

This is not a very impressive figure; primarily as a result of the short proof mass separation which SQUID used to improve the

acceleration sensitivity. There is a SQUID now available commercially (S.H.E. Corporation Model 330X) with one-fourth the noise energy, E_N , of 5×10^{-29} J/Hz. This will improve the gradient sensitivity to 0.33E for a 1 Hz bandwidth above 0.01 Hz.

Substituting the design parameters into (3.82), the SQUID current produced by a gradient signal is

$$I_s(t) = 1.097 \Delta a(t) \quad A \quad (3.87)$$

where $\Delta a(t)$ is given in m/s^2 .

The motions of the proof masses are influenced by the magnetic field of the pickup coil. The total electro-magnetic energy stored in the space between the proof masses is given by

$$E(t) = \frac{1}{2} [L_1(t) + L_2] I_1^2(t) \quad (3.88a)$$

$$= \frac{1}{2} L_{10} I_0^2 \left[(1+\gamma) - \frac{d_{10}}{d_{20}} \frac{x_2 - x_1}{d_{10} + d_{20}} \right] \quad (3.88b)$$

$$+ \frac{d_{10}}{d_{20}} \left(1 + \frac{1}{1+\gamma} \frac{d_{10}}{d_{20}} \right) \left(\frac{x_2 - x_1}{d_{10} + d_{20}} \right)^2 \left] \right]$$

where x_1 and x_2 are time functions of displacements. The forces exerted on the two proof masses are obtained by differentiating (3.88b) with respect to x_1 and x_2 respectively. The variable component of the force is given by

$$F_1(t) = -F_2(t) = -L_{10} I_0^2 \frac{d_{10}}{d_{20}} \left[1 + \frac{1}{1+\gamma} \frac{d_{10}}{d_{20}} \right] \frac{x_1 - x_2}{(d_{10} + d_{20})^2} \quad (3.89a)$$

$$= K (x_1 - x_2) \quad (3.89b)$$

Using the design parameters of the DDGG given earlier, the value of K is

$$K = 3.75 \times 10^5 \text{ N/m} . \quad (3.90)$$

This is about 10 times greater than the equivalent mechanical spring rate calculated from the equivalent mass and natural frequency. This indicates tight coupling between the two proof masses as expected for such a design.

D. SUMMARY

In this Chapter, the following were covered.

D-1 Gradiometer Design

The optimal configuration of the diaphragm proof mass with regards to acceleration sensitivity has been derived. Its natural frequency as a function of its dimensions is determined. The third order nonlinearity of the displacement is analyzed and found to be small. The optimization of the proof mass dimensions to produce the best sensitivity has been carried out. The critical bound on this optimization process is the thickness of the diaphragm. With the relative dimensional accuracy required, thinner diaphragms require increasingly greater machining accuracy and great care to avoid buckling during fabrication.

D-2 Superconducting Gravity Gradiometers

The output relations of the two superconducting gravity gradiometers are derived. The displacement differencing gravity gradiometer (DDGG) is simpler to construct but is less flexible. The axes of the two proof masses must be in line and the separation small. Since it is made up of two individual accelerometers, the current DDGG is more flexible. It also has an adjustable baseline. Thus it is the most promising device and is the subject of this thesis. Both gradiometers offer very good gradient sensitivity. With the development of lower noise SQUID (superconducting quantum interference device), the sensitivity in the future will be extremely difficult to match with room temperature devices.

Chapter IV

NOISE AND ERROR SOURCES

The performance of an instrument is limited by its largest error. In some instruments, the performance requirements are so exacting that thermal noise becomes a consideration. It is a fundamental limiting factor for gravity gradiometers. In the cryogenic environment, the thermal noise is reduced significantly compared with the three instruments currently under development. In this chapter, the noise which determines the threshold sensitivity and the means of reducing it will be analysed and discussed, along with the other error sources which are identified and evaluated.

A. THERMAL NOISE

The gradiometers currently being developed at MIT, Bell Aerospace, and Hughes are operating near or at their respective thermal noise limits. This noise originate from the basic energy dissipation of the molecules in the devices. One may reduce this noise by building sensors with low loss mechanism. The trade-offs in doing so are analyzed in Ch. IV-A.2. The temperature of the sensor may be reduced to decrease the thermal noise. This is discussed in the next section. Another alternative is to start with a sensor with ultra-low loss mechanism. The low intrinsic damping will then be increased to the value desired through electronic feedback. The superior noise performance of such "electronic cooling" is investigated in Sect. IV-B.

A.1 Thermal Noise of the Diaphragm

The thermal noise of a diaphragm proof mass is generated by the vibrations of its crystal lattice. It is a white noise force and has a constant power spectrum. The mechanical structure of the diaphragm transforms the white thermal noise into a highly "colored" noise. Around the resonant frequency of the diaphragm the noise output response can be modeled as a single degree-of-freedom oscillator. The thermal noise output power spectrum of a 50 Hz diaphragm of $Q = 10$ is given in Fig. IV-1. A fairly complete analysis of random processes is given in Crandall & Mark [1963]. In App. D the derivation of Fig. IV-1 for the diaphragm is discussed.

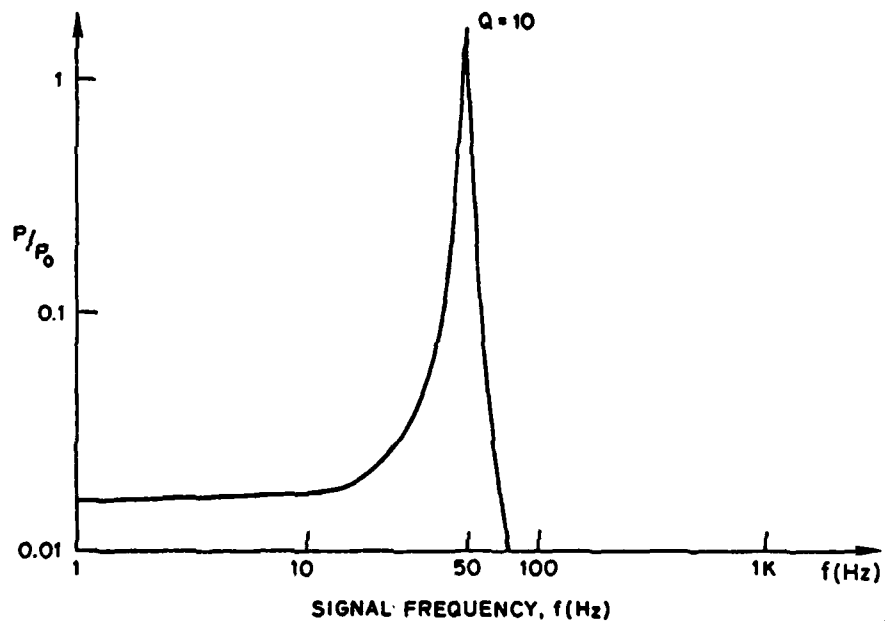


FIG. IV-1 POWER SPECTRUM OF THE THERMAL NOISE AT THE OUTPUT OF THE ACCELEROMETER. A Q of 10 is selected so that a reasonable graph can be drawn. The Q of the diaphragm used is of the order of 10^5 or better.

In the low frequency range of the spectrum, the spectral density of the noise force, $W_F(f)$, acting on the diaphragm is given by Eq. (E.5). Dividing $W_F(f)$ by the square of the mass, m , gives

$$W_a(f) = \left(\frac{4kT\omega_0}{mQ} \right) . \quad (4.1)$$

This is the Nyquist equation for thermal acceleration noise. For an ideal sensor with parameters $Q = 2 \times 10^5$, $m = 0.3$ kg, $\omega_0 = 2\pi(50)\text{s}^{-1}$, the acceleration noise is 1.10×10^{-13} g/ $\sqrt{\text{Hz}}$ (g = earth's average gravitational acceleration).

From manufacturer's data [SHE Co.] the best available low noise SQUID has an equivalent input noise current of 7×10^{-12} rms A/ $\sqrt{\text{Hz}}$.

Used in conjunction with the cryogenic accelerometer discussed in Ch. III-A, this is an equivalent input acceleration noise of 4.61×10^{-13} g per $\sqrt{\text{Hz}}$. Thus in the low frequency range, the thermal noise of the diaphragm is ten times less than the SQUID thermal noise.

In (4.1), if Q is increased, the acceleration noise power is reduced. This is not surprising since higher Q implies lower dissipative losses. On this basis, Q should be as large as possible.

However, a high Q system will transform broadband input noise into highly "colored" output noise. In the case of the accelerometer, a broadband thermal noise will be transformed into displacement noise with peak power at the resonant frequency of the proof mass. An output power spectrum of a system with $Q = 10$ and a constant broadband input noise is given in Fig. IV-1. Higher Q will produce higher peak power and lower sideband power.

Most signal detectors and amplifiers have dynamic range and slew rate limits at their inputs. A high Q system will produce large noise excursions at the input of the signal processing unit (SPU). These fluctuations at the resonant frequency of the device may exceed

either the dynamic range and/or the slew rate of the SPU. These noise excursions are produced by the thermal noise, as well as the ambient environmental noise. The higher the Q of the system is, the more acute is the problem. The tradeoff of increasing system Q to decrease thermal noise vs decreased stability is discussed in the next section.

A-2 Dynamic Range of Accelerometer

It is known [Crandel, 1963] that a high Q system will channel wide-band noise at its input into narrow band noise at its output. This process is briefly outlined in App. E. Let us consider the output response of the diaphragm to Brownian noise. From Eq. (E.3), the mean square response of the diaphragm to thermal noise is

$$\langle x^2(t) \rangle = \frac{kT}{2m\omega_0^2}; \quad \langle x^2(t) \rangle \equiv E[x^2(t)]. \quad (4.2)$$

Using Eq. (3.8), the SQUID noise current induced by the thermal noise of the diaphragm is

$$\langle i_n^2 \rangle^{\frac{1}{2}} = c \langle x_n^2 \rangle^{\frac{1}{2}}. \quad (4.3)$$

For the ideal accelerometer discussed in Ch. III, [$M = 0.3$ kg, $\omega_0 = 2\pi(50)$, $T = 4.2$ K.], the noise current is 5.44×10^{-9} A. The noise is centered about the natural frequency of the diaphragm, f_0 .

The block diagram of the r-f biased SQUID used in the signal detection is given in Fig. II-8. In this feedback mode of operation, the SHE SQUID system behaves like a linear system with an input dynamic range of 50×10^{-6} A peak to peak in the 0 - 120 Hz range with its control set to $\times 1$ sensitivity and FAST mode [SHE]. Above 120 Hz, the dynamic range rolls off at 40 dB/decade. Unlike linear systems which saturate when their inputs exceed their dynamic ranges, the SQUID system will shift its quiescent operation point until equilibrium is established again in its flux circuit. Forgacs [1967] gave a description on how this property of the SQUID may be used to extend its dynamic range indefinitely.

However, in the present implementation, when the SQUID "unlocks", all past information are lost. Thus it is important to keep the input current below the dynamic range of the SQUID at all times throughout its frequency spectrum.

However, thermal noise is not the only noise source at the input. As will be shown, environmental noise would cause the SQUID to "unlock" unless great care is taken to provide sufficient vibration isolation.

An estimate of the maximum background noise which is tolerated by the SQUID can be made if it is assumed to be white. Let $A_M(f)$ be this maximum spectral density of environmental white acceleration. Using Eq. (E.6), the expected value of the noise displacement is

$$\langle x_e^2 \rangle = \frac{A_M(f)Q}{\frac{3}{4\omega_0}} \quad . \quad (4.4)$$

From Eq. (3.8), the displacement, x_{\max} , that will produce full scale deflection current of $50\mu\text{A}$ is 4.07×10^{-10} m. For an order of magnitude estimate, we set

$$\langle x_e^2 \rangle = \frac{1}{2} x_{\max}^2 \quad . \quad (4.5)$$

Solving for $A_M(f)$ with $Q = 2 \times 10^5$, $\omega_0 = 2\pi(50 \text{ Hz})$, we have

$$A_M(f) = 5.14 \times 10^{-17} \quad (\text{m/s}^2)^2/\text{Hz} \quad . \quad (4.6)$$

In other words, to ensure the stability of the SQUID, the background acceleration noise must be less than $7.31 \times 10^{-10} \text{ g}/\sqrt{\text{Hz}}$. These limits are derived from the slew rate response of the SQUID to sinusoidal inputs.

In Eq. (4.4) the variables are ω_0 and Q . Since the fundamental frequency of the diaphragm should be low to increase acceleration sensitivity, only Q can be changed to increase the tolerable background acceleration noise (TBAN). However, reducing Q would increase the thermal noise of the proof mass if it were done passively. Table IV-1 shows that reducing Q readily introduces enough thermal noise from the mechanical system to exceed the SQUID noise.

Table IV-1
EFFECT OF Q ON NOISE

Q	TBAN (10^{-9} g/ $\sqrt{\text{Hz}}$)	Nyquist Noise (10^{-12} g/ $\sqrt{\text{Hz}}$)
2×10^5	0.731	0.112
1.88×10^3	7.54	1.16
300	18.9	2.90
10	103	15.9

As Q decreases, both TBAN and Nyquist noise increase. For high Q , the SQUID noise limits the resolution of the system. When Q is less than 1880, the threshold of the accelerometer is limited by the thermal noise of the diaphragm proof mass. Thus, lowering Q through dissipative mechanism would degrade the resolution of the accelerometer. This will be discussed in greater detail in Sect. D.

Table IV-1 is very illuminating but not too realistic as the full scale deflection for sinusoidal input is used to calculate the limits. A more meaningful measure is the statistical mean time between failures. Failure is defined as the SQUID losing its quiescent locking point. It is assumed for the analysis that the MTBF has a Poisson distribution. Then, T_0 the MTBF is given with a 99% certainty by (4.7) [Crandall, 1963].

$$T_0 = \frac{0.01}{f_0} \exp \left[\frac{\lambda_2}{2\sigma_x^2} \right] \quad (4.7)$$

where f_0 is the natural frequency of the system in Hz, λ is the maximum level of excursion, 4.07×10^{-10} m, and $\sigma_x^2 = \langle x^2 \rangle$ for the zero mean distribution assumed here.

For $\lambda = 5\sigma_x$, and $f_0 = 50$ Hz, T_0 is 54 sec. This is too short

for practical purposes. Using (4.4) in conjunction with (4.7), for $T_0 = 4000$ sec, and $Q = 2 \times 10^5$, the statistical tolerable background acceleration noise is 1.78×10^{-10} g/ $\sqrt{\text{Hz}}$. Comparing this with TBAN of 7.31×10^{-10} g/ $\sqrt{\text{Hz}}$, the statistical tolerable background acceleration noise is a more stringent requirement.

An interpretation of $T_0 = 4000$ sec with 99% certainty is that in a hundred gradiometers, each operating for 4000 sec, there will be on the average one failure.

A.3 Q and Dynamic Range of Gradiometer

The two cryogenic gradiometers described in Ch. III will reject common mode acceleration in the low frequency range. However, as the thermal noise of the two proof masses in a gradiometer are white and uncorrelated, they are not rejected. The power spectrum of the gradiometer noise is

$$A_g(f) = \frac{2A_a(f)}{\ell^2} \quad (4.8)^{\dagger}$$

where ℓ is the baseline of the gradiometer. The subscripts g and a stand for gradiometer and accelerometer respectively. The thermal noise are assumed to have zero mean and equal magnitude.

As given above, the acceleration noise is

$$\alpha_a(f) = \sqrt{A_a(f)}, \quad (4.9)$$

which has a value of 1.12×10^{-13} g/ $\sqrt{\text{Hz}}$ for the ideal accelerometer. For a baseline of 10 cm., the gradient noise is 1.58×10^{-2} E/ $\sqrt{\text{Hz}}$. The SQUID noise is 0.13 E/ $\sqrt{\text{Hz}}$ for the current differencing gradiometer and 0.66 E/ $\sqrt{\text{Hz}}$ for the displacement differencing gradiometer discussed in Ch. III. The gradiometer threshold sensitivity is therefore governed by the noise level of the SQUID. Better sensitivity may be achieved by

[†] $\langle \Delta a^2 \rangle = \langle (a_1 - a_2)^2 \rangle = \langle a_1^2 \rangle + \langle a_2^2 \rangle - 2 \langle a^2 \rangle$

using SQUID with lower noise which awaits superconductivity advances in the physics.

Unlike thermal noise, linear environmental vibration would produce acceleration on the gradiometer that is common to both proof masses if they have matched suspension. Equations (3.57) and (3.80) show that through scale factor matching, these common acceleration will be rejected by the gradiometers. This is true for the low frequency range. It will be shown that common mode rejection of environmental noise will be poor near the resonant frequencies of the proof masses.

For the current differencing gradiometer, the scale factor balancing is achieved when (3.57) holds. The transfer function of the gradiometer maybe defined as the output current per unit acceleration. Without using the simplifying assumptions, (3.56) gives

$$H(\omega) = \lambda \left[\frac{\omega_1^2}{\omega_1^2 - \omega^2 + j \frac{\omega_1 \omega}{Q_1}} - \frac{\omega_2^2}{\omega_2^2 - \omega^2 + j \frac{\omega_2 \omega}{Q_2}} \right] \quad (4.10)$$

where

$$\lambda = \frac{2 I_1}{\pi(1 + \gamma) \omega_1^2 d_{10}} .$$

The spectral density transfer function is simply the square of $H(\omega)$. Furthermore, if the environmental is assumed white, and has a constant power of S_0 , the output power spectrum is

$$S_{out} = |H(\omega)|^2 S_0 . \quad (4.11)$$

In the typical gradiometer, $\omega_1 \neq \omega_2$ and the Q's are of the order of 10^5 . Under these conditions, (4.11) may be written as

$$S_{out} = [H_1^2(\omega) + H_2^2(\omega)] S_0 . \quad (4.12)$$

The power spectrum will have two very sharp peaks at the resonant frequencies of the proof masses. The required vibration isolation is the same as for the individual accelerometers. Table IV-1 shows that these requirements are very stringent for proof masses with high Q . We conclude that in order to build a practical instrument, the Q 's of the proof masses must be lowered. At a value of $Q = 300$, the Nyquist noise would be the limiting factor of the resolution of the gradiometer. For the current differencing gradiometer, the Nyquist noise is an equivalent $0.41 \text{ E}/\sqrt{\text{Hz}}$ (Eq. 3.8). It is preferable to lower Q without increasing the Nyquist noise. This may be achieved using feedback. The next section will discuss damping by electronic feedback, sometimes called electronic cooling since the equivalent resistance added has a noise temperature considerably lower than the component operating temperature.

B. Q REDUCTION BY FEEDBACK

As discussed in the previous section, the high mechanical Q of the proof masses places a very stringent requirement on vibration isolation of the gradiometer. This Q must be lowered for a practical device. Processes by which the energy dissipation is increased to reduce Q will inadvertently increase the background thermal noise (see Table IV-1).

By feeding back the signals of resonant oscillations detected by the SQUID with proper phase shift, Q can be suppressed without increasing the background thermal noise proportionally. Kittel [1958] has demonstrated this concept of electronic cooling. Recently, Hirakawa [1978] and Forward [1977, 1979] have applied this principle to gravity wave detector and gravity gradiometer, and damping of optical structures. In this section, the theory of the feedback circuit is formulated. The experimental circuit and the results obtained are given in Ch. V.

B.1 Thermal Noise and Feedback Damping

To demonstrate the concept, the case of an accelerometer will be considered. We would model the equivalent circuit of the diaphragm proof mass at its fundamental resonant mode by the circuit in Fig. IV-2. It includes the effects of mechanical components transformed by the transducer into equivalent electrical quantities as seen looking into the pickoff coils of the accelerometer.

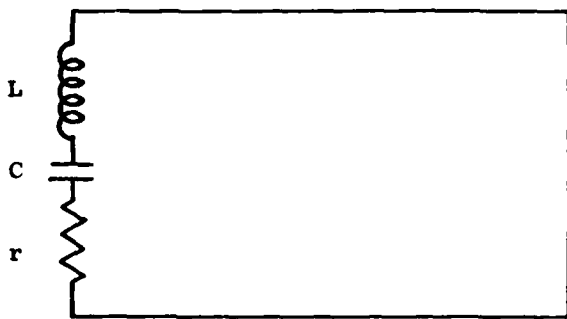


FIG. IV-2 ELECTRICAL EQUIVALENT CIRCUIT OF THE RESONANT MODE OF THE DIAPHRAGM ACCELEROMETER. The parallel inductance of the pickup coil is L ; r is the internal dissipative resistance of the diaphragm; C is a fictitious capacitance determined from the resonant frequency of the accelerometer.

In this model, L is taken as the effective inductance of the pick-up coils. C and r are defined as follows:

$$\omega_0^2 = \frac{1}{LC} \quad (4.13a)$$

$$r = \frac{\omega_0 L}{Q_0} \quad (4.13b)$$

where ω_0 and Q_0 are the measured resonant frequency and quality factor respectively. For the ideal accelerometer used in our theoretical calculations, C is $0.203F$ and r is $7.85 \times 10^{-9} \Omega$. When $L = 50\mu H$ and $\omega_0 = 2\pi(50)\text{sec}^{-1}$.

The thermal noise is given by Nyquist as

$$\langle v_n^2 \rangle = 4kTr\Delta f \quad v^2 \quad (4.14)^*$$

Figure IV-3 gives the equivalent circuit with feedback damping at the modal frequency.

N_p is the current gain of the pick-up transformer and N_f is the voltage gain of the feedback transformer. R_f is the equivalent resistance accounting for all the noise energy sources in the feedback path. A is an ideal, infinite gain operational amplifier. This is the

* expected value of the noise voltage

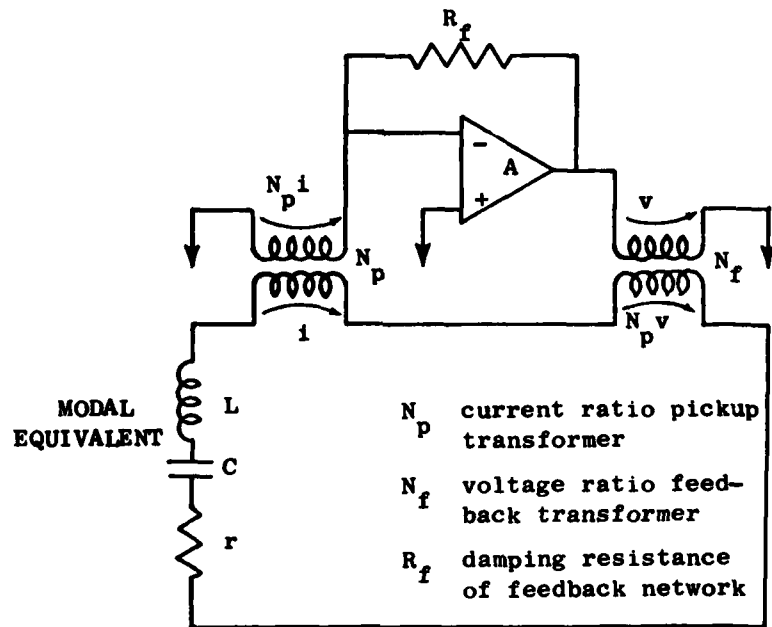


FIG. IV-3 EQUIVALENT CIRCUIT OF FEEDBACK DAMPING OF THE ACCELEROMETER [from Forward, 1977].

same model used by Forward [1977, 1979].

Considering the ratio of the output voltage to the input current of the feedback, we can show that the equivalent resistance, R_{eq} , as seen by the modal resonance is

$$R_{eq} = N_p N_f R_f . \quad (4.15)$$

The resulting damping will give a new value of Q_{fb} which is given by

$$Q_{fb} = \frac{\omega_0 L}{r + R_{eq}} . \quad (4.16)$$

For large R_{eq} , Q_{fb} can be made quite small.

The thermal noise of R_f is given by Nyquist as in (4.14). The total voltage noise of the circuit with feedback becomes

$$\begin{aligned} \langle v_n^2 \rangle &= (4kT r + 4kT R_f N_f^2) \Delta f \\ &= 4kT (r + N_f^2 R_f) \Delta f . \end{aligned} \quad (4.17a)$$

Had the reduction in Q we've achieved by using a dissipative element of magnitude equal to R_{eq} , the corresponding thermal noise would be

$$\langle v_n^2 \rangle = 4kT(r + R_{eq})\Delta f = 4kT(r + N_p N_f R_f)\Delta f. \quad (4.17b)$$

Feedback will be better in damping the vibrations so long as the noise in (3.18) is less than that in (4.17b), i.e.,

$$\frac{r + N_f^2 R_f}{r + N_p N_f R_f} < 1. \quad (4.18)$$

This can be simplified to

$$N_f < N_p. \quad (4.19)$$

The thermal noise of the feedback circuit has been ignored. This is a justifiable assumption with modern electronic components [Forward, 1977]. This assumption will be examined in Ch. V-B.

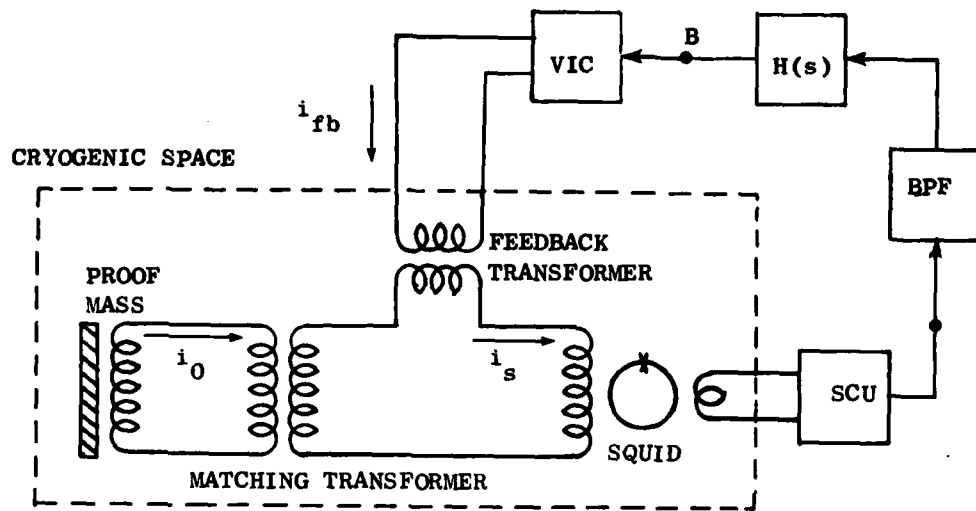
B-2 Feedback Circuit Design

The block diagram of the feedback circuit for an accelerometer is shown in Fig. IV-4.

The bandpass filter is used to select only the resonant mode. The VIC is used for current feedback and its low noise pickup. The SQUID control unit (SCU) produces a voltage v_s that is proportional to the input current i_0 , i.e.,

$$v_s(t) = -G_s i_0(t). \quad (4.20)$$

For simplicity, the bandpass filter is assumed to have unity gain and zero phase shift. If the gain of VIC is G_v , the current flowing in the feedback transformer is



BPF bandpass filter
 SCU SQUID control unit
 VIC voltage-to-current converter
 $H(s)$ transfer function of feedback circuit
 SQUID superconducting quantum interference device

FIG. IV-4 BLOCK DIAGRAM OF FEEDBACK CIRCUIT. The voltage output of the SCU is filtered by the BPF which is turned to the frequency of the diaphragm mode to be suppressed. The output of the transfer function $H(s)$ drives the VIC which provides a feedback current i_{fb} . Current feedback is used for noise suppression.

$$i_{fb}(t) = -G_v h(t) * G_s i_0(t) , \quad (4.21)$$

where $*$ stands for convolution. Now the voltage feedback seen by i_0 in the feedback transformer is given by

$$v_{fb}(t) = -M \frac{\partial i_{fb}(t)}{\partial t}$$

where M is the mutual inductance by the feedback transformer.

In the Laplace domain,

$$V_{fb}(s) = -SMI_{fb}(s) = SMG_v H(s) G_s I_0(s) . \quad (4.22)$$

For an equivalent resistance feedback, the ratio of $V_{fb}(s)/I_0(s)$ must be purely real, i.e.,

$$R_{eq} = \frac{V_{fb}(s)}{I_0(s)} = SMG_v G_s H(s) . \quad (4.23)$$

Alternatively, $H(s)$ must be given by

$$H_I(s) = \frac{R_{eq}}{G_v G_s M} \frac{1}{s} , \quad (4.24)$$

thus the feedback circuit must include an integrator. There will be a pole-zero cancellation in the overall feedback transfer function. The gains of VIC and SCU can be adjusted to obtain the desired equivalent resistance.

The same circuit may be used for damping the two modes of a gradiometer. A simple method of doing so is to build a bandpass filter with two pass bands, one at each resonant frequency. The output signal of the filter will be fed to same integrator and voltage-to-current converter as before. This will perform satisfactorily but one would not be able to adjust the dampings of the two modes independently. One way to do this is to replace the bandpass filter and integrator in Fig. IV-4 by a parallel circuit as given in Fig. IV-5.

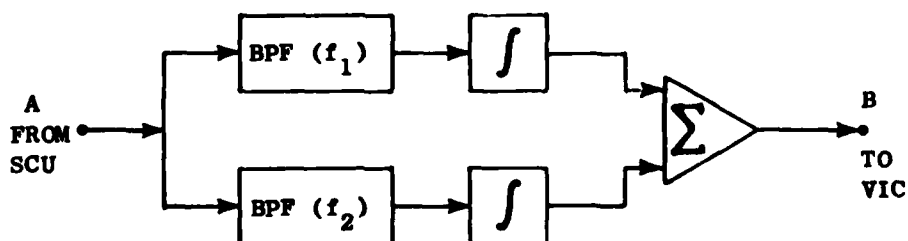


FIG. IV-5 BLOCK DIAGRAM OF FEEDBACK FOR GRADIOMETER. For a gradiometer with two diaphragms, the feedback circuit shown here may replace the circuit between points A and B in Fig. IV-4.

By designing different gains into the two paths, the feedback resistance for the two modes will be different. The analysis will be the same as for the accelerometer.

B-3 The Minimum Q Achievable

Using Eq. (4.23), R_{eq} may be as large as we want through the simple process of increasing the gain of the feedback path. Thus it would seem that the Q of the oscillating system can be made as low as desired. This is not true since the current induced by the feedback in the SQUID is not considered in this model.

The induced current is in quadrature with respect to the signal current. The current detected by the SQUID is the difference of the signal and the induced feedback current. The block diagram of the closed-loop feedback is shown in Fig. IV-6. The Laplace operator is s , and M is the mutual inductance of the feedback transformer.

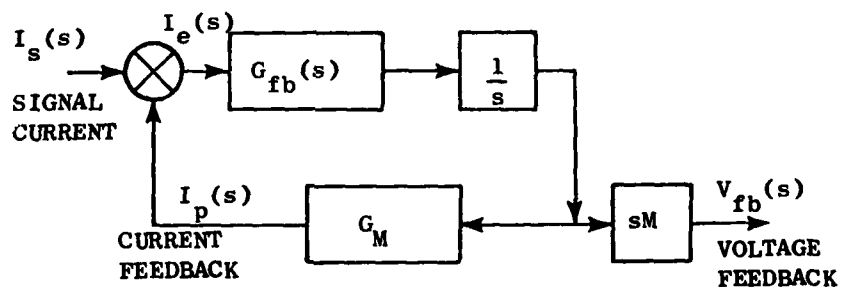


FIG. IV-6 BLOCK DIAGRAM OF CLOSED-LOOP FEEDBACK.
The effect of the feedback current is included in this block diagram.

$G_{fb}(s)$ is the gain of the feedback path comprising the SQUID control, the bandpass filter, the integrator, and the voltage-to-current converter.

G_M is the current feedback factor. It can be derived by the consideration of the inductances of the system given in Fig. IV-7.

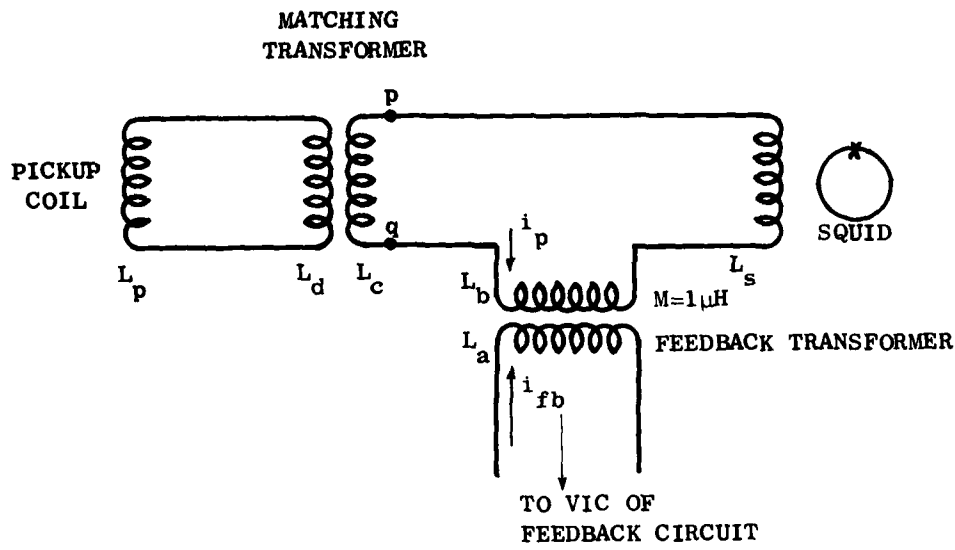


FIG. IV-7 THE INDUCTANCES OF THE FEEDBACK DAMPING CIRCUIT. The parallel inductance of the accelerometer is L_p ; L_c and L_d are the inductances of the matching transformer; L_a and L_b are the inductances of the feedback transformer; L_s is the inductance of the SQUID.

The induced current flowing in the primary circuit is i_p , which is due to i_{fb} flowing through L_a .

Using flux conservation rule for superconducting loops, the inductance to the left of terminals p and q may be given by

$$L_{eq} = L_c \left[1 - k^2 \frac{L_d}{L_p + L_d} \right] \quad (4.25)$$

where k is the coupling coefficient of the matching transformer. Using the same rule, i_p is related to i_{fb} by

$$i_p = \frac{M}{(L_{eq} + L_s + L_b)} i_{fb} \quad (4.26)$$

Thus, G_M is given as

$$G_M = \frac{i_p}{i_{fb}} = \frac{M}{(L_{eq} + L_s + L_b)} . \quad (4.27)$$

G_M is a constant of a given circuit and is independent of frequency.

Solving the closed-loop equation, the feedback voltage is

$$V_{fb}(s) = \frac{M}{G_M} \left(\frac{as}{s+a} \right) I_s(s) \quad (4.28)$$

where $a = G_{fb}(s) \cdot G_M$. The impedance seen by the input circuit is

$$Z_{fb}(s) = \frac{M}{G_M} \left(\frac{as}{s+a} \right) I_s(s) . \quad (4.29)$$

For a high Q diaphragm, only the impedance at the resonant frequency need be considered. Substituting $j\omega_0$ for s , the impedance is

$$Z_{fb}(\omega_0) = \frac{M}{G_M} \left(\frac{\omega_0^2 a_0 + ja_0^2 \omega_0}{a_0^2 + \omega_0^2} \right) \quad (4.30)$$

where $a_0 = G_{fb}(\omega_0)G_M$.

The real part of $Z_{fb}(\omega_0)$ is the equivalent resistance feedback where the imaginary part increases the inductance of the resonating circuit. They are

$$R_{fb} = \frac{M}{G_M} \left(\frac{\omega_0^2 a_0}{a_0^2 + \omega_0^2} \right) \quad (4.31a)$$

$$L_{fb} = \frac{M}{G_M} \left(\frac{a_0^2}{a_0^2 + \omega_0^2} \right) . \quad (4.31b)$$

Note that as the feedback gain $G_{fb}(\omega_0)$ is varied, R_{fb} attains a maximum at $a_0 = \omega_0$ while L_{fb} will increase asymptotically.

$$R_{fb}|_{a_0=\omega_0} = \frac{\pi f_0 M}{G_M} \quad (4.32a)$$

$$L_{fb} \xrightarrow{a_0 \rightarrow \infty} \frac{M}{G_M} . \quad (4.32b)$$

Hence the effects of increasing feedback are twofold. The resistive feedback will increase energy dissipation while the inductive feedback will pump energy back into the system. System Q will be minimum when these two effects are balanced.

From (4.13), the expression for Q is

$$Q = \frac{1}{r} \sqrt{\frac{L}{C}} . \quad (4.33)$$

In this feedback scheme, both r and L are effects of the feedback gain G_{fb} , especially

$$r \approx r_{int} + R_{fb} (N_p/N_s)^2 \quad (4.34a)$$

$$L \approx L_{int} + L_{fb} (N_p/N_s)^2 \quad (4.34b)$$

where R_{fb} and L_{fb} are given in (4.31), int stands for "internal", and (N_p/N_s) is the turn ratio of feedback transformer.

Differentiating (4.33) with respect to G_{fb} , and equating to zero, we get

$$\frac{dr}{dG} = \frac{r}{2L} \frac{dL}{dG} \quad (4.35)$$

for the condition of minimum Q .

The exact solution of (4.35) is rather complicated. Since L_{fb} is typically very small compared to L_{int} , we can assume that ω_0 remains constant. Equations (4.35) would be reduced to

$$(\omega_0^2 - a_0^2) \left[L_{int} (a_0^2 + \omega_0^2) + \frac{M}{G_M} \left(\frac{N_p}{N_s} \right)^2 a_0^2 \right] = a_0 \left[r_{int} (a_0^2 + \omega_0^2) + \frac{M}{G_M} \left(\frac{N_p}{N_s} \right)^2 a_0 \omega_0^2 \right]. \quad (4.36)$$

The value of a_0 satisfying this expression would give the feedback gain that produces the minimum Q .

Replacing the integrator transfer function of s^{-1} in Fig. IV-7 by $H(s)$, the transfer function from $I_s(s)$ to $V_{fb}(s)$ becomes

$$\frac{V_{fb}(s)}{I_s(s)} = \frac{sMG_{fb}H(s)}{[1 + G_{fb}G_MH(s)]}. \quad (4.37)$$

Setting this ratio to R_{eq} , the transfer function for a purely resistive feedback is

$$H(s) = \frac{R_{eq}}{G_{fb}[sM - R_{eq}G_M]}. \quad (4.38)$$

This transfer function has a positive pole rendering it inconvenient for implementation.

The feedback scheme of Fig. IV-7 is adequate for the purpose of noiseless damping. The fact that inductive feedback will eventually dominate does not diminish the usefulness of feedback damping.

C. ERROR SOURCES

The various error sources of the cryogenic gravity gradiometers are identified. The requirements to keep the error of each source below the maximum allowed are discussed. The nature of the drift and bias of the SQUID based system are unique. It is assumed that the gradiometers are operating in a quiet environment unless mentioned otherwise.

C-1 Drift

When the cryogenic space is maintained at the constant boil-off temperature of liquid helium, the structure of the gradiometer has great mechanical stability. Unlike the room-temperature gradiometers being developed, the need for an elaborate enclosure to reduce thermal gradient across the instrument is avoided. The two major sources of drift in the cryogenic gradiometers are: (1) the drift of the SQUID electronic circuit, and (2) the flux creep in the pickup coils of the accelerometers.

The drift of the electronic circuit can be minimized by proper design. The SHE Corp. SQUID is a well designed package. According to manufacturer's data [SHE], the SQUID has a drift referred to its input of $\pm 2 \times 10^{-4} \phi_0/\text{hr}$ and $\pm 3 \times 10^{-4} \phi_0$ over a 24 hour period on the most sensitive range. This drift rate is measured when the input terminals are shorted by a superconducting wire. These drift rates are equivalent to $\pm 1.84 \times 10^{-3} \text{ E}/\text{hr}$ and $\pm 2.76 \times 10^{-3} \text{ E}$ over a 24 hour period for the current differencing gravity gradiometer (CDGG). These drift rates are rather sensitive to the operating temperature of the SQUID. They are, however, negligible when the sensitivity of the gradiometers is in the range of 0.1 E.

When the pickup coils of the gradiometers are connected to the SQUID, the performance of the system is degraded by the noise thus introduced. The drift of the detector system would be drastically increased. Fortunately superconducting materials are superior shields against electrostatic and electromagnetic interferences which are the main source for the noise. A lead cylinder with closed bottom surrounding the

vacuum can of the gradiometer is a standard item. Leads that are part of the superconducting loop are shielded with strip-lines formed of lead foils. Noise introduced through telemetry leads may be bypassed by a short length of resistive wire (connected across the inputs of the SQUID). This resistor ($\cong 2 \Omega$) forms a R-L filter which will bypass most high frequency noises. When all these measures are taken, flux creep remains the major source of drift. Most of the pickup coils of the accelerometers are wound of niobium-titanium (T-42) wire which is a Type II superconducting material. It is a well known phenomenon that flux enclosed by a Type II superconductor will "leak" out of the loop as discrete parcels known as fluxoids [Rose-Innes, 1969]. Luckily, this creep decays logarithmically with time. For these gradiometers, within a half hour of any current adjustment, drift due to flux creep should stabilize to an negligible value. The drift due to flux creep is not as serious in the CDGG since the creeps in the two accelerometers would tend to cancel one another. The displacement differencing gravity gradiometer (DDGG) does not have this tolerance as it has only one pickup coil.

Flux creep may be eliminated in the first place if pure niobium were used to wind the pickup coils. Pure niobium wire is harder to work with as the wire tends to break readily during coil winding. The performance of such coils is being investigated by Maples (of Stanford).

In summary, the stability of the SQUID-based gradiometers can be truly unsurpassed when proper care is taken.

C-2 Bias

The SQUID is an integral part of the cryogenic gradiometers. It has many unique characteristics [Forgacs, 1967] as a detector. When operated in the flux-locked loop mode, its quiescent operating point can be reset to remove any steady-state bias. For the SHE SQUID used in our gradiometers, the residual steady-state bias is within ± 20 mV in a full-scale output of ± 10 V. This bias (or any other bias voltage) does not affect the linearity or sensitivity of the SQUID. A large bias voltage does degrade the dynamic range of the SQUID. Thus the SQUID is

reset routinely to maximize its stability. Under such conditions, a meaningful output bias cannot be defined.

The diaphragm proof masses of the gradiometer have some mechanical bias. Although great care is taken during fabrication to assure uniformity, it is inevitable that some mechanical bias exists in the diaphragm proof mass. The standard practice in the industry is to measure bias in accelerometers by rotating them through 360° in the earth's field; this is not possible in our laboratory setup. The cryogenic gradiometers are designed to have a $0.1E$ sensitivity. The displacements of the diaphragm proof mass are on the order of 10^{-16} m for $0.1E$ though the earth-field gradient is of the order of 3000 E .

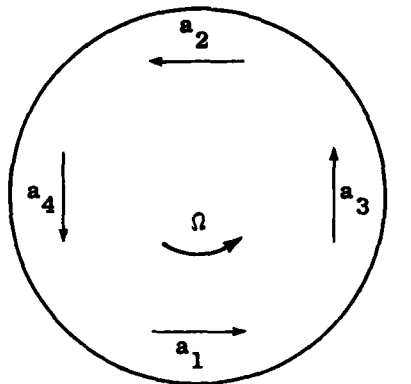
In Chapter III, Sect. A-4, it was shown that linearization about large deflections of the diaphragm proof mass would produce negligible errors. Thus, mechanical bias is not a significant source of error. In addition, the ability of the SQUID to detect incremental flux changes with equal sensitivity irrespective of the actual flux has eliminated electrical circuit bias as a source of error.

C-3 Effects of Rotation on Noise

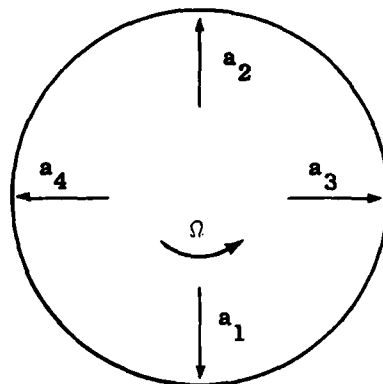
The power spectral density of the noise of a SQUID is given in Fig. II-9. Below the cross-over frequency of 0.01 Hz , the noise is dominated by $1/f$ noise. Above the cross-over frequency, the noise is primarily thermal noise and has a constant amplitude up to 1 kHz . This constant power level is used to determine the minimum resolution of the cryogenic accelerometer and gradiometer in the previous sections.

If the gradiometer were used to measure gradient signal with frequency component below the cross-over frequency (0.01 Hz using this SQUID), the resolution is degraded inversely with the frequency. One way to overcome the $1/f$ noise is to rotate the gradiometer about its geometric center.

For a rotating gradiometer comprising pairs of accelerometers, there are two possible axes alignment schemes. They are represented by the sketches of Fig. IV-8.



(a) Tangential Alignment



(b) Radial Alignment

FIG. IV-8a,b ACCELEROMETER AXES ALIGNMENT FOR A ROTATING GRAVITY GRADIOMETER. The two configurations of aligning two pairs of matched accelerometers on a rotating platform to measure gradient are shown. The configuration given in (a) is used in the Bell Aero-space rotating gravity gradiometer.

In Fig. IV-8a, the accelerometers have their sensitive axes perpendicular to the line joining each pair. In Fig. IV-8b, the axes are along the line joining the pair. In both cases, the accelerometers are placed equidistant from the center of the rotating platform.

Figure IV-9 gives the notations used in the derivation of the gradiometer output equation. The gravity vector, \bar{g}_0 , is at the origin of the platform axes reference system and defines the local horizontal plane. At any of the point, say p_1 , the gravity vector can be written in terms of \bar{g}_0 as:

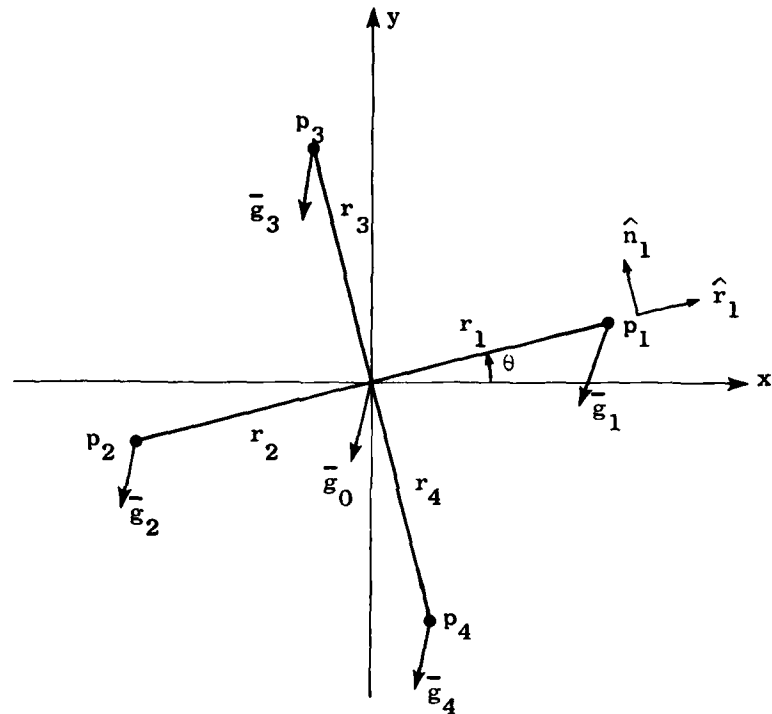


FIG. IV-9 PLANAR PROJECTION OF THE GRAVITY FORCES ACTING ON THE PROOF MASSES OF A ROTATING GRAVITY GRADIOMETER. The gravity force \underline{g}_0 acting at the center of the rotating platform is \underline{g}_0 . The resolutions of the forces at the four proof masses give an indication of the gravity gradient.

$$g_{1x} = g_{0x} + \frac{\partial g_x}{\partial x} \Delta x + \frac{\partial g_x}{\partial y} \Delta y + \frac{\partial g_x}{\partial z} \Delta z \quad (4.39a)$$

$$g_{1y} = g_{0y} + \frac{\partial g_y}{\partial x} \Delta x + \frac{\partial g_y}{\partial y} \Delta y + \frac{\partial g_y}{\partial z} \Delta z \quad (4.39b)$$

$$g_{1z} = g_{0z} + \frac{\partial g_z}{\partial x} \Delta x + \frac{\partial g_z}{\partial y} \Delta y + \frac{\partial g_z}{\partial z} \Delta z . \quad (4.39c)$$

Defining $\bar{\Gamma}$ as the gradient tensor of Eq. (2.3), and

$$\bar{\Delta r} = (\Delta x, \Delta y, \Delta z)^T , \quad (4.40)$$

the gravity at p_1 may be written as

$$\bar{g}_1 = \bar{g}_0 + \bar{\Gamma} \cdot \bar{\Delta r}_1 . \quad (4.41a)$$

In the rotating gradiometer,

$$\bar{\Delta r}_1 \triangleq \bar{r}_1 \quad (4.42)$$

and (4.41a) becomes

$$\bar{g}_1 = \bar{g}_0 + \bar{\Gamma} \cdot \bar{r}_1 . \quad (4.41b)$$

We shall define the unit vector \hat{n}_1 such that

$$\hat{r}_1 \times \hat{n}_1 = 0 \quad (4.43)$$

where \hat{r}_1 is the unit vector of \bar{r}_1 .

In Fig. IV-8a, the acceleration a_1 sensed by the accelerometer at point 1 is

$$a_1 = \bar{g}_1 \cdot \hat{n}_1 . \quad (4.44)$$

Thus the output of the gradiometer is given by

$$(a_1 + a_2) - (a_3 + a_4) = (\bar{g}_1 \cdot \hat{n}_1 + \bar{g}_2 \cdot \hat{n}_2) - (\bar{g}_3 \cdot \hat{n}_3 + \bar{g}_4 \cdot \hat{n}_4) \quad (4.45)$$

where

$$\hat{n}_1 = (-\sin \theta \hat{i} + \cos \theta \hat{j}) \quad (4.46a)$$

and

$$\hat{n}_2 = -\hat{n}_1 \quad (4.46b)$$

where \hat{n}_3 and \hat{n}_4 are similarly defined. The rotation angle θ is

$$\theta = \Omega t . \quad (4.47)$$

Substituting and simplifying (4.45), the gradiometer output becomes

$$(a_1 + a_2) - (a_3 + a_4) = 2r[\Gamma_{xy} - \Gamma_{xx}] \cos(2\Omega t) + r[\Gamma_{yy} - \Gamma_{xx}] \sin(2\Omega t) \quad (4.48)$$

where r is the distance of the accelerometer from the center of platform axis. This is the same equation derived by Bell Aerospace [1971].

For configuration IV-8b, the acceleration sensed by the accelerometer at point 1 is

$$a_1 = \bar{g}_1 \cdot \hat{r}_1 . \quad (4.49)$$

The output of the gradiometer is given by

$$(a_1 + a_2) - (a_3 + a_4) = (\bar{g}_1 \cdot \hat{r}_1 + \bar{g}_2 \cdot \hat{r}_2) - (\bar{g}_3 \cdot \hat{r}_3 + \bar{g}_4 \cdot \hat{r}_4) \quad (4.50)$$

where

$$\hat{r}_1 = (\cos \theta \hat{i} + \sin \theta \hat{j}) \quad (4.51a)$$

and

$$\hat{r}_2 = -\hat{r}_1 , \quad (4.51b)$$

where \hat{r}_3 and \hat{r}_4 are defined similarly. Simplifying (4.50), the output of the gradiometer becomes

$$(a_1 + a_2) - (a_3 + a_4) = r[\Gamma_{xx} + \Gamma_{yy} + 2\Gamma_{xy}] + r[\Gamma_{xx} - \Gamma_{yy}] \cos(2\Omega t) . \quad (4.52)$$

Equations (4.48) and (4.52) show that when the gradiometer is rotated, the gradient signal is shift spectrally to a frequency twice the rotation rate, Ω . Thus by rotating the gradiometer by a frequency Ω such that 2Ω is more than half the bandwidth of the detection circuit above the cross-over frequency, the gradiometer will operate in the white noise region.

However, rotating the gradiometer introduces another set of problems. Amongst them are the noise and error sources associated with rotation. These tend to be more prominent as the rate of rotation is increased. Fortunately, most of the noise associated with rotating such as bearing noise have an output frequency equal to the rotation rate. They are inherently separated in the frequency domain from the output signal and may be selectively filtered.

Of the two possible arrangements shown in Fig. IV-8, Bell Aerospace has picked the first configuration. In this arrangement, there is no steady force acting on the accelerometers in a steady state. In the second configuration, the proof mass experienced a constant centrifugal force. This "pre-loading" of the accelerometers may introduce dynamic range problems and other problems related to a constant bias. However, in this arrangement, the gradiometer is unaffected by the fluctuations in the rotation rate since these are cancelled out. This is not the case in the first configuration. In fact, any fluctuations is enhanced by the gradiometer. On the other hand, very precise frequency control is relatively easy to achieve and this error can be kept small.

C-4 Axes Misalignment

In the fabrication of precision instruments, parallelism is always costly to achieve. It is no exception for the two cryogenic gradiometers despite their simple construction. The requirements of the parallelism

of the diaphragms for a given error in the gradiometers will be determined.

Figure IV-10 gives the rectangular coordinate system of the gradiometer. The origin of the coordinates is the geometric center of the gradiometer. Unit vectors \hat{n}_1 and \hat{n}_2 are the normals to the planes of the two diaphragms. They are not in line when the planes are not parallel to each other. The z axis is the sensitive axis of the gradiometer. The x and y axes are arbitrarily fixed to the body. The baseline of the gradiometer is l .

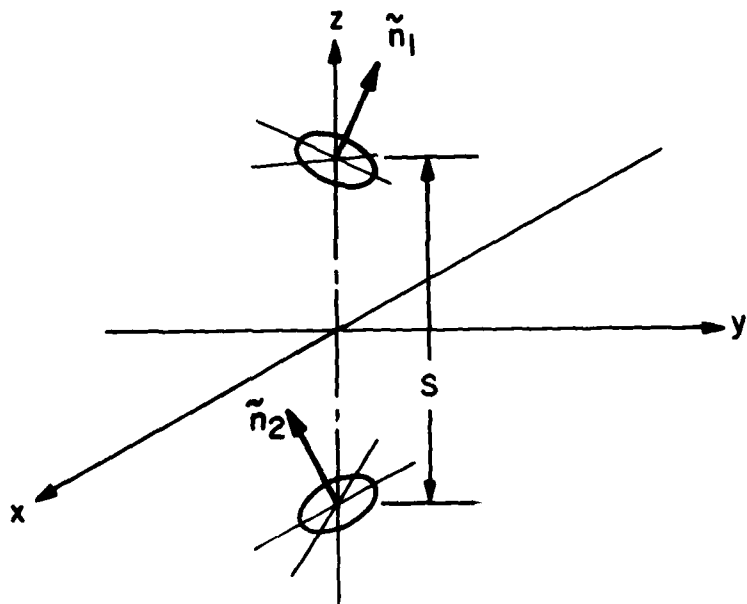


FIG. IV-10 COORDINATE FRAME OF THE GRADIOMETER. Unit vectors \hat{n}_1 and \hat{n}_2 are normal to the planes of the two diaphragm transducers. The z axis is the nominal sensitive axis; s is the distance between the centers of the two proof masses. That \hat{n}_1 and \hat{n}_2 may not coincide with the z axis produces the "misalignment" error.

The unit vectors of the normals are given by

$$\hat{n}_p = \epsilon_{xp} \hat{i} + \epsilon_{yp} \hat{j} + \epsilon_{zp} \hat{k} \quad (4.53)$$

where p can be 1 or 2. The acceleration vectors at the same points as the normals will be denoted by $\bar{a}_p(t)$. These acceleration vectors may be due to the constant earth's field or a time-varying field generated by an external device, to be discussed in Ch. V, Sect. C-2.

A generalized equation for the output current to the SQUID for the two gradiometers may be derived from (3.56) and (3.78). It is

$$i_s(t) = \beta [\sigma_1 \bar{a}_1(t) \cdot \hat{n}_1 - \sigma_2 \bar{a}_2(t) \cdot \hat{n}_2]. \quad (4.54)$$

For the CDGG,

$$\beta = h \frac{2}{1+\gamma}, \quad \sigma_1 = \frac{1}{\eta} \left(\frac{1}{d\omega^2} \right)_1.$$

For the DDGG,

$$\beta = h \frac{\lambda I_0}{1+\gamma}, \quad \sigma_1 = \frac{1}{\frac{2}{\omega_1}}.$$

For both cases,

$$i = \frac{I_0}{5}, \quad d = \frac{d_0}{-4}, \quad h = 1.08 \times 10^5,$$

To balance the gradiometer, a common sinusoidal acceleration $\bar{a}_1(t) = \bar{a}_2(t) = A \cos \omega t \hat{k}$ is applied along the sensitive axis. Using (4.53) and simplifying, the output becomes

$$i_{sb}(t) = \beta [\sigma_1 \epsilon_{z1} - \sigma_2 \epsilon_{z2}] A \cos \omega t. \quad (4.55)$$

The parameters σ_1 and/or σ_2 are adjusted such that the output due to a common acceleration vanishes. The condition is

$$\sigma_1 \epsilon_{z1} - \sigma_2 \epsilon_{z2} = 0 . \quad (4.56)$$

The balanced gradiometer may now be used to measure gravity gradient. Let the gravity vector at the center of the gradiometer be

$$\bar{g}_0 = g_{0x} \hat{i} + g_{0y} \hat{j} + g_{0z} \hat{k} . \quad (4.57)$$

The displacement vectors, $\Delta \bar{r}_1 \triangleq (0, 0, \ell/2)^T$ and $\Delta \bar{r}_2 \triangleq (0, 0, -\ell/2)^T$. Using (4.41a), the gravity vectors at points 1 and 2 are

$$\bar{g}_1 = (g_{0x} + \Gamma_{xz} \frac{\ell}{2}) \hat{i} + (g_{0y} + \Gamma_{yz} \frac{\ell}{2}) \hat{j} + (g_{0z} + \Gamma_{zz} \frac{\ell}{2}) \hat{k} \quad (4.58a)$$

$$\bar{g}_2 = (g_{0x} - \Gamma_{xz} \frac{\ell}{2}) \hat{i} + (g_{0y} - \Gamma_{yz} \frac{\ell}{2}) \hat{j} + (g_{0z} - \Gamma_{zz} \frac{\ell}{2}) \hat{k} . \quad (4.58b)$$

Using (4.54), the output of balanced gradiometer is

$$i_s(t) = \beta [\sigma_1 \epsilon_{z1} \Gamma_{zz} \ell + e_1] \quad (4.59)$$

where

$$\begin{aligned} e_1 &= \sigma_1 [(g_{0x} + \Gamma_{xz} \frac{\ell}{2}) \epsilon_{x1} + (g_{0y} + \Gamma_{yz} \frac{\ell}{2}) \epsilon_{y1}] \\ &\quad - \sigma_2 [(g_{0x} - \Gamma_{xz} \frac{\ell}{2}) \epsilon_{x2} + (g_{0y} - \Gamma_{yz} \frac{\ell}{2}) \epsilon_{y2}] . \end{aligned} \quad (4.60)$$

For any ideal gradiometer, the output would have been

$$i_s(t) = \beta \sigma_1 \Gamma_{zz} \ell . \quad (4.61)$$

Equation (4.60) shows that when the sensitive axes are not aligned, gravity gradient perpendicular to the sensitive axis of gradiometer will produce errors.

To get an idea of the constraints on parallelism, let the normal of diaphragm No. 2 be parallel to the sensitive axis of the instrument, i.e.,

$$\hat{n}_2 = \hat{k} \quad (4.62a)$$

$$\epsilon_{x2} = \epsilon_{y2} = 0, \quad \epsilon_{z2} = 1. \quad (4.62b)$$

If we further choose the body axes such that

$$\epsilon_{y1} = 0 \quad (4.62c)$$

the error term, e_1 of (4.60), is simplified to

$$e_1 = \sigma_1 (g_{0x} + \Gamma_{xz} \frac{\ell}{2}) \epsilon_{x1} \quad (4.63a)$$

and for earth-bound application, it becomes

$$e_1 = \sigma_1 \epsilon_{x1} g_{0x} \quad (4.63b)$$

since

$$g_{0x} \gg \Gamma_{xz} \ell. \quad (4.63c)$$

The relative error ξ is given by the second term of (4.59) divided by the first. For e_1 given by (4.63b), ξ is given as

$$\xi = \frac{g_{0x}}{\Gamma_{zz} \ell} \frac{\epsilon_{x1}}{\epsilon_{z1}} \quad (4.64a)$$

$$= \frac{g_{0x}}{\Gamma_{zz} \ell} \cdot \theta \quad (4.64b)$$

where θ is the angle (rad) that \hat{n}_1 makes with the z axis. It is assumed that θ is small and the error is not spectrally separated from the signal.

Table IV-2 tabulates the gravity that will give a 1% error for

a given θ in a field where $\Gamma_{zz} = 50E$ and $\ell = 0.1$ m.

Table IV-2
THE TOLERABLE GRAVITY FOR 1% ERROR

θ (deg):	0.5	0.1	0.01	0.001	0
$g_{0x} (10^{-9} g)$:	0.57	2.86	28.6	286.4	∞

In determining the tolerable misalignment of the two accelerometers, it is necessary to specify the environment in which the instrument will be used. For the experiment described in Ch. VI-B using a swinging ball as the gradient generator, θ should be less than 3 arcmin for a 1% measurement error. If the gradiometer were used for geodetic survey on a moving base vehicle, the limits become rather severe. When operated with its sensitive axis vertical (SAV), $\theta < 0.5$ arcsec. In the sensitive axis horizontal (SAH) mode, $\theta < 3.4$ arcsec. It is assumed that the displacement of the gradiometer from its balancing location is 100 m in the SAV mode, and ± 1 m in the SAH mode.

For our laboratory experiment, the tolerance of parallel surfaces are readily achieved by careful machining to approximately 3 arcmin.

C-5 Scale Factor Matching

Unless the two scale factors of the proof masses are matched, the output of the gradiometers include error proportional to gravitational acceleration. The degree of matching for a given level of accuracy will be investigated using a gradiometer with no axis misalignment. In other words,

$$\hat{n}_1 = \hat{k} \quad (4.65a)$$

$$\hat{n}_2 = \hat{k} . \quad (4.65b)$$

The instrument is balanced if

$$\sigma_1 = \sigma_2 . \quad (4.65c)$$

Substituting (4.58) and (4.65) into (4.54), the output current is

$$i_s(t) = \beta [g_{0z}(\sigma_1 - \sigma_2) + \frac{1}{2}(\sigma_1 + \sigma_2)\Gamma_{zz} \cdot \ell] . \quad (4.66)$$

Subtracting the output of an ideal instrument, (4.63b) from (4.66) gives the error term

$$e_2 = \beta(\sigma_1 - \sigma_2)[g_{0z} - \frac{1}{2}\Gamma_{zz} \cdot \ell] . \quad (4.67)$$

The percent error ξ_2 due to scale factor mismatch is

$$\xi_2 = \left(\frac{\sigma_1 - \sigma_2}{\sigma_1} \right) \left(\frac{g_{0z}}{\Gamma_{zz} \cdot \ell} - \frac{1}{2} \right) \approx \left(\frac{\sigma_1 - \sigma_2}{\sigma_1} \right) \left(\frac{g_{0z}}{\Gamma_{zz} \cdot \ell} \right) \quad (4.68)$$

since $g_{0z} \gg \Gamma_{zz} \ell$ typically. Evidently, the scale factors σ_1 and σ_2 must be better matched if a_z , the common axial acceleration becomes bigger.

In the laboratory experiment using the swinging ball (Ch. VI-B), we have $\Gamma_{zz} = 50$ E, $\ell = 0.1$ m and $g_{0z} = 10^{-8}$ g. Equation (4.68) shows that for a 2% error, balancing must be close to one part per thousand.

The output of the gradiometer at different levels of scale factor matching can be determined. When the gradiometer is shaken by a common sinusoidal acceleration along the z axis, the gradient term may be ignored. The output current is derived from (4.66) by setting $\Gamma_{zz} = 0$, viz,

$$i_s(t) = \beta(\sigma_1 - \sigma_2)a_z(t) = \beta\sigma_1 \left(\frac{\sigma_1 - \sigma_2}{\sigma_1} \right) A \cos \omega t . \quad (4.69)$$

Using the DDGG as an example, $\beta = 1.08 \times 10^5$, $\sigma_1 = 1/\omega_1^2$, where $\omega_1 = 2\pi(50)\text{sec}^{-1}$. With the SQUID sensitivity of 200 kV/A, the amplitude of the shaking acceleration, A , for a peak output of 100 mV and a scale factor balancing of 1 in 1000 is 4.7×10^{-5} g. The voltage output is suggested for easy detection. Thus the balancing common

acceleration is small. For a scale factor balancing of 1 in 10, the acceleration will be ten times smaller for the small output voltage.

In (4.69), the scale factors σ_1 and σ_2 are assumed to be constant. The analysis of the gradiometer given in App. D-4 shows that they are functions of frequency, damping factors, and persistent currents. For a pair of 800 Hz diaphragm, the scale factors at the low frequency range are plotted as solid lines in Fig. IV-11. The intersection gives the frequency at which the two scale factors are balanced. When the persistent current in accelerometer 1 is changed, the plot of σ_1 shifts as shown by the dotted lines. The balance point shifts to p_1 when the current is increased, and to p_2 when the current is decreased. Since the balancing conditions are different at p_1 or p_2 , the gradiometers will be balanced only at one frequency. For a high Q ($Q \geq 10^5$) suspension, the error introduced in measuring gradients at frequency different from that of the balancing frequency will be smaller than the resolution of the instrument (0.1E). See App. D for details.

We conclude that the gradiometers must be balanced at a frequency as close to the operating frequency range as possible. However, it becomes increasingly difficult to do the balancing experiment as the forcing frequency is reduced. These difficulties arise from the practical problems of the mechanical shaker and the detection of a low frequency output signal.

D. SUMMARY

The high Q of the diaphragm proof mass suspension of the accelerometer should be reduced. A method to accomplish this without unduly increasing the thermal noise is devised.

The isolation required to limit error contribution from environmental vibrations is determined. These requirements are very demanding unless precisely matched accelerometers are used in the gradiometer. An alternative way to remove error is to model them mathematically using additional measurements. The block diagram of a simple scheme is given in Fig. IV-12.

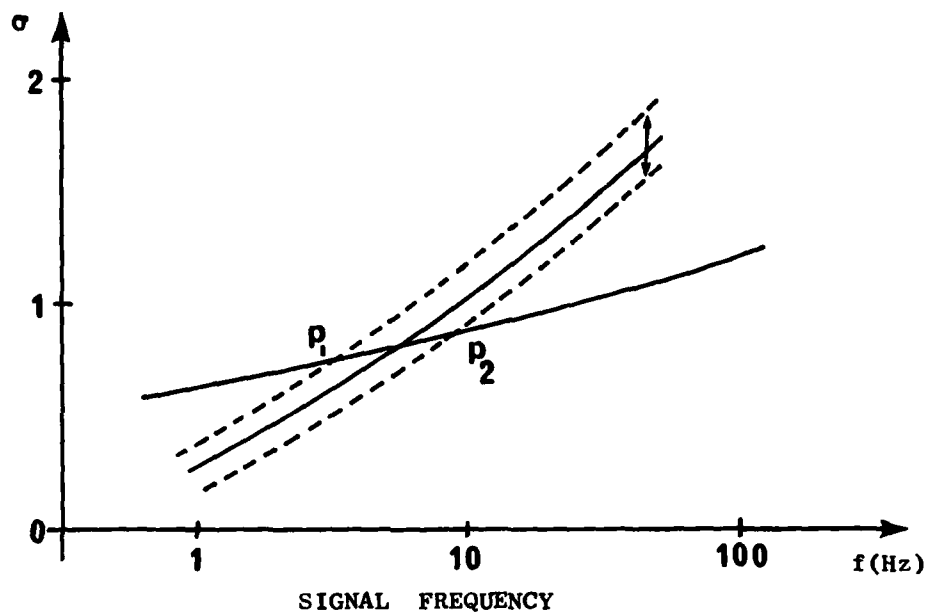


FIG. IV-11 FREQUENCY PLOTS OF SCALE FACTORS OF THE TWO GRAVITY GRADIOMETER ACCELEROMETERS. As the scale factor, σ , of the No. 1 accelerometer is changed, the balancing points change to p_1 or p_2 . The plots are theoretical curves for a pair of accelerometers.

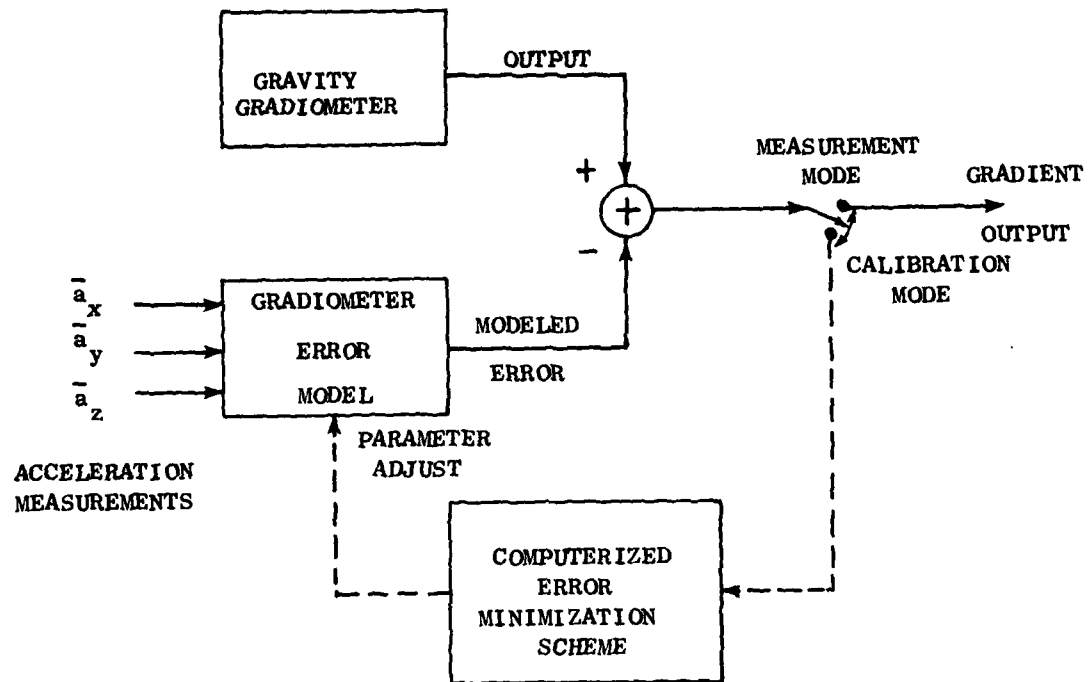


FIG. IV-12 GRADIOMETER ERROR COMPENSATION MODEL. The calibration of the error model is performed by placing the gravity gradiometer in a known gradient field. Three accelerometers are mounted orthogonally on the gradiometer platform to determine the accelerations experienced by the gradiometer. These measurements are input into the error model where parameters are adjusted using an on-line computerized algorithm to minimize error.

In this scheme, the gradiometer is mounted on a stabilized platform together with three accelerometers. The error model transforms these measurements into an equivalent error signal which can be used to remove the actual error. The parameters of the model may be adjusted in the calibration mode through an optimization algorithm using an on-line computer. During calibration of the error model, the platform is shaken with known sinusoidal forces.

The drift and bias of the cryogenic gradiometer are examined and found to be favorable. We concluded that the cryogenic gradiometers are superior to room temperature devices in most respects. The price we pay is the provision of a cold space. In some applications where increased sensitivity is required, a cryogenic design may be the only instrument of acceptably small size.

Chapter V

SUPERCONDUCTING HARDWARES

A. CONSTRUCTION OF THE CRYOGENIC GRADIOMETER

The two cryogenic gradiometers operating on different principles are discussed in Ch. II. Results of the experiments using the current-differencing device will be reported here; those of the displacement-differencing device will appear in E. Mapoles' dissertation.

The cryogenic gradiometer comprises two accelerometers separated by a fixed baseline of 10 cm. The accelerometers are of the design developed by Dr. Paik. They are described in detail in his Doctoral thesis [1974]. Only a brief description will be given here. In our experiments, the accelerometers are mounted with their sensitive axes aligned.

The individual accelerometer consists of a niobium diaphragm shown in Fig. V-1. On each side of it a pancake-shaped coil is placed a small distance of 0.1mm (0.004") away. These coils are wound with 300 turns of Nb-Ti 48 wire of 0.002" dia. Under these conditions, the wire should be carrying at least 5 A at $T = 4.2$ K before the critical field at the surface of the diaphragm is exceeded.

The output leads of the accelerometers and the input leads to the SQUID are connected in parallel. The electrical schematic is shown in Fig. III-9. To facilitate assembly and disassembly of the gradiometer, a common bus-bar concept (suggested by Paik) for making connection is used. The construction of these joints is described in the next section.

The cross-sectional view of the assembled gradiometer is given in Fig. V-2. Titanium* studs are used to hold the assembly together. The other components in the assembly are machined out of niobium or niobium zirconium stock.

* Ti is used for strength and its close thermal coefficient expansion with Nb.

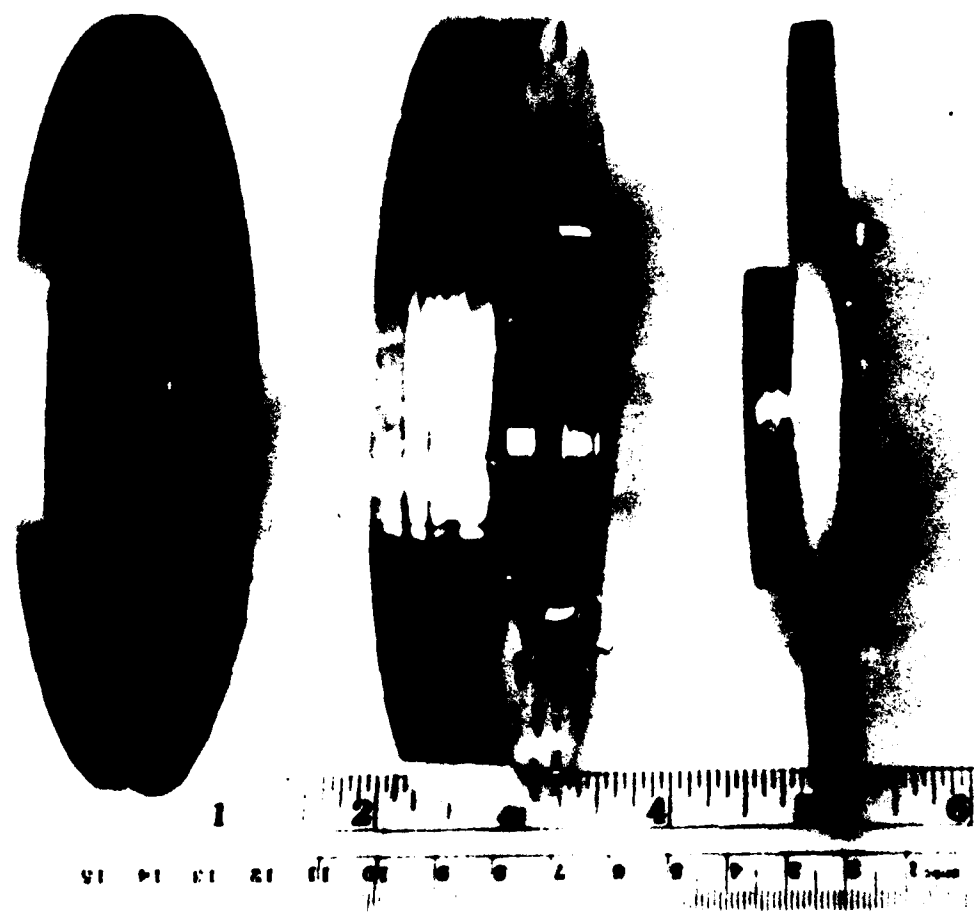


FIG. V-1 SUPERCONDUCTING ACCELEROMETER COMPONENTS

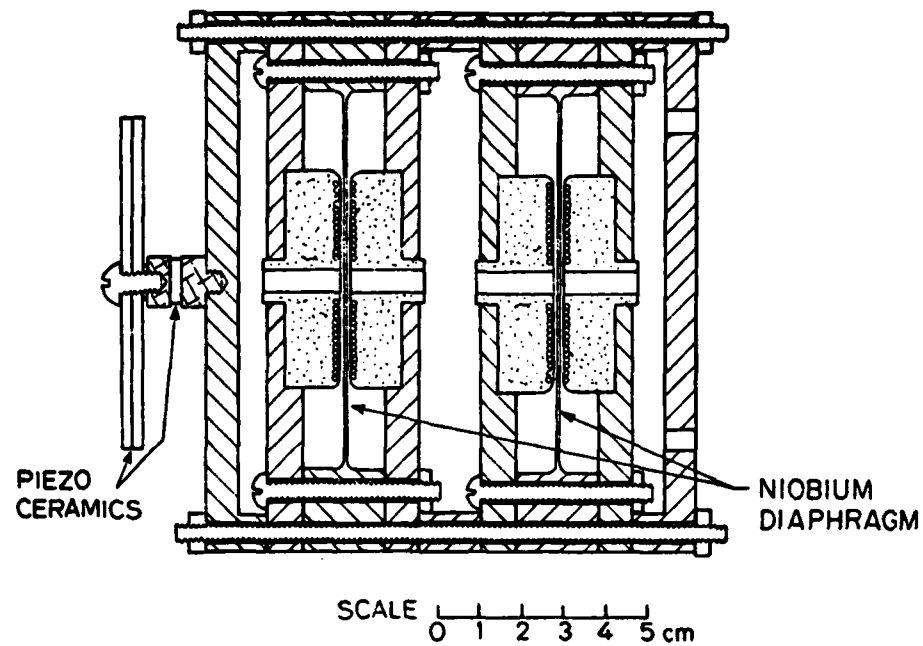


FIG. V-2 CROSS-SECTIONAL VIEW OF THE CURRENT DIFFERENCING GRAVITY GRADIOMETER (CDGG). The distance between the diaphragm is about 5 cm here. It was increased to 10 cm in the experimental gradiometer. The piezoelectric shaker to produce the linear acceleration is shown attached to the assembly.

In the majority of our experiments, a pair of closely matched diaphragms of frequency of 855 Hz were used. We decided to build a matched pair when we encountered difficulties when we tried to demonstrate the current-differencing concept. The frequency was selected so that the diaphragms can be used as sensors for the gravity wave experiment going on concurrently at Stanford. We were to pay heavily in this compromise in the reduced sensitivity of the sensors.

The theory discussed in Ch. III-A-1 is used to determine the thickness of the diaphragm after its resonant frequency is chosen. The diaphragms are then machined, cleaned, and vacuum annealed for stress release. They are electro-chemically polished to increase its Q factor [Paik, 1974]. The polishing is done in a mixed solution of sulphuric and hydrochloric acid in a procedure outlined by Drepers et al. [1971]. The same process may be used to fine-tune the frequencies of the diaphragm.

Four pancake coils are wound following the procedure in Paik's thesis [1974]. The idea is to leave a shoulder near the center of the coil form such that when a lucite disk is pressed against the shoulder, a well defined gap is left to wind the coil. The plates are held together by means of a dowel pin pushed into a hole which is bored through the centers of both plates perpendicular to their surfaces. The shoulder height is 0.003 ± 0.0005 in. and the hole size is 0.1870 in. (4.75 mm) with the dowel pin 0.1875 in. (4.76 mm). The improvement we made is to machine the backup plate, the G-10 coil, form the hole through the G-10 and then the lucite disk all in one setting of the work tool and the chuck. With care, almost perfect coils of 300 turns of 0.0025 in. Ti-Nb wires are obtained. We have also tried to replace the G-10 coil form with machinable ceramics. Although satisfactory in most aspects, the ceramics are brittle and chip easily. Moreover, the coils tend to peel off easily from a ceramic coil form.

When assembled, the gradiometer is totally shielded from external interferences by its superconducting cover. It is compact and rugged. Current leads into the gradiometer and output leads to the SQUID are shielded by lead tubings.

A pair of loaded diaphragms of design described in Ch. III were built by Dr. Paik. These sensors were built before the analysis was done. The schematic is given in Fig. V-3. Note that $\alpha = b/a = 0.286$. The sensor was constructed by electron-beam welding a central post to a corresponding hole cut at the center of a diaphragm. Additional annular disks were then welded onto the posts to increase the central load. Electron-beam welding is done in vacuum. The heat generated inevitably tends to warp the annular portion of the diaphragm. Heat treatment for stress release must be carefully done since the central mass is heavy. A permanent sag could easily occur. Correction measures have been taken for both sensors so fabricated. Despite these problems, welding is chosen because the resultant sensor will have high Q . It has been pointed out in Ch. IV that high Q is not necessarily favorable in all respects. Clamping the load on to the diaphragm would be an alternative if lower Q (say, 10^4) is acceptable. It is indeed the method adopted by Evan Mapoles* in the design of a new sensor. The loaded diaphragm proof masses

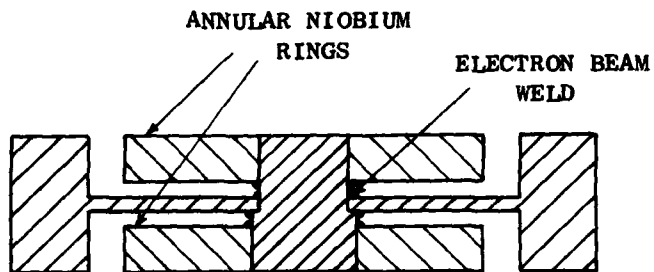


FIG. V-3 CROSS-SECTtONAL VIEW OF THE CENTRALLY LOADED DIAPHRAGM. The diaphragm comprises 4 individual components: a diaphragm with a centrally located hole, a cylindrical post, and 2 annular rings that are welded onto either ends of the post. All parts are made from Stanford-graded niobium.

* Ph.D. Candidate in Physics Dept, Stanford University

built are used mainly in the displacement differencing gradiometer. The experiments are performed primarily by Mapoles and will be described in his dissertation.

B. SUPERCONDUCTING JOINTS

Making high current density superconducting joints has always been an art especially in the construction of the superconducting accelerometer. To maximize sensitivity of the pick-up coils, tiny wires (0.002 in dia.) are selected. To achieve its theoretical sensitivity, the coils should have a persistent current of 5 A. The method developed by Paik is to twist the ends of the wires together and clamp the twisted bunch tightly between two washers. The surface areas of the wires in contact with one another provide the conduction. Joints made this way have been satisfactory. For an assembly of ten joints or more, a few iterations of cooling down and identifying the faulty joints are normally required since there is no way to check at room temperature whether the joints will be superconducting when cooled. However, every time the accelerometer is dismantled, all the joints have to be remade. One should minimize the number of joints disturbed during disassembly.

Paik suggested the bus-bar concept. The resultant design is shown in Fig. V-4. A joint for three wires is picked as the design since it is most common in our work. The base, a brass slab of $3/16 \times 1/2 \times 1\frac{1}{2}$ in. has three 8-32 threaded holes to hold three short screws. It also serves as the heat sink. The proper spot for the joint holes are drilled in the two $1/2 \times 1\frac{1}{2}$ in., 0.002 in. foils such that they may be assembled as shown in the figure. The wires to be jointed are placed between the foils with one wire to each screw. The "sandwich" pile is then pressed together by torquing the screw to 13 in.-lb. To prevent the washers from cutting the wires, their edges are rounded on the sides touching the foils. The niobium foils serve as the common bus between the wires. To improve reliability, the two foils should be a continuous piece bent-double. To ensure good surface contact, the foils and the ends of the wires are cleaned by dipping into concentrated nitric acid just before they are put together. This procedure has been successful in reducing the turn-around time between trial runs.

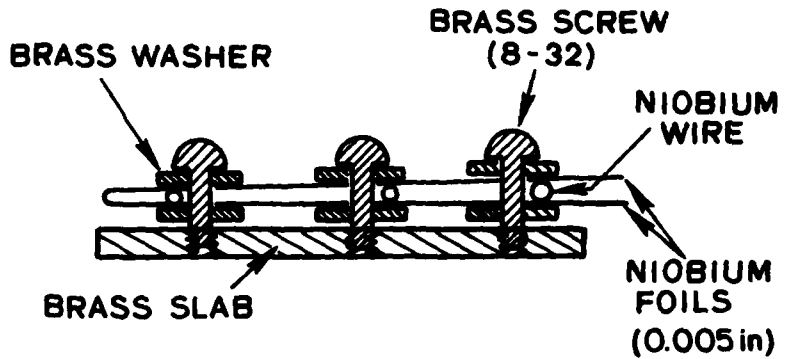


FIG. V-4 CROSS-SECTIONAL VIEW OF THE SUPERCONDUCTING "BUS-BAR" CONNECTIONS. The joints are formed by pressing the niobium coils. The actual joints are made between the wire and the foils. By using a continuous strip of foil, a superconducting bus-bar joint is made.

B-1 Ultra Low Resistance

The analysis for the current-differencing gradiometer (Ch. III) shows that the persistent currents in the two accelerometers should be adjusted for common mode rejection. In superconductivity work, small current adjustments are typically done using an external coil that is coupled to the first coil through a transformer link. By storing current in the external loop, the net flux in the first coil can be reduced. This scheme cannot be used in the gradiometer which makes use of the same flux conservation principle for detection. Instead ultra low resistor is used.

The idea is to switch an ultra-low resistor on command in series with the coil in the loop. If we can achieve an L/R time constant of 1000 sec or more, balancing the currents to one part per thousand is easily achieved by manual control. With L of the order of $100 \mu\text{H}$, the resistance required is of the order of $0.1 \mu\Omega$. This is a rather low resistance value. To achieve this, the following circuit element is developed.

A piece of copper clad niobium wire is non-inductively wound a few turns about a carbon resistor (150Ω). The wires are then soldered using ordinary lead-tin soldered on to a copper block with a 10 mm wide step, see Fig. V-5. At 4.2 K, the solder will be superconducting while copper is not.

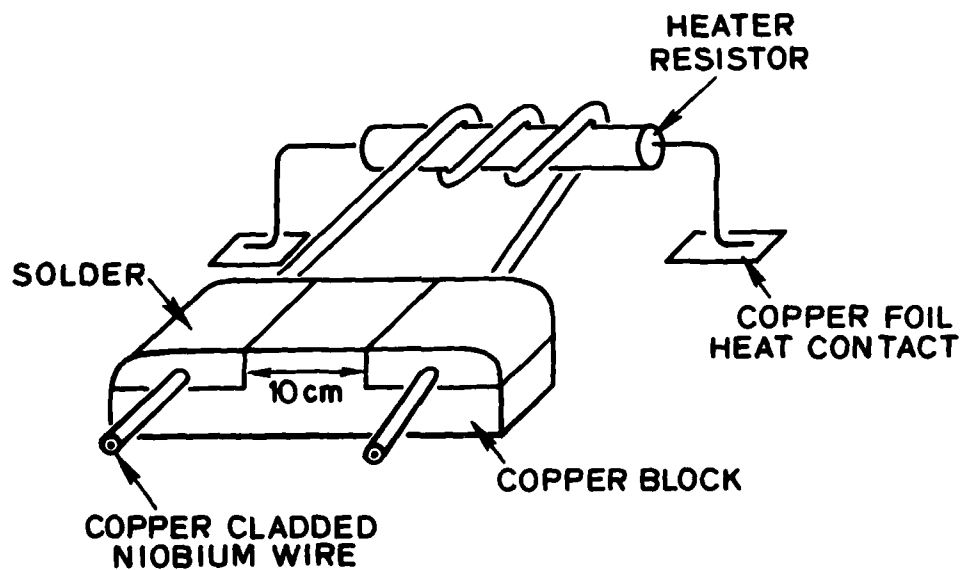


FIG. V-5 PICTORIAL SKETCH OF THE ULTRA-LOW RESISTANCE RESISTOR. The resistor is heat activated. A current flowing through the heater resistor will turn the niobium wire that is wrapped around the resistor normal. Any super current that flows in the wire will be forced to flow through the copper-niobium bond in the copper cladded wire, the solder plug, and the short length of copper of the copper block. The resistance of this path at cryogenic temperature is about $10^{-7} \Omega$.

The copper cladding at the ends of the wires are removed by dissolving the copper in concentrated nitric acid. The exposed niobium core may be used to connect to the other elements through a superconducting joint. The copper block also serves as a heat sink for the element. A circuit diagram of a typical arrangement is given in Fig. V-6.

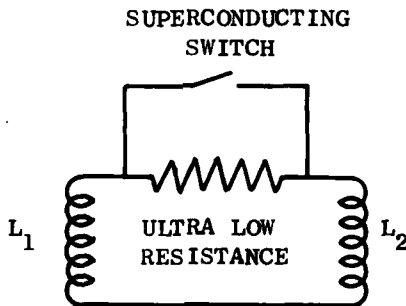


FIG. V-6 SCHEMATIC OF TUNING CIRCUIT.
 L_1 and L_2 are the superconducting pickup coils of the accelerometer. The sketch of the ultra-low resistance and the superconducting switch is given in Fig. V-4.

L_1 and L_2 are the superconducting pick-up coils of the accelerometer.

At 4.2 K, the niobium core of the copper clad is superconducting and a persistent current may be stored in the loop. To change the persistent current, the superconducting switch is opened by passing a small current (10 mA) through the carbon resistor. The current will either flow through the "normal" part of the niobium wire ($\sim 0.1 \Omega$) or crosses the niobium-copper interface, the superconducting solder joint and the raised step of the copper block.

Experiments were performed to determine the decay time constant of the arrangement. Current was stored in an accelerometer and the

frequency of the diaphragm determined. The heater was turned on and the current allowed to decay for a given time. The frequency of the diaphragm was then determined and the process was repeated. The experiment can be performed using an accelerometer or the accelerometer half of a gradiometer. A typical result is given in Table V-1 and plotted in Fig. V-7. The energy decay time constant is 630 sec giving a resistance value of $2 \times 10^{-7} \Omega$.

Table V-1
ENERGY DECAY OF INDUCTANCE COIL
($f_0 = 855.1$ Hz)

τ	f_1	$f_1^2 - f_0^2$
0	857.8	4625
200	857.05	3339
400	856.5	2396
600	856.1	1711
800	855.8	1198
1000	855.6	855

Adjusting current by means of the ultra-low resistor has been demonstrated successfully. This procedure is used in our gradiometer work. Another possibility is to connect a resistor in series through a transformer link. This method has been successfully employed by Prof. Goodkind but is not developed further here.

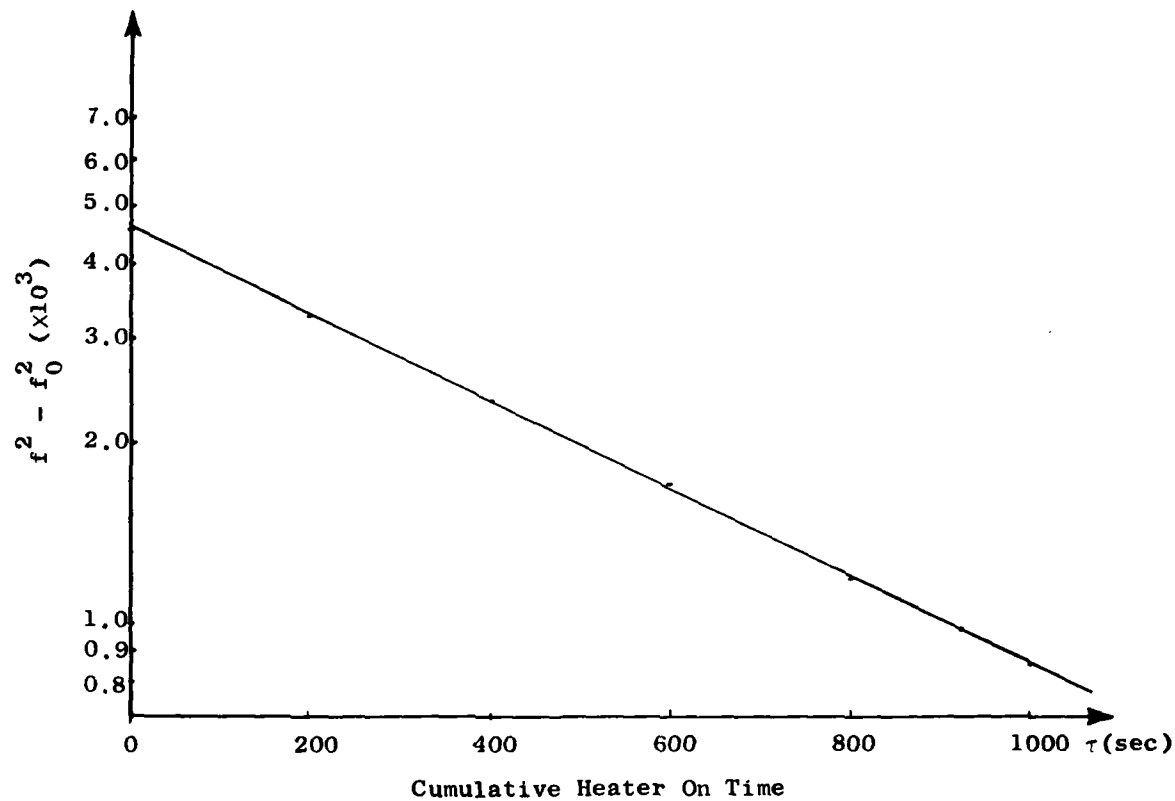


FIG. V-7 ENERGY DECAY OF PERSISTENT CURRENT. The plot showing the difference between the square of the frequency with current and that without vs the cumulative time the ultra-low resistance is switched into the circuit is plotted on log-linear scale. The slope of the line gives the decay time constant of the stored energy.

G-2 The SQUID (Superconducting Quantum Interference Device) Detection System

The operation principles of an a-c SQUID [Zimmerman, 1972] are described in the literature [Forgacs, 1967], [Lounasmaa, 1974], [Rose-Innes, 1967]. The SQUID used in the initial phase of this research is the toroidal SQUID developed by Paik who described it in detail [Paik, 1974]. Since it is custom designed for the accelerometer, it has very high sensitivity. However, it is dropped in favor of the commercially available SHE SQUID System 330 for its simplicity and reliability. The reader is referred to the manufacturer handbook for the complete description of the SHE system. Some salient characteristics are listed in Table V-2.

Table V-2
CHARACTERISTICS OF (SHE) SYSTEM 330

maximum equivalent input current noise i_0 (rms A/\sqrt{Hz})	2×10^{-11}
input coil inductance, L (μH)	2
mutual inductance between input coil and SQUID, M (nH)	20
guaranteed energy sensitivity, $\frac{1}{2} L i_0^2$ (Joules/Hz)	4×10^{-28}
maximum input signal without resetting output I_m (Ap-p)	10^{-4}
dynamic range I_m/I_0 ($\sqrt{Hz}/2\sqrt{2}$)	5×10^6

This is indeed a very sensitive detection device with a maximum theoretical sensitivity of $20V/\mu A$ for a full scale deflection input of $0.5 \mu A$.

This system also provides a suitable voltage with 100Ω output impedance, $\pm 5\text{mA}$ maximum current and $\pm 10\text{V}$ range for external feedback. This is very important since this output was used in the implementation of the feedback damping scheme described in Ch. V-B.

In the experiments to verify the feedback damping scheme described earlier, the SHE multiple-function probe (MFP) SQUID is used as the sensor as well as the feedback element. The MFP has a built-in transformer which is ideal for feedback purposes. The input leads of the feedback transformer has noise suppression ballast inductors and bypass capacitors. The mutual inductance of the feedback transformer is $1\mu\text{H}$.

Note that the inductance L_p of the gradiometer has a theoretical value of $25\mu\text{H}$ while that of the input coil of the SQUID is $2\mu\text{H}$. A matching transformer is designed and built to maximize energy transfer to the SQUID. The transformer is of the solenoidal design of Prof. Giffard (Stanford University).

The coil form is made of G10 rod and its dimensions are given in Fig. V-8. The solenoidal coils are wound on the thinner rod in the center. The primary of the transformer are wound first, consisting of 282 turns of 2 mil niobium T48 wire. The secondary is wound on top with 79 turns of the same wire. Being superconducting, the gauge of the wire in the secondary needn't be larger. This gives a turn ratio of 3.57, the square* of which is 12.7 which is fairly close to the desired value of 12.5. The number of turns of the primary is selected to give an inductance about three to four times that of the gradiometer.

* inductance of solenoid is $L = \mu_0 N^2 a / l$

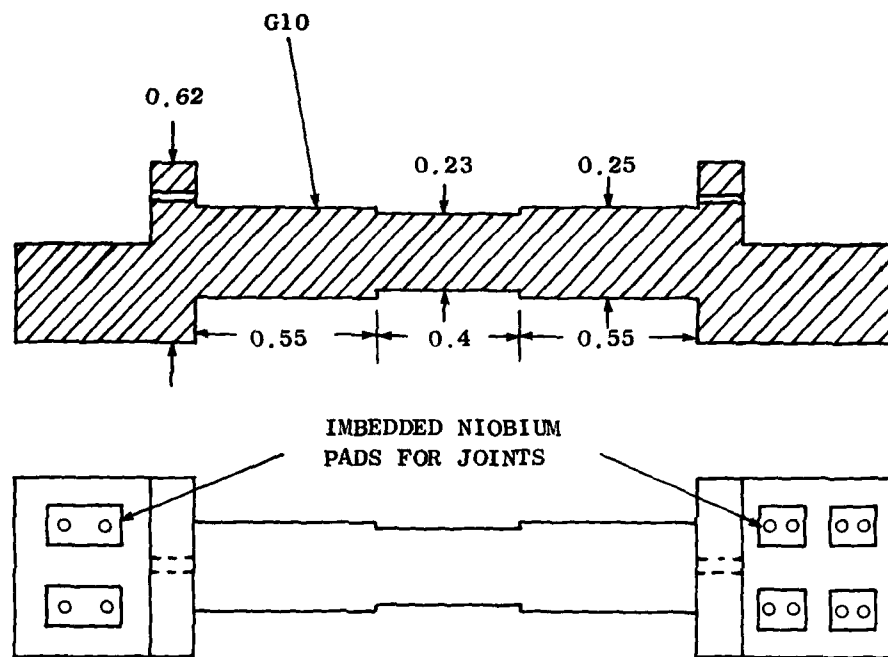


FIG. V-8 MATCHING TRANSFORMER COIL FORM. The transformer windings are wound in the central portion of the coil form. The imbedded niobium pads at either end allow external leads to be connected to the windings of the transformer. All dimensions are in inches.

To improve coupling and shield against interference, a 5 in. length of 0.002 in. lead foil 1.45 in. wide overlayed on a slightly bigger strip of 0.001 in. mylar is wrapped around the central portion of the form. The mylar prevents shorts between layers of this continuous cylindrical superconducting shield. The transformer is encased in a copper enclosure which has a thin solder film covering its entire surface. The cylindrical enclosure is designed for mating with the SHE SQUID.

The parameters of this transformer is determined in a simple test performed by Hollenhorst of Stanford. The schematics is given in Fig. V-9.

The primary is connected across a superconducting capacitor of known value. The frequency and Q of the resonance are determined from the resonance as seen from the SQUID connected by the secondary. The value of resonance and Q are 48013 and 1726 kHz respectively. This works out to be an inductance of $92 \mu\text{H}$ for the primary. The secondary is then determined from the turn ratio. Using the same procedure, the coupling constant for the transformer without its lead shield is determined to be 0.927.

The parameters of the transformer are also measured at d-c using the SQUID. Figure V-10 gives the experimental setup under cryogenic conditions.

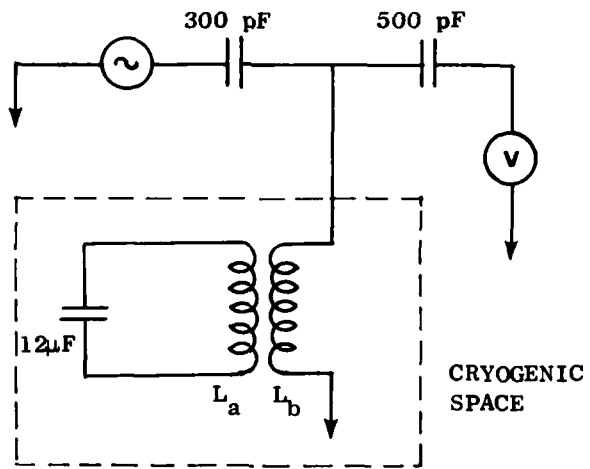


FIG. V-9 CIRCUIT FOR THE TESTING OF TRANSFORMER
 [courtesy J. Hollenhorst]

With this setup, the resonant frequency of the L - C circuit in the transformer's secondary winding can be determined. The inductances may be calculated.

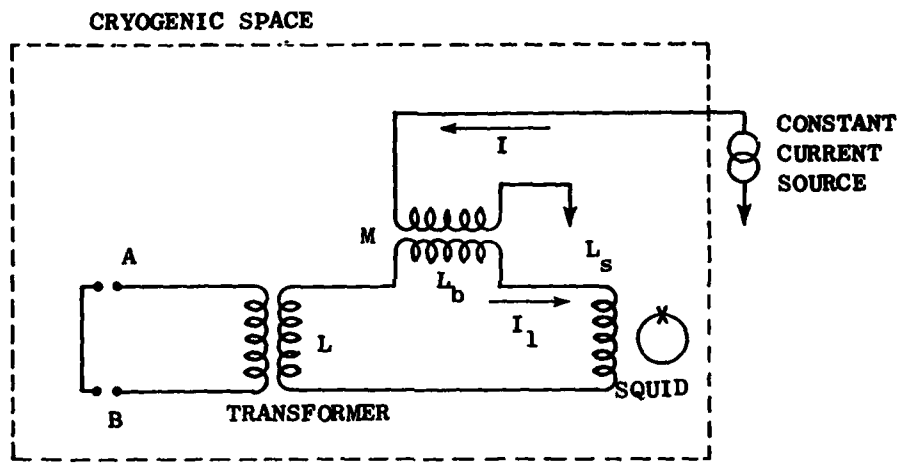


FIG. V-10 CIRCUIT FOR INDUCTANCE MEASUREMENTS OF THE MATCHING TRANSFORMER. By pumping d-c current in the primary of the feedback transformer and measuring the corresponding voltage change in the output of the SQUID, the inductances of the matching transformer can be determined.

The SHE Corp. SQUID used has a current sensitivity of $0.0980 \mu\text{A}/\phi_0$ and a flux sensitivity of $19.9 \text{ mV}/\phi_0$. The mutual inductance M and $L_s + L_b$ are determined by Jim Hollenhorst for the SHE multiple function probe as $0.967 \mu\text{H}$ and $2.56 \mu\text{H}$ respectively. The terminals A & B may be shorted by a piece of superconducting wire. A given current, I , may be forced through the external circuit using the precision SHE constant current supply. The corresponding rise in the SHE control unit is then noted. From the quoted sensitivity, the loop current I_1 is

$$I_1 = \frac{0.98 \times 10^{-4}}{19.9} \left(\frac{\Delta V}{V} \right) * \Delta I \quad (5.1)$$

where ΔV is the change in the d-c output voltage of the SQUID control unit. From the consideration of flux, we have

$$I_1(L + L_b + L_s) = IM \quad (5.2)$$

when the terminals A and B are open. When they are shorted, the relation is

$$I_1[L(1 - k^2) + L_s + L_b] = IM \quad (5.3)$$

where k is the coupling coefficient of the matching transformer. Table V-3 gives the experimental results.

Table V-3
DATA OF TRANSFORMER TESTING

Terminal AB Winding Connected to SQUID	Open		Closed	
	ΔV	ΔI	ΔV	ΔI
primary	1 V	$0.261 * 0.2\text{mA}$	1 V	$0.096 * 0.2\text{mA}$
secondary	0.6 V	$0.275 * 1\text{mA}$	1 V	$0.392 * 0.2\text{mA}$

Using the data and the Eqs. (4.2) and (4.3), the parameters of the transformer were determined to be

$$\begin{aligned}L_1 &= 87.4 \mu\text{H} \\L_2 &= 7.69 \mu\text{H} \\k &= 0.924 \\M &= 23.9 \mu\text{H}.\end{aligned}\tag{5.4}$$

D. DAMPING BY FEEDBACK

D-1 Test Circuit for Feedback Damping

An experiment to demonstrate the concept of "noiseless" damping in a cryogenic environment is shown in Fig. IV-4. The SHE Model 30 SQUID control unit provides a voltage output for external feedback purposes with a transfer function given by

$$v(t) = -G_s i_s(t)\tag{5.5}$$

where $i_s(t)$ is the input SQUID current and G_s is the constant gain. The constant gain, G_s , can be one of three values: 200 V/mA, 2,000 V/mA, or 20,000 V/mA depending on a front panel selection. This external feedback voltage is unfiltered. The package arrangement of SHE SQUID and the transformer available in the SHE multiple function probe SQUID is used for the sensor and feedback unit. Ballast inductances and bypass capacitances are built into the transformer for noise suppression. The compact unit is well-shielded against interference and spurious pickup.

The inductances of the circuit as given in Fig. IV-7 are determined: $L_b = 0.56 \mu\text{H}$, $L_s = 2 \mu\text{H}$, $L_c = 7 \mu\text{H}$, $L_d = 92 \mu\text{H}$, and $k = 0.927$. The design value of L_p , 100 μH , is used for the inductance of the pickup coil for a high Q diaphragm of resonant frequency 418 Hz. The Q of this diaphragm was determined as the feedback was varied. The feedback scheme of Fig. IV-4 was implemented and the parameters picked to produce a theoretical Q of 6.6. For this diaphragm, this meant an

equivalent resistance of $200 \text{ m}\Omega$ using the simple theory formulated in Ch. IV-B.

The circuit of the bandpass filter, the integrator and the voltage-to-current converter is given in Fig. V-11. Using (4.24) with $M = 1\mu\text{H}$, $\text{Req} = 200\text{m}\Omega$, $G_s = 200 \text{ V/mA}$, it becomes

$$H_I(s) = \frac{1}{G_v s} . \quad (5.6)$$

For the voltage-to-current converter, the load current is approximately 10 mA for 5V input. Thus,

$$G_v = -\frac{1}{500} \quad (5.7a)$$

and

$$H_I(s) = -\frac{500}{s} . \quad (5.7b)$$

The resultant RC time constant of $39 \text{ m}\Omega$ is obtained by setting $R = 39 \text{ k}\Omega$ and $C = 1 \mu\text{F}$.

In actual design, a voltage-controlled-voltage source non-inverting filter was selected for the bandpass filter with a Q of 8 and a gain at the passband of 27.3. The design of these circuits are taken from the Burr Brown source book [Graeme, 1971]. The gain of the bandpass filter has been assumed to be unity in the design. To compensate for this discrepancy and to adjust the overall feedback gain, an attenuator is inserted in front of the bandpass filter. The actual gain of the feedback loop was determined experimentally.

Using the notations for voltages in Fig. V-11, the voltage ratios V_4/V_1 and V_2/V_1 were determined at different frequencies for a particular adjustment of the bandpass filter. The results are plotted in Fig. V-12. By considering the loop gain, we obtain:

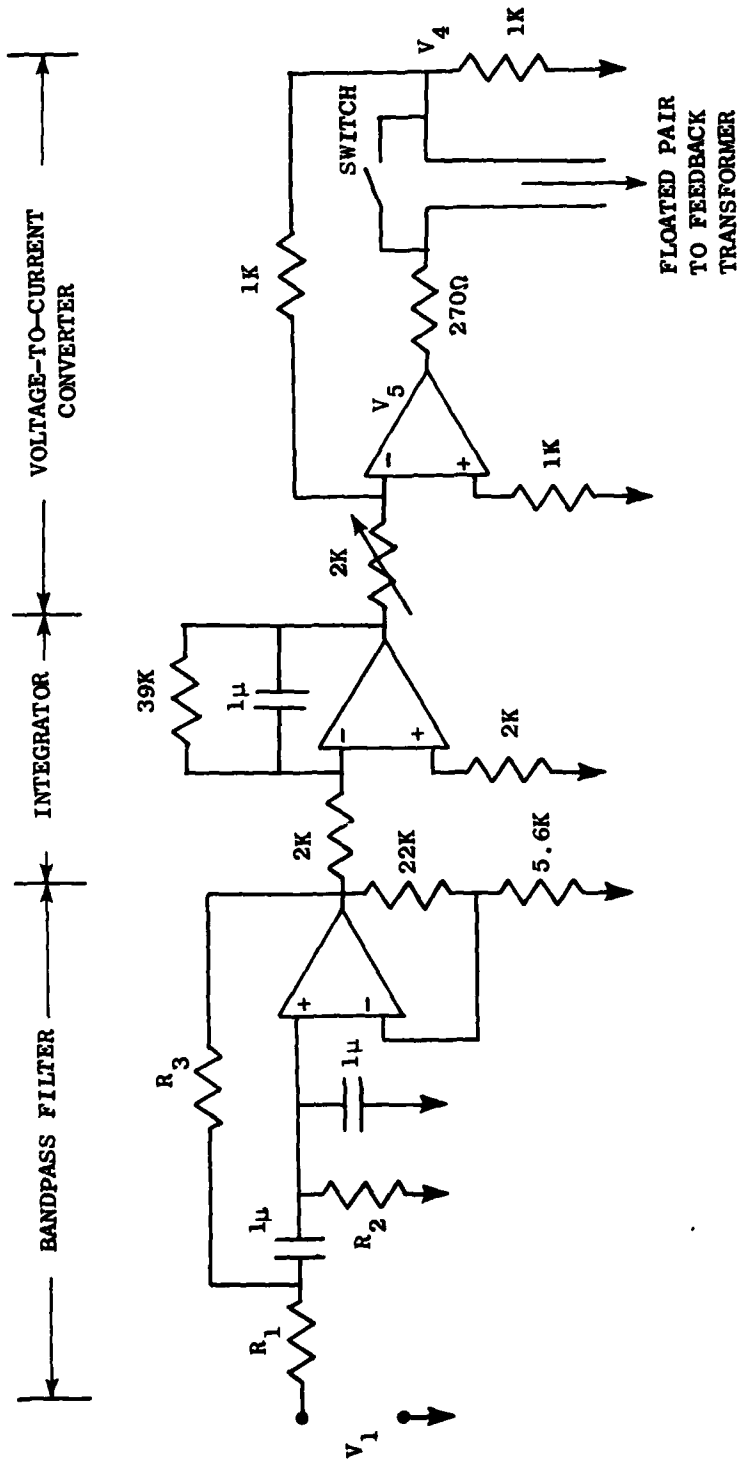


FIG. V-11 GRADIOMETER FEEDBACK DAMPING CIRCUIT. The designs of the individual circuits are taken from Burr Brown Source Book [Graeme, 1971]. All operational amplifiers are CA 3140 with offset potentiometers and compensation capacitors provided.

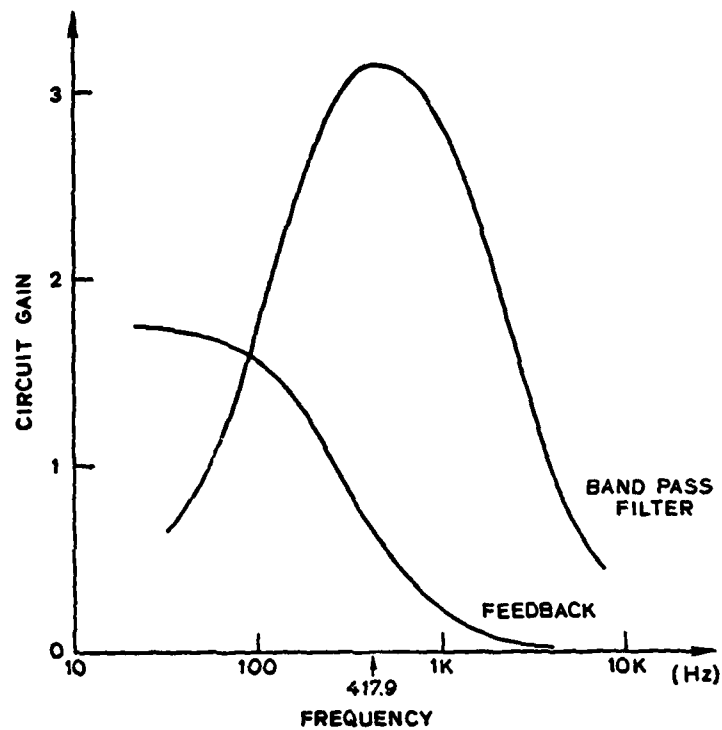


FIG. V-12 TRANSFER FUNCTIONS OF THE BANDPASS FILTER AND THE OVERALL FEEDBACK. The bandpass filter is tuned at 417.9 Hz which is the resonant frequency of the resonance of the diaphragm proof mass.

$$Z_{fb} = \frac{V_{fb}}{I_e} = 8\pi f \frac{V_4}{V_1} 10^{-4} \text{ antilog } \left(\frac{G_A}{20} \right) \quad (5.8a)$$

and

$$|G_{fb}| = \frac{Z_{fb}}{M} = 10^6 Z_{fb} \quad (5.8b)$$

where Z_{fb} is the feedback voltage seen by the input current I_e and $|G_{fb}|$ is the magnitude of the feedback loop gain, G_{fb} ; G_A is the attenuation of the attenuator expressed in db. For zero db attenuation, Z_{fb} was 713.1 mΩ at the resonant frequency.

The calibrated circuit was then used in the feedback loop with different G_A . The Q of the diaphragm at the different feedback gains were determined. The results are plotted in Fig. V-13. It shows the initial decrease in Q and its subsequent increase as the feedback gain is increased. This is predicted by the discussion given in Ch. IV-C. The minimum time constant of 1.85 sec ($Q_{min} = 2430$) occurs at $G_A = -45$ dB. Using (5.8a), the resistance produced by the feedback circuit is 4.01 mΩ. This is the resistance seen by the input SQUID circuit. Assuming perfect coupling, the resistance seen by the diaphragm is given by (4.34a). For $(N_p/N_s) = (282/79)$, the equivalent resistance is 51.1 mΩ.

We shall check the accuracy of the predictions of (4.36) which give the theoretical value of G_{fb} that will produce the minimum Q . Using (5.8b) and $R_{fb} = 4.01$ mΩ, the experimental value of G_{fb} is

$$G_{fb} \Big|_{f=f_0} = 4010 . \quad (5.9)$$

For the inductance values given in the beginning of this section in Eqs. (4.25) and (4.27), we have

$$L_{eq} = 4.118 \mu H \quad (5.10a)$$

and

$$G_M = 0.1498 . \quad (5.10b)$$

Furthermore,

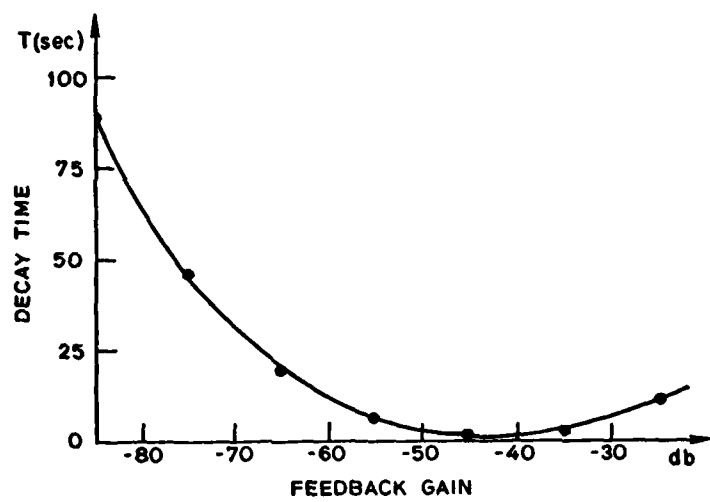


FIG. V-13 THE VARIATION OF THE RESONANCE DECAY TIME VS FEEDBACK GAIN. As the feedback gain is increased, the Q of the resonance decreases to a minimum and then starts to increase again. The minimum Q occurs approximately at the attenuator setting of 45 dB.

$$L_{int} \approx 100\mu H \quad (5.11a)$$

$$r_{int} = \frac{2L_{int}}{\tau} \approx 1\mu\Omega \quad (5.11b)$$

where L_{int} is the inductance of a single coil, τ is the time constant of the resonant decay without feedback. The parameters of the feedback transformer and the matching transformer are

$$M = 1\mu H \quad (5.12)$$

and

$$\frac{N_p}{N_s} = \frac{282}{79} . \quad (5.13)$$

Substituting these values into (4.36) with $\omega = 2\pi(418)\text{sec}^{-1}$, we obtain a quartic equation in a_0 ,

$$a_0 + 5.404^{-3} a_0^3 + 3.727^{-4} a_0 - 2.571^{-13} = 0 . \quad (5.14)$$

The solution for a_0 is dominated by the last term in (5.14). It is $a_0 = 2.252^{-3}$. Using $a_0 = G_{fb} G_M$, the value of G_{fb} is 1.503^{-4} . This is 3.7 times the experimental value determined in (5.9).

When deviations of the parameter values of (5.11) to (5.13) are considered, the optimistic estimate of G_{fb} is slightly less than twice (1.7) the experimental value. For the simple modal equivalent model in Fig. IV-2, the agreement between these values is good. The experimental result confirms the theoretical basis used for the feedback design, thus fulfilling the aim of the experiments.

D-2 NOISE OF FEEDBACK

Equation (4.19) gives the condition under which feedback damping is advantageous compared to damping by dissipative mechanisms. The two schemes are compared using the noise each produces at the sidebands as the criterion.

For the experimental circuit designed and used in the previous section, the feedback transfer N_f is

$$N_f = \frac{\omega M}{R_L} \quad (5.15)$$

where M is the mutual inductance of the feedback transformer, and R_L is the load of the voltage-to-current converter. For the feedback circuit at the resonant frequency, N_f is 5.25×10^{-6} . Under the same circumstances, the equivalent resistance feedback at minimum Q is $R_{eq} = 1.036 \text{ m}^{\circ}$ at the low frequency band. Equation (5.9) is used. Now from (4.15), we need only know R_f to determine N_p . R_f must be considered as the equivalent resistor in the feedback path that generated all the noise in the feedback circuit. The noise produced by the feedback is

$$\langle v_n^2 \rangle = 4kT N_f^2 R_f \Delta f \quad (5.16)$$

which is part of (4.17).

The noise of the SQUID at low frequency is given by manufacturer's data as

$$[\langle v_n^2 \rangle / \Delta f]^{\frac{1}{2}} = 1.44 \mu\text{V}/\sqrt{\text{Hz}} \quad (5.17)$$

It is assumed that the circuits in the feedback path are well designed and have a voltage noise

$$[\langle v_n^2 \rangle / \Delta f]^{\frac{1}{2}} = 0.03162 \mu\text{V}/\sqrt{\text{Hz}} \quad (5.18)$$

per stage. This is a rather simplified assumption but should suffice for

this discussion. Using the stage gains of the experimental circuit, the voltage noise due to SQUID noise feedback is

$$[\langle V_n^2 \rangle / \Delta f]^{\frac{1}{2}} = 0.1850 \text{ pV}/\sqrt{\text{Hz}}. \quad (5.19)$$

Equating (5.16) and (5.17), and using $N_f = 5.26^{-6}$, the value of R_f is

$$R_f = 74.96 \text{ k}\Omega \quad (5.20)$$

at 4 K. Using (4.15), we have

$$N_p = \frac{R_{eq}}{N_f R_f} = 3.51^{-5}. \quad (5.21)$$

Thus N_p is greater than N_f , justifying the use of feedback. However, the difference is not very large. It is due to the large R_f introduced by the feedback circuit. At the level of feedback gain in the circuit, the amplifier's noise dominated.

The power spectra of the accelerometer with and without the feedback circuit are determined using digital technique. The data are sampled and stored using the SPASMADAM (semi-portable data recording device), and later fast Fourier transformed in a PDP-11 computer. The increase in sideband noise is not evident as the resolution of the system is not high enough. Noise peak due to resonance is suppressed by 35 db. Unfortunately, noise peaks due to harmonics of the power frequency are introduced by the feedback. It is felt that with proper care, the performance of the circuit can be drastically improved.

We conclude that to improve the dynamic stability of the accelerometer system using SQUID as the detector, feedback damping of the resonant oscillations is necessary.

E. GRAVITY GRADIENT GENERATORS

To test the cryogenic gradiometers, a detectable gravity gradient signal must be produced. Since the resolution of the test gradiometer is expected to be low (50 E), a periodic signal is preferred. Standard methods of synchronous detection may then be used to process the output of the gradiometer. One of these methods is signal averaging whereby repetitive outputs are added to reduce noise.

Three methods of signal generation are considered. A mass ball (50 kg) at the end of a piano wire swinging as a pendulum is used for the first two methods. The ball is swung to and from the gradiometer which lies in the plane of the swing. Alternatively, the ball is swung across the gradiometer with the plane of the pendulum a given distance from the gradiometer. Lastly, a mass quadrupole can be rotated to generate the required signal. The gradient generated by each method will be derived in the subsequent section.

E-1 Planar Swing

The sensitive axis of the gradiometer is vertical. The coordinates of the planar pendulum system are given in Fig. V-14 with vector notations. Thus the vector from the center of the ball to the center of the gradiometer is

$$\bar{R} = \bar{H} + \bar{d} - \bar{L} = \begin{bmatrix} -d - L \sin \theta \\ 0 \\ -H + L\omega\theta \end{bmatrix}. \quad (5.22)$$

Assuming that the baseline of the gradiometer is small, the acceleration due to the ball at point 1 is

$$\hat{a}_1 = \hat{a}_0 + \bar{\Gamma} \cdot \bar{\Delta R} \quad (5.23)$$

where $\bar{\Delta R}$ is the vector from the center of the gradiometer to the upper proof mass. With the sensitive axis vertical, $\bar{\Delta R}$ is

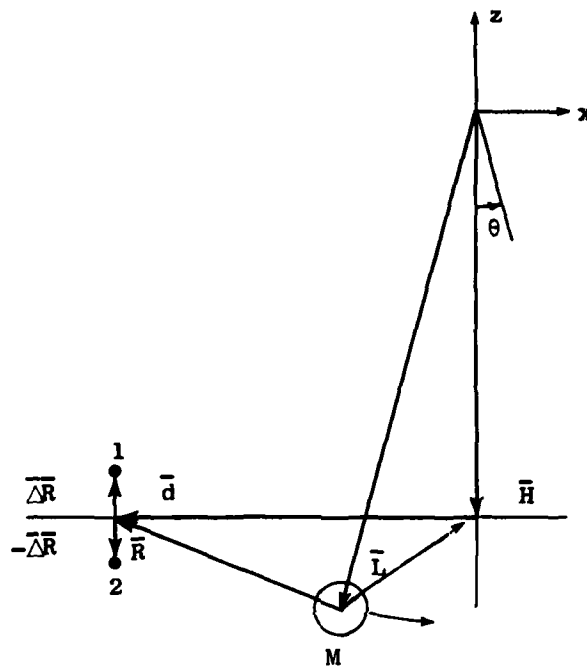


FIG. V-14 VECTOR DIAGRAM OF "IN-OUT" PENDULUM SWING. The pendulum is swinging in the x, z plane. The gradiometer is placed at $(-d, 0, 0)$ in this coordinate frame. The position vectors, \bar{L} and \bar{R} are a function of time.

$$\overline{\Delta r} = s\hat{k} \quad (5.24)$$

and

$$\bar{\Gamma} = \frac{MG}{R^3} (\hat{i} - 3\hat{R}\hat{R}) . \quad (5.25)$$

where G is the constant of gravitation, M is the mass of the ball, \hat{i} is the idem vector, and \hat{R} is the unit vector of \bar{R} . Similarly,

$$\hat{a}_2 = \hat{a}_0 - \bar{\Gamma} \cdot \overline{\Delta R} . \quad (5.26)$$

Hence the gradient produced along the sensitive axis is

$$G_z = \frac{\hat{a}_1 - \hat{a}_2}{2s} \cdot \hat{k} = \hat{k} \cdot \bar{\Gamma} \cdot \hat{k} . \quad (5.27)$$

Substituting (5.25) into (5.27) and simplifying, we have

$$G_z = \frac{MG}{R^3} \left[-1 + \frac{3}{R^2} (L \cos \theta - H)^2 \right] \quad (5.28)$$

where R is the amplitude of the vector given in (5.22). To second order in θ with θ small, it is

$$R^2 = R_0^2 + 2Ld\theta + LH\theta^2 \quad (5.29)$$

where

$$R_0^2 = (L - H)^2 + d^2 . \quad (5.30)$$

For L approximately equal to H , (5.28) can be simplified to

$$G_z = \frac{GM}{d^3} \left[-1 + 3 \frac{L}{d} \theta - 6 \left(\frac{L}{d} \right)^2 \theta^2 + \dots \right] . \quad (5.31)$$

For a swinging pendulum,

$$\theta = \theta_0 \sin \omega t . \quad (5.32)$$

Thus the gradient sensed by the gradiometer with its sensitive axis vertical is

$$G_z = -\frac{GM}{d^3} [1 + 3\beta_0^2 - 3\beta_0 \sin \omega t - 3\beta_0^2 \cos 2\omega t + \dots] \quad (5.33)$$

where

$$\beta_0 = \frac{L}{d} \theta_0. \quad (5.34)$$

Note that when $\beta_0 \approx 1$, the twice-frequency signal has the same magnitude as that of the once frequency.

Using the same arguments, the gradient sensed by the gradiometer with its sensitive axis horizontal is

$$\begin{aligned} G_x &= \hat{i} \cdot \bar{f} \cdot \hat{i} \\ &= 2 \frac{GM}{d^3} [1 + 3\beta_0^2 - 3\beta_0 \sin \omega t - 3\beta_0^2 \cos 2\omega t + \dots]. \end{aligned} \quad (5.35)$$

The signal along the horizontal is twice the magnitude of that along the vertical. There is significant gradient component along the y coordinate axis at the site of the gradiometer since $\hat{j} \cdot \bar{R} = 0$.

E-2 Symmetric Swing

The gradiometer is placed symmetrically with respect to the swing of the pendulum, a distance d from the plane of the swing. The distance from the point of support of the pendulum to the center of the gradiometer is H . The length of the pendulum is L , and R is the instantaneous center-to-center distance from the ball to the gradiometer. The coordinates system of this set-up is given in Fig. V-15 where the plane of the swing is the y, z plane.

Summing the vectors, the vector \bar{R} is

$$\bar{R} = \bar{H} + \bar{d} - \bar{L} = \begin{bmatrix} -d \\ -L \sin \theta \\ L \cos \theta - H \end{bmatrix}. \quad (5.36)$$

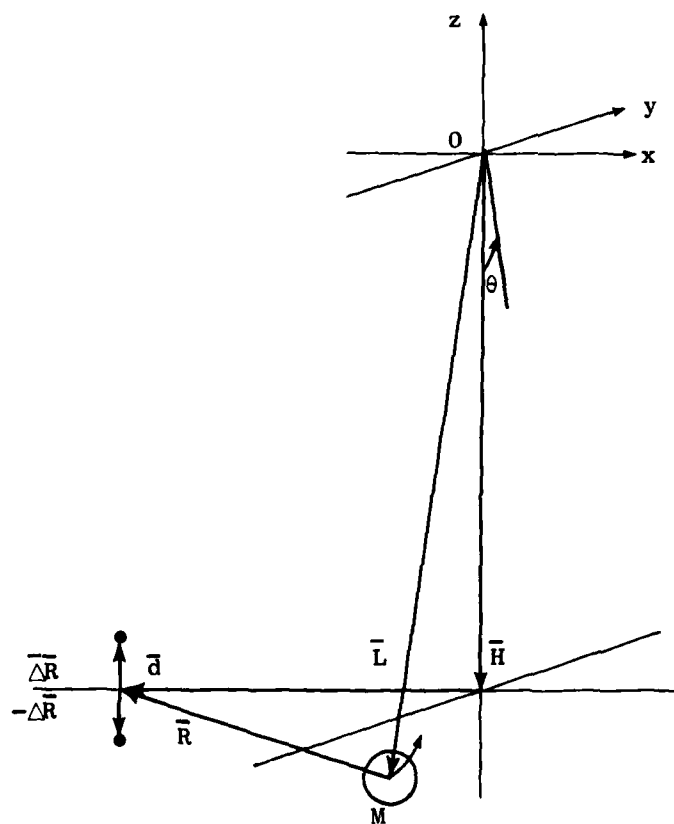


FIG. V-15 VECTOR DIAGRAM OF CROSS PENDULUM SWING.
 The plane of the pendulum swing is the y, z plane. The gradiometer is placed in the x, z plane at a distance d from the y, z plane.

With the sensitive axis vertical, the gradient sensed by the gradiometer is given by (5.27). In this case, the magnitude of the vector R is, to second order in θ ,

$$R^2 = R_0^2 + LH\theta^2 \quad (5.37)$$

where again, $R_0^2 = (L - H)^2 + d^2$.

Substituting and simplifying, the gradient at the gradiometer along the vertical axis is

$$G_z = -\frac{GM}{d^3} \left(1 - \frac{3}{4} \beta_0^2 + \frac{3}{4} \beta_0^2 \cos 2\omega t \right) \quad (5.38)$$

where β_0 is given as per (5.34). The most significant aspect of (5.38) is the absence of the term of the fundamental frequency. This is very advantageous as most noise produced by the pendulum are of the fundamental frequency. This allows for better identification of the gradient. It may be noted that the coefficient of $\cos 2\omega t$ term in (5.38) is four times smaller than that of (5.33). However, the distance d here can be significantly smaller than that in (5.33). For d here, about half of the planar swing system, the gradient signal is about eight times as large.

If the sensitive axis of the gradiometer is set horizontal, the gradient produced by the pendulum is either

$$G_x = \hat{i} \cdot \bar{r} \cdot \hat{i} = \frac{GM}{d^3} (2 - 3\beta_0^2 + 3\beta_0^2 \cos 2\omega t + \dots) \quad (5.39)$$

or

$$\begin{aligned} G_y &= \hat{j} \cdot \bar{r} \cdot \hat{j} \\ &= \frac{GM}{d^3} \left(-1 + \frac{9}{4} \beta_0^2 - \frac{9}{4} \beta_0^2 \cos 2\omega t + \dots \right) \end{aligned} \quad (5.40)$$

or a combination thereof.

E-3 Mass Quadrupole

Two identical balls are attached to the ends of a bar and the dipole formed is rotated to produce the required signal. The coordinate system for the analysis is given in Fig. V-16.

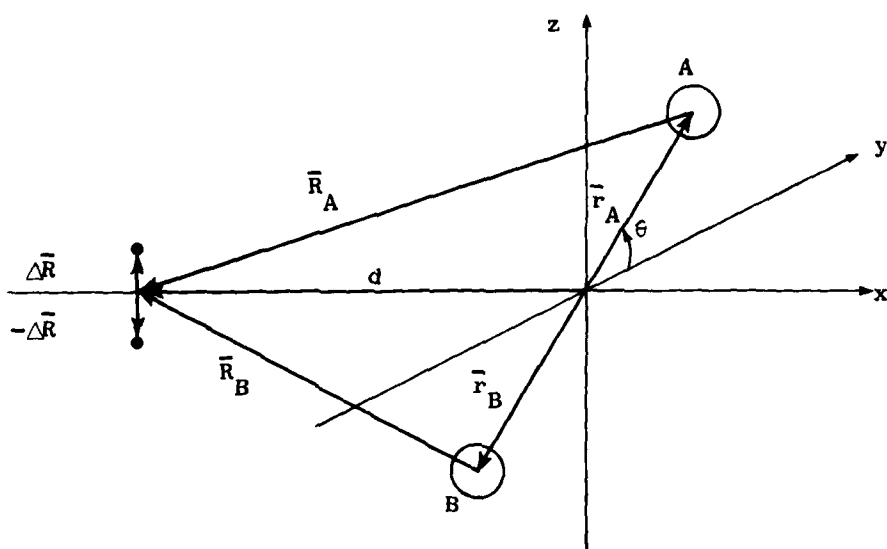


FIG. V-16 VECTOR DIAGRAM OF ROTATING ARM. The plane of the rotation of the demb-bel is the y,z plane. The gradiometer is placed on the x axis at a distance d from the origin of the coordinate system.

The vector \bar{R}_A is

$$\bar{R}_A = \bar{d} - \bar{r}_A = \begin{bmatrix} -d \\ -r \cos \theta \\ -r \sin \theta \end{bmatrix}. \quad (5.41)$$

Similarly, that of \bar{R}_B is

$$\bar{R}_B = \begin{bmatrix} -d \\ r \cos \theta \\ r \sin \theta \end{bmatrix}. \quad (5.42)$$

With the sensitive axis of the gradiometer vertical, it is readily shown that

$$G_z = \hat{k} \cdot (\bar{F}^A + \bar{F}^B) \cdot \hat{k} \quad (5.43)$$

where

$$\bar{F}^A = -\frac{MG}{3} (1 - 3\hat{R}_A \hat{R}_A)$$

and \bar{F}^B has the identical form except for \hat{R}_B replacing \hat{R}_A . Simplifying (5.47), we obtain

$$G_z = \frac{MG}{5} (-2R^2 + 3r^2 - 3r^2 \cos 2\omega t) \quad (5.44)$$

where ω is the angular velocity of the rotating arm. By the same arguments, the horizontal components of the gradient are

$$G_y = \frac{MG}{5} (-2R^2 + 3r^2 + 3r^2 \cos 2\omega t) \quad (5.45)$$

$$G_x = \frac{MG}{3} (-2 + 6d^2). \quad (5.46)$$

Note that the x component is a constant and the y, z components have no fundamental frequency term. As mentioned earlier, this is advantageous when noise is considered. In (5.44) and (5.45), the coefficient of the $\cos 2\omega t$ term is

$$A_2 = \pm \frac{3MG}{R} r^2 \quad (5.47)$$

but

$$R^2 = r^2 + d^2 \quad (5.48)$$

where d is typically made as small as possible, the limit being structural constraints. Thus expression (5.47) can be optimized by choosing r given d . We have

$$r_{\text{opt}} = \sqrt{\frac{2}{3}} d \quad (5.49)$$

With this value for r , (5.44) becomes

$$G_{z,\text{opt}} = \frac{MG}{d} \left(\frac{3}{5}\right)^{5/2} \left(-\frac{4}{3} - 2 \cos 2\omega t\right) \quad (5.50)$$

A similar expression for the optimal value of G_y can be obtained.

Table V-4 compares the three systems of generating gradients using the gradient along the z axis as a criterion.

Table V-4
COEFFICIENTS OF THE HARMONIC COMPONENTS OF THE GRADIENT GENERATORS

G_z	$\omega \left(x \frac{MG}{d^3}\right)$	$2\omega \left(x \frac{MG}{d^3}\right)$
Pendulum In-Out	$3\left(\frac{L\theta_0}{d}\right)$	$3\left(\frac{L\theta_0}{d}\right)^2$
Pendulum Across	0	$\frac{3}{4}\left(\frac{L\theta_0}{d}\right)^2$
Rotating Arm	0	$2\left(\frac{3}{5}\right)^{5/2}$

Note that for $L\theta_0/d$ close to unity, the fundamental and the twice frequency component for the first system are of comparable magnitude. The next two systems are preferred since the signals produced would be spectrally separated from the noise generated by the motions. Since the value of d in the second system is about half that of the first, the signal strength produced is close to eight times that of the first and six times that of the third in practice for the same M . Thus the system where the pendulum swings across the gradiometer seems favorable. However, the frequency of the signal is still low, not easy to change, and not readily separated spectrally from other low frequency noise. For our future tests, a rotating mass quadrupole is built.

Most of our initial testings of the gradiometer are performed with the signals generated by the first method. This is done primarily for convenience.

A photograph of the mass quadrupole gravity gradient generator is shown in Fig. V-17.

F SUMMARY

The cryogenic accessories of the gravity gradiometer developed during the research have been described. The ultra-low resistor developed for scale factor matching works well. High current density joints have been developed with probability of success being about 0.9.

The 'cold' damping concept has been demonstrated successfully using a simple circuit. Q was reduced significantly without introducing proportionally higher thermal noise.

Three simple means of producing gravity gradient signals for calibration of the gradiometer are compared. The mass quadrupole is preferred since it provides greater flexibility. Both systems have been built and employed experimentally.

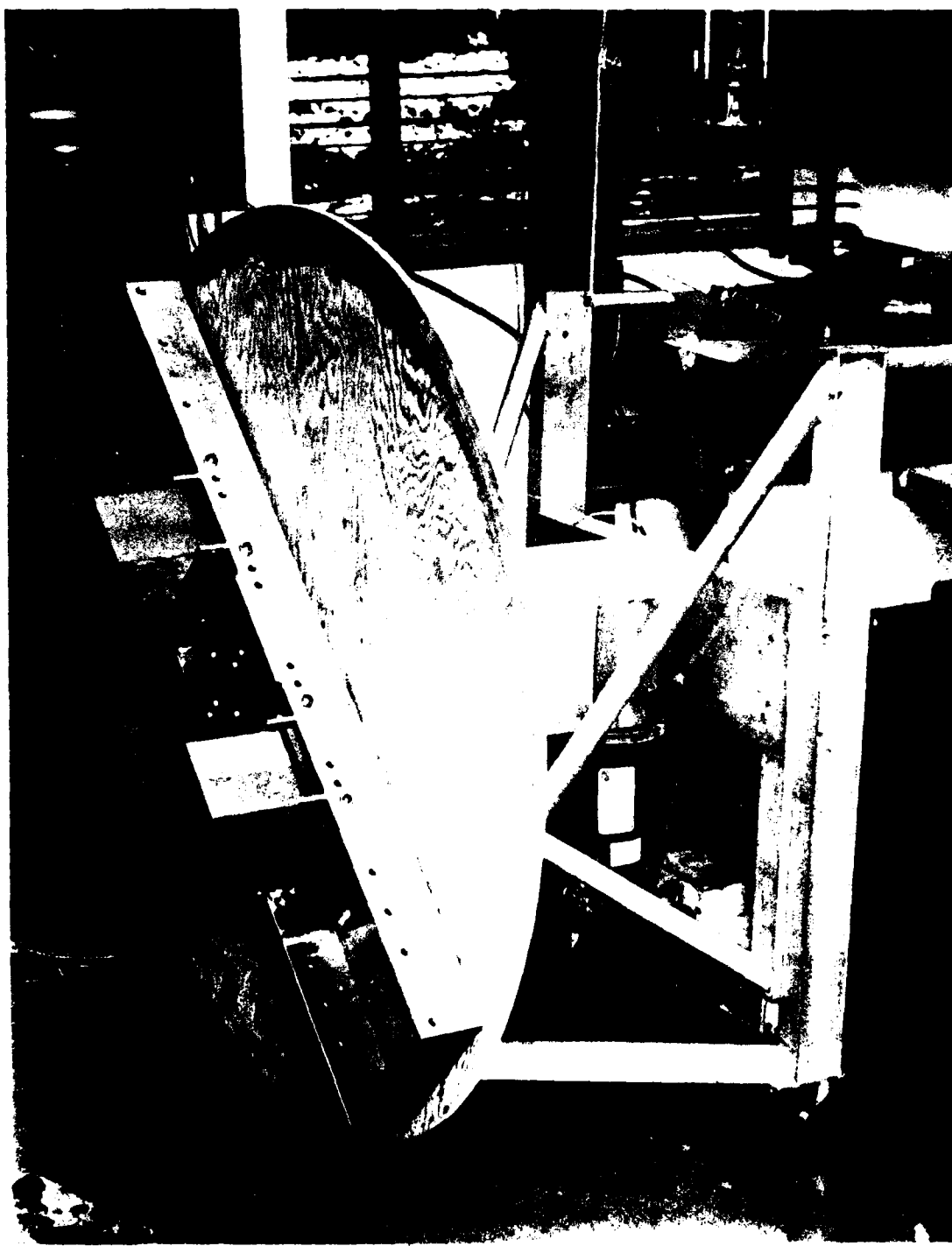


FIG. V-17 THE MASS QUADRUPOLE GRAVITY GRADIENT GENERATOR

Chapter VI

TESTING OF CRYOGENIC GRAVITY GRADIOMETER

The current differencing gravity gradiometer (CDGG) has been tested in a series of experiments performed over the past three years. The experiments were performed by the author in close cooperation with H.J. Paik, T. Orlando, and E. Mapoles, all of the Physics Department at Stanford University. The experimental results of the tests of the CDGG will be discussed here. Those of the displacement differencing gravity gradiometer (DDGG) which is briefly discussed in Ch. III will be reported in Mapoles' dissertation (to be published).

A. EXPERIMENTAL SETUP

A-1 Cryogenic Space

The cryogenic space for the experiment is the interior of a cylindrical copper vacuum can immersed in liquid helium. The helium is stored in a helium-vapor-cooled nonmagnetic dewar manufactured by Cryogenic Associates, Inc. The helium space is 8 in. in diameter and 45 in. deep. The schematic of the dewar and the dewar insert is shown in Fig. VI-1. The bottom plate of the dewar insert is the cover for the copper can which is sealed using indium wire. Telemetry wires feed into the helium space through the 2 in. outer diameter stainless steel tubes and then heat-sunk by means of sapphire heat sinks attached to the cover. Aluminized mylar baffles are located inside the stainless steel tubes to reduce radiation heat loss. The earth's magnetic field is screened using three layers of mu-metal shields. A superconducting lead shield in the form of an open can is provided to attenuate any remaining field changes.

The gradiometer is suspended by a spring from the end of a rod which slides between guides and has two lockable positions. During balancing, the rod is raised so that the gradiometer is freely hanging. After the balancing has been accomplished, the rod is lowered so that the gradiometer is sitting squarely on the bottom of the can. Doing so

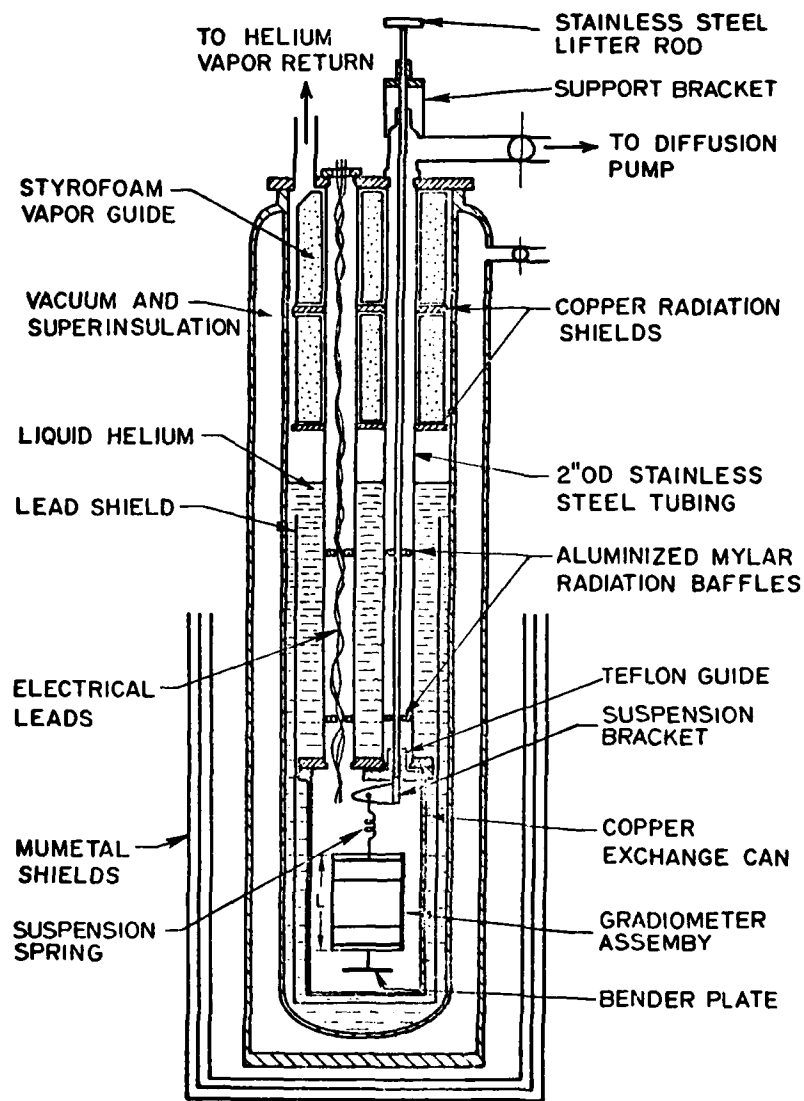


FIG. VI-1 CROSS-SECTIONAL VIEW OF THE EXPERIMENTAL SETUP. The gradiometer assembly is suspended from the suspension bracket by a spring which facilitate the shaking of the assembly by the bender plate.

reduces the swing motions of the gradiometer produced by the environment.

A typical cooling cycle for experiment is described here. The vacuum can is evacuated to a pressure of about $10\mu\text{m}$ Hg (micron). Outgassing from the more volatile materials limits the vacuum attainable. The pump is shut off and an exchange gas of helium is introduced through a valve to about 500 micron pressure. Liquid nitrogen is then transferred into the dewar to precool the interior to 77 K. The time required for this pre-cooling is typically four hours.

Given this lengthy preparation time, liquid nitrogen is transferred in the morning before the experiment to allow overnight cooling. Early the next morning, the excess liquid nitrogen is removed by generating high internal pressure through vaporization inside the dewar using a heater immersed in the liquid. The high pressure will force the remaining liquid nitrogen out through a tube inserted into the dewar to a level beneath the surface of the liquid nitrogen. Any remaining nitrogen would vaporize through the normal heat leak of the dewar and is vented.

When the pressure in the dewar becomes atmospheric, liquid helium is transferred slowly into the 77 K environment. The cooling from 77 K to 4 K requires another 2 to 3 hours. Enough helium is transferred to allow a 6-hour period for experimentation. Additional helium may be added as necessary.

After an experiment, the vacuum can is allowed to warm up slowly over a 24-hour period. Gradual warm-up is desirable to minimize thermal strain and water condensation (and absorption) on the porous components of the gradiometer.

With these cooling and warm-up times, the minimum turn-around time for an experiment is close to two days.

A-2 Shaker and Vibration Isolation

To excite the resonant mode of each diaphragm and to provide the common mode acceleration for the balancing of the gradiometer, a piezoelectric bimorph shaker is used. The bimorph is formed by cementing two PZT discs together. These discs have been polarized to contract radially

when a voltage is applied across its surfaces. If faces of the same polarity are cemented together, the composite plate will flex axi-symmetrically upon application of a sinusoidal voltage. The bender plate is mounted axially on to the gradiometer using a bolt.

The gradiometer assembly is suspended from the top plate of the vacuum plate by a stiff spring as shown in Fig. VI-2. The resonant frequency of the resultant spring-mass system is about 7 Hz. This simple arrangement allows the gradiometer to be shaken axially using the bender plate. The suspension also provides some measure of vibration isolation. Since the gradiometer has multiple degrees of freedom with respect to the suspension, portions of its motions could be rotational. These may be reduced by lowering the gradiometer so that it rests on the bottom of the can after it has been balanced. The helium dewar is then suspended from the ceiling using surgical tubing to provide additional isolation. Figure VI-3 shows the dewar suspended from the ceiling by the tubing. Three tubes attached to the ceiling at the corners of an equilateral triangle are used to provide stability. Also shown in the diagram

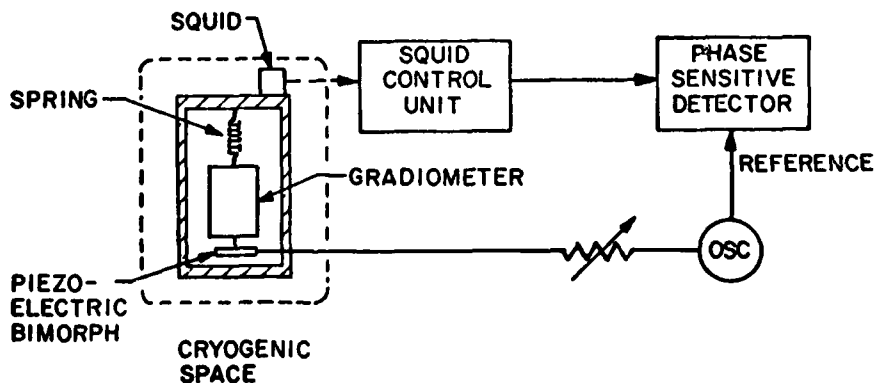


FIG. VI-2 BLOCK DIAGRAM OF THE BALANCING GRADIOMETER. The gradiometer is shaken using the piezoelectric bimorph. Its output is detected by the SQUID control unit. The phase sensitive detector would selectively detect the signal component that has the same frequency as the oscillator.

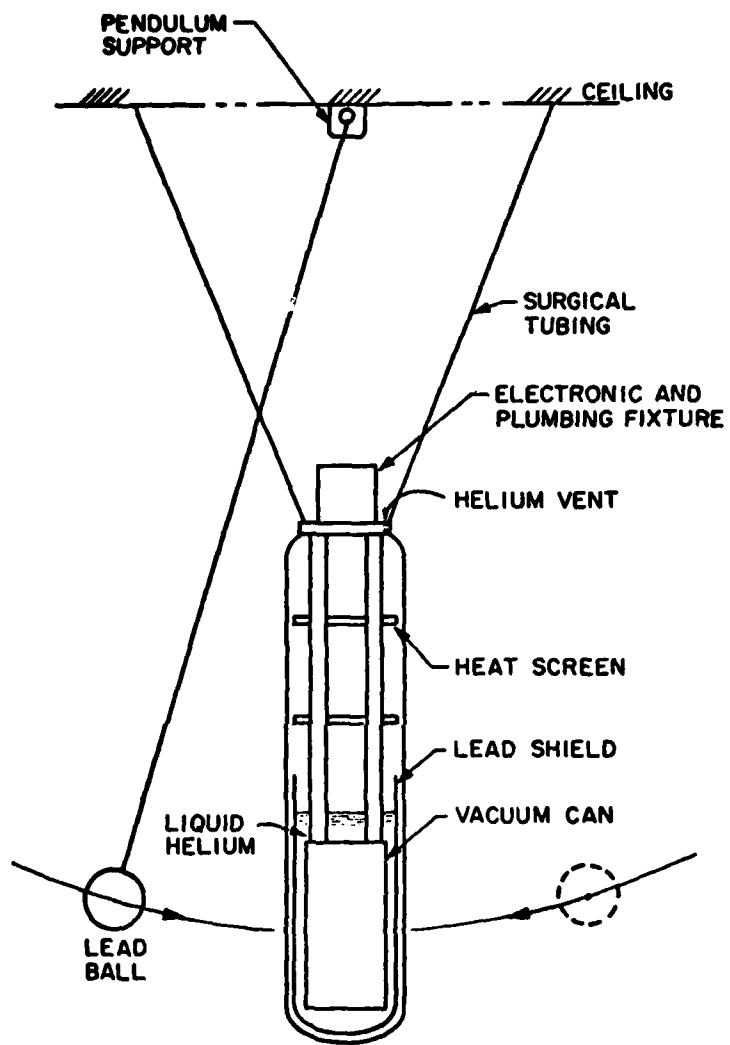


FIG. VI-3 GRADIOMETER CALIBRATION SETUP. Surgical tubing provides the vibration isolation of the test setup. The gradient generated by the swinging ball is the signal used in the calibration.

is the swinging pendulum used for generating gradient signal (Ch. V-C).

A signal generator is used to supply the voltage to the bimorph. As the frequency of the driving voltage approaches the resonant frequency of the diaphragm, the mechanical reluctance of the bimorph decreases. The sudden change in bimorph reactance is an easy means to determine resonant frequencies of the diaphragm as well as those of the whole assembly. Figure VI-4 shows the capacitance bridge used to drive the bimorph and to measure its response. The output of the bridge is connected to the vertical plates of an oscilloscope with the horizontal plates connected to the signal generator. The Lissajous figure on the oscilloscope provides a ready indication.

A typical procedure is described as follows. For a given bimorph, the value of C_3 is selected by trial and error such that the bridge can be roughly balanced as C_2 is adjusted over its range. The resistor R is adjusted to compensate for the resistance in the circuit. As the frequency of the driver signal source hits that of the diaphragm, the equivalent element in parallel with the bimorph becomes purely resistive. A sudden phase change and an accompanying ringing of the Lissajous figure will characterize a resonant mode.

Using this procedure, the modal frequencies for different values of current stored in the accelerometer are determined. A typical plot is shown in Fig. VI-5.

A-3 Persistent Current Storage and Adjustment

The construction of the CDGG is described in Ch. V-A. Figure V-2 showed a sketch of the assembled gradiometer. A cup-shaped aluminum structure is bolted onto the assembly over the matching transformer. An eye bolt is mounted centrally on the cup to suspend the assembly. Most of the experimental results reported in the next section were performed using a high frequency (850 Hz) diaphragm pair. The last experimental

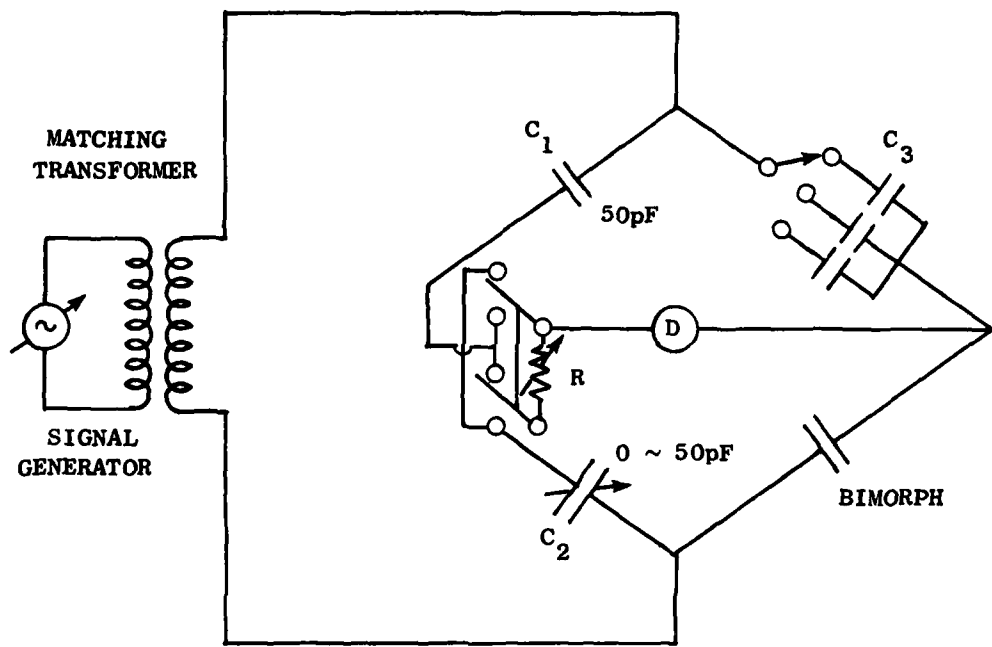


FIG. VI-4 CAPACITANCE BRIDGE TO DETECT RESONANCES OF BIMORPH [courtesy H. Paik]. The matching transformer provides impedance matching between the signal generator and the capacitance bridge. The capacitance of the proper range for a given bimorph is selected by the switch. A balance is indicated by the ringing in the detector as the frequency of the generator is changed slowly.

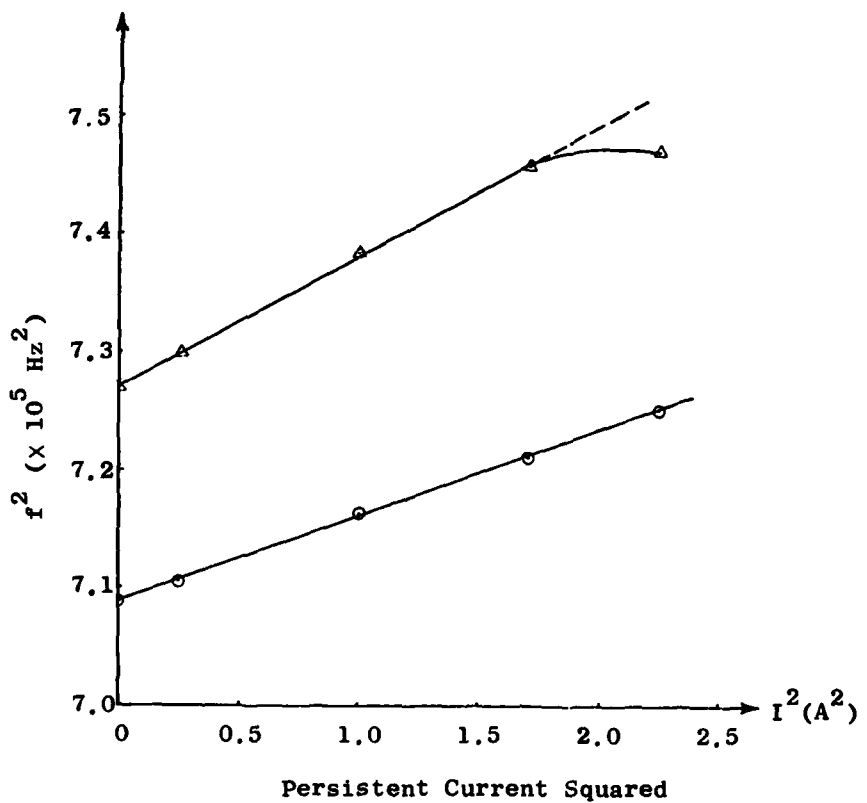


FIG. VI-5 SHIFTS IN THE RESONANT FREQUENCY OF THE NIOBIUM DIAPHRAGM. The deviation of the upper plot from the straight at higher values of the stored current is an indication that the current actually stored in the loop is less than the current driven through the coil. Flux penetration occurs at much higher current levels.

run made use of the low frequency (50 Hz) loaded diaphragm pair. The sketch is identical with Fig. V-2 with the thin diaphragm pair shown replaced by the loaded diaphragms of Fig. III-3.

The schematic of the circuit connection of the CDGG was shown in Fig. III-9. A more elaborate circuit with charging leads and heater switches is given in Fig. VI-6. Leads A and B are two lengths of copper-clad niobium wires which are soldered to external current leads. The external leads are heat-sunk to the copper top-plate to minimize heat loss. All connecting wires are shielded either by the niobium enclosure of the gradiometer or lead strip lines.

There are two types of heat switches in the circuit: the high resistance switches denoted by H_i , and the low resistance switches, LH_i . When power is supplied to the heater element of the high resistance switch, no current will flow through it when there exists a superconducting path in parallel. On the other hand, when the low resistance heater is turned on, the R-L time constant of the circuit is about 2000 sec. The construction of these switches was described in Ch. V-A.

To 'charge' the persistent current loop, the heat switches H_1 and H_2 are used, either separately or in tandem. When both heaters are turned on, the charging current, supplied by an external source, will flow through A, L_{11} , L_{12} , L_{22} , L_{21} and B, in that order. Note that for a pair of identical accelerometers, the currents stored in the loop are such that output due to equal acceleration will be zero. When H_1 and H_2 are used singly, the same charging leads A and B can be used to charge either accelerometer to its deserved current level. During the charging process, H_3 is turned on to confine the charging current to its designated path as well as to protect the SQUID.

Equation (3.57) showed that the accelerometer pair of the CDGG can be balanced by adjusting the stored current ratio if their responses to common acceleration are unequal. Once the nominal persistent current is stored in the loops of the gradiometer, adjustment of the currents may be done using the appropriate low resistance current switch.

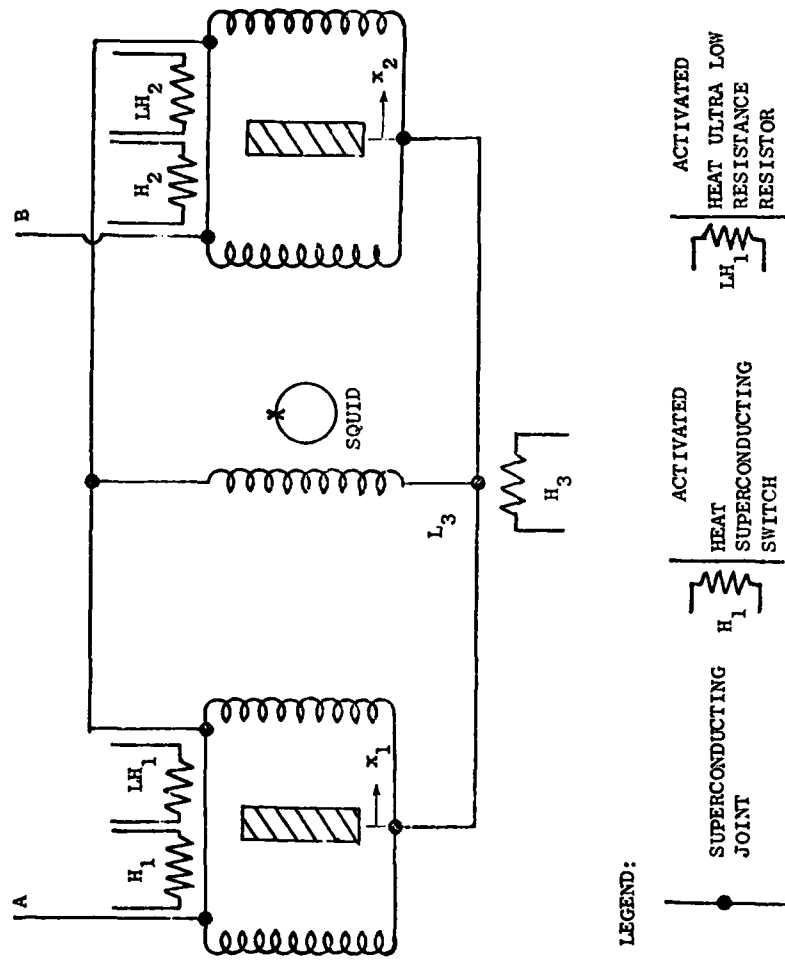


FIG. VI-6 PERSISTENT CURRENT CHARGING CIRCUIT. The charging leads are connected in such a way that the accelerometers are in a push-pull mode.

The procedure for adjusting current is described, using Fig. VI-4. We shall assume that the persistent current stored in loop L_{11} and L_{12} is to be reduced for balance. Heater H_3 is turned on first. This isolates accelerometer 1 from accelerometer 2 and protects the SQUID from circuit transients of the current adjustment. Ultra-low resistance LH_1 is then turned on and the current stored in loop L_{11} and L_{12} will decay with a time constant of about 2000 sec. After the pre-determined decay time, heater LH_1 is turned off and the persistence loop re-established. The time decay of the heater is about 1/2 sec for warm-up and 1 sec for cool-down. Thus the current may be adjusted to an accuracy of about 1/1000.

B. GRADIOMETER EXPERIMENTAL RESULTS

Most of the results reported in this dissertation are obtained from experiments using a pair of the high frequency (850 Hz) accelerometers described in Ch. V-A. When a different accelerometer pair is used, it will be specifically mentioned.

The frequency curve of each accelerometer as a function of the stored current is presented. The gradiometer balancing results are then presented. Lastly, the attempts to measure gradients using the balanced gradiometers are described.

B-1 Frequency-Current Relation

The experiment to determine the frequency shift of the accelerometer with respect to the persistent current also yields information regarding the state of the accelerometer. Any circuit faults such as breaks in coil windings and leads, faults in superconducting joints, etc., will be revealed. From the frequency shift the actual persistent stored (which can be different from the current carried by the circuit) is determined. Thus this experiment is performed for every cool-down of the gradiometer.

The determination of the frequencies of the diaphragm was described in VI-A-2 using the bender plate. Currents are stored using leads A, B, and the heater switches as given above. Figure II-12 showed the general

form of the experimental results although only the linear part of the curve is determined most of the time. The frequency variations of the two diaphragms as the current is changed was shown in Fig. VI-6.

The slopes of the straight line curves under the different conditions are given in Table VI-1.

Table VI-1
CHARACTERISTICS OF THE ACCELEROMETERS

Condition	Accelerometer 1	Accelerometer 2
Slope (Hz^2/A^2) H3 ON	8000	3800
I_{opt}	9.5	13.8
$S(\text{A/g})$	2.06	1.42

Two facts are noted in the results. The maximum current storable in Accelerometer 1 is only about 1.34 A. This is significantly below the targeted value of 5A. The problem probably lies in a poorly made joint. Using Eq. (2.32), the optimal currents for the accelerometers 1 and 2 are 9.5 A and 13.8 A respectively. Although the optimal currents are much higher than the value of the critical current of the diaphragm, the maximum sensitivity of the accelerometers is not attained. The maximum theoretical sensitivity is calculated using (2.34). Secondly, it is evident that the two accelerometers are quite different.

The frequency response of the two accelerometers was determined by Paik. They are given in Fig. VI-7. The setup given in Fig. VI-2 was used in the experiment. Persistent current of 1 A was stored in the accelerometer being measured with zero current in the other accelerometer. The gradiometer assembly was shaken using the bender plate which was driven by a sinusoidal voltage with a constant amplitude of 1.5 V p-p. The large peaks of the PSD at about 1150 Hz are due to the resonant response of the bender plate. The resonant frequencies of the diaphragms (about 850 Hz) were avoided. Note that the difference

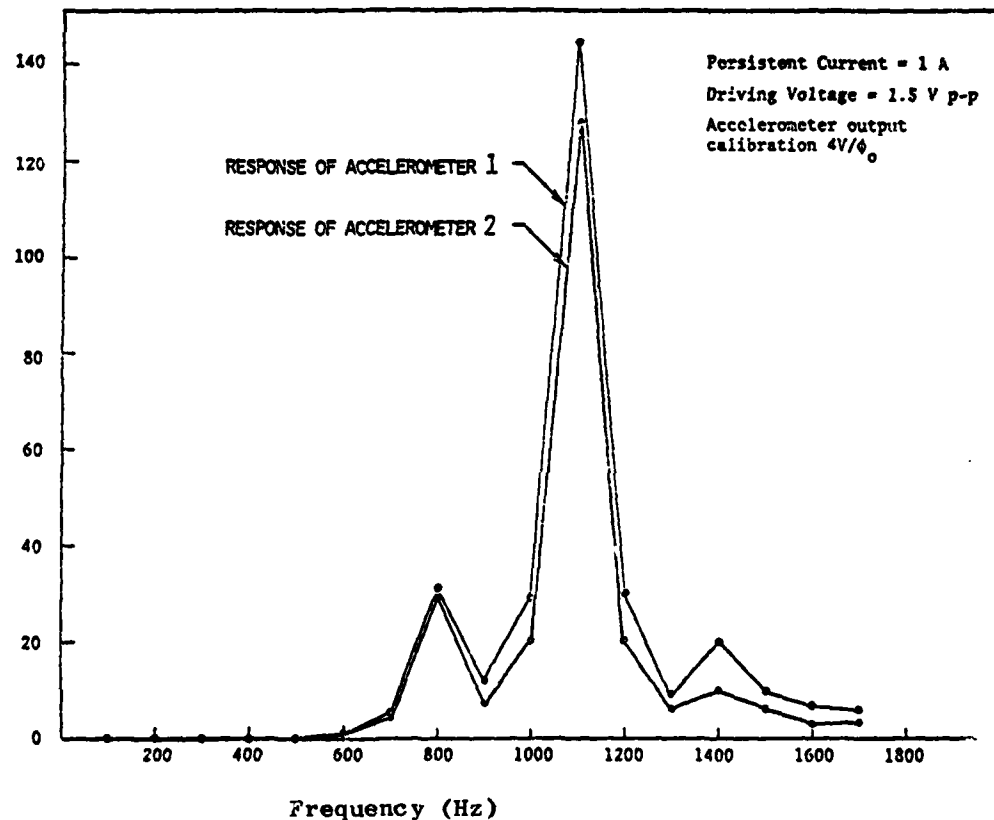


FIG. VI-7 FREQUENCY RESPONSE OF THE TWO ACCELEROMETERS IN CDGG. The peaks at 1150 Hz and 1400 Hz are due to resonances of piezoelectric vibrator.
 [from Paik]

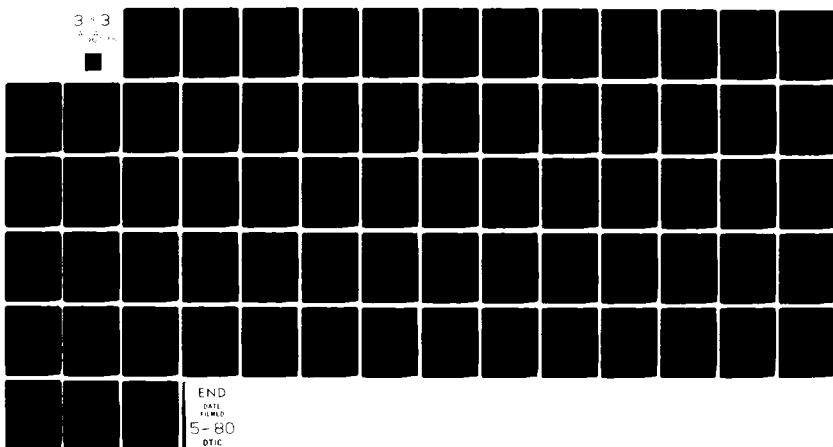
AD-A082 535 STANFORD UNIV CALIF GUIDANCE AND CONTROL LAB F/6 17/7
MODELING AND ERROR ANALYSIS OF A SUPERCONDUCTING GRAVITY RADIO—ETC(U)
AUG 79 K Y WANG AFOSR-76-2913

UNCLASSIFIED

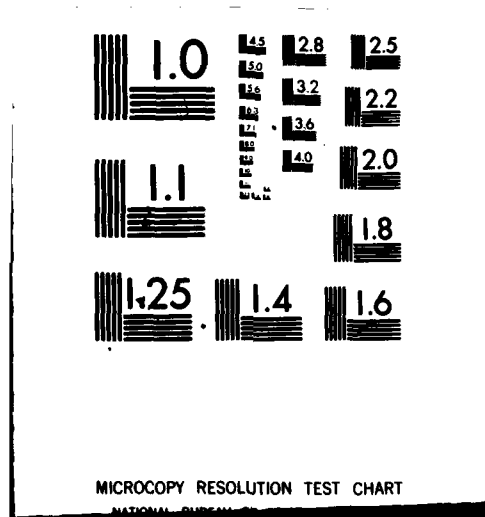
AFOSR-TR-80-0219

NL

3 x 3
AFOSR



END
DATE
FILED
5-80
DTIC



between the characteristics of the two accelerometers is not reflected in their PSD.

The theoretical minimum resolvable acceleration δa can be calculated using (2.41). With $d_0 = 10^{-4}$ m, $I_0 = 1.3A$, $L_s = 2\mu H$, $\omega_r = 2\pi(8.50)s^{-1}$, $k_x \approx 1$, $E_N = 2 \times 10^{-28}$ J/Hz, we have

$$\delta a = 3.27 \times 10^{-9} g. \quad (6.1)$$

The cryogenic accelerometer is very sensitive indeed.

B-2 Gradiometer Balancing

A major advantage of CDGG is that the unbalance between the accelerometers to a common mode acceleration can be nulled by adjusting the persistent currents. By this simple means the common mode rejection ratio of the gradiometer can be made very high.

The ideal vibration isolation requirement of the gradiometer in the measurement mode are set out in Ch. IV-a. In addition, the balancing of the gradiometer should be performed on a linear shaker which produces negligible errors. A platform that satisfies both requirements is by its own right a major undertaking and costly. The design of a shaker costing half a million dollars is given by Bell Aerospace [1978].

In our experiment, a simple spring-mass system with the piezoelectric vibrator is used as the shaking mechanism for the balancing of the gradiometer. It is the same setup used for determining the resonant frequencies. In this case, the SQUID is used to measure the resulting current flowing in coil L_3 (Fig. VI-6) as the assembly is shaken. The block diagram of the detection scheme is given in Fig. VI-2. The output of the SQUID is demodulated in the SQUID control unit. The output of the SCU (SQUID control unit) is fed into a phase sensitive detector built by Princeton Applied Research. The reference input of the phase sensitive detector is taken from the same oscillator that drives the bimorph. The steady-state output of the phase sensitive detector is the amplitude and phase angle of the component of the gradiometer output having the same frequency as the shaker. A built-in feature of the phase

sensitive detector also allows the tracking of the twice-frequency component in the SQUID output.

A typical balancing process is outlined here. Initially, the same currents are stored in the two accelerometers using leads A and B, and heaters H_1 , H_2 and H_3 (Fig. VI-6). A shaking frequency is selected based on the responses of the bender plate and the diaphragm when they are shaken. The lowest frequency which still provides a detectable output will be the frequency used in the experiment. For the experiment using the 850 Hz diaphragm pair, the shaking frequency is 200 Hz. Since the gradient calibration signal used has a very low frequency of $\frac{1}{2}$ Hz, it is very probable that the gradiometer will be unbalanced at this frequency.

After the amplitude and phase of the synchronous output are measured, the current in the more sensitive accelerometer is reduced and the process is repeated. Current reduction is achieved through slow energy dissipation in the ultra-low resistor switch. Using the output of the phase sensitive detector as the criterion, the currents in the accelerometers are adjusted to reduce the amplitude of the output. As the gradiometer becomes better balanced, the output signal of the phase sensitive detector becomes smaller. When the signal becomes difficult to track as the signal-to-noise ratio is decreased, the voltage of the bimorph is increased to produce a larger shaking motion. The process is repeated until the output starts to increase instead of continuing to decrease.

The results of one experimental run using the 850 Hz diaphragm pairs are given in Fig. VI-8. The output of the detector reaches a minimum of 1.3 volts after the current in loop 1 has decayed for an accumulated time period of 500 sec. Further changes in loop 1 produces greater unbalance. As shown in the figure, the resulting unbalance is reduced by decreasing the current in loop 2. The different output response times of the two loops are due to their different decay time constants. One amp is initially stored in the loops.

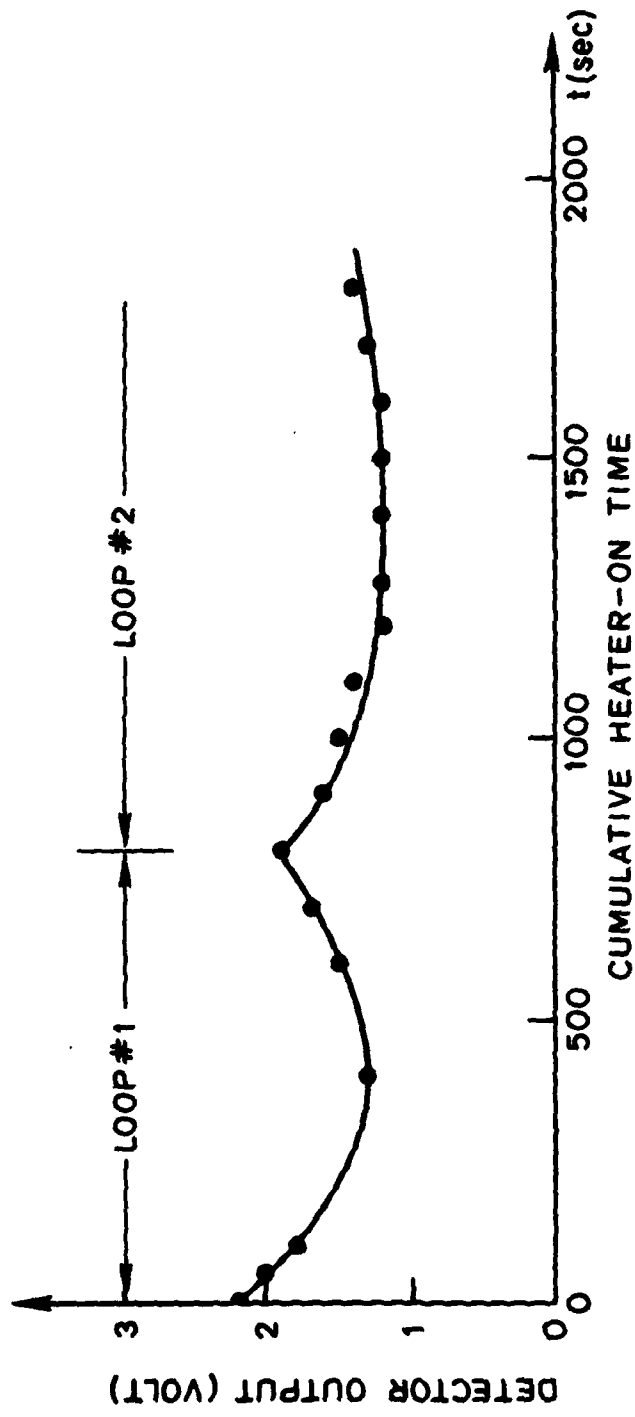


FIG. VI-8 BALANCING OF THE CURRENT DIFFERENCING GRAVITY GRADIOMETER (CDGG). The gradiometer output shows that balancing of the two accelerometers as the currents are adjusted. The heaters for the appropriate loops are used although the data are plotted against the cumulative on time of both heaters.

The SQUID used in this experiment is the toroidal point contact SQUID developed by Paik. The SQUID control unit is built by DEVELCO. The transfer function is $4.65 \text{ V}/\phi_0$ which has been determined in an earlier experiment.

After the gradiometer is balanced, its output power spectrum is measured using a Hewlett Packard spectrum analyzer (HP 3580A). The ramp tracking signal of the spectrum analyzer is used to drive the bimorph while the analyzer is sampling the output of the gradiometer. The results of the measurement are presented in Fig. VI-9(b). The point where the output of the gradiometer exceeds the dynamic range of the SQUID is indicated by the vertical arrow. The power peaks that occurred at 180 Hz, 300 Hz, and 600 Hz are the power density of the harmonics of the power line frequency. As a comparison, the power spectral density of a gradiometer with known slight unbalance (no current in accelerometer 1 and 0.1 A stored in accelerometer 2) is given in Fig. VI-10a. In the figure, the gradiometer was driven by the bender plate using the ramp tracking output of the analyzer as it is in Fig. VI-8b. The "noise" power spectra of the gradiometer determined with the drive of the bender plate cut off are given in Figs. VI-10a and b. The current stored in the accelerometers are the same as those in Fig. VI-9a. Figure VI-10a gives the power spectral density (PSD) from d-c to 50 Hz, while Fig. VI-10b covers the PSD up to 1 kHz. The switches setting of the analyzer are the same in the four plots.

When the gradiometer is balanced, the output is essentially flat to 650 Hz while a slightly unbalanced gradiometer shows an output magnitude increase starting at 300 Hz until the SQUID unlocks at 770 Hz. The improved linearity of the balanced gradiometer is demonstrated here. From these readings, it is estimated that a balancing of one part in 300 had been achieved.

B-3 Gradiometer Calibration

In this section, the laboratory setup to provide a calibration signal for the gradiometer is described. The calibration results using the gradiometer which has been balanced as described in Sect. B-2 are presented.

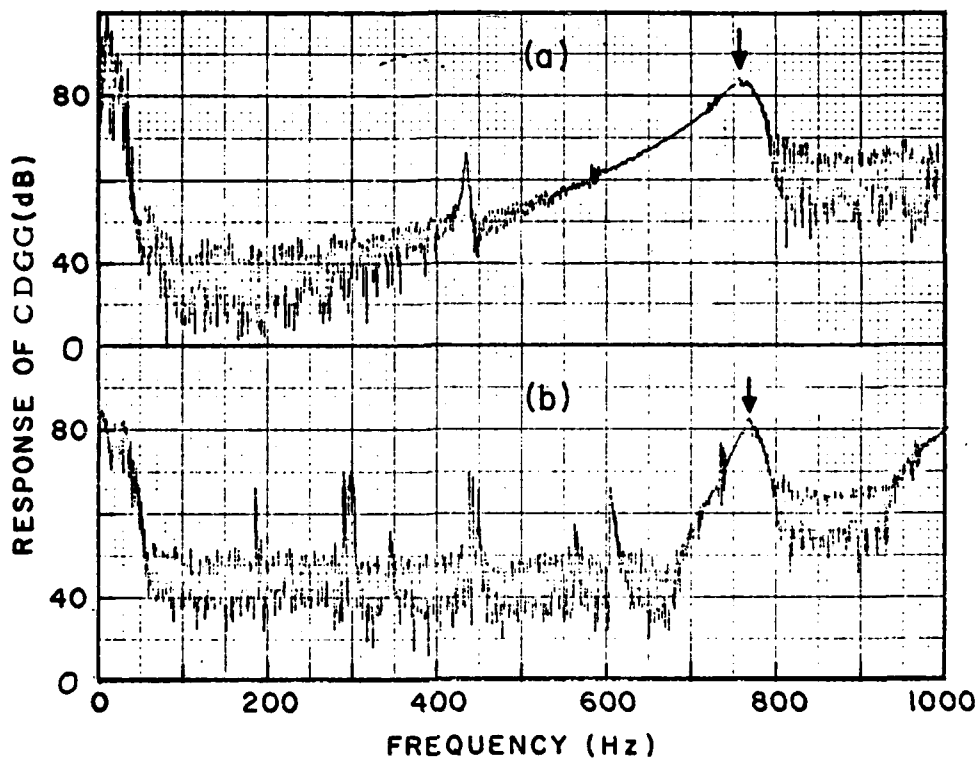


FIG. VI-9 FREQUENCY RESPONSES OF THE CDGG. In plot (a), the gradiometer is unbalanced. The off balanced condition was simulated by storing a small current, $I_1 = 0.1$ A while keeping $I_2 = 0$ A. Plot (b) shows the response of the CDGG balanced to 1 part in 10^3 at 200 Hz. In both cases, the large resonant response of the proof mass causes the magnetometer to unlock at 770 Hz which is indicated by the arrows. The background noise level around 40 dB corresponds to the wideband noise of the SQUID. As shown in plot (b), the common mode signal is suppressed over a wide frequency range, d-c to 700 Hz, when the gradiometer is balanced.

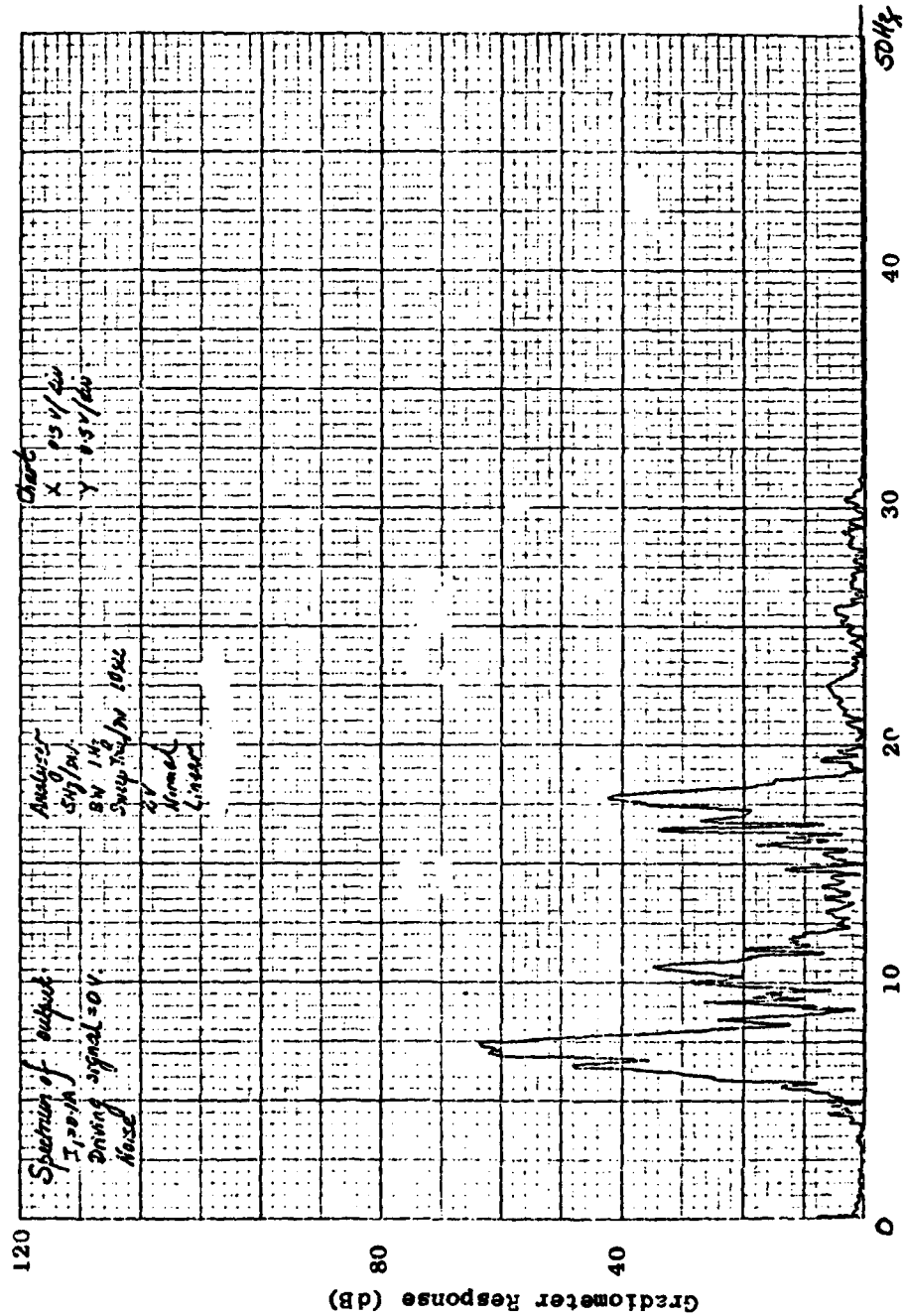


FIG. VI-10a NOISE OUTPUT OF THE GRADIOMETER AT REST WITHOUT CALIBRATION SIGNAL.
 A slight imbalance was simulated with $I_1 = 0.1A$ and $I_2 = 0A$. The peaks at 7.5 Hz and 18 Hz represent the vibrational modes of the suspension spring. These responses were driven by environmental noise.

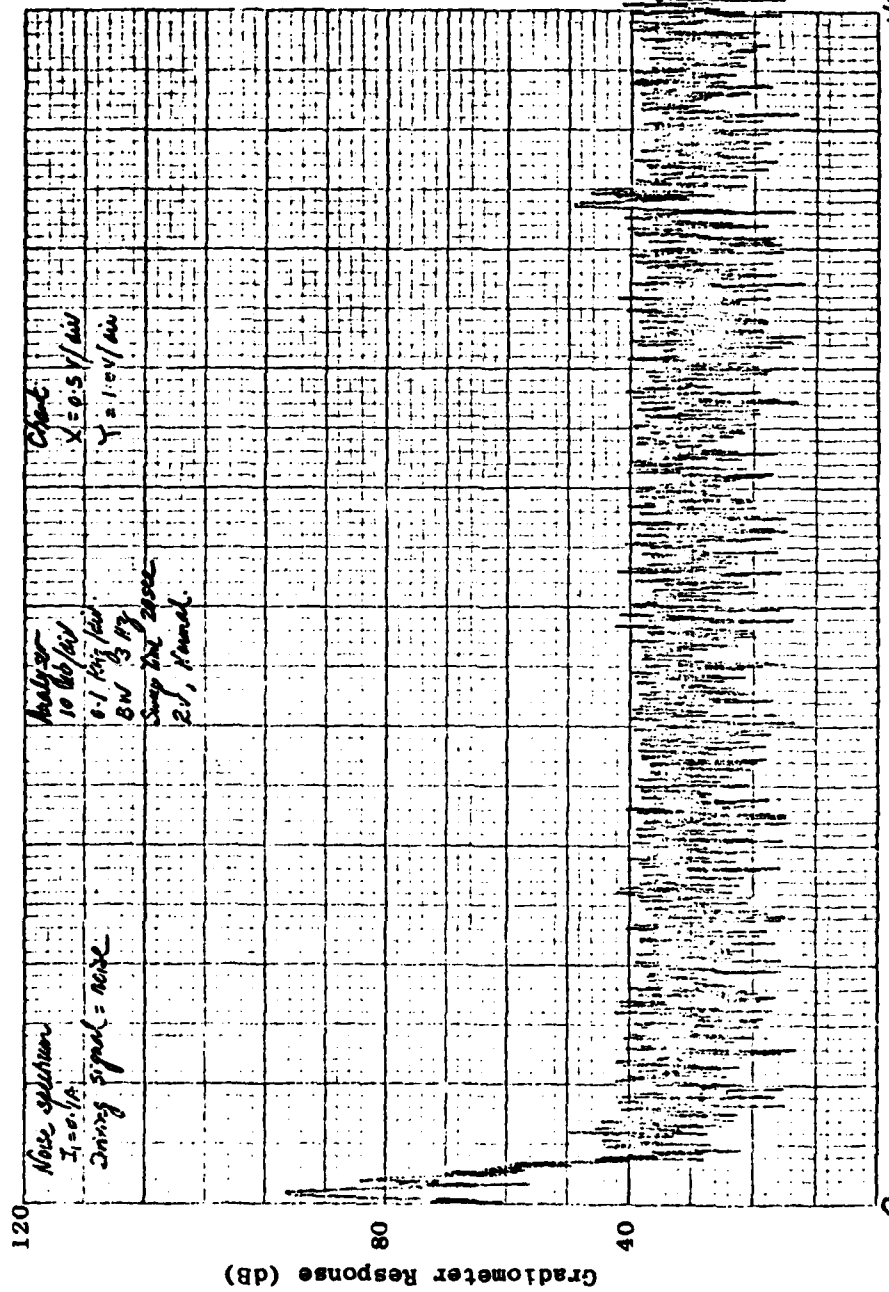


FIG. VI-10B NOISE OUTPUT OF THE GRADIOMETER AT REST WITHOUT CALIBRATION SIGNAL.
A slight unbalance was simulated with $I_1 = 0.1A$ and $I_2 = 0A$. The peaks at 7.5 Hz and 18 Hz represent the vibrational modes of the suspension spring. These responses were driven by environmental noise.

The two different processes to produce a calibration signal with a periodic cycle was discussed in Ch. V-C. At the time when the calibration experiment is performed, the rotating quadrapole is still only a design concept. The gradient signal is produced by a massive ball swinging at the end of a pendulum. The experimental setup was shown in Fig. VI-3. The pendulum swings in a plane freely about an axis supported by bearings which are mounted in a bracket. The bracket is fixed rigidly onto the ceiling. The helium dewar is suspended from the same ceiling using surgical tubings. By changing the points of suspension, the dewar may be positioned so that the ball may swing across or to and from it. These two modes are analyzed in Ch. V. The to-and-fro mode is used in the experiment and the ball is made of iron instead of lead as shown in Fig. VI-3.

The mass of the iron ball is close to 40 kg. The position of the ball is adjusted such that at the top of its swing, it is at the same level as the mid-point of the gradiometer and as close to the dewar as physically possible. The gradient signal may be calculated using (5.33). For the experimental setup, the maximum magnitude of the gradient signal is approximately 50 E. The expected waveform of the signal is given in Fig. VI-11 for a 10 cm baseline gradiometer. The waveform starts at the point when the ball reaches its lowest point of the swing and starts swinging towards the dewar. On the same plot is a phase-shifted output expected at the output of the SQUID control unit.

For the gradiometer balanced discussed in Sect. B-2 above, the resolution of the instrument is estimated to be about 50E. Even when the signal strength is at its greatest, it is barely resolved by the instrument. Fortunately, the swing of the pendulum is repetitive and regular. By adding the output signals repetitively, the noise can be reduced. When N replications of the output signal are added, the noise is reduced by a factor of \sqrt{N} if it is random and uncorrelated with the signal.

The output signals are added using a HP signal averager (HP 5480A). The averager is triggered by a pulse generated by a photo sensitive

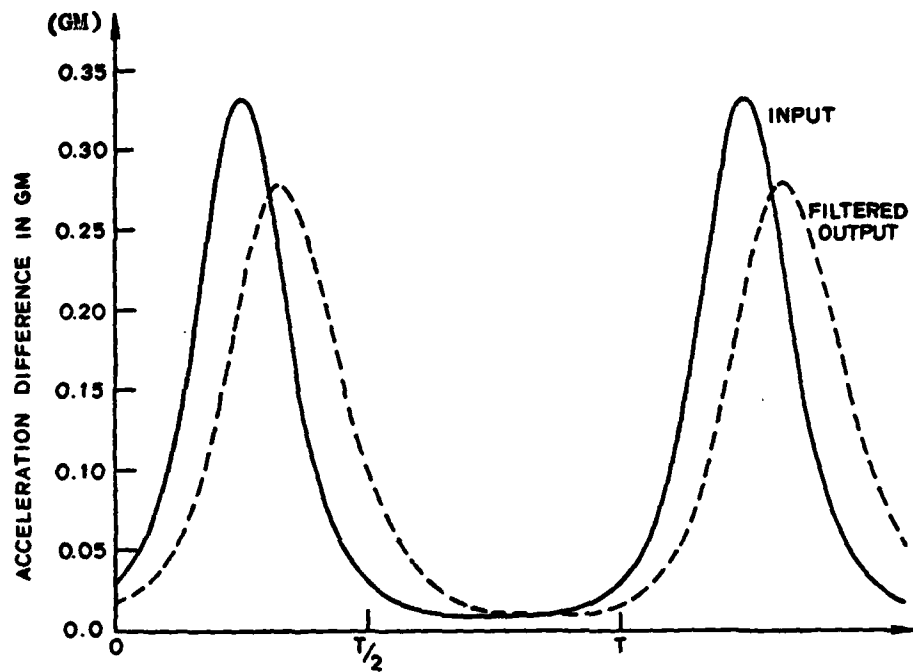


FIG. VI-11 GRADIENT SIGNAL OF THE SWINGING PENDULUM. The gradient signal produced at the gradiometer by the swinging pendulum is given in terms of GM . G is the universal gravitation constant, and M is the mass of the ball. The filtered output is the ideal signal one would expect to see at the output of the SQUID.

diode when the pendulum intersects a light beam at the lowest point of its swing. The averager then takes 256 samples of the signal at a 128 Hz rate. The digitalized samples are stored in memory of the sampler. When the next trigger pulse occurs, the sampled data are added to those in memory. After the $2N^{\text{th}}$ sample, where $N = 1, 2, 3 \dots N_p$, and 2^{N_p} is the total number of addition to be performed, the magnitude of the stored values are halved. Thus at the completion of the addition, the stored sample data are the average of the desired signal. This is the operation of the averager in the summation mode. The other functions of the averager will not be discussed.

Several experimental runs using the balanced gradiometer were recorded and averaged in the HP5480A. They are shown in Fig. VI-12. Unfortunately, the theoretical wave shape of Fig. VI-11 cannot be discerned.

Paik performed a manual averaging of these data and the results of his analysis are given also in Fig. VI-12. Using the rough estimate of the resolution of the gradiometer, the expected gradient signal due to the swinging ball is also plotted. Given the accuracies of the experiment, we may deduce that the common mode acceleration is not sensed by the gradiometer. This is to be expected as the balancing is done to about one part in 300, while a part in 1000 is the desired goal.

The calibration of the gradiometer is repeated twice and the results are similar to those presented here. Thus it is concluded that a detectable signal source will be provided and the sensitivity must be improved. A rotating quadrupole is designed and built. This device is capable of generating a gradient sensor of 40E at 5Hz. The high frequency improves the detectability very significantly. Efforts are also diverted to improve the design of an improved gradiometer, the displacement differencing gravity gradiometer.

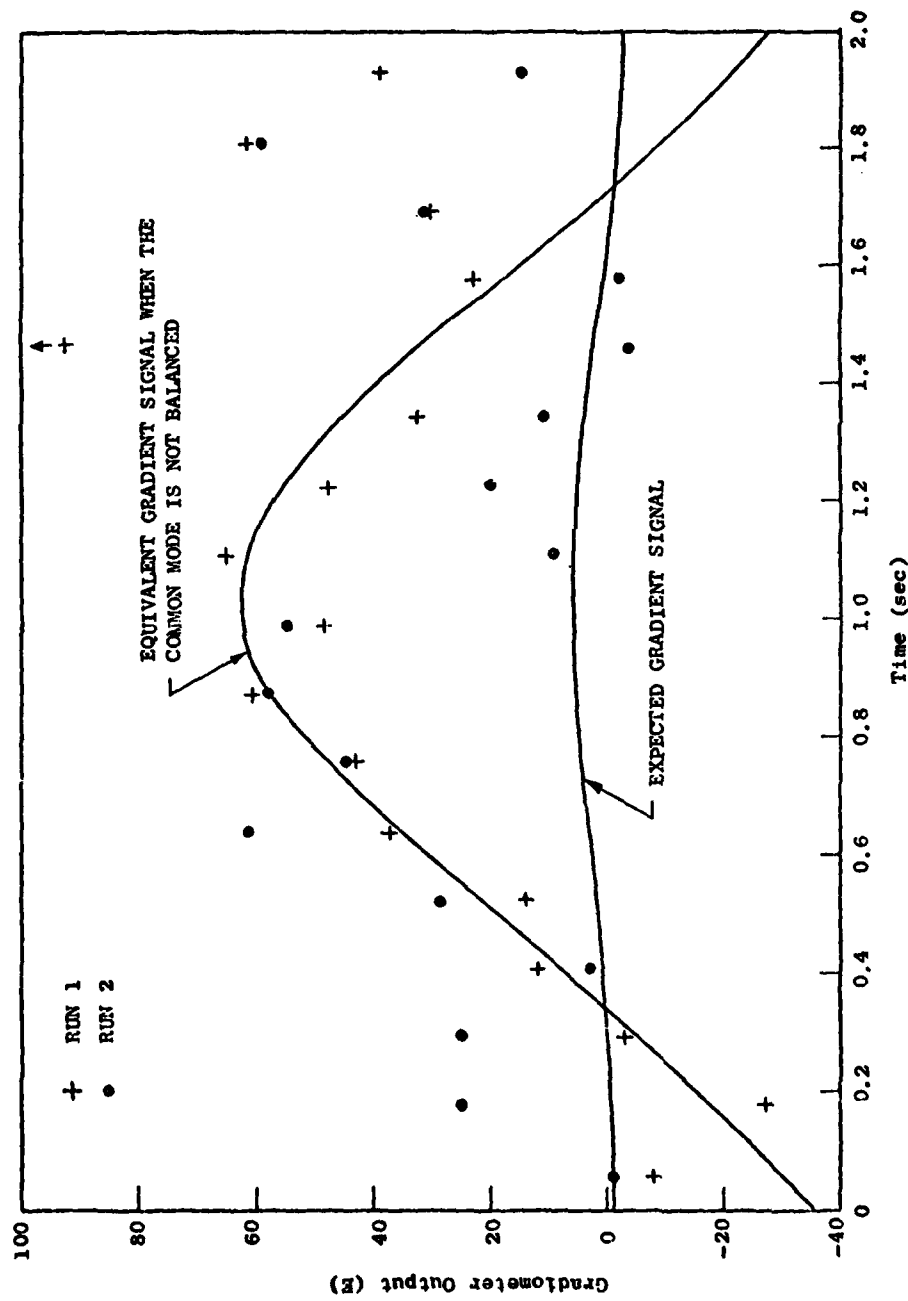


FIG. VI-12 RESPONSE OF CDGG TO A SWINGING PENDULUM IN A CALIBRATION EXPERIMENT.
 The agreement of the data with the common mode acceleration suggests that current was lost in one of the pickup coils [from Park].

C. DISCUSSION

The results of the various experiments performed with the current differencing gravity gradiometer are presented in the previous section. In this section, some conclusions derived from the experiments are discussed.

The major shortcoming of the present gradiometer is the limited sensitivity of the instrument. This is due to the high resonant frequency of the proof mass, high noise level due to poor balancing, and poor dimensional tolerances as a result of mediocre fabrication.

The sensitivity of high frequency diaphragms may be remedied by using loaded diaphragms as described in Ch. III-A. Despite repeated attempts to develop a procedure for the construction of a reliable, high current density joint, none has been found to be satisfactory. Twisting the wires together and clamping them remains the only reliable method.

As shown in Eq. (2.21), the output current flowing through the SQUID input coil is inversely proportional to the separation d , between the diaphragm and the coil. One of the reasons that d cannot be made smaller than the current value of 0.006 in. \sim 0.008 in. is the limit of fabrication. The planes of the coils and diaphragm are not exactly parallel to each other. Even if all mating surfaces are machined parallel, the current method of winding the pancake coil would not produce a perfectly aligned surface. Attempts to plane the finished coils on a lathe have not been successful. An alternative that may produce better coil is the technique of vapor deposition. Paul Worden of Stanford had produced some experimental coils using thin film deposition technique. His experience may be explored for future use. Since niobium cannot be soldered, the fabrication of a high current density joint to a thin film coil is a difficult problem.

At present, the method of reducing persistent current through decay in a resistor is done manually, and the accuracy is about 1 part in 2000. A target accuracy of 1 part in 10^5 is desired. To achieve this, elimination of noise and erroneous signal and feedback control of the current reduction in the calibration process is necessary. The first part

would be hard to do, requiring the installation of expensive vibration isolation platform and linear shaking mechanism. The second requires an on-line computer feedback control incorporating the characteristics of the resistors and heater turn-on time delay.

Chapter VII

CONCLUSIONS AND RECOMMENDATIONS

The mathematical model of the cryogenic gradiometer is developed in this research. Error sources of the instrument are identified. Based on the response of the gradiometer to background noise, an electronic damping scheme is implemented. The current differencing gravity gradiometer (CDGG) is designed, constructed, and tested. The model is validated by the experimental results.

A. CONCLUSIONS

The experimental results show that scale factors of the component accelerometers in the CDGG can be adjusted by changing the stored persistent currents. The currents are reduced through energy dissipation in a L-R network. Tighter control on the duration of energy decay is required to achieve the desired accuracy in the balancing of the gradiometer. A computerized decision scheme implemented in an adaptive feedback loop may be required. The results also show that as the gradiometer becomes better matched, its common mode rejection ratio improves significantly. The concept of the CDGG is thus shown to be correct.

The mathematical model of the CDGG is used in an effort to optimize the performance of the gradiometer. Changes in the size and dimensions of the diaphragm proof mass are considered. These efforts lead to the development of the centrally loaded diaphragm and its model. Operational limitations of the gradiometer are also identified, the most demanding of which is the vibration isolation required to reduce background noise. The high Q diaphragm transformed the ambient environmental noise into highly colored noise centered at the resonant frequencies of the diaphragms at the input of the SQUID. To prevent the system noise from exceeding the dynamic range of the SQUID, damping has to be introduced. Passive damping which increases thermal noise would eliminate most of the additional sensitivity of the cryogenic gradiometer. The idea of

electronic feedback damping has been conceived and successfully implemented using the model. The results of the feedback experiments have shown that there is an optimal feedback in the damping of the gradiometer.

Error sources of the gradiometer have been determined and their contributions incorporated into the model. The major error sources are fabrication, alignment, calibration, and rectification errors of the diaphragm. Errors due to angular motions of the gradiometer typically have twice the rotational frequency and can be separated spectrally from the signal. Consideration of linearity leads to the investigation of a more linear spring support. A null position accelerometer using feedback techniques may be needed eventually to retain the very high sensitivity of the cryogenic accelerometer without the disadvantages of nonlinearity as a result of displacement.

Given a theoretical error budget, the tolerances in the fabrication and the assembly of these components of the gradiometer have been determined. In view of these requirements, the techniques currently employed to fabricate the parts of the accelerometers are strained to the limit. New procedures and technologies must be explored for the sensing coils, high current density joints, and low frequency sensors. In the case of the coils, thick film deposition seems like a viable technique. Automatic on-line methods of determining alignment and correcting it, and similar compensation for nonlinearities, may be necessary as it had been for the Bell instrument.

In the present setup, the gradiometer is balanced with its sensitive axis vertical. In this mode the earth field is acting directly on the proof masses, producing a 1 g deflection on the diaphragms. It is expected that in its sensitive axis horizontal mode, the gradiometer may be more sensitive.

A persistently troublesome problem in the experiment has been the flux creep. Since the coils are wound of niobium-titanium wire, which is a Type II material, the flux stored in the loops gradually decreases as the fluxoids migrate through the wires. Fortunately, the rate of flux

creep decreases logarithmically with time. In the CDGG, the effects of flux creep tend to cancel out. Niobium wire will be used in future coils although it is somewhat mechanically weak.

B. RECOMMENDATIONS

This research revealed a number of technological developments which will improve the sensitivity of the gravity gradiometer. There are other areas of technology which are not considered or are briefly mentioned in this thesis. Some of them could have significant impact on the potential of the cryogenic gravity gradiometer. It is recommended that additional research be performed in the following areas:

1. Improvement on high current density joints;
2. Fabrication of a low frequency proof mass that is easy to fabricate;
3. Design of null displacement cryogenic accelerometer using force rebalancing feedback to improve linearity;
4. Design of an active feedback to adjust storage current for accelerometer scale balancing;
5. Design of vibration isolation platform and linear shaker for the helium dewar;
6. Gradiometer configuration with axes of the accelerometers in parallel rather than in line;
7. Active damping by other feedback techniques capable of producing critically damped instruments with negligible increase in noise;
8. Technology for rotating a gradiometer at a frequency near the minimum of the SQUID power spectral density;
9. Techniques for altering the orientation of the sensitive axes of accelerometers to provide for on-line alignment of a gravity gradiometer;
10. Technology for producing coil by vapor deposition and making high current density joints with the deposited superconducting circuit.

Appendix A

SCALE FACTOR OF THE CRYOGENIC ACCELEROMETER

Equation (2.31) gives the output current of the cryogenic accelerometer as a function of the stored current, I_0 , and the acceleration sensed, a . It can be simplified to

$$\beta = \frac{1}{a} = \zeta \frac{I}{I^2 + \lambda} \quad (A.1)$$

where

$$\lambda = f_0^2/\alpha \quad (A.2)$$

$$\zeta = m_0 d_0 / L_0 \quad (A.3)$$

The variables were described in Ch. II-D-2. Simplifying (A.3), we have

$$f(I) = \frac{\beta}{\zeta} = \frac{I}{I^2 + \lambda} \quad (A.4)$$

To determine the value of I that will give a maximum value of $f(I)$, (A.4) is differentiated with respect to I and set equal to zero. The optimal condition is

$$I_{opt} = \sqrt{\lambda} \quad (A.5)$$

The curves of $f(I)$ for different values of λ are given in Fig. A-1. The magnitude of the maxima increases as λ becomes smaller; λ can be made smaller by reducing f_0 , the resonant frequency, or increasing α , the electromagnetic coupling coefficient.

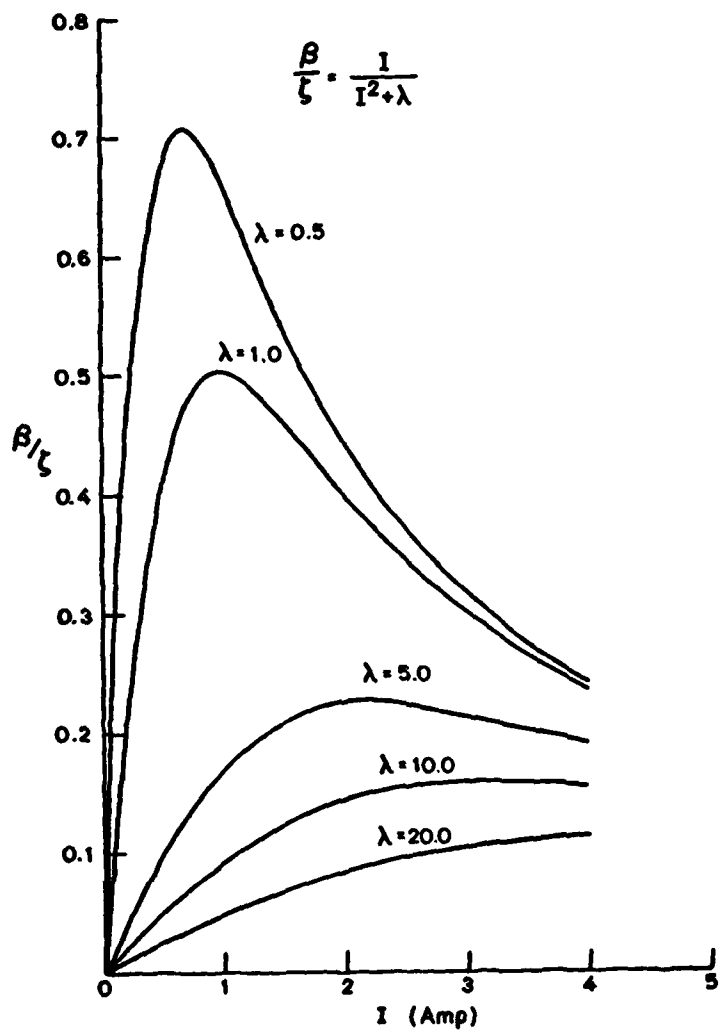


FIG. A-1 SCALE FACTORS OF THE ACCELEROMETER. The curves show that the sensitivity of the accelerometer improves as the frequency is lowered or the coupling is made stronger.

Appendix B
MOTIONS OF DIAPHRAGM WITH CENTRAL LOAD

The equations (3.1) and (3.4) may be simplified by introducing the following nondimensional variables:

$$x = r/a$$

$$u = w/a$$

$$\alpha = b/a$$

$$\gamma = \left(\frac{\rho' h'}{\rho h} \right) = \frac{h'}{h}$$

for a uniform density plate. The set of first four equations becomes

$$\left(\frac{1}{x} \frac{d}{dx} x \frac{d}{dx} \right) \left(\frac{1}{x} \frac{d}{dx} x \frac{d}{dx} \right) = k^4 x \quad (B.1)$$

$$u(1) = \left. \frac{du}{dx} \right|_1 = 0 \quad (B.2)$$

$$\left. \frac{du}{dx} \right|_\alpha = 0 \quad (B.3)$$

$$\frac{d}{dx} \left. \frac{1}{x} \frac{d}{dx} x \frac{du}{dx} \right|_\alpha = \frac{1}{2} k^4 \alpha \gamma u(\alpha) \quad (B.4)$$

where

$$k^4 = (\omega^2 \rho n a^4)/D. \quad (B.5)$$

The general solution for $n = 0$ to (B.1) can be expressed as a linear combination of the four Bessel functions $J_0(kx)$, $Y_0(kx)$, $I_0(kx)$, and $K_0(kx)$. As is customary, J represents the Bessel function of the first kind, Y the second kind, and I and K are Bessel functions of purely imaginary arguments of first and second kind. After applying

boundary conditions (B.2), (B.3), (B.4), and the standard recursive formula of the derivatives of the Bessel functions, the resulting transcending equation for the eigenvalue k can be reduced to

$$\begin{aligned}
 & - [J_0(k)I_1(k) + J_1(k)I_0(k)] [4kY_1(k\alpha)K_1(k\alpha) \\
 & \quad + \alpha k^2 \gamma (Y_1(k\alpha)K_0(k\alpha) - K_1(k\alpha)Y_0(k\alpha))] \\
 & + [J_0(k)K_1(k) - K_0(k)J_1(k)] [4kI_1(k\alpha)Y_1(k\alpha) \\
 & \quad - \alpha k^2 \gamma (I_1(k\alpha)Y_0(k\alpha) + I_0(k\alpha)Y_1(k\alpha))] \\
 & + [Y_0(k)I_1(k) + I_0(k)Y_1(k)] [4kJ_1(k\alpha)K_1(k\alpha) \\
 & \quad + \alpha k^2 \gamma (J_1(k\alpha)K_0(k\alpha) - K_1(k\alpha)J_0(k\alpha))] \\
 & + [Y_0(k)K_1(k) - K_0(k)Y_1(k)] [-4kJ_1(k\alpha)I_1(k\alpha) \\
 & \quad + \alpha k^2 \gamma (J_1(k\alpha)I_0(k\alpha) + I_1(k\alpha)J_0(k\alpha))] \\
 & = \frac{4\gamma}{\pi} .
 \end{aligned} \tag{B.6}$$

Equation (B.6) is very tedious to solve. Fortunately, the lowest frequency may be approximated by a Rayleigh-Ritz approximation. Let

$$D(u) = \int_{\alpha}^1 \frac{1}{x} \left[\frac{du}{dx} \times \frac{du}{dx} \right]^2 dx \tag{B.7a}$$

$$H(u) = \int_{\alpha}^1 x u^2 dx + \frac{1}{2} \alpha^2 \gamma u^2(x) \tag{B.7b}$$

then $k^4 = \min_u [D(u)/H(u)]$. The reader is referred to the original reference for greater details.

The simple trial equation, (B.8) is used.

$$u(x) = \left[1 - \left(\frac{x-\alpha}{1-\alpha} \right)^2 \right]^2; \quad x \geq \alpha. \quad (B.8)$$

Then

$$D(u) = \frac{16}{(1-\alpha)^4} [I_1 + I_2]$$

where

$$I_1 = \frac{2}{15} (1-\alpha)(5-3\alpha)$$

$$I_2 = A_1 + A_2 + A_3$$

$$A_1 = -\ln(\alpha) \left[\alpha^2 - \frac{2\alpha^4}{(1-\alpha)^2} + \frac{\alpha^6}{(1-\alpha)^4} \right]$$

$$A_2 = -\frac{2\alpha^2}{(1-\alpha)^2} \left(\frac{1}{2} - 2\alpha + \frac{3}{2} \alpha^2 \right)$$

$$A_3 = \frac{\alpha^2}{(1-\alpha)^4} \left(\frac{1}{4} - \frac{4}{3} \alpha + 3\alpha^2 - 4\alpha^3 + \frac{25}{12} \alpha^4 \right)$$

and

$$H(u) = (1-\alpha) \left(\frac{7}{10} \alpha - \frac{1}{6} \right) + \frac{1}{2} \alpha^2 \gamma u^2(x).$$

To minimize the ratio of $D(u)/H(u)$ for the trial function $u(x)$, $H(u)$ must be as large as possible. Note that $D(u)$ is a constant. This occurs when $x = \alpha$ and $u(x) = 1$,

$$\therefore k^4 = \frac{D(u)}{(1-\alpha) \left(\frac{7}{10} \alpha - \frac{1}{6} \right) + \frac{1}{2} \alpha^2 \gamma}. \quad (B.9)$$

The accuracy of this approximation is shown by Handelman & Cohen [1957].

The trial function used as given in (B.8) described approximately the shape of the bent surface when $u(0)/h$ is less than 0.72 [Votmir, 1967].

Appendix C

LARGE DEFLECTION OF THIN PLATES

The analysis of the large deflections of the loaded diaphragm was discussed in Ch. III-A-4. The solution of (3.23) and (3.24) is given in Yeh's [1952] paper. As his paper is published in an old Chinese journal with some typographical errors, the solution is reproduced here.

The solution of Karman's equations by perturbation requires that (3.28) be substituted into (3.23) through (3.26). By collecting terms and equating coefficient of Y_m , the following equations are obtained.

For γ_1 , y , the relation is

$$\frac{d^2}{dx^2} x \frac{dy_1}{dx} = \frac{\gamma_1}{x} \quad (C.1a)$$

$$y_1(1) = 0, \quad \frac{dy_1}{dx} = 0, \quad y_1(\beta) = 1, \quad \frac{dy_1}{dx}(\beta) = 0. \quad (C.1b)$$

The solution of (C.1) is

$$\frac{dy_1}{dx} = \gamma_1 \ln x + A - \frac{A}{x} \quad (C.2)$$

$$y_1 = \gamma_1 x \ln x + (A - \gamma_1)x - A \ln x + \gamma_1 - A \quad (C.3)$$

where

$$\gamma_1 = \frac{1 - \beta}{\Delta}, \quad A = \frac{\beta \ln \beta}{\Delta} \quad (C.4a)$$

$$\Delta = (1 - \beta)^2 - \beta(\ln \beta)^2. \quad (C.4b)$$

Equation (C-3) describes the surface of the deflection plate for small deflection. It is the same equation as (3.12).

For S_2 we have

$$\frac{d^2}{dx^2} (xS_2) + \frac{1}{2} \left(\frac{dy}{dx}\right)^2 = 0 \quad (C-5a)$$

$$2\lambda \frac{dS_1(1)}{dx} + S_1(1) = 0, \quad 2\lambda\beta \frac{dS_1(\beta)}{dx} + S_2(\beta) = 0. \quad (C-5b)$$

Integrating equations (C-5) and using the boundary conditions, the solutions are

$$m = \frac{\beta}{2(1-\beta)(2\lambda-1)} \left[\int_{\beta}^1 \left(\frac{dy_1}{dx}\right)^2 dx + \left(\frac{2\lambda-1}{\beta}\right) \int_{\beta}^1 x \left(\frac{dy_1}{dx}\right)^2 dx \right] \quad (C.6)$$

$$S_2 = \frac{1}{2} \int_x^1 \left(\frac{dy_1}{dx}\right)^2 dx - \frac{1}{2x} \int_x^1 x \left(\frac{dy_1}{dx}\right)^2 dx + m(2\lambda-1) + \frac{1}{x}. \quad (C.7)$$

The next approximation gives the equations

$$\frac{d^2}{dx^2} x \frac{dy_3}{dx} = S_2 \frac{dy_1}{dx} + \frac{\gamma_3}{x} \quad (C-8)$$

$$y_3(1) = \frac{dy_3(1)}{dx} = y_3(\beta) = \frac{dy_3(\beta)}{dx} = 0. \quad (C.9)$$

Integrating (C.9) twice, we have

$$\frac{dy_3}{dx} = \frac{1}{x} \int_1^x dx' \int_1^{x'} S_2 \left(\frac{dy_1}{dx''} \right) dx'' + \frac{\tau}{x} + \gamma_3 \ln x + \eta \quad (C.10a)$$

and

$$y_3 = \int_1^x \frac{dx'}{x'} \int_1^{x'} dx'' \int_1^{x''} S_2 \left(\frac{dy_1}{dx'''} \right) dx''' + \tau \ln x + \gamma_3 (x \ln x - x) + \eta u + U \quad (C.10b)$$

At this point, Yeh's solution is inaccurate. The boundary conditions yield

$$\eta = -\tau \quad (C.11a)$$

$$\gamma_3 = U + \eta \quad (C.11b)$$

$$\eta = [(A + \gamma_1)I_1 - AI_2] \quad (C.11c)$$

$$U = [(A - \gamma_1)I_2 + A(\frac{1}{\beta} - 1)I_1] \quad (C.11d)$$

where

$$I_1 = \int_1^{\beta} dx \int_1^x S_2 \frac{dy_1}{dx'} dx' \quad (C.12)$$

$$I_2 = \int_1^{\beta} \frac{dx}{x} \int_1^x dx' \int_1^{x'} S_2 \frac{dy_1}{dx''} dx'' . \quad (C.13)$$

Equation (C.11) may be rewritten as

$$y_3 = \int_1^x \frac{dx'}{x'} \int_1^{x'} dx'' \int_1^{x''} S_2 \frac{dy_1}{dx'''} dx''' + \gamma_3 (x \ln x - x + 1) - \eta (\ln x - x + 1) \quad (C.14)$$

$$\gamma_3 = -\gamma_1 I_2 + (\gamma_1 + A/\beta) I_1 . \quad (C.15)$$

Expressions (C.12) through (C.15) are tedious and cumbersome to solve

manually. The MIT university program MACSYMA is used to evaluate the integrals and solve the equations.

Table C-1 tabulates the values of γ_1 and γ_3 for two different values of Poisson ratios. When compared to the results of Yeh's work, we conclude that Yeh has made some simplifying assumptions that are non-trivial for values of $b/a > 0.4$.

To check our results, MACSYMA is used again to calculate the curvature of the deflected surface at different values of b/a . It is determined using (3.28b) that the y_s calculated in (C.15) satisfied boundary conditions at $r = b$ and $r = a$; y_s calculated using Yeh's results do not.

Table C-1
COEFFICIENTS γ_1 , γ_3

$\frac{b}{a}$	γ_1	$\mu = 0.30$			$\mu = 0.397$
		γ_3 (Yeh)	γ_3	$\Delta\gamma_3$	
0.1	1.289	-	0.2536	-	0.2770
0.2	1.893	0.418	0.4184	0	0.4586
0.22	2.061	4.463	0.4632	-	0.5080
0.24	2.250	0.513	0.5132	0	0.5631
0.26	2.462	0.569	0.5692	0	0.6250
0.28	2.701	0.632	0.6322	0	0.6944
0.30	2.971	0.703	0.7031	0	0.7127
0.32	3.277	0.785	0.7833	0.002	0.8621
0.34	3.624	0.878	0.8744	0.004	0.9617
0.36	4.020	0.984	0.9780	0.006	1.0761
0.37	4.239	-	-	-	1.1393
0.38	4.473	1.109	1.0965	0.012	1.2069
0.40	4.992	1.258	1.2324	0.026	1.3570
0.50	9.141	3.252	2.3187	0.933	2.5562
0.60	18.911	48.982	4.8812	44.102	5.3857
0.70	47.421	3865.056	12.3745	3852.681	13.6610
0.80	169.029	1228192.0	44.3926	1228148.0	49.0239

PROGRAM LISTINGS

The symbolic integration of the equation (C.12) and (C.13) are performed by these programs. Using these solutions, (C.15) is evaluated. The listings of the computer programs are given here. The interested reader is referred to the MIT Math Lab MACSYMA Manual [MAC SYMA, 1975] for details on the syntax of the language.

The following list gives the variable symbol in (C.1) through (C.15) and their corresponding character strings in the programs.

<u>Variable</u>	<u>Character String</u>
α	ALP
γ_1	GL
γ_3	G3
λ	LAM
μ	M
η	NETA
A	A
x	X

I2 in the program listing is (C-13).

The program SESS7-MAC determined the coefficient $y_3(x)$ in Eq. (3.28b). This provides a check for the accuracy of the integration. At $x = 1.0$, the outer radius of the diaphragm, the displacement is zero; thus $y_1(1)$ and $y_3(1)$ are both zero. At $x = r$, the inner radius of the annular diaphragm, $y = Y_M$, thus $y_1(r) = 1$ and $y_3(r) = 0$. The program SESS8-MAC shows that y_3 are indeed zero at the boundaries of the diaphragm for all values of r starting with $r = 0.8$ to $r = 0.1$ where r is the ratio of the inner radius to the outer radius. These are determined for a standard Poisson ratio of 0.3.

The Program SESS11-MAC determines the values of γ_1 and γ_3 , and

some intermediate results for $\mu = 0.397$ which is the Poisson's ratio for niobium. Program SESS13-MAC provides an additional value at $r = 0.37$ which is the value which will provide the low frequency of the diaphragm. Program SESS20-MAC determines the same constants for a range of r between 0.2 and 0.4.

The following is the MIT Program.

28 Oct 1978 6:42

SESS7,MACP 1.WKY]

Page 1-2

playback()

(Dg)

NONE

(C7) CP(ALP,A,G1):=(G1+2*((2*ALP+2*LOG(ALP)+2-2*ALP+2*LOG(ALP)+ALP+2-ALP)*(2*ALP+4*ALP+2*LOG(ALP)+2-8*ALP+2*LOG(ALP)+8*ALP+2-8*ALP)+G1+((4*A*ALP+2-8*A*ALP)*LOG(ALP)-2*A*ALP+2+2*A*ALP)+(2*ALM-1)-4*A*ALP+LOG(ALP)+2+8*A*ALP+2*LOG(ALP))-8*A*ALP+2+8*A*ALP)+(4*A+2*LOG(ALP)+2+4+2*ALP+2+2*A+2*ALP-4*A+2)*(2*ALM-1)-8*A+2*ALP+LOG(ALP)+4*A+2*ALP+2-4*A+2)/(18*ALP-8)*(2*ALM-1))S

(C77) I2(X,ALP,A,BMC,CP,G1):=(2*G1+3*x+3*(9*LOG(X)+3-9*LOG(X)+2+6*LOG(X)-2)/8+1-A*G1+2*X+2*(4*LOG(X)+3-6*LOG(X)+2+6*LOG(X)-3)/2+4+A+3*LOG(X)+3/3-11*A+3*x+3+9*LOG(X)+2-6*LOG(X)+2)/81+2+A*G1+2*x+3*(9*LOG(X)+2-6*LOG(X)+2)/27+6+A*G1+2*x+2*(2*LOG(X)+2-2*LOG(X)+1)-3+A+2*G1*x+2*(2*LOG(X)+2-2*LOG(X)+1)-8*CP+G1*x*(LOG(X)+2-2*LOG(X)+2)-8*A+2*G1*x*(LOG(X)+2-2*LOG(X)+2)+4+A+3*3*x*(LOG(X)+2-2*LOG(X)+2)-8*A*CP+LOG(X)+2-4+A+3*LOG(X)+2+7*G1+3*(X+3*LOG(X)+3-x+3/9)/9+22*A*G1+2*(X+2*LOG(X)/2-X+2/4)-8*A+3*(X+2*LOG(X)/2-X+2/4)-8*A+3*(X+2*LOG(X)/2-X+2/4)+16*CP+G1*(X*LOG(X)-X)+16+A+2*G1*(X*LOG(X)-X)-16+A*CP*(X*LOG(X)-X)+16+A*BMC*(X*LOG(X)-X)-8*A+3*(X*LOG(X)-X)-74*G1+3*LOG(X)/27+38*A*G1+2*LOG(X)/9+16*CP+G1*LOG(X)+4*BMC*G1*LOG(X)+26+A+2*G1*LOG(X)/3-32*A*CP+LOG(X)+8*A*BMC*LOG(X)-38*A+3*LOG(X)/3-142*A*G1+3*x+3/81+78*A*G1+2*x+3/27-112*A+2*G1*x+3/9+2*A+3*x+3/9+25*A*G1+2*x+2+6*BMC*G1*x+2-21*A+2*G1*x+2-4*A*BMC*x+2+5*A+3*x+2+8*G1+3*x-62*A+G1+2*x-16*CP+G1*x-16*BMC*G1*x+37*A+2*G1*x+32*A*CP+X+2+4+3*x-412*A*G1+3/81+112*A+G1+2/9+48*CP+G1+8*BMC*G1+274*A+2*G1+9+48*A*CP+23*A*BMC+227*A+3/9)/16S

(C78) G3(ALP,A,BMC,CP,G1):=G1*(2*ALP+3*(9*LOG(ALP)+3-9*LOG(ALP)+2+6*LOG(ALP)-2)+G1+3/81+11*ALP+3*(9*LOG(ALP)+2-6*LOG(ALP)+2)+G1+3/81+72*(ALP+3*LOG(ALP)/3-ALP+3/9)+G1+3/9+74*LOG(ALP)+G1+3/27+142*ALP+3*G1+3/81+8*ALP+G1+3-410*A+3/81-A*A+LP+2*(4*LOG(ALP)+3-6*LOG(ALP)+2+6*LOG(ALP)-3)*G1+2/2+2*A*ALP+3*(9*LOG(ALP)+2-6*LOG(ALP)+2)*G1+2/27+6*A*ALP+2*(2*LOG(ALP)+2-2*LOG(ALP)+1)*G1+2-22*A*(ALP+3*LOG(ALP)/3-ALP+3/9)*G1+2/3-54*A*(ALP+2*LOG(ALP)/2-ALP+2/4)*G1+2+38*A*LOG(ALP)*G1+2/9+70*A*ALP+3*G1+2/27+25*A*ALP+2*G1+2-62*A*ALP+G1+2+312*A*G1+2/9-8*A*ALP*(LOG(ALP)+2-2*LOG(ALP)+2)*CP+G1+16*(ALP+LOG(ALP)-ALP)*CP+G1+16*LOG(ALP)*CP+G1-16*ALP+CP+G1+48*CP+G1+8*(ALP+2*LOG(ALP)/2-ALP+2/4)*8MC*G1+4*9LOG(ALP)*BMC*G1+6*ALP+2*BMC*G1+16*ALP+2*BMC*G1+8*BMC*G1+36*A+2*ALP+2*(2*LOG(ALP)+2-2*LOG(ALP)+1)*G1-8*A+2*ALP*(LOG(ALP)+2-2*LOG(ALP)+2)*G1+2+4*(ALP+3*LOG(ALP)/3-ALP+3/9)*G1+40*A+2*(ALP+2*LOG(ALP)/2-ALP+2/4)*G1+16*A+2*(ALP+LOG(ALP)-ALP)*G1+26*A+2*LOG(ALP)*G1/3-12*A+2*ALP+3*G1/9-21*A+2*ALP+2*G1+37*A+2*ALP+G1+274*A+2*G1/9-9*A*LOG(ALP)+2*C*P-16*A*(ALP+LOG(ALP)-ALP)*CP-32*A*LOG(ALP)*CP+32*A*ALP+CP-48*A*CP+16*A*(ALP+LOG(ALP)-ALP)*BMC+8*A*LOG(ALP)*BMC-4*A+3*LOG(ALP)+3/3+4*A+3*ALP*(LOG(ALP)+2-2*LOG(ALP)+2)-4*A+3*LOG(ALP)+2-8*A+3*(ALP+2*LOG(ALP)/2-ALP+2/4)-8*A+3*(ALP+LOG(ALP)-ALP)-38*A+3*LOG(ALP)/3+2*A+3*ALP+3/9+5*A+3*ALP+2+2*A+3*ALP-227*A+3/9)/16-(G1+A/ALP)*(2*ALP+3*(9*LOG(ALP)+3-9*LOG(ALP)+2+6*LOG(ALP)-2)*G1+3/27+ALP+3*(9*LOG(ALP)+2-6*LOG(ALP)+2)*G1+3/3+16*(ALP+3*LOG(ALP)/3-ALP+3/9)*G1+3-8*ALP+3*G1+3/3+8*ALP+G1+3-74*G1+3/27-4*ALP+2*(4*LOG(ALP)+3-6*LOG(ALP)+9+6*LOG(ALP)+3)*G1+2+2*A*ALP+3*(9*LOG(ALP)+2-6*LOG(ALP)+2)*G1+2/9+9*A*ALP+2*(2*LOG(ALP)+2-2*LOG(ALP)+1)*G1+2-18*A+ALP+3*LOG(ALP)/3+ALP+3/9)*G1+2-60*A*(ALP+2*LOG(ALP)/2-ALP+2/4)*G1+2+16*A*ALP+3*G1+2/3+23*A*ALP+2*G1+2-62*A*ALP+G1+2+38*A+G1+2/9+8*A*ALP*(LOG(ALP)+2-2*LOG(ALP)+2)*CP+G1+16*CP+G1-16*(ALP+2*LOG(ALP)/2-ALP+2/4)*BMC*G1+8*ALP+2*BMC*G1-16*ALP+2*BMC*G1+4*BMC*G1+6*A+2*ALP+2*(2*LOG(ALP)+

28 Oct 1978 6142

98857,MACC 1,WKYJ

Page 1-2

2+2*LOG(ALP)+1)*G1-A=2+2*ALP*(LOG(ALP)+2)+G1+6+A+2*(ALP+3*LOG(ALP)+3-ALP+3/9)*G1+56+A+2*(ALP+2*LOG(ALP)+2-ALP+2/4)*G1-3+A+2*ALP+3*G1-22+A+2*ALP+2+G1+53+A+2*ALP+G1+26+A+2*G1/3-16+A*(ALP+LOG(ALP)-ALP+CP-16+A*LOG(ALP)+CP+16+A*ALP+CP-32+A*CP+16+A*(ALP+LOG(ALP)-ALP)+BMC-8+A*ALP+2*BMC+16+A*ALP+8+A*BMC+4+A+3*ALP*(LOG(ALP)+2-2*LOG(ALP)+2)-4+A+3*LOG(ALP)+2-16+A+3*(ALP+2*LOG(ALP)+2-ALP+2/4)-8+A+3*LOG(ALP)+2+A+3*ALP+3/3+6+A+3*ALP+2-6+A+3*ALP+38+A+3/3)/165

(C79) NETA(ALP,A,BMC,CP,G1):=A*(2*ALP+3*(9*LOG(ALP)+3-9*LOG(ALP)+246*LOG(ALP)-2)*G1+3/81-11*ALP+3*(9*LOG(ALP)+2+6*LOG(ALP)+2)*G1+3/81+70*(ALP+3*LOG(ALP)/3-A*LP+3/9)*G1+3/9-74*LOG(ALP)*G1+3/27-142*ALP+3*G1+3/81+8*ALP+G1+3-418+G2+3/81-A*ALP+2*(4*LOG(ALP)+3-6*LOG(ALP)+2+8*LOG(ALP)-3)*G1+2/2+2+A*ALP+3*(9*LOG(ALP)+2-6*LOG(ALP)+2)*G1+2/27+6+A*ALP+2*(2*LOG(ALP)+2-2*LOG(ALP)+1)*G1+2-22+A*(ALP+3*L0G(ALP)/3+ALP+3/9)*G1+2/3-54+A*(ALP+2*LOG(ALP)/2-ALP+2*4)*G1+2+38+A*LOG(ALP)+G1+2/9+78+A*ALP+3*G1+2/27+25+A*ALP+2*G2+2-62+A*ALP+G1+2+112+A*G1+2/9+8*ALP*(LOG(ALP)+2-2*LOG(ALP)+2)*CP+G1+16*(ALP+LOG(ALP)-ALP)*CP+G1+16*LOG(ALP)+CR+G1-16+A*LP+CP+G1+48*CP+G1+8*(ALP+2*LOG(ALP)+2+ALP+2/4)*BMC+G1+4*LOG(ALP)+BMC+G1+6*ALP+2*BMC+G1-16*ALP+8*BMC+G1+8+8*BMC+G1-3*8+A+2*ALP+2*(2*LOG(ALP)+2-2*LOG(ALP)+1)*G1-8+A+2*ALP*(LOG(ALP)+2-2*LOG(ALP)+2)*G1+29+A+2*(ALP+3*LOG(ALP)/3-ALP+3/9)*G1+40+A+2*(ALP+2*LOG(ALP)/2-ALP+2/4)*G1+16+A+2*(ALP+LOG(ALP)-ALP)*G1+26+A+2*LOG(ALP)+G1+3-11+A+2*ALP+3*G1/9-21+A+2*ALP+2+G1+37+A+2*ALP+G1+274+A+2*G1/9-8+A+LOG(ALP)+2*CP-16+A*(ALP+LOG(ALP)-ALP)*CP-32+A*LOG(ALP)*CP+32+A*ALP+CP-48+A*CP+16+A*(ALP+LOG(ALP)-ALP)*BMC+8+A*LOG(ALP)+BMC-4+A*ALP+2*BMC+20+A*BMC-4+A+3*LOG(ALP)+3/3+4+A+3*ALP*(LOG(ALP)+2-2*LOG(ALP)+2)-4+A+3*LOG(ALP)+2-8+A+3*(ALP+2*LOG(ALP)/2-ALP+2/4)-8+A+3*ALP+LOG(ALP)-ALP)-38+A+3*LOG(ALP)/3+2+A+3*ALP+3/9+5+A+3*ALP+2+2+A+3*ALP-227+A+3/9)/16*(G1+A)*(2*ALP+3*(9*LOG(ALP)+3-9*LOG(ALP)+2+6*LOG(ALP)-2)*G1+3/27-ALP+3*(9*LOG(ALP)+2-6*LOG(ALP)+2)*G1+3/3+16*(ALP+3*LOG(ALP)/3-ALP+3/9)*G1+3-8+ALP+3*G1+3/3+8+A*ALP+G1+3-74*G2+3/27-8*ALP+2*(4*LOG(ALP)+3-6*LOG(ALP)+2)*G1+2/9+9+A*ALP+2*(2*LOG(ALP)+2-2*LOG(ALP)+1)*G1+2+18+A*(ALP+3*LOG(ALP)/3-ALP+3/9)*G1+2-68+A*(ALP+2*LOG(ALP)/2-ALP+2/4),+G1+2+16+A*ALP+3*G1+2/3+23+A*ALP+2+G1+2-62+A*ALP+G1+2+38+A*G1+2/9-8*ALP*(LOG(ALP)+2-2*LOG(ALP)+2)*CP+G1+16*(ALP+2*LOG(ALP)/2-ALP+2/4)*BMC+G1+8*ALP+2*BMC+G1-16*ALP+8*BMC+G1+4*BMC+G1-6+6+2*ALP+2*(2*LOG(ALP)+2-2*LOG(ALP)+1)*G1-8+A+2*ALP*(LOG(ALP)+2-2*LOG(ALP)+2)*G1+6+A+2*(ALP+3*LOG(ALP)/2-ALP+2/4)*G1-3+A+2*ALP+3*G1-22+A+2*ALP+2+G1+53+A+2*ALP+G1+26+A+2*G1/3-16+A*(ALP+LOG(ALP)-ALP)*CR-16+A*LOG(ALP)+CP+16+A*ALP+CP-32+A*CP+16+A*(ALP+LOG(ALP)-ALP)*BMC-8+A*ALP+2*BMC+16+A*ALP+8*A*BMC+4+A+3*ALP*(LOG(ALP)+2-2*LOG(ALP)+2)-4+A+3*LOG(ALP)+2-16+A+3*(ALP+2*LOG(ALP)/2-ALP+2/4)-8+A+3*LOG(ALP)+2+A+3*ALP+3/3+6+A+3*ALP+2-6+A+3*ALP-38+A+3/3)/165

(C123) FYEH(M):=BLOCK[CAA,BB,CC,BBMC,SCP,LL,L2,L,NNETA;GG3,Y3,DELTA,N,XP,GG1,A,ALP],LAM:1,0B0/(1.0B0-M),N:0,LOOP3,IF N = 0 THEN GO(LOOP10),IF N > 6 THEN GO(L0OP5),XP:1.0B-1*N,GO(L0OP6),LOOP5:XP:5,0B-3*N,L0OP6,AALP1XP*XP,DELTA:(1.0B2-AA*LP)+2*AALP+LOG(AALP)+2,GG1:(1.0B0-AALP)/DELTA,AA+AALP+LOG(AALP)/DELTA,BBMC(BMC(AALP,AA,GG1)),CCP:CP(AALP,AA,GG1),GG3:G3(AALP,AA,BBMC,SCP,GG1),NNETA:NETA(AALP,AA,BBMC,SCP,GG1),PRINT(XP,GG1,AA,BBMC,SCP,GG3),L:10,L0OP2,IF L < N THEN GO(L0OP3),LL:1,0B-1*L,L2:LL,Y3:12(L2,AALP,AA,BBMC,SCP,GG3)+GG3*(L2*LOG(L2)-L2+1.0B0)-NNETA*(LOG(L2)-L2+1.0B0),PRINT(LU,Y3),L:1,L0OP3,N:N-1,GO(L0OP10)

(C124) KILL(C119,0119,C120,0120,C121,0121,C122,0122)

(D124)

BONE

THIS PAGE IS BEST QUALITY PRACTICABLE
FROM COPY FURNISHED TO DDC

25 Oct 1978 0142

SESS7,NAME 1.WKY

Page 1-3

(C126) BNG(ALP,A,G1);=OPTIMIZE(ALP+2*LOG(ALP)+2*G1+2*(2*LAM-1)/(4*ALP-4)-ALP+2*
LOG(ALP)+G1+2*(2*LAM-1)/(4*ALP-4)+ALP+2*G1+2*(2*LAM-1)/(8*ALP-8)-G1+2*(2*LAM-
1)/(8*ALP-8)+A*ALP+2*LOG(ALP)+G1*(2*LAM-1)/(2*ALP-2)-A*ALP*LOG(ALP)+G1*(2*LAM-
1)/(2*LAM-1)/(ALP-1)-A*ALP+2*G1*(2*LAM-1)/(4*ALP-4)-3+A*G1*(2*LAM-1)/(4*ALP-4)+A*ALP*G1*
(2*LAM-1)/(ALP-1)+A+2*LOG(ALP)*(2*LAM-1)/(2*ALP-2)+A+2*ALP+2*(2*LAM-1)/(4*ALP-
4)+3+A+2*(2*LAM-1)/(4*ALP-4)-A+2*ALP*(2*LAM-1)/(ALP-1)+ALP+2*LOG(ALP)+2*G1+2/(
2*ALP-2)-ALP+2*LOG(ALP)+G1+2/(ALP-1)+ALP+2*G1+2/(ALP-1)-G1+2/(ALP-1)-A*ALP*LOG
(ALP)+2*G1/(2*ALP-2)+A*ALP+2*LOG(ALP)+G1/(ALP-1)-A*ALP+2*G1/(ALP-1)+A*ALP*G1/(
ALP-1)-A+2*ALP*LOG(ALP)/(ALP-1)+A+2*ALP+2/(2*ALP-2)+A+2/(2*ALP-2)-A+2*ALP/(ALP-
1))

(C127) KILL(C2,D2,C125,D125,D126)

(D127)

DONE

(C128) PLAYBACK();

(D128)

DONE

(D129)

DONE

(C130)

THIS PAGE IS BEST QUALITY
FROM COPY PUBLISHED TO PDC

28 Oct 1978 6:43

SESS8.MACT i.WKYJ

Page 1-1

Typed (3b01)

8,00-1 1,69029471932891782 - 1,34307803622620782 1,0595966025020584

- 6,67016211210792284 4,43926429494237681

1,00-1 - 6,0776983445975938-10

9,00-1 1,9546171760795328-4

8,00-1 1,520718725892098-9

7,00-1 4,742135008060956881 - 3,25014284459958381 1,1964604410208183

- 4,0811607063616083 1,23744632302800781

1,00-1 6,7714722717937558-11

9,00-1 2,2939059989518558-3

8,00-1 - 2,0312782218385438-3

7,00-1 9,1798790791131078-12

6,00-1 1,89112206138866481 - 1,0867882745480181 2,41781928844112892

- 4,79688662813341382 4,88119149480400582

1,00-1 1,7670309659933998-12

9,00-1 2,2990880176703638-3

8,00-1 4,1199589985199688-4

7,00-1 - 2,3264142983800858-3

6,00-1 1,5985823775821478-12

5,00-1 9,14110300193207880 - 4,22408679259038782 6,70839285733537681

- 7,71724321344625881 2,31870277477134488

1,00-1 1,3117285035946228-13

9,00-1 1,8993957141149198-3

8,00-1 1,8808388315143468-3

7,00-1 - 1,1089079639489898-3

6,00-1 - 2,1748961962190928-3

5,00-1 8,2239770549108478-14

4,00-1 4,99217807127640780 - 1,7425853279004982 2,27761644756496691

- 1,742716348384433881 1,23243600532516380

1,00-1 6,3805156647477638-15

9,00-1 1,4924065118458289-3

8,00-1 2,3336636770691118-3

7,00-1 5,7937607058358368-4

6,00-1 - 1,9421632495671938-3

5,00-1 - 1,9799100235923348-3

4,00-1 8,0768725041480148-15

3,00-1 2,97131393818850180 - 2,07613883873059258-1 8,93622001882433180

- 2,764963125434852388 7,031088615815088-1

1,00-1 4,4235448637408588-16

9,00-1 1,1465393184149628-3

8,00-1 2,2632710871784728-3

7,00-1 1,5676260627000758-3

6,00-1 - 6,2334053173080523-4

5,00-1 - 2,4365841234078828-3

4,00-1 - 1,8505994409255198-3

THIS PAGE IS BEST QUALITY PRACTICAL
FROM COPY FURNISHED TO DDC

28 Oct 1970 6143

58558,MACP 1,WKY3

Page 1-2

3,88-1 9,5756735873919738-16
2,88-1 1,69291788389860180 - 2,538783728924498-1 3,94681437138686980

4,671452067741676978-1 4,1841211572543578-1

1,88-1 1,3877787807814468-16
9,88-1 8,5584737372797388-4
9,88-1 1,934046602862668-3
7,88-1 1,85258003681383318-3
6,88-1 3,6210513151603568-4
9,88-1 - 1,7338092932944018-3
4,88-1 - 2,9131662625115498-3
3,88-1 - 1,8745876236640888-3
2,88-1 - 8,3266726846886748-17
1,88-1 1,28902209120385680 - 5,996127377263738-2 1,96368718153355380

4,3/3903377203001418-2 2,5364838788778948-1

1,88-1 2,2442984970449948-17
9,88-1 5,9418083493236488-4
8,88-1 1,4285516157021698-3
7,88-1 1,5221457285358138-3
6,88-1 5,0596010522639338-4
5,88-1 - 1,3547805108365578-3
4,88-1 - 3,199587051354668-3
3,88-1 - 3,7934489555962178-3
2,88-1 - 2,2993185282968688-3
1,88-1 - 9,5511151231257838-17
(D143)

8

(C144)

THIS PAGE IS BEST QUALITY FRACTICARUS
MAIN COPY FURNISHED TO RIA

Playback()

(D8)

NONE

(C73) $CP(ALP, A, G1) := G1 + 2 * ((2 * ALP + 2 * LOG(ALP) + 2 * ALP * LOG(ALP) + ALP * 2 * ALP) * (2 * ALP - 1) + 4 * ALP * 2 * LOG(ALP) + 2 * 8 * ALP * 2 * LOG(ALP) + 8 * ALP * 2 * 8 * ALP * LOG(ALP) - 2 * A * ALP * 2 * 2 * A * ALP) * (2 * LAM - 1) - 4 * A * ALP * LOG(ALP) + 2 * 8 * A * ALP * 2 * LOG(ALP) - 8 * A * ALP * 2 * 8 * A * ALP) + (4 * A + 2 * LOG(ALP) + 2 * A + 2 * ALP + 2 * 2 * A + 2 * ALP = 4 * A + 2 * (2 * LAM - 1) - 8 * A + 2 * ALP * LOG(ALP) + 4 * A + 2 * ALP * 2 * 4 * A + 2) / (18 * ALP - 8) * (2 * LAM - 1))$

(C77) $i2(X, ALP, A, BMC, CP, G1) := (2 * G1 + 3 * X + 3 * (9 * LOG(X) + 3 * 9 * LOG(X) * 2 * 6 * LOG(X) - 2) / 8 * 1 - A * G1 + 2 * X + 2 * (4 * LOG(X) * 3 - 6 * LOG(X) * 2 * 6 * LOG(X) - 3) / 2 - 4 * A + 3 * LOG(X) * 3 / 3 - 11 * G1 + 3 * X + 3 * (9 * LOG(X) * 2 - 6 * LOG(X) + 2 / 81 + 2 * A * G1 + 2 * X + 3 * (9 * LOG(X) * 2 - 6 * LOG(X) + 2) / 27 + 6 * A * G1 + 2 * X + 2 * (2 * LOG(X) * 2 - 2 * LOG(X) + 1) - 3 * A + 2 * G1 * X + 2 * (2 * LOG(X) * 2 - 2 * LOG(X) + 1) - 8 * CP * G1 * X * (LOG(X) * 2 - 2 * LOG(X) + 2) - 8 * A + 2 * G1 * X * (LOG(X) * 2 - 2 * LOG(X) + 2) + 4 * A + 3 * X * (LOG(X) * 2 - 2 * LOG(X) + 2) - 8 * A + 2 * CP * LOG(X) * 2 - 4 * A + 3 * LOG(X) * 2 + 70 * G1 + 3 * (X + 3 * LOG(X) / 3 - X + 3 / 9) / 9 - 22 * A * G1 + 2 * (X + 3 * LOG(X) / 3 - X + 3 / 9) / 3 + 2 * A + 2 * G1 * (X + 3 * LOG(X) / 3 - X + 3 / 9) - 54 * A * G1 + 2 * (X + 2 * LOG(X) / 2 - X + 2 / 4) - 8 * BMC * G1 * (X * 2 * LOG(X) / 2 - X + 2 / 4) + 40 * A + 2 * G1 * (X * 2 * LOG(X) / 2 - X + 2 / 4) - 8 * A + 3 * (X + 2 * LOG(X) / 2 - X + 2 / 4) + 16 * CP * G1 * (X * LOG(X) - X) + 18 * A + 2 * G1 * (X * LOG(X) - X) - 18 * A + CP * (X * LOG(X) - X) + 16 * A + BMC * (X * LOG(X) - X) - 8 * A + 3 * (X * LOG(X) - X) - 74 * G1 + 3 * LOG(X) / 27 + 38 * A * G1 + 2 * LOG(X) / 9 + 16 * CP * G1 * LOG(X) + 4 * BMC * G1 * LOG(X) + 26 * A + 2 * G1 * LOG(X) / 3 - 32 * A + CP * LOG(X) + 8 * A + BMC * LOG(X) - 38 * A + 3 * LOG(X) / 3 - 142 * G1 + 3 * X + 3 / 91 + 73 * A * G1 + 2 * X + 3 / 27 - 11 * A + 2 * G1 * X + 3 / 9 + 2 * A + 3 * X + 3 / 1 + 25 * A + G1 + 2 * X + 2 * 6 * BMC * G1 * X + 2 - 21 * A + 2 * G1 * X + 2 - 4 * A + BMC * X + 2 + 5 * A + 3 * X + 2 + 8 * G1 + 3 * X - 62 * A * G1 + 2 * X - 16 * CP * G1 * X - 16 * BMC * G1 + X + 37 * A + 2 * G1 * X + 32 * A + CP * X + 2 * A + 3 * X + 41 * G1 + 3 / 81 + 112 * A * G1 + 2 / 9 + 48 * CP * G1 + 8 * BMC * G1 + 274 * A + 2 * G1 / 9 - 48 * A + CP + 20 * A + BMC * 227 * A + 3 / 9) / 165$

(C78) $G3(ALP, A, BMC, CP, G1) := G1 * (2 * ALP + 3 * (9 * LOG(ALP) + 3 * 9 * LOG(ALP) + 2 * 6 * LOG(ALP) - 2) * G1 + 3 / 81 + 11 * ALP + 3 * (9 * LOG(ALP) + 2 * 6 * LOG(ALP) + 2) * G1 + 3 / 81 + 73 * (ALP + 3 * LOG(ALP) / 3 - ALP + 3 / 9) + G1 + 3 / 9 - 74 * LOG(ALP) * G1 + 3 / 27 + 142 * ALP + 3 * G1 + 3 / 81 + 8 * ALP * G1 + 3 - 412 * G1 + 3 / 81 - 4 * A * LOG(ALP) + 2 * (4 * LOG(ALP) + 3 - 6 * LOG(ALP) + 2 * 6 * LOG(ALP) - 3) * G1 + 2 * 2 / 2 + 2 * A * ALP + 3 * (9 * LOG(ALP) * 2 - 6 * LOG(ALP) + 2) * G1 + 2 / 27 + 6 * A * ALP + 2 * (2 * LOG(ALP) + 2 - 2 * LOG(ALP) + 1) * G1 + 2 * 2 - 22 * A * (ALP + 3 * LOG(ALP) / 3 - ALP + 3 / 9) * G1 + 2 * 3 - 54 * A * (ALR * 2 * LOG(ALP) / 2 - ALP + 2 / 4) * G1 + 2 * 38 * A * LOG(ALP) * G1 + 2 / 9 + 78 * A * ALP + 3 * G1 + 2 / 27 + 25 * A * ALP + 2 * 01 + 2 - 62 * A + ALP + 2 + 2 * 12 * A + G1 + 2 / 9 - 8 * ALP * (LOG(ALP) * 2 - 2 * LOG(ALP) + 2) * CP + G1 + 16 * (ALP * LOG(ALP) - ALP) * CP + G1 + 16 * LOG(ALP) * CP + G1 - 16 * ALP * CP + G1 + 48 * CP + G1 - 8 * (ALP + 2 * LOG(ALP) / 2 - ALP + 2 / 4) * BMC * G1 + 4 * LOG(ALP) * BMC * G1 + 6 * ALP + 2 * BMC * G1 - 16 * ALP * BMC * G1 + 8 * BMC * G1 - 3 * A + 2 * ALP + 2 * (2 * LOG(ALP) + 2 - 2 * LOG(ALP) + 1) * G1 - 8 * A + 2 * ALP * (LOG(ALP) * 2 - 2 * LOG(ALP) + 2) * G1 + 2 * 4 * 2 * (ALP + 3 * LOG(ALP) / 3 - ALP + 3 / 9) * G1 + 40 * A + 2 * (ALP + 2 * LOG(ALP) / 2 - ALP + 2 / 4) * G1 + 16 * A + 2 * (ALP * LOG(ALP) - ALP) * G1 + 26 * A + 2 * LOG(ALP) * G1 - 11 * A + 2 * ALP + 3 * G1 / 9 - 21 * A + 2 * ALP + 2 * G1 + 37 * A + 2 * ALP * G1 + 274 * A + 12 * G1 / 9 - 8 * A * LOG(ALP) * 2 * C - P - 16 * A * (ALP * LOG(ALP) - ALP) * CP - 32 * A * LOG(ALP) * CP + 32 * A * ALP * CP - 48 * A * CP + 16 * A * (ALP * LOG(ALP) - ALP) * BMC + 8 * A * LOG(ALP) * BMC - 4 * A * ALP + 2 * 8 * BMC + 20 * A * BMC - 4 * A + 3 * LOG(ALP) + 3 / 3 + 4 * A + 3 * ALP * (LOG(ALP) * 2 - 2 * LOG(ALP) + 2) * 4 * A + 3 * (ALP + 2 * LOG(ALP) / 2 - ALP + 2 / 4) - 8 * A + 3 * (ALP * LOG(ALP) - ALP) - 38 * A + 3 * LOG(ALP) / 3 + 2 * A + 3 * ALP + 3 / 9 + 5 * A + 3 * ALP + 2 + 2 * A + 3 * ALP - 227 * A + 3 / 9) / 16 - (G1 + A * ALP) * (2 * ALP + 3 * (9 * LOG(ALP) + 3 * 9 * LOG(ALP) + 2 * 6 * LOG(ALP) - 2) * G1 + 3 / 27 - ALP + 3 * (9 * LOG(ALP) + 2 * 6 * LOG(ALP) + 2) * G1 + 3 / 23 + 162 * (ALP + 3 * LOG(ALP) / 3 - ALP + 3 / 9) * G1 + 3 - 8 * ALP + 3 * G1 + 3 / 3 + 8 * ALP * G1 + 3 - 74 * G1 + 3 / 27 - A * ALP + 2 * (4 * LOG(ALP) * 3 - 6 * LOG(ALP) + 2 * 6 * LOG(ALP) - 3) * G1 + 2 * 2 * A * ALP + 3 * (9 * LOG(ALP) + 2 * 6 * LOG(ALP) + 2) * G1 + 2 / 9 + 9 * A * ALP + 2 * (2 * LOG(ALP) + 2 - 2 * LOG(ALP) + 1) * G1 + 2 - 18 * A + 1 ALP + 3 * LOG(ALP) / 3 - ALP + 3 / 9) * G1 + 2 * 68 * A * (ALP + 2 * LOG(ALP) / 2 - ALP + 2 / 4) * G1 + 2 + 16 * A * ALP + 3 * G1 + 2 / 3 - 23 * A * ALP + 32 * G1 + 2 - 62 * A * ALP * G1 + 2 + 38 * A * G1 + 2 / 9 + 8 * ALP * (LOG(ALP) * 2 - 2 * LOG(ALP) + 2) * CP + G1 + 16 * CP + G1 - 16 * (ALP + 2 * LOG(ALP) / 2 - ALP + 2 / 4) * BMC * G1 + 8 * ALP + 2 * BMC * G1 - 16 * ALP * BMC * G1 + 4 * BMC * G1 - 8 * A + 2 * ALP + 2 * LOG(ALP) * 2$

28 Oct 1978 7:09

SESSION.MAGE 1.WKY3

Page 1-2

$$\begin{aligned}
 & 2-2*\log(ALP)+1)*G1-8*A+2*ALP*(\log(ALP)+2-2*\log(ALP)+2)*G1+6*A+2*(ALP+3*\log(ALP) \\
 &)/3-ALP+3/9)*G1+56*A+2*(ALP+2*\log(ALP)+2-ALP+2/4)*G1-32A+2*ALP+3*G1-22*A+2*ALP \\
 & +2*G1+53*A+2*ALP+G1+26*A+2*G1/3-16*A*(ALP*\log(ALP)-ALP)*CP+16*A*\log(ALP)*CP+16 \\
 & *A*ALP*CP+32*A*CP+16*A*(ALP*\log(ALP)-ALP)*BMC-8*A*ALP+2*BMC+16*A*ALP*BMC+8*A*B \\
 & MC+4*A+3*ALP*(\log(ALP)+2-2*\log(ALP)+2)-4*A+3*\log(ALP)+2-16*A+3*(ALP+2*\log(ALP) \\
 & /2-ALP+2/4)-8*A+3*\log(ALP)+2*A+3*ALP+3/3+6*A+3*ALP+2-6*ALP+3*ALP-38*A+3/3)/16S
 \end{aligned}$$

$$\begin{aligned}
 & (C79) NETA(ALP,A,BMC,CP,G1):=A*(24ALP+3*(9*\log(ALP)+3-9*\log(ALP)+2+6*\log(ALP) \\
 & -2)*G1+3/81-11*ALP+3*(9*\log(ALP)+2+6*\log(ALP)+2)*G1+3/81+70*(ALP+3*\log(ALP)/3-A \\
 & LP+3/9)*G1+3/9-74*\log(ALP)*G1+3/27-142*ALP+3*G1+3/81+8*ALP+G1+3-410*G2+3/81-A* \\
 & ALP+2*(4*\log(ALP)+2)*G1+3-6*\log(ALP)+2+6*\log(ALP)-3)*G1+2/2+2*A*ALP+3*(9*\log(ALP)+2- \\
 & 6*\log(ALP)+2)*G1+2/27+6*A*ALP+2*(2*\log(ALP)+2-2*\log(ALP)+1)*G1-2-22*A*(ALP+3*L \\
 & OG(ALP))/3+4ALP+3/9)*G1+2/3-54*A*(ALP+2*\log(ALP)+2-ALP+2/4)*G1+2+38+A*\log(ALP)*G \\
 & 2+2/9+70*A*ALP+3+G1+2/27+25*A*ALP+2+G1+2-62*A*ALP+G1+2+112*A*G1+2/9-8*A*ALP*(\log \\
 & (ALP)+2-2*\log(ALP)+2)*CP+G1+16*(ALP*\log(ALP)-ALP)*CP+G1+16*\log(ALP)*CP+G1-16*A \\
 & LP*CP+G1+48*CP+G1-8*(ALP+2*\log(ALP)/2-ALP+2/4)*BMC+G1+4*\log(ALP)*BMC+G1+6*A*ALP+ \\
 & 2*BMC+G1-16*A*ALP*BMC+G1+8*BMC+G1-34+2*ALP+2*(2*\log(ALP)+2-2*\log(ALP)+1)*G1-8*A \\
 & +2*ALP*(\log(ALP)+2-2*\log(ALP)+2)*G1+2+4+2*(ALP+3*\log(ALP)/3-ALP+3/9)*G1+40*A+2 \\
 & *(ALP+2*\log(ALP)/2-ALP+2/4)*G1+16+A+2*(ALP*\log(ALP)-ALP)*G1+26*A+2*\log(ALP)*G1 \\
 & /3-11*A+2*ALP+3*G1+9-21*A+2*ALP+24G1+37*A+2*ALP+G1+274*A+2+G1/9-8*A*\log(ALP)+2 \\
 & *CP-16*A*(ALP*\log(ALP)-ALP)*CP-32*A+L3G(ALP)*CP+32*A*ALP*CP-48*A*CP+16*A*(ALP*\log \\
 & (ALP)-ALP)*BMC+8*A*\log(ALP)*BMC-4*A*ALP+2*BMC+20*A*BMC+4*A+3*\log(ALP)+3/3+4 \\
 & *A+3*ALP*(\log(ALP)+2-2*\log(ALP)+2-4*A+3*\log(ALP)+2-8*A+3*(ALP+2*\log(ALP)/2-AL \\
 & P+2/4)-8*A+3*(ALP*\log(ALP)-ALP)-38*A+3*\log(ALP)+3/2+2*A+3*ALP+3/9+5+A+3*ALP+2+2 \\
 & A+3*ALP-227*A+3/9)/16-(G1+A)*(2+ALP+3*(9*\log(ALP)+3-9*\log(ALP)+2+6*\log(ALP)-2) \\
 & *G1+3/27-ALP+3*(9*\log(ALP)+2-6*\log(ALP)+2)*G1+3/3+16*(ALP+3*\log(ALP)/3-ALP+3/9) \\
 &)*G1+3-8*ALP+3+G1+3/3+8*ALP+G1+3-74*G1+3/27-A*ALP+2*(4*\log(ALP)+3-6*\log(ALP)+2 \\
 & +6*\log(ALP)-3)*G1+2+2*A*ALP+3*(9*\log(ALP)+2-6*\log(ALP)+2)*G1+2/9+9*A*ALP+2*(2 \\
 & \log(ALP)+2-2*\log(ALP)+1)*G1+2-18*A*(ALP+3*\log(ALP)/3-ALP+3/9)*G1+2-68*A*(ALP+2 \\
 & *\log(ALP)/2-ALP+2/4)*G1+2+16*A*ALP+3+G1+2/3+23*A*ALP+2+G1+2-62*A*ALP+G1+2+38+A \\
 & *G1+2/9-8*A*ALP*(\log(ALP)+2-2*\log(ALP)+2)*CP+G1+16*CP+G1+16*(ALP+2*\log(ALP)/2-AL \\
 & P+2/4)*BMC+G1+8*A*ALP+2*BMC+G1-16*A*ALP*BMC+G1+4*BMC+G1-6+A+2*ALP+2*(2*\log(ALP)+2 \\
 & +2*\log(ALP)+1)*G1+8*A+2*ALP*(\log(ALP)+2-2*\log(ALP)+2)*G3+6+A+2*(ALP+3*\log(ALP)+3 \\
 & -ALP+3/9)*G1+56*A+2*(ALP+2*\log(ALP)+2-ALP+2/4)*G1+3+A+2+ALP+3+G1-22+A+2*ALP+2 \\
 & G1+53*A+2*ALP+G1+26+A+2+G1/3-16*A*(ALP*\log(ALP)-ALP)*CP+16*A*\log(ALP)*CP+16*A* \\
 & ALP*CP+32*A*CP+16*A*(ALP*\log(ALP)-ALP)*BMC-8*A*ALP+2*BMC+16*A*ALP*BMC+8*A*BMC+ \\
 & 4*A+3*ALP*(\log(ALP)+2-2*\log(ALP)+2)+4+A+3*\log(ALP)+2-16*A+3*(ALP+2*\log(ALP)/2- \\
 & ALP+2/4)-8*A+3*\log(ALP)+2+A+3*ALP+3/3+6*A+3*ALP+2-6+A+3*ALP-38*A+3/3)/16S
 \end{aligned}$$

$$\begin{aligned}
 & (C131) BMC(ALP,A,G1):=OPTIMIZE(ALP+2*\log(ALP)+2+G1+2*(2*\log(ALP-1)/(4+ALP-4)-ALP+2 \\
 & *\log(ALP)+G1+2*(2*\log(ALP-1)/(4+ALP-4)+ALP+2+G1+2*(2*\log(ALP-1)/(8+ALP-8)-G1+2*(2*\log \\
 & (ALP-1)/(8+ALP-8)+A*ALP+2*\log(ALP)+G1+2*(2*\log(ALP-1)/(2+ALP-2)-A*ALP*\log(ALP)*G1+2*(2*\log \\
 & (ALP-1)/(ALP-1)-A*ALP+2+G1+2*(2*\log(ALP-1)/(4+ALP-4)-3+A*G1+2*(2*\log(ALP-1)/(4+ALP-4)+A*ALP+G1+ \\
 & (2*\log(ALP-1)/(ALP-1)+A+2*\log(ALP)*(2*\log(ALP-1)/(2+ALP-2)+A+2*\log(ALP+2*(2*\log(ALP-1)/(4+ALP- \\
 & 4)+3+A+2*(2*\log(ALP-1)/(4+ALP-4)-A+2*ALP+2+G1+2*(2*\log(ALP-1)/(ALP-1)+ALP+2*\log(ALP)+2+G1+2*(2 \\
 & +2*\log(ALP-2)-ALP+2*\log(ALP)+G1+2*(ALP-1)+ALP+2+G1+2*(ALP-1)-G1+2*(ALP-1)-A*ALP+2*\log \\
 & (ALP)+2+G1/(2+ALP-2)+A*ALP+2*\log(ALP)+G1/(ALP-1)-A*ALP+2+G1/(ALP-1)+A+2*ALP+2/(2+ALP-2)+A+2/(2+ALP-2)-A+2*ALP/(ALP \\
 & -1))S
 \end{aligned}$$

$$\begin{aligned}
 & (C147) FYEH(M):=BLOCK{AA, BB, CC, ABMC, CCP, LL, LZ, L, NNETA, GG3, Y3, DELTA, N, XP, GG1, A \\
 & L(P), LAM1, BB/(1, BB0.M), N18, LOOP1, IF N = 0 THEN GO(LOOP1), XP11, SR=1+N, ALPIX
 \end{aligned}$$

28 Oct 1978 1:09

SESS13.MAUE 1,WK73

Page 1-3

P=XP,DELTA:(1.080-AA1P)+2-AA1P=LOG(AA1P)+2,GG1:(1.080-AA1P)/DELTA,AA:AA1P=LOG(AA1P)/DELTA,BBMC:BMG(AA1P,AA,GG1),CCP1CP(AA1P,AA,GG1),GG3:G3(AA1P,AA,BBMC,CCP,GG1),NNETA1NETA(AA1P,AA,BBMC,CCP,GG1),CC:(1.080-2*LAM)*CCP,PRINT(XP,GG1,AA,BBMC,CC,GG3),L10,LOOP2,IF L < N THEN G8(LOOP3),LL:1.08-1+L,L2+LL,Y3:12(L2,AA1P,AA,BBMC,CCP,GG1)+GG3*(L2*LOG(L2)-L2+1.08)-NNETA*(LOG(L2)-L2+1.08),PRINT(LL,Y3),L1L=1,G0(LOOP2),LOOP3,N:N=1,G0(LOOP1),LOOP10)S

(C150) KILL(C124,D124,C132,D132,C133,D133,C134,D134,C148,D148,C149,D149);

(C151) BONE
(C151) BONE

(C152) PAssave([supyeh, user, dsk, guest3], all);

FASDMP FASL DSK LIBLSP being loaded

15132) NO CORE = eARRAY
Error In LOADFILE att.mpt
(C153) save([supyeh, user, dsk, guest3], all);

(C153) [[SUPYEH, USER, DSK, GUEST3], 26 BLOCKS. D0, C31 D3, D38, C77, D77, C78, D78, C79, D79, C131, D131, C147, D147, C150, D150; C151, D151, C152, C153, CPP, BMCC, AA, BB, LAM, CC, D0; FLOATSBE, C, B, Y2, G3, NETA, CP; BMC, FYEH, FLOAT28F, LINENUM]

(C154) fyeh(.397b0);

8.00-1 1.69029471932851782 - 1.34107883822620782 1.05926854248433584

7.00-1 4.74213500060956881 - 3.29814204459958381 1.19742181888008983

6.00-1 1.89112206138866481 - 1.08678780745480181 2.4220756392392282

5.00-1 9.14110360193207880 - 4.22408679259238780 6.7353696232984581

4.00-1 9.99217807127640788 - 1.74258533279084581 2.29607378631160381

3.00-1 2.97131393818850180 - 7.0761385873059258-1 9.06080585543358380

2.00-1 1.89291788389860180 - 2.5387781728924498-1 4.04411166409147180

1.00-1 5.171064809871918-1 4.5861237871942938-1

THIS PAGE IS BEST QUALITY PRACTICABLY
FROM COPY FURNISHED TO CDC

28 Oct 1978 7189

SESSIS, MAGE 1, WKYJ

Page 1-4

1,00-1 1.28902209120365680 - 5.9961273772637358-2 2.03722142288219480

• 4.4768764598508598-2 2.7699377101585568-1
8

(0154)

(0155)

THIS PAGE IS A HIGH QUALITY FAX TRANSMISSION
EXACT COPY FURNISHED TO DDCI

28 Oct 1978 7109

SESSION, NAME 1, WKYJ

Page 1-1

Playback()

(Dg)

NONE

(C7) CP(ALP,A,G1) := G1+2*((2*ALP+2*LOG(ALP)+2-2*ALP+2*LOG(ALP)+ALP+2*ALP)*(2*ALP+2*LOG(ALP)+2-2*ALP+2*LOG(ALP)+2-8*ALP+2*LOG(ALP)+8*ALP+2*ALP)+G1*((4*A*ALP+2-8*A*ALP)*LOG(ALP)-2*A*ALP+2+2*A*ALP)+(2*ALM-1)-4*A*ALP*LOG(ALP)+2+8*A*ALP+2*LOG(ALP)-8*A*ALP+2+8*A*ALP)+(4*A+2*LOG(ALP)+2+2*A+2*ALP+2+2*A+2*ALP=4*A+2)*(2*ALM-1)-8*A+2*ALP*LOG(ALP)+4*A+2*ALP+2-4*A+2)/(18*ALP-8)*(2*ALM-1))S

(C77) I2(X,ALP,A,BMC,CP,G1) := -(2+G1+3*x+3*(9*LOG(X)+3-9*LOG(X)+2+6*LOG(X)-2)/8-1-A*G1+2*x+2*(4*LOG(X)+3-6*LOG(X)+2+6*LOG(X)-3)/2-4+A+3*LOG(X)+3/3-11*G1+3*x+3*(9*LOG(X)+2-6*LOG(X)+2)/81+2+A*G1,2*x,3*(9*LOG(X)+2-6*LOG(X)+2)/27+6+A*G1+2*x+2*(2*LOG(X)+2-2*LOG(X)+1)-3+A+2*G1*x+2*(2*LOG(X)+2-2*LOG(X)+1)-8*CP+G1*x*(LOG(X)+2-2*LOG(X)+2)-8*A+2*G1*x*(LOG(X)+2-2*LOG(X)+2)+4+A+3*x*(LOG(X)+2-2*LOG(X)+2)-8*A*CP*LOG(X)+2-4+A+3*LOG(X)+2+7*G1+3*(X+3*LOG(X)/3-X+3/9)/9-22+A*G1+2*(X+3*LOG(X)/3-X+3/9)/3+2+A+2*G1*(X+3*LOG(X)/3-X+3/9)-54+A*G1+2*(X+2*LOG(X)/2-X+2/4)-8*BMC+G1*(X+2*LOG(X)/2-X+2/4)+40+A+2*G1*(X+2*LOG(X)/2-X+2/4)-8*A+3*(X+2*LOG(X)/2-X+2/4)+16*CP+G1*(X+LOG(X)-X)+16+A+2*G1*(X+LOG(X)-X)-16+A*CP*(X+LOG(X)-X)+16*A*BMC*(X+LOG(X)-X)+8*A+3*(X+LOG(X)-X)-74*G1+3*LOG(X)/27+38*A*G1+2*LOG(X)/9+16*CP+G1*LOG(X)+4*BMC+G1*LOG(X)+26+A+2*G1+LOG(X)/3-32+A*CP*LOG(X)+8*A*BMC*LOG(X)-38+A+3*LOG(X)/3-14*G1+3*x+3/81+78+A*G1+2*x,3/27-11*A+2*G1*x+3/9+2*A+3*x+3/9+25*A*G1+2*x+2+6*BMC+G1*x+2-21*A+2*G1*x+2-4*A*BMC*x+2+8*A+3*x+2+8*G1,8*x-62+A*G1+2*x-16*CP+G1*x-16*BMC+G1*x+37+A+2*G1*x+32+A*CP*x+2+A+3*x-410*G1,3/81+12*A*G1+2*x+9+48*CP+G1+8*BMC+G1+274+A+2*G1+9+48*A*CP+29+A*BMC+227+A+3/9)/16S

(C78) G3(ALP,A,BMC,CP,G1) := G1*(2*ALP+3*(9*LOG(ALP)+3-9*LOG(ALP)+2+A*LOG(ALP)-2)*G1+3/81+11*A*LP+3*(9*LOG(ALP)+2-6*LOG(ALP)+2)*G1+3/81+70*(ALP+3*LOG(ALP)/3-ALP+3/9)*G1+3/9-74*LOG(ALP)*G1+3/27+4*G1+3*G1+3/81+8*ALP+G1+3-410*G1+3/81-A*ALP+2*(4*LOG(ALP)+3-6*LOG(ALP)+2+6*LOG(ALP)-3)*G1+2/2+2+A*ALP+3*(9*LOG(ALP)+2-6*LOG(ALP)+2)*G1+2/2+7+A*ALP+2*(2*LOG(ALP)+1)*G1+2-22*A*(ALP+3*LOG(ALP)/3-ALP+3/9)*G1+2/3-54*A*(ALP+2*LOG(ALP)/2-ALP+2/4)*G1+2+38*A*LOG(ALP)*G1+2/9+78*A*ALP+3*G1+2/27+25*A*ALP+2*G1+2-62*A*ALP+G1+2+112*A*G1+2/9-8*A*ALP*(LOG(ALP)+2-2*LOG(ALP)+2)*CP+G1+16*(ALP*LOG(ALP)-ALP)*CP+G1+16*LOG(ALP)*CP+G1-16*ALP+CP+G1+48*CP+G1-8*(ALP+2*LOG(ALP)/2-ALP+2/4)*BMC+G1+42*LOG(ALP)*BMC+G1+6*ALP+2*BMC+G1-16*ALP+8*BMC+G1-3*A+2*ALP+2*(2*LOG(ALP)+2-2*LOG(ALP)+1)*G1-8*A+2*ALP*(LOG(ALP)+2-2*LOG(ALP)+2)*G1+2+A+2*(ALP+3*LOG(ALP)/3-ALP+3/9)*G1+40*A+2*(ALP+2*LOG(ALP)/2-ALP+2/4)*G1+16+A+2*(ALP*LOG(ALP)-ALP)*G1+26*A+2*LOG(ALP)*G1/3-11*A+2*ALP+3*G1/9-21*A+2*ALP+2*G1+37+A+2*ALP+G1+274+A+2*G1/9-8*A+1*LOG(ALP)+2*C-16*A*(ALP*LOG(ALP)-ALP)*CP-32+A*LOG(ALP)*CP+32+A*ALP+4*CP+48*A*CP+16*A*(ALP+LOG(ALP)-ALP)*BMC+8*A+LOG(ALP)+BMC+4*A*ALP+2+20*A*BMC-4*A+3*LOG(ALP)+3/3+4*A+3*ALP*(LOG(ALP)+2-2*LOG(ALP)+2)-4*A+3*LOG(ALP)+2+8*A+3*(ALP+2*LOG(ALP)/2-ALP+2/4)-8*A+3*(ALP*LOG(ALP)-ALP)-38+A+3*LOG(ALP)/3+2+A+3*ALP+3/9+5*A+3*ALP+2+2+A+3*ALP-227+A+3/9)/16-(G1+A/ALP)*(2*ALP+3*(9*LOG(ALP)+3-9*LOG(ALP)+2+6*LOG(ALP)-2)*G1+3/27-ALP+3*(9*LOG(ALP)+2-6*LOG(ALP)+2)*G1+3/3+16*(ALP+3*LOG(ALP)/3-ALP+3/9)*G1+3-B*ALP+3*G1+3/3+8*ALP+G1+4-74*G1+3/27-A*ALP+2*(4*LOG(ALP)+3-6*LOG(ALP)+2+6*LOG(ALP)-3)*G1+2+A*ALP+3*(9*LOG(ALP)+2-6*LOG(ALP)+2)*G1+2/9+9*A*ALP+2*(2*LOG(ALP)+2-2*LOG(ALP)+1)*G1+2-18*A*(ALP+3*LOG(ALP)/3-ALP+3/9)*G1+2-60*A*(ALP+2*LOG(ALP)/2-ALP+2/4)*G1+2+16*A*ALP+3*G1+2/3+23*A*ALP+2+G1+2-62*A*ALP+G1+2+38*A*G1+2/9-8*A*ALP*(LOG(ALP)+2-2*LOG(ALP)+2)*CP+G1+16*CP+G1-16*(ALP+2*LOG(ALP)/2-ALP+2/4)*BMC+G1+8*A*ALP+2*BMC+G1-16*ALP+3*MC+G1+4*BMC+G1-6*A+2*ALP+2*(2*LOG(ALP)+2

18 Oct 1978 7:09

SESSION.MAGE 1.WKY3

Page 1-2

2-2*LOG(ALP)+1)*G1+8*A+2*ALP*(LOG(ALP)+2-2*LOG(ALP)+2)*G1+6*A+2*(ALP+3*LOG(ALP)+3-ALP+3/9)*G1+56*A+2*(ALP+2*LOG(ALP)+2-ALP+2/4)*G1-32A+2*ALP+3*G1-22*A+2*ALP+2*G1+53*A+2*ALP+G1+26*A+2*G1/3-16*A*(ALP+LOG(ALP)-ALP)+CP-16*A+LOG(ALP)+CP+16*A+ALP+CP+32*A+CP+16*A*(ALP+LOG(ALP)-ALP)+BMC-8*A+ALP+2*BMC+16*A+ALP+ALP+8*A+BMC+4*A+3*ALP*(LOG(ALP)+2-2*LOG(ALP)+2-4*A+3*LOG(ALP)+2-16*A+3*(ALP+2*LOG(ALP)+2-ALP+2/4)-8*A+3*LOG(ALP)+2*A+3*ALP+3/3+6*A+3*ALP+2-69A+3*ALP+38*A+3/3)/165

(C79) NETA(ALP,A,BMC,CP,G1):=A*(2*ALP+3*(9*LOG(ALP)+3-9*LOG(ALP)+2+6*LOG(ALP)-2)*G1+3/81-11*ALP+3*(9*LOG(ALP)+2+6*LOG(ALP)+2)*G1+3/81+70*(ALP+3*LOG(ALP)/3-A*LP+3/9)*G1+3/9-74*LOG(ALP)+G1+3/27-142*ALP+3*G1+3/81+8*ALP+G1+3-41A+G2+3/81-A+ALP+2*(4*LOG(ALP)+3-6*LOG(ALP)+2+6*LOG(ALP)-3)*G1+2/2+2*A+ALP+3*(9*LOG(ALP)+2-6*LOG(ALP)+2)*G1+2/27+6*A+ALP+2*(2*LOG(ALP)+2-2*LOG(ALP)+1)*G1+2-22*A+(ALP+3*LOG(ALP)/3+ALP+3/9)*G1+2/3-54*A+(ALP+2*LOG(ALP)/2-ALP+2/4)*G1+2+38*A+LOG(ALP)+G1+2/9+70*A+ALP+3*G1+2/27+25*A+ALP+2*G2+2-62*A+ALP+G1+2+112*A+G1+2/9-8*A+ALP*(LOG(ALP)+2-2*LOG(ALP)+2)*CP+G1+16*(ALP+LOG(ALP)-ALP)+CP+G1+16*LOG(ALP)+CP+G1-16*A+LP+CP+G1+48*CP+G1-8*(ALP+2*LOG(ALP)/2-ALP+2/4)*BMC+G1+4*LOG(ALP)+BMC+G1+6*A+ALP+2*BMC+G1-16*A+LP+CP+G1+8*BMC+G1-3*A+2*ALP+2*(2*LOG(ALP)+2-2*LOG(ALP)+1)*G1-8*A+2*ALP*(LOG(ALP)+2-2*LOG(ALP)+2)*G1+16*A+2*(ALP+LOG(ALP)/2-ALP+2/4)*G1+16*A+2*(ALP+LOG(ALP)-ALP)+G1+26*A+2*LOG(ALP)+G1+3-11*A+2*ALP+3*G1+9-21*A+2*ALP+2*G1+37*A+2*ALP+G1+274*A+2*G1+9-8*A+LOG(ALP)+2*CP-16*A*(ALP+LOG(ALP)-ALP)+CP-32*A+LOG(ALP)+CP+32*A+ALP+CP-48*A+CP+16*A+(ALP+LOG(ALP)-ALP)+BMC+8*A+LOG(ALP)+BMC-4*A+ALP+2*BMC+20*A+ALP+2*BMC-4*A+3*LOG(ALP)+3/3+4*A+3*ALP*(LOG(ALP)+2-2*LOG(ALP)+2)*G1-4*A+3*LOG(ALP)+2-8*A+3*(ALP+2*LOG(ALP)/2-ALP+2/4)-8*A+3*(ALP+LOG(ALP)-ALP)+38*A+3*LOG(ALP)+3+2*A+3*ALP+3/9+5*A+3*ALP+2+2*A+3*ALP-227*A+3/9)/16-(G1+A)*(2*ALP+3*(9*LOG(ALP)+3-9*LOG(ALP)+2+6*LOG(ALP)-2)*G1+3/27-ALP+3*(9*LOG(ALP)+2-6*LOG(ALP)+2)*G1+3/3+16*(ALP+3*LOG(ALP)/3-ALP+3/9)*G1+3-8*A+ALP+3*G1+3/3+8*A+ALP+G1+3-74*A+G2+3/27-A+ALP+2*(4*LOG(ALP)+3-6*LOG(ALP)+2+6*LOG(ALP)-3)*G1+2+2*A+ALP+3*(9*LOG(ALP)+2-6*LOG(ALP)+2)*G1+2/9+9*A+ALP+2*(2*LOG(ALP)+2-2*LOG(ALP)+1)*G1+2-18*A+(ALP+3*LOG(ALP)/3-ALP+3/9)*G1+2-69*A+(ALP+2*LOG(ALP)/2-ALP+2/4)*G1+2+16*A+ALP+3*G1+2/3+23*A+ALP+29G1+2-62*A+ALP+G1+2+38*A+G1+2/9-8*A+LOG(ALP)+2-2*LOG(ALP)+2)*CP+G1+16*CP+G1+16*(ALP+2*LOG(ALP)/2-ALP+2/4)*BMC+G1+8*A+ALP+2*BMC+G1+16*A+ALP+G1+6*A+2*ALP+2*(2*LOG(ALP)+2)*G1+8*A+2*ALP*(LOG(ALP)+2-2*LOG(ALP)+2)*G1+8+6*A+2*(ALP+3*LOG(ALP)+3-ALP+3/9)*G1+56*A+2*(ALP+2*LOG(ALP)/2-ALP+2/4)*G1-3*A+2*ALP+3*G1-22*A+2*ALP+2*G1+53*A+2*ALP+G1+26*A+2*G1/3-16*A*(ALP+LOG(ALP)-ALP)+CP-16*A+LOG(ALP)+CP+16*A+ALP+CP-32*A+CP+16*A*(ALP+LOG(ALP)-ALP)+BMC-8*A+ALP+2*BMC+16*A+ALP+ALP+8*A+BMC+4*A+3*ALP*(LOG(ALP)+2-2*LOG(ALP)+2)*4*A+3*LOG(ALP)+2-16*A+3*(ALP+2*LOG(ALP)/2-ALP+2/4)-8*A+3*LOG(ALP)+2*A+3*ALP+3/3+6*A+3*ALP+2-6*A+3*ALP+38*A+3/3)/165

(C131) BMC(ALP,A,G1):=OPTIMIZE(ALP+2*LOG(ALP)+2*G1+2*(8*ALM-1)/(4*ALP-4)-ALP+2*LOG(ALP)+G1+2*(2*ALM-1)/(4*ALP-4)+A+ALP+2*LOG(ALP)+G1+2*(2*ALM-1)/(8*ALP+8)+A+ALP+2*LOG(ALP)+G1+2*(2*ALM-1)/(2*ALP+2)-A+ALP+LOG(ALP)+G1+2*(2*ALM-1)/(ALP-1)+A+ALP+2*G1+2*(2*ALM-1)/(4*ALP-4)-3*A+G1+2*(2*ALM-1)/(4*ALP-4)+A+ALP+G1+2*(2*ALM-1)/(ALP-1)+A+2*LOG(ALP)*(2*ALM-1)/(2*ALP+2)+A+2*ALP+2*(2*ALM-1)/(4*ALP-4)+3*A+2*(2*ALM-1)/(4*ALP-4)-A+2*ALP*(2*ALM-1)/(ALP-1)+ALP+2*LOG(ALP)+2*G1+2*(2*ALP-2)-ALP+2*LOG(ALP)+G1+2/(ALP-1)+ALP+2*G1+2/(ALP-1-G1+2/(ALP-1)-A+ALP+LOG(ALP)+(ALP-1)+A+2*ALP+2/(2*ALP-2)+A+2/(2*ALP-2)-A+2*ALP/(ALP-1))

(C147) FYEH(M):=BLOCK([AA, BB, CC, BBH0, CCP, LL, L2, L, NNETA, GG3, Y3, DELTA, N, XP, GG1, A, ALP], LAM1, BB0/(1, BB0-M), N18, LOOP1, IF N = 0 THEN GO(LOOP10), XPI1, BR-1+N, AALP) X

28 Oct 1978 7189

SESSION.MASC 1.WKY3

Page 1-3

XP,DELTA1(1.000-AALP)+2-AALP+LOG(AALP)+2,GG1:(1.000-AALP)/DELTA,AA;AALP+LOG(AA
LP)/DELTA,BBMC;BMC(AA,P,AA,GG1),CCP1CP(AALP,AA,GG1),GG3;G3;AALP,AA,BBMC,CCP,GG
1),NNETA;NETA1AALP,AA,BBMC,CCP,GG1)+CG1(1.3B-2*LAM)+CCP,PRINT(XP,GG1,AA,BBMC,
CC,GG3),L10,LOOP2,IF L < N THEN G0(LOOP3),LL(1,3B-1+L,62)LL,LL,Y3;I2(L2,AALP,A
A,BBMC,CCP,GG1)+GG3,(L2+LOG(L2)-L2+1.000)-NNETA+(LOG(L2)-L2+1.000).PRINT(LL,Y3
,L1L-1,G0(LOOP2),LOOP3,NIN-1,G0(LOOP2),LOOP10)S

(C157) PLAYBACK(20);

(D157)

BONE

(C158) KILL(C151,D151,C155,D155,C148,D148,C149,D149,C152,D152,C153,D153,C154,D
154);

(D158)
(D159)

BONE
BONE

(C160) ?y6h(.39760);

3.7B-1 4.23881080914744380 - 1.33694318669095480 1.71379497650291481

+ 1.0887080554882381 ? 1.3930092539321180
0

(D160)
(C161)

THIS PAGE IS BEST QUALITY PRACTICABLE
FROM COPY FURNISHED TO DDC

Name:

Project: 1 Programmer: WKY

File Name: SESS20.MAC[1,WKY]

File Last Written: 16:48 21 Oct 1978

Time: 18:34 Date: 21 Oct 1978

Stanford University
Artificial Intelligence Laboratory
Computer Science Department
Stanford, California

THIS PAGE IS OF BEST QUALITY
FROM COPY FURNISHED TO BDC

21 Oct 1978 18:34

SESS20.MAC[1,WKY]

PAGE 1-1

fyeh(.397b0);

2.0B-1 1.892917883898681B0 - 2.538778172892449B-1 4.044111664051471B0
- 5.17106480987191B-1 4.586123787194293B-1
2.2B-1 2.061085177077259B0 - 3.174529578284189B-1 4.709155844186585B0
- 7.696496698827404B-1 5.079747242714554B-1
2.4B-1 2.2498571168135B0 - 3.924926452864021B-1 5.509068762588557B0
- 1.12695633889539B0 5.631380473528801B-1
2.6B-1 2.462107758166664B0 - 4.809199837256892B-1 6.474651901599728B0
- 1.628773212506969B0 6.249519525553335B-1
2.8B-1 2.701244546666852B0 - 5.850381524454815B-1 7.64478714266234B0
- 2.3297671496256B0 6.944178139120044B-1
3.0B-1 2.971313938188501B0 - 7.076138587305925B-1 9.068805855433583B0
- 3.305363443841588B0 7.7272008665462B-1
3.2B-1 3.277134934913673B0 - 8.519825786466818B-1 1.080964778749077B1
- 4.660025053028231B0 8.612655866169745B-1
3.4B-1 3.624467823386744B0 - 1.022181864837844B0 1.294810212993135B1
- 6.539076699265395B0 9.617328962013918B-1
3.6B-1 4.020228013530225B0 - 1.223121133074559B0 1.558854504691232B1
- 9.145721055238938B0 1.076134805159009B0
3.8B-1 4.472758357844417B0 - 1.460799255798733B0 1.886676596645493B1
- 1.27657292487095B1 1.206897698713914B0
4.0B-1 4.992178071276407B0 - 1.742585332790845B0 2.296073786311603B1
- 1.780358582241836B1 1.356963181148589B0
(D157) 8
(C158)

Name:

Project: 1 Programmer: WKY

File Name: SESS20.MAC[1, WKY]

File Last Written: 16:48 21 Oct 1978

Time: 18:34 Date: 21 Oct 1978

Stanford University
Artificial Intelligence Laboratory
Computer Science Department
Stanford, California

21 Oct 1978 18:34

SESS20.MAC[1,WKY]

PAGE 1-1

fyeh(.397b0);

2.0B-1 1.892917883898601B0 - 2.538778172892449B-1 4.044111664051471B0
- 5.17106480987191B-1 4.586123787194293B-1
2.2B-1 2.061085177077259B0 - 3.174529578284189B-1 4.709155844186585B0
- 7.696496698827404B-1 5.079747242714554B-1
2.4B-1 2.2498571168135B0 - 3.924926452064021B-1 5.509068762588557B0
- 1.12695633889539B0 5.631380473528001B-1
2.6B-1 2.462107758166664B0 - 4.809199837256092B-1 6.474651901599728B0
- 1.628773212506969B0 6.249519525553335B-1
2.8B-1 2.701244546666852B0 - 5.850381524454815B-1 7.64478714266234B0
- 2.3297671496256B0 6.944178139120044B-1
3.0B-1 2.971313938188501B0 - 7.076138587305925B-1 9.068805855433583B0
- 3.305363443841588B0 7.7272008665462B-1
3.2B-1 3.277134934913673B0 - 8.519825786466818B-1 1.080964778749077B1
- 4.660025053028231B0 8.612655866169745B-1
3.4B-1 3.624467823306744B0 - 1.022181864837844B0 1.294810212993135B1
- 6.539076699265395B0 9.617328962013918B-1
3.6B-1 4.020228013530225B0 - 1.223121133074559B0 1.558854504691232B1
- 9.145721055238938B0 1.076134805159009B0
3.8B-1 4.472758357844417B0 - 1.460799255798733B0 1.886676596645493B1
- 1.27657292487095B1 1.206897698713914B0
4.0B-1 4.992178071276407B0 - 1.742585332798845B0 2.296873786311683B1
- 1.780358582241836B1 1.356963181148589B0
(D157) 0
(C158)

Name:

Project: 1 Programmer: WKY

File Name: SESS20.MAC[1,WKY]

File Last Written: 16:48 21 Oct 1978

Time: 18:34 Date: 21 Oct 1978

Stanford University
Artificial Intelligence Laboratory
Computer Science Department
Stanford, California

21 Oct 1978 18:34

SESS20.MAC[1,WKY]

PAGE 1-1

fyeh(.397b0);

2.0B-1 1.892917883898601B0 - 2.5387781728924498-1 4.044111664051471B0
- 5.17106480987191B-1 4.5861237871942938-1
2.2B-1 2.861085177077259B0 - 3.174529578284189B-1 4.709155844186585B0
- 7.696496698827404B-1 5.079747242714554B-1
2.4B-1 2.2498571168135B0 - 3.924926452064021B-1 5.509968762588557B0
- 1.12695633889539B0 5.631380473528001B-1
2.6B-1 2.462107758166664B0 - 4.809199837256092B-1 6.474651901599728B0
- 1.628773212506969B0 6.2495195255533358-1
2.8B-1 2.701244546666852B0 - 5.850381524454815B-1 7.64478714266234B0
- 2.3297671496256B0 6.944178139120044B-1
3.0B-1 2.971313938188501B0 - 7.076138587305925B-1 9.068805855433583B0
- 3.305363443841588B0 7.7272008665462B-1
3.2B-1 3.277134934913673B0 - 8.519825786466818B-1 1.088964778749077B1
- 4.660025053028231B0 8.612655866169745B-1
3.4B-1 3.624467823306744B0 - 1.022181864837844B0 1.294810212993135B1
- 6.539076699265395B0 9.617328962013918B-1
3.6B-1 4.020228013530225B0 - 1.223121133074559B0 1.558854584691232B1
- 9.145721055238938B0 1.876134805159889B0
3.8B-1 4.472758357844417B0 - 1.460799255798733B0 1.886676596645493B1
- 1.27657292487095B1 1.206897698713914B0
4.0B-1 4.992178071276407B0 - 1.742585332790845B0 2.296873786311603B1
- 1.780358582241836B1 1.356963181148589B0
8
(D157)
(C158)

21 Oct 1978 18:34

SESS20.MAC[1,WKY]

PAGE 1-1

fyeh(.397b0);

2.0B-1 1.89291788389860180 - 2.5387781728924498-1 4.04411106405147180

- 5.17106480987191B-1 4.5861237871942938-1
2.2B-1 2.06108517707725980 - 3.174529578284189B-1 4.70915584418658580

- 7.696496698827404B-1 5.079747242714554B-1
2.4B-1 2.249857116813580 - 3.9249264520640218-1 5.50906876258855780

- 1.1269563388953980 5.6313804735280018-1
2.6B-1 2.462107758166664B0 - 4.809199837250092B-1 6.474651901599728B0

- 1.62877321250696980 6.249519525553335B-1
2.8B-1 2.70124454666685280 - 5.850381524454015B-1 7.64478714266234B0

- 2.3297671496256B0 6.944178139128044B-1
3.0B-1 2.971313938188501B0 - 7.076138587305925B-1 9.06880585543358380

- 3.305363443841588B0 7.7272008665462B-1
3.2B-1 3.27713493491367380 - 8.5198257864668188-1 1.08096477874907781

- 4.660025053028231B0 8.612655866169745B-1
3.4B-1 3.624467823306744B0 - 1.022181864837844B0 1.294810212993135B1

- 6.53907669926539580 9.6173289620139188-1
3.6B-1 4.02022801353022580 - 1.223121133074559B0 1.558854504691232B1

- 9.145721055238938B0 1.076134805159009B0
3.8B-1 4.472758357844417B0 - 1.460799255798733B0 1.886676596645493B1

- 1.27657292487095B1 1.206897698713914B0
4.0B-1 4.992178071276407B0 - 1.742585332790845B0 2.296073786311683B1

- 1.780358582241836B1 1.356963181148589B0

(D157)

8

(C158)

Name:

Project: 1 Programmer: WKY

File Name: SESS20.MAC[1, WKY]

File Last Written: 16:48 21 Oct 1978

Time: 18:34 Date: 21 Oct 1978

Stanford University
Artificial Intelligence Laboratory
Computer Science Department
Stanford, California

Appendix D
VIBRATIONAL MODELS OF THE GRADIOMETER

D-1 Simple Spring Mass System

The notations used in the models to be developed are established using the first-order example in Fig. D-1

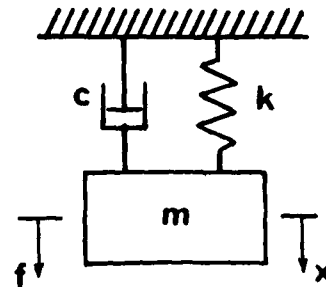


FIG. D-1 SIMPLE DAMPED SPRING-MASS SYSTEM

The equation of motion is

$$\ddot{x} + \frac{c}{m} \dot{x} + \frac{k}{m} x = 0 \dots \quad (D.1)$$

where the solution is

$$x = c_1 e^{[-(c/2m) + \sqrt{(c/2m)^2 - k/m}]t} + c_2 e^{[-(c/2m) - \sqrt{(c/2m)^2 - k/m}]t} \dots \quad (D.2)$$

Defining ξ , the damping factor $= c/c_c$; c_c , the critical damping constant, equals $2m\omega_n$; $\omega_n = \sqrt{k/m}$. Equation (D-2) can be simplified to

$$x = c_1 e^{(-\xi + \sqrt{\xi^2 - 1})\omega_n t} + c_2 e^{(-\xi - \sqrt{\xi^2 - 1})\omega_n t} \quad (D.3)$$

Since our diaphragms have high Q , $\xi < 1$, (D.2) can be written as

$$x = A e^{-\xi \omega_n t} \sin(\sqrt{1 - \xi^2} \omega_n t + \phi) \dots \quad (D.4)$$

We can relate Q and ξ , the damping factor, by the definition of Q :

$$Q \triangleq \pi f_n \tau \dots \quad (D.5)$$

where τ is the time required for the amplitude of the resonant oscillation to decrease by a ratio of e , the natural number. From (D.4)

$$\begin{aligned} e^{-\xi \omega_n \tau} &= e^{-1} \\ \therefore \tau &= \frac{1}{\xi \omega_n} \\ \therefore Q &= \pi f_n \tau = \frac{1}{2\xi} \dots \end{aligned} \quad (D.6)$$

D-2 Dynamics of Accelerometers

The motions of the diaphragm may be modeled by a simple spring-mass damper system with moving support as shown in Fig. D-2 [Crede, 1961].

Define

$$x(t) = z(t) - y(t)$$

where $z(t)$ and $y(t)$ are time displacements with respect to a fixed reference, and $x(t)$ is the measurement of acceleration. The equation of motion is

$$\ddot{x} + 2\xi \dot{x} + \frac{\omega_n^2}{n} x = -\ddot{y} \dots \quad (D.7)$$

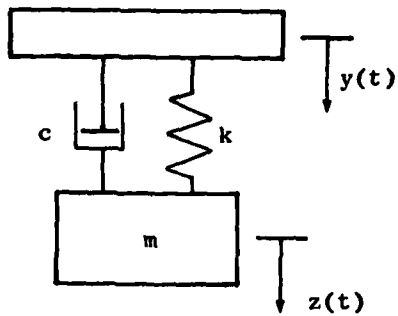


FIG. D-2 SIMPLE MODEL OF ACCELEROMETER. The movable support in this model is analogous to the motions of the case of the actual accelerometer.

For sinusoidal forcing function $y = Y_e^{j\omega_f t}$ we can write $x = X e^{j(\omega_f t - \phi)}$. This leads to

$$\frac{X}{Y} = \frac{r^2}{[(1-r^2)^2 + (2\xi r)^2]^{\frac{1}{2}}} \quad (D.8a)$$

$$\phi = \tan^{-1} \frac{2\xi r}{1 - r^2} \quad (D.8b)$$

where $r \triangleq \omega_f/\omega_n$.

Differentiating (D.8a) with respect to r and equating to zero, the maximum value of X is

$$\frac{X_{\max}}{Y} = \frac{1}{2\xi\sqrt{(1-\xi^2)}} \quad (D.9)$$

for $\xi \ll 1$.

$$\frac{X_{\max}}{Y} \approx \frac{1}{2\xi} = Q \dots \quad (D.10)$$

For acceleration measurement with

$$y = Ye^{j\omega_f t}$$

$$|\ddot{y}| = \omega_f^2 y$$

and for perfect correlation of X with $\omega^2 Y$

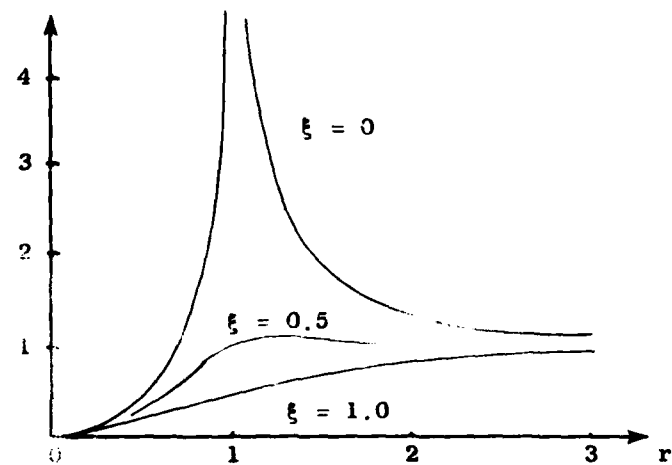
$$\frac{X}{Y} = K\omega_f^2 \dots \quad (D.11)$$

where K is an arbitrary constant.

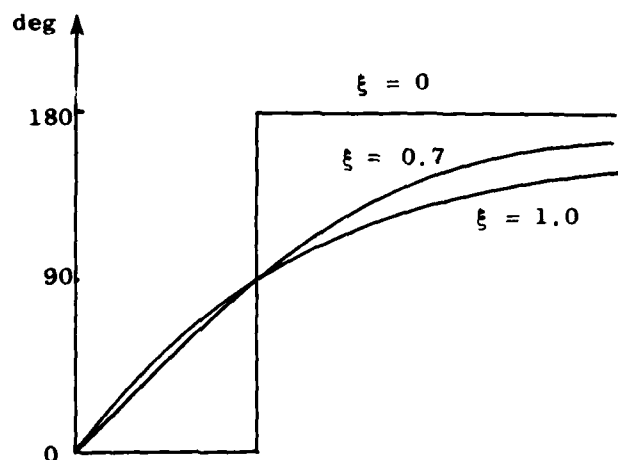
Equation (D.11) describes a family of parabolas. A study of Fig. D-3 will show that for a value of $r \ll 1$, all curves irrespective of damping, are good approximation of parabolas. It can also be noted that when $r > 1$, no curve even remotely resembles a parabola. Thus seismic (spring-mass-damper) systems used to measure acceleration will be "stiff" systems with relatively high natural frequencies. That is, if we lowered the natural frequency of the system to increase its displacement under a given acceleration, the useful frequency range of the device is reduced proportionally.

Although the degree of damping does not appear to be critical with respect to amplitude, the question of phase angle must still be addressed. Valid results for motion that are not simple harmonic will be given only when the phase angle is zero deg, + 180 deg or varies linearly with the frequency. Referring to Fig. D-3b will show that for $r < 1$, $\phi = 0$ (deg) for $\xi = 0$ and the curve for ξ slightly less than 0.7 is almost a straight line. Therefore the only amplitude ratio curves we need to consider further are those for $\xi = 0$ and $\xi \approx 0.65$.

The acceleration error will be



(a) Transfer Functions of the Accelerometer



(b) Phase Shifts of the Accelerometer

FIGS. D-3 FREQUENCY RESPONSE OF THE ACCELEROMETER UNDER DIFFERENT DAMPING RATIOS.

$$\begin{aligned}
 e &= \frac{X - K\omega_f^2 Y}{K\omega_f^2 Y} \times 100\% \\
 &= \left[\frac{1/\omega_n^2}{\frac{K\sqrt{(1-r^2)^2 + (2\xi r)^2}}{1/\omega_n^2} - 1} \right] \times 100\% \quad (D.12)
 \end{aligned}$$

after substituting (D.8) for X/Y . The optimum value of K will depend upon the definition of optimum value with respect to an error which is a function of frequency. However, K will not differ greatly from $1/\omega_n^2$ and that value will be used. For $K = 1/\omega_n^2$, (D.12) becomes

$$e = \left[\frac{1}{\sqrt{(1-r^2)^2 + (2\xi r)^2}} - 1 \right] \quad (D.13)$$

and the curves for $\xi = 0$ and $\xi = 0.65$ are given in Fig. D-4.

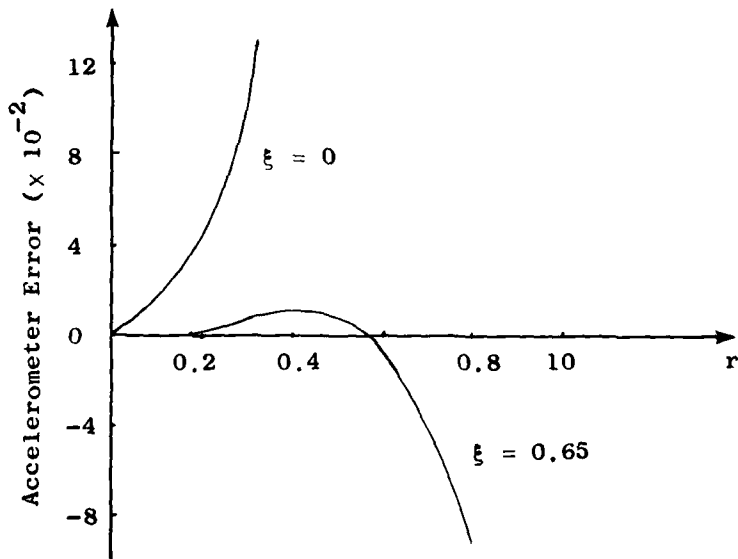


FIG. D-4 VARIATION OF THE ACCELERATION ERROR WITH FREQUENCY.
The largest range of frequency at which the acceleration error stays within set bounds is largest at $\xi = 0.65$.

As can be seen, if a 5% error can be tolerated, an accelerometer with zero damping will be good up to $r \geq 0.22$ while if damping is 0.65, the range will be extended to $r = 0.74$, approximately three times the useful range of the undamped system. In our diaphragm accelerometer, the system is undamped. Typically the useful range is then below $0.22 \omega_n$, about 180 Hz for 850 Hz diaphragm and 20 Hz for 50 Hz diaphragm. The system suffers from the typical disadvantages of an undamped system, i.e., the response near ω_n is many times greater than those of low frequencies and ringing introduced by transients will be great and will not die off quickly.

When two accelerometers are combined in the gradiometer, the useful range may be extended by the differencing action. This will be investigated in the next section.

D-3 Vibrational Analysis of the Gradiometer

Since the diaphragm with the lowest Q has a damping factor ξ on the order of 0.0001, the gradiometer can be modeled as an undamped spring mass system of two degree-of-freedom as given in Fig. D-5.

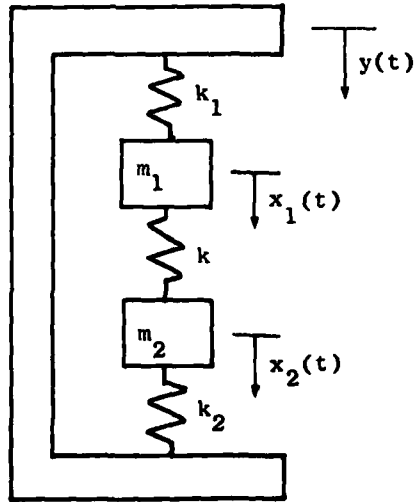


FIG. D-5 SIMPLE MODEL OF GRADIOMETER. The spring constant, k , models the coupling between the two proof masses in the assembly.

The constants k_1 and k_2 are the equivalent spring rates as in diaphragms 1 and 2, and m_1 and m_2 are its equivalent mass; k accounts for the coupling between the two diaphragms; $y(t)$ is the displacement of the frame and is sinusoidal with amplitude Y ; $x_1(t)$ and $x_2(t)$ are coordinate systems relative to a frame of reference fixed to the support.

The equations of motion are

$$m_1 \ddot{x}_1 + (k + k_1)x_1 - kx_2 = -m_1 \ddot{y} \quad (D.14a)$$

$$-kx_1 + m_2 \ddot{x}_2 + (k+k_2)x_2 = -m_2 \ddot{y}. \quad (D.14b)$$

Since there is no damping, we have

$$y(t) = Y \cos \omega_f t \quad (D.15a)$$

$$x_1(t) = X_1 \cos \omega_f t \quad (D.15b)$$

$$x_2(t) = X_2 \cos \omega_f t \quad (D.15c)$$

where ω_f is the angular velocity of the forcing function.

Substituting these equations into (D.14) we get

$$\begin{bmatrix} -m_1 \omega_f^2 + (k+k_1) & -k \\ -k & -m_2 \omega_f^2 + (k+k_2) \end{bmatrix} \begin{bmatrix} X_1 \\ X_2 \end{bmatrix} = \begin{bmatrix} m_1 \\ m_2 \end{bmatrix} \omega_f^2 Y \quad (D.16)$$

The determinant D is

$$D = \omega_f^4 - 2(\alpha + \beta)\omega_f^2 + 4\alpha\beta - \gamma\epsilon \quad (D.17)$$

where

$$2\alpha = \frac{k+k_1}{m_1}, \quad 2\beta = \frac{k+k_2}{m_2} \quad (D.18a)$$

$$\gamma = \frac{k}{m_2}, \quad \epsilon = \frac{k}{m_2}. \quad (D.18b)$$

Equating (D.17) to zero, we have for the resonant frequencies of the gradiometer

$$\omega_n^2 = (\alpha + \beta) \pm \sqrt{(\alpha - \beta)^2 + \gamma \epsilon} . \quad (D.19)$$

The displacements x_1 and x_2 are derived from (D.15). They are

$$\frac{x_1}{\omega_f^2 Y} = \frac{2\beta + \gamma - \omega_f^2}{D} \quad (D.20a)$$

$$\frac{x_2}{\omega_f^2 Y} = \frac{2\alpha + \epsilon - \omega_f^2}{D} \quad (D.20b)$$

where D , α , β , and ω_f are defined above; $\omega_f^2 Y$ is the acceleration of the frame.

Using the output equation (3.75) for the DDGG, and (D.20), the result becomes

$$i_s(t) = \beta [2(\beta - \alpha) + \gamma - \epsilon] \frac{\omega_f^2 Y}{D} = \beta (\omega_2^2 - \omega_1^2) \frac{\omega_f^2 Y}{D} \quad (D.21)$$

where

$$\omega_1^2 = \frac{k_1}{m_1} \quad (D.22a)$$

$$\omega_2^2 = \frac{k_2}{m_2} . \quad (D.22b)$$

Thus if $\omega_1^2 = \omega_2^2$, output due to common acceleration will be zero independent of the forcing frequency. This is not true for the CDGG whose output is

$$i_s(t) = \beta [\sigma_1 (2\beta + \gamma - \omega_f^2) - \sigma_2 (2\alpha + \epsilon - \omega_f^2)] \frac{\omega_f^2 Y}{D} \quad (D.23)$$

where

$$\beta = h \frac{2}{1 + \gamma} , \quad \sigma_1 = \frac{1}{\eta} \left(\frac{1}{d} \right) ,$$

and i , d , and h are defined in Eq. (4.40). The balancing condition is

$$\sigma_1(2\beta + \gamma - \omega_b^2) = \sigma_2(2\alpha + \epsilon - \omega_b^2) \quad (D.24)$$

where ω_b is the frequency of the balancing acceleration. Thus the scale factors adjusted at the balancing frequency are not matched at any other frequency. The output owing to this mismatch is

$$i_s(t) = \beta \sigma_2(2\alpha + \epsilon - \omega_b^2) \left[\frac{2\beta + \gamma - \omega_f^2}{2\beta + \gamma - \omega_b^2} - \frac{2\alpha + \epsilon - \omega_f^2}{2\alpha + \epsilon - \omega_b^2} \right] \frac{\omega_f^2 Y}{D} \quad (D.25)$$

Using this simple model, the DDGG will remain balanced over a broad range of frequency after it has been balanced. On the other hand, CDGG is balanced only at one frequency. The degree of unbalance at a frequency different from the balancing frequency depends on how close the two diaphragms are matched. The CDGG will be matched over a broad range of frequency below the resonant frequency if the two diaphragms are identical, i.e.,

$$2\beta + \gamma = 2\alpha + \epsilon. \quad (D.26)$$

Equation (D.19) may be rewritten as

$$\begin{aligned} 2\omega_n^2 &= \omega_1^2 + \omega_2^2 + (\gamma + \epsilon) \pm \sqrt{(\omega_1^2 - \omega_2^2 + \gamma - \epsilon)^2 + 4\gamma\epsilon} \\ &\approx \omega_1^2 + \omega_2^2 \pm \sqrt{(\omega_1^2 - \omega_2^2)^2 + 4\gamma\epsilon} \quad \dots \end{aligned} \quad (D.27)$$

since γ and ϵ are almost equal and small.

When the lower of the two frequencies is increased, typically by increasing the current stored in the current loop, the curve of ω_n^2 is as sketched in Fig. D-6.

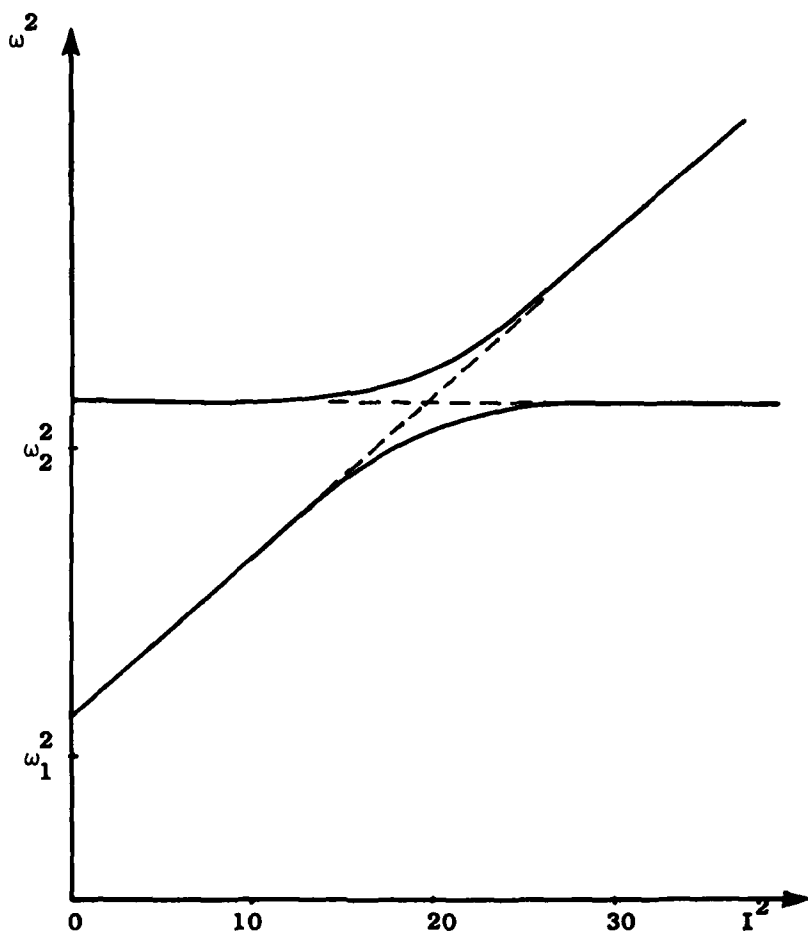


FIG. D-6 VARIATION OF RESONANT MODES OF THE GRADIOMETER. The results are obtained when the frequency of the lower frequency proof mass is increased while that of the second proof mass is left unchanged.

D-4 A More Detailed Model

The model given in Fig. D-3 is not accurate for vibrational frequency close to the natural frequencies of the diaphragms. Since we frequently excite the resonant frequencies of the gradiometer assembly, the following equivalent model including damping is outlined, see Fig. D-7. With

$$\begin{aligned} y(t) &= Y e^{j\omega_f t} \\ \text{and} \quad x_1(t) &= \bar{x}_1 e^{j\omega_f t}, \quad \bar{x}_1 = x_1 e^{-i\phi_1} \\ x_2(t) &= \bar{x}_2 e^{j\omega_f t}, \quad \bar{x}_2 = x_2 e^{-i\phi_2} \end{aligned}$$

The equation of motion in matrix form is

$$\begin{bmatrix} -m_1 \omega_f^2 + (k+k_1) + jc_1 \omega_f & -k \\ -k & -m_2 \omega_f^2 + (k+k_2) + jc_2 \omega_f \end{bmatrix} \begin{bmatrix} \bar{x}_1 \\ \bar{x}_2 \end{bmatrix} = \begin{bmatrix} m_1 \\ m_2 \end{bmatrix} \omega_f^2 Y \dots \quad (D.28)$$

Using the notation of $\omega_1^2 = k_1/m_1$, $\gamma = k/m_1$, $c_1/m_1 = 2\xi_1 \omega_1$, $\omega_2^2 = k_2/m_2$, $\epsilon = k/m_2$, $c_2/m_2 = 2\xi_2 \omega_2$, we have

$$\frac{x_1}{\omega_f^2 Y} = \frac{[\omega_2^2 + \epsilon + \gamma - \omega_f^2 + j2\xi_2 \omega_2 \omega_f]}{D} \quad (D.29a)$$

$$\frac{\bar{x}_2}{\omega_f^2 Y} = \frac{[\omega_1^2 + \gamma + \epsilon - \omega_f^2 + j2\xi_1 \omega_1 \omega_f]}{D} \quad (D.29b)$$

where

$$\begin{aligned} D &= \left[\omega_f^4 - 2(\alpha+\beta)\omega_f^2 + 4\alpha\beta - \gamma\epsilon - 4\xi_1 \xi_2 \omega_1 \omega_2 \omega_f^2 \right] \\ &\quad + j \left[-2\xi_1 \omega_1 \omega_f^2 - 2\xi_2 \omega_2 \omega_f^3 + \xi_1 \omega_1 \beta \omega_f + \xi_2 \omega_2 \alpha \omega_f \right] \end{aligned} \quad (D.29c)$$

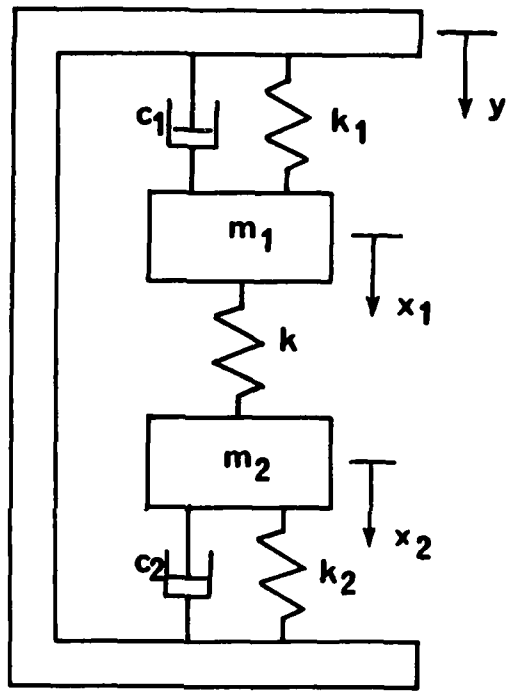


FIG. D-7 A REALISTIC MODEL OF THE GRAVITY GRADIOMETER.
 In this model, the damping elements are introduced to model the finite Q of the resonance oscillations of the proof masses.

$$2\alpha = \frac{k + k_1}{m_1} \quad (D.29d)$$

$$2\beta = \frac{k + k_2}{m_2} \quad . \quad (D.29e)$$

From Eqs. (D.29)

$$\frac{\bar{x}_1 - \bar{x}_2}{\omega_f^2} = \frac{[\omega_2^2 - \omega_1^2 + J^2(\xi_2 \omega_2 \xi_1 \omega_1) \omega_f]}{D} \quad \dots \quad (D.30)$$

Appendix E

SPECTRAL DENSITY OF RANDOM VIBRATION OF A SINGLE DEGREE OF FREEDOM SYSTEM

Consider the spring-mass-damper system given in Fig. D-1. The transfer function, $H(\omega)$ between force and displacement is given by

$$H(\omega) = \frac{X(\omega)}{F(\omega)} = \frac{1}{m(\omega_n^2 - \omega^2 + j2\xi\omega\omega_n)} \quad (E.1)$$

using standard notations.

If the mean square spectral density $S_F(\omega)$ of the actuating force $f(t)$ is white and wideband, the mean square spectral density of the displacement $S_x(\omega)$ is given by [Crandel, 1963]

$$S_x(\omega) = |H(\omega)|^2 S_F(\omega) = \frac{1}{m^2 |\omega_n^2 - \omega^2 + j2\xi\omega\omega_n|^2} S_0 \quad (E.2)$$

where $S_F(\omega) = S_0$ is a constant.

Using equipartition law in physics, we have

$$\frac{1}{2} K \langle x^2 \rangle = \frac{1}{2} kT \quad (E.3)$$

where K is the spring rate, k is Boltzmann's constant 1.38×10^{-23} J/K, and T is the temperature. Simplifying, the relation is

$$\langle x^2 \rangle = \frac{kT}{K} \quad (E.4)$$

As

$$\langle x^2 \rangle = \int_{-\infty}^{\infty} S_x(\omega) d\omega ,$$

for a constant $S_F(\omega)$ we have

$$\langle x^2 \rangle = \frac{S_0}{m^2} \frac{\pi}{2} \frac{1}{\xi \omega_n^3} . \quad (E.5)$$

Equating (E.5) to (E.4), we obtain

$$S_0 = \frac{2}{\pi} \xi \omega_n^3 m^2 \frac{kT}{K} .$$

However, $K = m\omega_n^2$, and using experimental units, the above expression becomes

$$W_0 = 4\pi S_0 = 8\xi m\omega_n kT = \frac{4kTm\omega_n}{Q} \quad (E.6)$$

where $1/2\xi = Q$, which is the Nyquist theorem. The force spectral density is W_0 . If A_0 is defined as W_0/m^2 , (E.4) becomes

$$\langle x^2 \rangle = \frac{W_0}{m^2} \frac{1}{4} \frac{Q}{\omega_n^3} = \frac{A_0 Q}{4\omega_n^3} . \quad (E.7)$$

The spectral density of the input force and one of its possible time history is plotted in Fig. E-1. The diaphragm is a sharply resonant system with high Q ($Q = 2 \times 10^5$). Using the single DOF model, the spectral density and time history of the displacement of the resonant circuit due to the thermal motions are plotted in Fig. E-2.

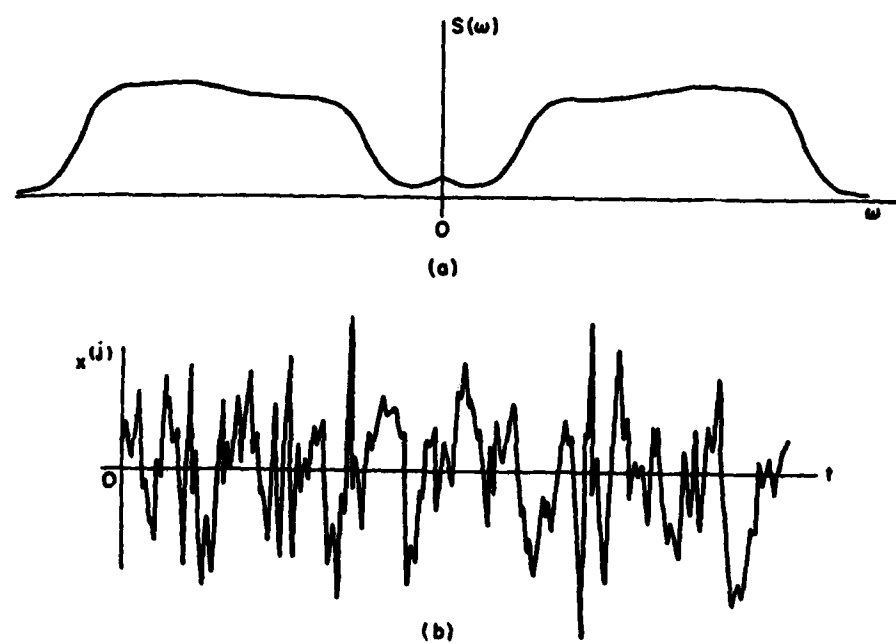
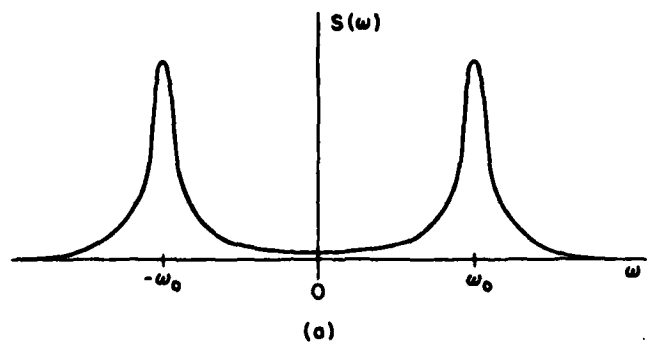
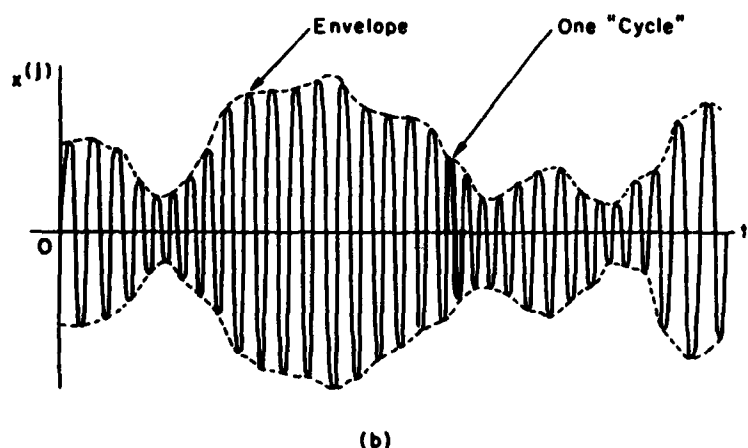


FIG. E-1 POWER DENSITY AND THE TIME FUNCTION OF A BROAD-BAND NOISE.



(a)



(b)

FIG. E-2 POWER SPECTRUM AND TIME FUNCTION OF A NARROW BAND NOISE. The energy is centered about the resonance frequency ω_0 .

Using Eq. (E.2), the spectral density in experimental units is

$$w_x(f) = \frac{4kT\omega_n}{Qm \left[(\omega_n^2 - \omega^2)^2 + \frac{\omega_n^2 \omega^2}{Q^2} \right]} . \quad (E.8)$$

For $f \ll f_n$ and $Q \gg 1$

$$w_x(f) = \frac{4kT}{mQ\omega_n^3} . \quad (E.9)$$

At $f = f_n$

$$w_x(f_n) = \frac{4kT}{m\omega_n^3} Q . \quad (E.10)$$

REFERENCES

Bell Aerospace Report, No. 6324-927001, Jan. 18, 1977.

Beyer, L.A., "Proposed Development of a Gravity Gradiometer for Energy Resource Exploration and Exploitation," U.S. Dept. of the Interior, Geological Survey Branch, Memo to R.P. Sheldon, Chief Geologist, Menlo Park, Calif., Jan. 1973.

Cabrera, Blas, "Electric and Magnetic Shielding with Superconductors," The Science and Technology of Superconductivity Proceedings, Aug. 1971, Georgetown University, Washington D.C., (Gregory, W.D. et al., editors) Vol. 2, Plenum Press, 1973.

Crandell, Stephen H. and Mark, William D., Random Vibration in Mechanical Systems, Academic Press, 1963.

Crede, C.E., Editor, Shock and Vibration Handbook, McGraw Hill, 1961.

Crowley, J.C., Kolodkin, S.S., and Schneider, A.M., "Some Properties of the Gravity Field and Their Possible Application to Space Navigation," Inst. Radio Engrs. Trans. on Space Electron, Telemetry SET-5, pp. 47-54, Mar. 1959.

Diepers, H., Schmidt, D., Martens, H., and Sun, F.S., Physics Letters, 37A, 139, 1971.

Diesel, John W., "A New Approach to Gravitational Gradient Determination of the Vertical," AIAA Journal, Vol. 2, No. 7, pp. 1189-1196, Jul. 1964.

Forgacs, R.L., "Digital-Analog Magnetometer Using Superconducting Sensor," Review of Scientific Instruments, Vol. 38, No. 2, pp 214-220, Feb. 1967.

Forward, Robert L., "Moving Base Rotating Gravity Gradiometer Development," Hughes Research Lab. Report No. 461, Feb. 1973.

Forward, R.L., "Research on Electronic Cooling of Resonant Mechanical Sensors," Hughes Research Report No. 77M-0673/E1197, Jul. 1977.

Forward, R.L., "Electronic Damping of Vibrations in Optical Structures," Applied Optics, Vol. 18, p. 690, Mar. 1, 1979.

Forward, R.L., "Geodesy with Orbiting Gravity Gradiometers," The Use of Artificial Satellites for Geodesy, Geophysical Monograph Series, Vol. 15, American Geophysical Union, Washington, D.C., circa 1973.

Graeme, Gerald G., Tobey, Gene E., Huelsman, Lawrence P., Operational Amplifier, Design and Application, McGraw Hill, 1971.

Handelman, George, et al., "On the Effects of the Addition of Mass to Vibrating Systems," Proc. 9th Int. Congr. Applied Mechanics, Vol. 2 pp. 509-518, 1957.

Hansen, S., "Horizontal Gravity Gradiometer," Hughes Research Labs., Malibu, Calif., Research Rept. 437, Mar. 1971.

Heller, W.G., "Gradiometer Aided Inertial Navigation," The Analytic Sciences Corp., Reading, Mass., TR-312-5, Apr. 1975.

Hirakawa, H., "Artificial Cold Resistors," Japanese J. of Applied Physics, Vol. 17, No. 2, pp. 429-532, Feb. 1978.

Kittel, C., Elementary Statistical Physics, pp. 141-156, Wiley & Sons, 1958.

Karamcheti, K., Vector Analysis and Cartesian Tensors, Holden-Day Inc., San Francisco, Calif., 1967.

Lounasmaa, O., Experimental Principles and Methods Below 1 Kelvin, (Ch. Seven), Academic Press, 1974.

Love, A.E.H., A Treatise on the Mathematical Theory of Elasticity, Dover Publication, New York, 1944.

MACSYMA Reference Manual, Version 8, Project MAC, Math Lab Group, MIT, Cambridge, Mass., 1975.

McCombie, C.W., "Fluctuation Theory in Physical Measurement," Rept. Prog. Physics, Vol. 16, pp. 266-, 1953.

McLaren, I., "Open and Closed-Loop Accelerometers," AGARDograph AG-160, AGARD, NATO, Jul. 1974.

Paik, H.J., "Analysis and Development of a Very Sensitive Low Temperature Gravitational Radiation Detector," Ph.D. Thesis, Dept. of Physics, Stanford University, Stanford, Ca., 94305, 1974.

Paik, H.J., "Superconducting Tunable Diaphragm Transducer for Sensitive Acceleration Measurements," J. Applied Physics, Vol. 47, No. 3, pp. 1168-1178, Mar. 1976.

Pelka, Eugene, "On-Line Parameter Estimation and Control for a Rotating Gravity Gradiometer," Ph.D. Thesis, Dept. Aeronautics and Astronautics, Guidance & Control Lab., Stanford, Calif., 94305, Aug. 1977.

Rao, S.S., "Vibrations of Annular Plates Including the Effects of Rotating Inertia and Transverse Shear Deformation," J. of Sound and Vibration, Vol. 42, No. 3, pp. 305-324, Oct. 1975.

Roberson, R.E., "Gravity Gradient Determination of the Vertical," American Rocket Society J., Vol. 31, pp. 1509-1515, 1961.

Rose - Innes, Introduction to Superconductivity, Pergamon Press, 1969.

Savet, P.H., "New Developments in Gravity Gradiometers," Advances in Dynamic Gravimetry, Proc. of the Symposium on Dynamic Gravimetry, Fort Worth, Texas, Mar. 1970.

SHE Manufacturer Handbook, S.H.E. Corporation, San Diego, Ca., 92121, 1976.

Thompson, L.G.D., et al., "Gravity Gradient Sensors and their Applications for Manned Orbital Spacecraft," 3rd Goddard Memorial Symposium, AAS, Washington, D.C., Mar. 1965.

Thompson, L.G.D., "Gravity Gradient Instruments Study," Final Report NASA Contract No. NASW-1328, Aug. 1966.

Thompson, L.G.D., "The Quartz Gravity Gradiometer," General Oceanology, Oct. 1970.

Timoshenko, S., and Woinowsky-Drieger, S., Theory of Plates and Shells, McGraw Hill, Second Edition, pp. 51-63, 1959.

Trageser, M.B., "A Gradiometer System for Gravity Anomaly Surveying," Advances in Dynamic Gravimetry (William Kattner, Editor); Proc. of the Symposium on Dynamic Gravimetry, Fort Worth, Texas, Mar. 1970.

Trageser, M.B., "Feasibility Model Gravity Gradiometer Test Results," Report No. P-179, C. S. Draper Lab., Cambridge, Mass., Jul. 1975.

Van der Ziel, Aldert, Noise, Prentice Hall, New York, 1954.

Van der Ziel, Aldert, Noise: Sources, Characterization, Measurement, Prentice Hall, Englewood Cliffs, New Jersey, 1970.

Vierck, R.K., Vibration Analysis, International Textbook Co., 1967.

Volmir, "A Translation of Flexible Plates and Shell," Technical Rept., Air Force Flight Dynamics Lab., Dayton, Ohio, No. AFFDL-TR-66-216, pp. 204-205, Apr. 1967.

Wahl and Lobo, "Stresses and Deflections in Flat Circular Plates with Central Holes," Trans. ASME, Vol. 52, APM, pp. 29-43, 1930.

Weber, Joseph, Phys. Rev. Letter, Vol. 22, 1969.

Weber, Joseph, Phys. Rev. Letter, Vol. 24, 1970.

Wigley, D.A., Mechanical Properties of Materials at Low Temperatures, Plenum Press, 1971.

William, O.P., "Gradiometry: An Assessment of the State of the Art," Defense Mapping Agency, Washington, D.C., Sept. 1974.

Worden, Paul W., "A Cryogenic Test of the Equivalence Principle," Physics Dept. Report, Stanford University, Mar. 1976.

Yeh, Kay-Yuan, "Large Deflections of a Circular Plate with a Circular Hole at the Center," ACTA Scientia Sinica, Vol. 2, pp. 127-144, 1952.

Zimmerman, J.E., "Josephson Effect Devices and Low Frequency Field Sensing," Cryogenics, pp. 19-30, Feb. 1972.